ISSN 2699-1020

Mahmoud Qarmout Tunnel face stability using Kinematical Element Method

70

RUHR-UNIVERSITÄT BOCHUM

Mahmoud Qarmout

Tunnel face stability using Kinematical Element Method (KEM)

Bochum 2019

Heft 70

Schriftenreihe des Lehrstuhls für
Bodenmechanik, Grundbau und Umweltgeotechnik

Herausgeber: Torsten Wichtmann

ISSN 2699-1020

Ruhr-Universität Bochum
Schriftenreihe Bodenmechanik, Grundbau und Umweltgeotechnik
Heft 70

Herausgeber:
Prof. Dr. -Ing. habil. Torsten Wichtmann
Ruhr-Universität Bochum
Fakultät für Bau- und Umweltingenieurwissenschaften
Lehrstuhl für Bodenmechanik, Grundbau und Umweltgeotechnik
44801 Bochum
Telefon: 0234/ 3226135
Telefax: 0234/ 3214236
Internet: www.bgu.ruhr-uni-bochum.de

ISSN 2699-1020

© 2019 der Herausgeber

Tunnel face stability using Kinematical Element Method (KEM)

Dissertation

as a requirement of the degree of
Doktor-Ingenieur (Dr.-Ing.)

at the Faculty of
Civil and Environmental Engineering
Ruhr-Universität Bochum

submitted by
Mahmoud Qarmout

Reviewers
Prof. Dr.-Ing. habil. Torsten Wichtmann
Prof. Dr.-Ing. Markus Thewes
Dr.-Ing. Peter Gussmann

Bochum, 2019

Vorwort des Herausgebers

Herr Qarmout hat sich in seiner Dissertation mit der Stabilität der Ortsbrust beim maschinellen Tunnelvortrieb auseinandergesetzt. Für den minimal erforderlichen Stützdruck, der vom Schild einer Tunnelbohrmaschine auf die Ortsbrust wirken muss, existiert eine Reihe analytischer und numerisch basierter Ansätze, die aufgrund unterschiedlicher Annahmen bezüglich der Kinematik oder Statik des Bruchmechanismus zum Teil jedoch deutlichvoneinander abweichende Ergebnisse liefern. Herr Qarmout hat erstmals die Kinematische Elemente Methode (KEM) zur Lösung des Problems der Ortsbruststabilität eingesetzt. Während die Anwendung der KEM bisher im Wesentlichen auf ebene Probleme (2D) begrenzt war, handelt es sich bei der Untersuchung von Herrn Qarmout um eine Erweiterung auf den 3D-Fall. Ziel der Arbeit ist es, kinematisch mögliche 3D-Bruchmechanismen für das Problem der Ortsbruststabilität mit Hilfe der KEM zu untersuchen, die Ergebnisse mit anderen Lösungen aus der Literatur zu vergleichen und â für ausgewählte Randbedingungen â die KEM-Modelle durch den Abgleich mit Messungen in Modellversuchen zu validieren. Herr Qarmout hat drei kinematisch mögliche Bruchmechanismen, jeweils bestehend aus mehreren Starrkörpern, mit Hilfe der KEM untersucht. Hierfür hat er die Gleichungen der KEM zur Lösung der Kinematik, Statik und Optimierung der Geometrie der Bruchkörper in ein Matlab-Skript mit graphischer Benutzeroberfläche implementiert. Die Visualisierung der Kinematik ist dabei besonders hilfreich, um eine Vorstellung von den Verschiebungsvorgängen in den komplexen 3D-Mehrkörpermodellen zu bekommen. Die Ergebnisse der eigenen KEM-Simulationen für den erforderlichen Stützdruck vergleicht Herr Qarmout mit den Prognosen anderer Ansätze aus der Literatur. Hierfür gibt er zunächst einen ausführlichen Überblick über die verschiedenen existierenden Ansätze, bevor er die Unterschiede der mit seinen und mit den verschiedenen vorhandenen Ansätzen berechneten Stützdrücke in Abhängigkeit der Bodenparameter und der Geometrie herausarbeitet. Für ausgesuchte Randbedingungen validiert er die KEM-Modelle anhand der Nachrechnung von 1g- bzw. ng-Modellversuchen. Auf Basis von Parameterstudien unter Einsatz der KEM-Modelle leitet Herr Qarmout einfache Bemessungsansätze für die praktische Anwendung ab. Beim maschinellen Tunnelvortrieb mit Flüssigkeitsstützung unterhalb des Grundwasserspiegels treten in Abhängigkeit der verwendeten Stützsuspension und der Bodenverhältnisse Porenwasserüberdrücke vor der Ortsbrust auf. Herr Qarmout hat seine KEM-Modelle dahingehend erweitert, dass er solche Porenwasserüberdrücke berücksichtigen kann und zeigt deren Einfluss auf die Ortsbruststabilität auf. Für einfache Randbedingungen, z.B. einen in Höhe der Geländeoberkante stehenden Grundwasserspiegel, leitet er auch hier Bemessungsansätze für die praktische Anwendung ab. Herr Qarmout hat mit dieser Arbeit einen sehr kompletten Satz anBemessungshilfen für das Problem der Ortsbruststabilität geschaffen.

Bochum, November 2019

Prof. Dr.-Ing. habil. Torsten Wichtmann

This work is dedicated to my beloved sons

Ahmed and Mohamed

Acknowledgements

This research was carried out in the Chair of Soil Mechanics, Foundation Engineering and Environmental Geotechnics at Ruhr-Universität Bochum. Firstly, I would like to thank Prof. Tom Schanz for giving me the wonderful opportunity to complete my Ph.D thesis under his supervision, it is truly an honor. Thank you for all the advice, ideas, moral support and patience in guiding me through my research work.

I would like to thank Prof. Torsten Wichtmann for his continuous support on my Ph.D thesis when Prof. Schanz passed away.

I am very much grateful to my committee members, Prof. Torsten Wichtmann, Prof. Markus Thewes and Prof. Peter Gussmann, for their insightful comments and continuous support. I would also wish to express my gratitude to Prof. Peter Gussmann for extended discussions and valuable suggestions which have contributed greatly to the improvement of my thesis.

My sincere gratitude also goes to Dr.-Ing Diethard König for his continuous help and innumerable constructive suggestions during my research work. His friendly guidance and expert advice have been invaluable throughout all stages of my research.

I would give my warm gratitude to my colleagues in RUB who provided me so much help in my research, especially Dr.-Ing Jamal Alabdullah, Mr. Firas Ghrairi, Mr. Reinhard Mosinski and our secretary Mrs. Traas for their help and support.

Last but not least, I wish to gratitude my family for the whole support they have always extended to me. Without their help I would not have been able to accomplish this work.

Bochum, Germany
August 2019
Mahmoud Qarmout

Abstract

The determination of adequate tunnel face support pressure is one of the fundamental issues in tunnel excavation using a tunnel boring machine, which ensures the safety of the excavation and prevents the collapse of the tunnel face. In this research, using KEM (Kinematical Element Method), a new calculation procedure is introduced to investigate the stability of a circular tunnel face. Three KEM models (M), (M1) and (M2) have been developed with different 3D failure mechanisms. KEM models (M1) and (M2) are developed based on KEM model M. In KEM models (M) and (M1), the cross section of the tunnel face is assumed to be a triangle, whereas, it is assumed to be a square in KEM model (M2). In order to incorporate the contribution of the 3D arching in predicting the minimum support pressure, a 3D active earth pressure acting on the vertical slip surfaces from the adjoining soil is presumed for the three KEM models.

To evaluate the validity of the KEM models, a comparison between the results of KEM models M and M2 with the results of analytical models, based either on the limit equilibrium method or the limit analysis method (upper bound solution), and numerical models using the finite element method has been undertaken. Also, a parametric analysis has been carried out on KEM models (M) and (M2) to study the influence of cover depth to tunnel diameter ratio (C/D), internal friction angle of the soil (φ) and soil cohesion (c) on the normalized support pressure ($p_u/(\gamma D)$). The results of the parametric study are provided in form of design equations and stability charts for convenient use in practice.

In case of open face tunneling, KEM models (M) and (M2) have been applied to estimate the factor of safety of the tunnel face using the Strength Reduction Method (SRM). The computed factors of safety have been compared to the results of other existing approaches. In addition, using KEM model (M2), the influence of hydrostatic and excess pore pressure on the stability of the tunnel face during tunnel excavation has been investigated.

Finally, general conclusions regarding the results of KEM models (M), (M1) and (M2) are drawn and further suggestions for future studies are presented.

Zusammenfassung

Das Festlegen des geeigneten Stützdrucks an der Ortsbrust ist eine wichtige Aufgabe beim maschinellen Tunnelvortrieb, um ein Versagen der Ortsbrust zu vermeiden und die Sicherheit des Vortriebs zu gewährleisten. In dieser Arbeit werden auf Basis der Kinematischen Element Methode (KEM) drei neue Ansätze zur Berechnung der Stabilität der Ortsbrust eines Tunnels mit Kreisquerschnitt entwickelt (M, M1 und M2). Ausgangspunkt der Entwicklung ist das Modell M, in dem ebenso wie bei Model M1 die kreisförmige Ortsbrust durch eine Dreiecksfläche ersetzt wird. Im Modell M2 wird die kreisförmige Ortsbrust durch ein Quadrat abgebildet. In allen drei Modellen wird die Gewölbebildung im Boden oberhalb des Tunnels berücksichtigt. Hierzu wird angenommen, dass ein räumlicher aktiver Erddruck auf die vertikalen Seitenflächen des Bruchmechanismus wirkt.

Die Ergebnisse der Modelle M und M2 werden mit den Ergebnissen existierender analytischer Ansätze, welche entweder auf der Limit Equilibrium Method oder auf der Limit Analyses Method (obere Schranke) beruhen, und mit Ergebnissen von numerischen Simulationen verglichen. Parameterstudien zeigen den Einfluss der Überdeckungshöhe, des Reibungswinkels und der Kohäsion des Bodens auf den erforderlichen Stützdruck. Die Ergebnisse der Parameterstudien werden in Form praktisch anwendbarer Bestimmungsgleichungen und Bemessungsdiagrammen aufbereitet.

Für den Fall des Tunnelvortriebs mit nicht gestützter Ortsbrust wird mit den Modellen M und M2 die Standsicherheit der Ortsbrust mit der Methode der φ - c Reduktion ermittelt. Die Ergebnisse werden mit denen vorhandener Methoden verglichen. Zusätzlich wird mit dem Model M2 der Einfluss des Grundwassers und von Porenwasserüberdrücken auf die Ortsbruststabilität untersucht.

Contents

Vorwort des Herausgebers iii

Acknowledgements vii

Abstract ix

Zusammenfassung xi

1 Introduction 1

1.1 Motivation and objectives 1

1.1.1 Motivation 1

1.1.2 Objectives 4

1.2 Contents of the thesis 7

2 State of the art 9

2.1 Introduction 9

2.2 Overview on various tunnel excavation methods 10

2.2.1 The conventional method 10

2.2.2 Mechanized method 11

2.2.2.1 Open face tunneling 12

2.2.2.2 Closed face tunneling 12

2.3 Overview on tunnel face stability analysis models 15

2.3.1 Tunnel face stability analysis in case of frictional or frictional-cohesive soil 15

2.3.1.1 Limit Equilibrium Method (LEM) 15

2.3.1.2 Limit Analysis Method (LAM) 26

2.3.1.3 Finite Element Limit Analysis (FELA) 30

2.3.1.4 Numerical methods 33

2.3.1.5 Physical model tests 36

2.3.2 Tunnel face stability analysis in case of purely cohesive soils 38

2.4 Comments on the wedge-silo model 44
  2.4.1 Failure mechanism and failure zone 44
  2.4.2 Shape of tunnel cross section 46
  2.4.3 Effect of K_{silo} on the vertical stress 49
2.5 Conclusions 50

3 Kinematical Element Method (KEM) 53
3.1 General 53
3.2 Application of KEM in geotechnical problems 54
3.3 Geometry 56
3.4 Kinematic analysis 58
3.5 Static analysis 60
3.6 Optimization process 61

4 KEM model (M) for tunnel face stability 65
4.1 Introduction 65
4.2 KEM model (M) for tunnel face stability 65
  4.2.1 Geometry of the failure mechanism 65
  4.2.2 Equivalent area of the tunnel face 67
  4.2.3 Half of KEM model (M) 67
  4.2.4 Kinematic analysis 68
  4.2.5 Acting forces 70
  4.2.6 Problem of indeterminacy 72
  4.2.7 Setting up the static system 72
4.3 3D lateral earth pressure coefficient 74
4.4 Optimization procedure 79
4.5 Development of failure mechanism by optimization process 81
4.6 Verification by physical model tests 81
4.7 Comparison of the KEM model (M) results with other approaches 84
  4.7.1 Comparison of the KEM model (M) results with the existing approaches 85
  4.7.2 Comparison of KEM model (M) with Finite Element Limit Analysis (FELA) results 87
    4.7.2.1 Modeling of tunnel face stability in OptumG3 87
    4.7.2.2 Results and discussion 88
4.8 Parametric studies with the KEM model (M) 92
  4.8.1 Influence of friction angle 92

4.8.2 Influence of the cohesion . . . 92
4.8.3 Influence of cover depth to diameter ratio (C/D) . . . 93
4.9 Development of design equations . . . 94
4.10 Limitations of KEM model (M) . . . 99
4.11 KEM 3D tunnel face stability software (KEM-3D-T) . . . 101
4.12 Summary . . . 111

5 Modified KEM models (M1 and M2) 113
5.1 Introduction . . . 113
5.2 Multiblocks failure mechanism (M1) . . . 114
5.2.1 Geometry . . . 114
5.2.2 Kinematic analysis . . . 114
5.2.3 Static analysis . . . 114
5.2.4 Discussion and comments on KEM model (M1) . . . 116
5.3 Multiblocks failure mechanism (M2) . . . 120
5.3.1 Geometry . . . 120
5.3.2 Kinematic analysis . . . 121
5.3.3 Static analysis . . . 121
5.4 Comparison of KEM model (M) with KEM model (M2) . . . 125
5.5 Comparison with other existing approaches . . . 125
5.5.1 Homogeneous soil . . . 125
5.5.2 Layered soil . . . 127
5.6 Development of design equations based on KEM model (M2) simulations . 131
5.7 Open-face tunneling . . . 132
5.7.1 Factor of safety for open-face tunneling . . . 136
5.7.2 Maximum tunnel diameter for open-face tunneling . . . 140
5.8 Practical examples . . . 142
5.8.1 Closed-face tunneling . . . 142
5.8.1.1 Determining the minimum support pressure . . . 142
5.8.1.2 Determination of maximum cover depth . . . 142
5.8.2 Open-face tunneling . . . 143
5.8.2.1 Determination of the safety factor . . . 143
5.8.2.2 Determination of the maximum tunnel diameter . . . 143
5.9 Summary . . . 144

6 Effect of excess pore pressure on the stability of the tunnel face 145
6.1 Introduction . . . 145

6.2 Stresses in soil under hydrostatic conditions . . . 147
6.3 Safety factors . . . 148
6.4 Blow out . . . 149
6.5 Bezuijen models . . . 149
  6.5.1 Bezuijen model for excess pore pressure distribution during drilling phase . . . 149
  6.5.2 Bezuijen model for decrease of pore pressure during stand-still phase 152
6.6 Implementation of excess pore pressures into different models. . . . 153
  6.6.1 Implementing the excess pore pressure in wedge-silo model . . . 154
  6.6.2 Implementing the excess pore pressure in KEM model (M2) . . . 158
6.7 Problem definition . . . 158
6.8 Results and discussion . . . 159
  6.8.1 Effect of hydrostatic pore pressure on the tunnel face stability . . . 159
  6.8.2 Effect of hydrostatic and excess pore pressures on the tunnel face stability . . . 164
6.9 Drops in piezometric head with time during stand-still phase . . . 168
6.10 Practical example . . . 177
  6.10.1 Determination of operational support pressure considering only hydrostatic pore pressure . . . 182
  6.10.2 Determination of operational support pressure considering hydrostatic and excess pore pressures . . . 182
6.11 Summary . . . 183

7 Conclusions and future work **185**
7.1 Conclusions . . . 185
7.2 Future work . . . 188

Bibliography **191**

List of Figures

1.1 Vertical and horizontal arching during excavation of the tunnel: (a) vertical arching above the tunnel face; (b) horizontal arching at the front of the tunnel face . . . 2
1.2 Guiding methodology for the proposed research using KEM models . . . 5
1.3 Guiding methodology for the existing approaches . . . 6

2.1 Tunnel San Fedele, Switzerland (tunnelingonline, 2019) . . . 11
2.2 Earth Pressure Balance TBM, Chapman et al. (2017): (a) 3D schematic representation of EPB; (b) longitudinal section through an EPB . . . 13
2.3 3D Horn's model, Horn (1961): (a) Horn's failure mechanism; (b) forces acting on the wedge . . . 15
2.4 3D limit equilibrium model: (a) failure mechanism of wedge-silo model; (b) a strip of soil in arching silo . . . 17
2.5 Vertical and shear stress distribution on the wedge: (a) vertical stress; (b) shear stress . . . 17
2.6 (a) Circular tunnel face approximated by a square and the force equilibrium on wedge; (b) forces acting on the wedge; (c) force polygon . . . 18
2.7 K_{silo} and K_{wedge} assumed by various approaches: (a) variation of K_{silo} with friction angle; (b) variation of K_{wedge} with friction angle . . . 20
2.8 Forces acting on infinitesimally small slices on the wedge . . . 22
2.9 Vertical stress distribution for different approaches, either considering arching or not: (a) vertical stress distribution; (b) top view of failure mechanism; (c) side view of failure mechanism . . . 23
2.10 Improved wedge-silo model, Chen et al. (2015) . . . 24
2.11 3D model for tunnel face stability, Liu et al. (2019): (a) 3D failure mechanism; (b) Rotational failure zone; (c) geometric relationships between the slip surface and tunnel face . . . 25
2.12 Failure mechanisms at the front of tunnel face, Krause (1987): (a) half cylinder; (b) quarter circle; (c) half sphere . . . 26

2.13 Upper bound failure mechanisms, Leca & Dormieux (1990): (a) one conical failure mechanism; (b) two conical failure mechanisms; (c) cross section of the tunnel face 27

2.14 Conical multiblocks failure mechanism, Mollon et al. (2010) 29

2.15 Combined multiblocks failure mechanism, Han et al. (2016) 29

2.16 Comparison of rigid block mechanism with finite element limit analysis, Yamamoto et al. (2011): (a) rigid block mechanism; (b) power dissipation; (c) deformed mesh 31

2.17 Finite Element Limit Analysis for the stability of dual circular tunnel, Yamamoto et al. (2013): (a) plane-strain dual circular tunnels in cohesive-frictional soil; (b) finite element mesh for $C/D = 1$, showing boundary conditions for numerical limit analysis 32

2.18 Principal stresses (a-c) and incremental displacements (d-f) at failure, C/D = 5 (The graded shades from blue to red describe the increase amount of displacement finite element simulations of Vermeer et al. (2002)) 33

2.19 Numerical results of incremental displacements for $C/D = 1$, Kirsch (2010*b*): (a) Mohr-Coulomb model; (b) hypoplastic model 34

2.20 Approximated extension of soil arching zone around a tunnel, Lin et al. (2018) 35

2.21 Shape of the failure mechanism observed in physical model tests: (a) observed failure mechanism for different C/D ratios, Chambon & Corte (1994); (b) observed failure mechanism in dense sand, Messerli et al. (2010); (c) observed failure mechanism in loose sand, Kirsch (2009); (d) observed failure mechanism in low-speed case, Liu et al. (2018) 37

2.22 Unsupported circular vertical opening, Broms & Bennermark (1967) . . . 39

2.23 Lower bound solution for tunnel heading, Davis et al. (1980): (a) plane strain circular tunnel; (b) plane strain tunnel heading; (c) circular tunnel heading for fully lined tunnels 41

2.24 Upper bound mechanisms, Davis et al. (1980): (a) mechanism A; (b) mechanism B; (c) mechanism C; (d) mechanism D 42

2.25 3D collapse mechanisms based on upper bound solution, Mollon et al. (2012): (a) two blocks failure mechanism; (b) three blocks failure mechanism; (c) five blocks failure mechanism 42

2.26 Comparison of failure geometries in physical model tests and wedge-silo model: (a) wedge-silo model failure mechanism; (b) schematic diagram of failure mechanism, Local collapse; (c) global collapse ($C/D = 0.5$), Idinger et al. (2011); (d) local collapse ($C/D = 1.5$), Idinger et al. (2011) 45

2.27 Different approximations of the circular tunnel cross-section by either a square or a rectangle in the wedge-silo model: (a) $A_c = A_s$; (b) $A_c < A_s$; (c) $A_c = A_r$ 47

2.28 Vertical stress distribution with different values of K_{silo} 49

3.1 KEM models for different geotechnical stability problems, Gussmann et al. (2016): (a) bearing capacity of footing; (b) trapdoor problem; (c) vertical anchor plate 54

3.2 Basic element of KEM 2D model: a) triangle element; b) irregular polygon element 55

3.3 Basic element of KEM 3D model: (a) tetrahedron element; (b) pyramid element; (c) triangular prism 55

3.4 KEM model for 3D passive earth pressure (modified from Gussmann (1986)) 57

3.5 Boundary conditions and kinematics for KEM 2D passive earth pressure problem 57

3.6 Forces acting on the edge of 2D KEM element 60

3.7 Flowchart for PSO algorithm 62

4.1 Geometry of the failure mechanism 66

4.2 Geometry of the triangle 67

4.3 Geometry of the failure mechanism: (a) KEM model (M); (b) KEM model (M) considering the symmetry of the failure mechanism 68

4.4 Approximated shape of the tunnel face: (a) KEM model (M); (b) half of KEM model 69

4.5 Kinematic of the blocks 69

4.6 Displacement hodograph with respect to the soil at rest O 70

4.7 The free-body diagram: (a) KEM model (M); (b) half of KEM model (M) 71

4.8 Shape of the failure mechanism observed in physical model tests and numerical simulations: (a) observed failure mechanism for different C/D ratios, Chambon & Corte (1994); (b) distribution of stress concentration, Chen et al. (2013); (c) failure zone from DEM simulations, Chen et al. (2011) (A: limited displacement of tunnel face displacement/diameter = 0.043, B: elevated displacement of tunnel face displacement/diameter = 0.269); (d) variation of horizontal stress, Chen et al. (2011) (A: limited displacement of tunnel face displacement/diameter = 0.043, B: elevated displacement of tunnel face displacement/diameter = 0.269) 73

4.9 Forces transferred from 3D active earth pressure model to tunnel face stability model 75

4.10 KEM model for 3D active earth pressure problem: (a) geometry of the failure mechanism; (b) half of KEM model 75

4.11 Comparison of K_{3D} value obtained from different methods with results from KEM model for 3D active earth pressure problem; (a) $\varphi = 20^o, \delta = 0^o$; (b) $\varphi = 30^o, \delta = 0^o$; (c) $\varphi = 40^o, \delta = 0^o$ 76

4.12 Comparison of experimental and numerical results with results from KEM model (M), $\varphi = 31.7^o$ 77

4.13 3D lateral earth pressure coefficient K_{3D} for different friction angles (φ) obtained from KEM model 78

4.14 3D lateral earth pressure coefficient K_{3D} obtained from KEM model and its approximation by Eq. (4.9) 78

4.15 Flow chart for the procedure of calculating the support pressure in KEM model (M) 80

4.16 Iteration steps in the optimization process: (a) the failure mechanism; (b) development of the failure mechanism; (c) minimum support pressure; (d) 3D active earth pressure coefficient 82

4.17 Comparison of $p_u/(\gamma D)$ value obtained from the KEM model (M) with physical model tests: (a) $p_u/(\gamma D)$ obtained from KEM model (M) compared to ng tests of Kirsch (2009); (b) $p_u/(\gamma D)$ obtained from KEM model (M) compared to ng tests of Chen et al. (2013); (c) $p_u/(\gamma D)$ obtained from KEM model (M) (c = 0 kPa) compared to ng tests of Chambon & Corte (1994); (d) $p_u/(\gamma D)$ obtained from KEM model (M) (c = 5 kPa) compared to ng tests of Chambon & Corte (1994) 83

4.18 Comparison of N_γ values obtained from different approaches in the literature for different friction angles with the results of KEM model (M) 86

4.19 Comparison of N_c value obtained from the theoretical methods using different friction angles with KEM model (M) 86

4.20 Geometry the boundary conditions of tunnel for the 3D model 89

4.21 Finite element mesh with mesh adaptivity 89

4.22 Upper bound results of 3D FELA model showing shear strain 90

4.23 Comparison of normalized support pressure as a function of C/D ratio obtained from KEM model (M), FELA (lower and upper bound solutions) and different approaches from the literature 91

4.24 Influence of friction angle on normalized support pressure for two different values of cohesion and different values of C/D ratio; results obtained with KEM model (M): (a) $c = 4$ kPa; (b) $c = 8$ kPa 92

4.25 Influence of cohesion on normalized support pressure for two different values of cohesion and different values of C/D ratio; results obtained with KEM model (M): (a) $C/D = 1$; (b) $C/D = 2$ 93

4.26 Influence of cover to diameter ratio C/D on normalized support pressure for two different values of cohesion and different friction angles for the results obtained with KEM model (M): (a) $c = 4$ kPa; (b) $c = 8$ kPa . . . 94

4.27 N_γ as function of the soil friction angle, KEM model (M) 95

4.28 N_c as function of the soil friction angle, KEM model (M) 95

4.29 N_q as function of the soil friction angle, KEM model (M) 96

4.30 Fitting curves for the approximated equations of (a) N_γ, (b) N_c, (c) N_q . . 97

4.31 Design charts for the minimum support pressure, KEM model (M) ($q = 0$ kPa): (a) $C/D = 0.5$; (b) $C/D = 1$; (c) $C/D = 1.5$; (d) $C/D = 2$ 98

4.32 Geometry of the tunnel face in KEM model (M) 100

4.33 Shape of the wedge in wedge-silo model and KEM model (M): (a) wedge-silo model; (b) KEM model (M) 100

4.34 Tunnel face collapse in undrained clays, Schofield (1980) 101

4.35 KEM-3D-T opening screen 102

4.36 KEM-3D-T shows the failure mechanism for KEM Model (M) 103

4.37 KEM-3D-T shows the support force for KEM Model (M) 104

4.38 KEM-3D-T shows the support force for KEM Model (M) without displaying the color and the number of the nodes 105

4.39 KEM-3D-T shows the virtual displacements for KEM Model (M) 106

4.40 KEM-3D-T shows the virtual displacements for KEM Model (M1) with three elements 107

4.41 KEM-3D-T shows the virtual displacements for KEM Model (M1) with four elements . . . 108

4.42 KEM-3D-T shows the failure mechanism of KEM Model (M2) . . . 109

4.43 KEM-3D-T shows the virtual displacements for KEM Model (M2) . . . 110

5.1 Geometry of the failure mechanism, KEM model (M1) using KEM-3D-T . 115

5.2 Geometry of equilateral triangle for KEM model (M1) . . . 115

5.3 Kinematic of the blocks for KEM model (M1) using KEM-3D-T . . . 116

5.4 Failure mechanism for different numbers of elements for KEM model (M1) using KEM-3D-T with $\varphi = 25^o$, $c = 0$ kPa: (a) 2 elements; (b) 3 elements; (c) 4 elements; (d) 5 elements . . . 117

5.5 Kinematics for different numbers of elements using KEM-3D-T with $\varphi = 25^o$, $c = 0$ kPa: (a) 2 elements; (b) 3 elements; (c) 4 elements; (d) 5 elements 118

5.6 Improvement of support pressure versus number of blocks for model (M1) . 119

5.7 Variation of the inclination angle θ of the surface at the bottom of the silo: (a) inclination angle for the silo (θ) with the number of blocks; (b) width of the silo (x) with the number of blocks . . . 120

5.8 KEM model (M2): (a) geometry of the failure mechanism; (b) geometry of the tunnel face; (c) half of the model . . . 122

5.9 Forces transferred from 3D active earth pressure model to tunnel face stability model (M2) . . . 123

5.10 3D lateral earth pressure coefficient (K_{3D}) as a function of C/D different friction angles (φ) used for KEM model (M2) . . . 123

5.11 3D lateral earth pressure coefficient (K_{3D}) obtained from the KEM simulations fitted by Eq. (5.4) . . . 124

5.12 Comparison of KEM model (M) with KEM model (M2) for (a) cohesionless soil and (b) frictional-cohesive soil . . . 124

5.13 Normalized support pressure ($p_u/(\gamma D)$) as function of normalized cohesion ($c/(\gamma D)$), comparison of results of KEM models (M1) and (M2) with other approaches from the literature: (a) $\varphi = 20^o$ and $C/D = 1$; (b) $\varphi = 40^o$ and $C/D = 1$ . . . 126

5.14 Model considering two layers of soil . . . 127

5.15 Minimum support pressure as a function of different friction angles . . . 129

5.16 $K_{silo} \cdot \tan\varphi$ as a function of the friction angle of the cover layer obtained from different approaches . . . 129

5.17 Vertical stress distribution in different models: (a) Anagnostou & Kovari (1994) model; (b) Broere (2001) model; (c) Jancsecz & Steiner (1994) model 130
5.18 N_γ as function of the soil friction angle, KEM model (M2) 132
5.19 N_c as function of the soil friction angle, KEM model (M2) 133
5.20 N_q as function of the soil friction angle, KEM model (M2) 133
5.21 Fitting curves for the approximated equations of (a) fitting curve for N_γ, (b) fitting curve for N_c and (c) fitting curve for N_q 134
5.22 Design charts for the minimum support pressure for KEM model (M2) (q = 0 kPa): (a) $C/D = 0.5$; (b) $C/D = 1$; (c) $C/D = 1.5$; (d) $C/D = 2$ . . . 135
5.23 Safety factor (F_s) as function of normalized cohesion ($c/(\gamma D)$) Comparison of different approaches for (a) $\varphi = 20^o$, $C/D = 1$ and (b) $\varphi = 40^o$, $C/D = 1$138
5.24 Safety factor as function of normalized cohesion for different friction angles ($q = 0$ kPa) for KEM model (M2): (a) $C/D = 0.5$; (b) $C/D = 1$; (c) C/D = 1.5; (d) $C/D = 2$ 139
5.25 Maximum diameter (D_{max}) in open face tunneling with q = 0 kPa 141

6.1 Infiltration mechanisms, Maidl et al. (2012): (a) penetration mechanism; (b) membrane mechanism 146
6.2 Pore pressure measured in the tunnel axis as a function of the distance to the slurry shield, data from Heinenoord tunnel, Bezuijen (2002) 146
6.3 Distribution of total stress, pore water pressure and effective stress with depth: (a) dry soil; (b) saturated soil 148
6.4 Point source and equipotential surface 150
6.5 Tunnel face flow, Bezuijen (2002) 151
6.6 Distribution of excess piezometric head ϕ_o with distance to the tunnel face 152
6.7 Excess piezometric head distribution in the wedge 155
6.8 Pressures and forces in each slice of the wedge 155
6.9 Distribution of hydrostatic and excess pore pressure in KEM model (M2) . 156
6.10 Schematic diagram for the applied pressure in TBM due to hydrostatic and excess piezometric head 159
6.11 Flow chart for the procedure of incorporating the excess pore pressure in tunnel face stability models 160
6.12 Minimum support pressure considering hydrostatic pore pressure: (a) total support pressure; (b) effective support pressure 161
6.13 Applied support pressure considering hydrostatic pore pressure: (a) operational support pressure; (b) piezometric head 162

6.14 Comparison of normalized minimum support pressure in dry condition and effective support pressure in saturated condition: (a) normalized support pressure in dry condition; (b) normalized effective support pressure in saturated condition 162

6.15 Required support pressures considering hydrostatic and excess pore pressures: (a) operational support pressure; (b) effective support pressure; (c) piezometric head 165

6.16 Percentage of increase in operational support pressure due to excess pore pressure 166

6.17 Penetration velocity versus effective friction angle 166

6.18 Design charts for normalized operational support pressure considering hydrostatic and excess pore water pressures: (a) Horn (1961) model; (b) Broere (2001) model; (c) Anagnostou & Kovari (1994) model; (d) KEM model (M2) 167

6.19 Development of piezometric head imposed to the soil with time for Horn (1961) model: (a) $C/D = 1$; (b) $C/D = 1.5$; (c) $C/D = 2$; (d) $C/D = 2.5$ 169

6.20 Development of piezometric head imposed to the soil with time for Anagnostou & Kovari (1994) model: (a) $C/D = 1$; (b) $C/D = 1.5$; (c) $C/D = 2$; (d) $C/D = 2.5$ 170

6.21 Development of piezometric head imposed to the soil with time for Broere (2001) model: (a) $C/D = 1$; (b) $C/D = 1.5$; (c) $C/D = 2$; (d) $C/D = 2.5$ 171

6.22 Development of piezometric head imposed to the soil with time for KEM model (M2): (a) $C/D = 1$; (b) $C/D = 1.5$; (c) $C/D = 2$; (d) $C/D = 2.5$. 172

6.23 Slurry penetration depth with time for Horn (1961) model: (a) $C/D = 1$; (b) $C/D = 1.5$; (c) $C/D = 2$; (d) $C/D = 2.5$ 173

6.24 Slurry penetration depth with time for Anagnostou & Kovari (1994) model: (a) $C/D = 1$; (b) $C/D = 1.5$; (c) $C/D = 2$; (d) $C/D = 2.5$ 174

6.25 Slurry penetration depth with time for Broere (2001) model: (a) $C/D = 1$; (b) $C/D = 1.5$; (c) $C/D = 2$; (d) $C/D = 2.5$ 175

6.26 Slurry penetration depth with time for KEM model (M2): (a) $C/D = 1$; (b) $C/D = 1.5$; (c) $C/D = 2$; (d) $C/D = 2.5$ 176

6.27 Operational support pressure considering hydrostatic pore pressure: (a) Horn (1961) model; (b) Anagnostou & Kovari (1994) model; (c) Broere (2001) model; (d) KEM model (M2) 178

6.28 Operational support pressure considering hydrostatic and excess pore pressures: (a) Horn (1961) model; (b) Anagnostou & Kovari (1994) model; (c) Broere (2001) model; (d) KEM model (M2) 179
6.29 Slurry penetration depth with time for different model: (a) Horn (1961) model; (b) Anagnostou & Kovari (1994) model; (c) Broere (2001) model; (d) KEM model (M2) 181

List of Tables

2.1 Relation between the stability number and deformation, according to Broms & Bennermark (1967) 40

2.2 Comparison of the failure geometry in wedge-silo model with physical model tests 46

2.3 Calculated support pressure using different tunnel cross-sections 48

3.1 PSO parameters 63

4.1 Selected physical model tests for verification of KEM model (M) 81

4.2 Soil parameters and tunnel geometry 88

4.3 Comparison of the minimum support pressures obtained from KEM model (M) and FELA for $C/D = 1$ 90

4.4 Values of N_γ, N_c and N_q for various internal friction angles and C/D ratios; results obtained with KEM model (M) 96

5.1 Influence of the number of blocks on the minimum support ($C/D = 1$ and $\gamma = 18$ kN/m^3) 119

5.2 Soil parameters and tunnel geometry (soil with two layers) 128

5.3 N_γ, N_c and N_q for various internal friction angles and C/D ratios for KEM model (M2) 136

6.1 Soil parameters and tunnel geometry 160

6.2 Soil parameters and tunnel geometry 177

6.3 Operational support pressure for different models considering only hydrostatic pore pressure 178

6.4 Piezometric head for different models considering only hydrostatic pore pressures 179

6.5 Operational support pressure for different models considering hydrostatic and excess pore pressures 180

6.6 Piezometric head for different models considering hydrostatic and excess pore pressures 180
6.7 Penetration velocity (v_p) for different models 180

Nomenclature

$[K_s]$	Static coefficient matrix
$[K_v]$	Kinematics matrix
γ	Dry unit weight of the soil
γ'	Submerged unit weight of the soil
γ_s	Unit weight of slurry
γ_{sat}	Saturated unit weight of the soil
γ_w	Unit weight of water
μ_e	Safety factor for earth force
μ_w	Safety factor for water pressure
ϕ	Excess piezometric head at distance from the tunnel
ϕ_o	Excess piezometric head at the tunnel face
σ'	Effective normal stress
τ	Shear stress
i	Hydraulic gradient
k	Coefficient of permeability of the soil
n	Porosity of the soil
A_c	Circular area of tunnel cross section
b	Side of equilateral triangle

c	Cohesion of the soil
C	Cover depth
C_e	Equivalent cover depth
C_n	Cohesion force
c_u	Undrained shear strength
D	Tunnel diameter
F_i	Known resultant force
Fs	Factor of safety
G_s	Weight of the silo
G_w	Weight of the wedge
h_w	Water table elevation
K_0	Coefficient of lateral earth pressure at rest
L	Height of the silo
N_γ	Non-dimensional coefficient representing the contribution of soil weight
N_c	Non-dimensional coefficient representing the contribution of cohesion
N_n	Total normal force
N'_n	Total normal effective force
N_q	Non-dimensional coefficient representing the contribution of surcharge
P	Mnimum support force
P_e	Support force due to the earth pressure
p_u	Minimum support pressure
P_w	Support force due to the pore pressure

p_{max}	Maximum support pressure
Q	Discharge of the point source
q	Surcharge pressure
R	Radius of the tunnel
R_n	Shear force
S_i	Resultant force
T_n	Total shear force
u	Pore water pressure
U_n	Pore water pressure force
v	Virtual displacement
Vol	Volume of the block
v_p	Penetration velocity
W	Width of the silo
σ_h	Horizontal stress above the tunnel crown
$\sigma_{v_{silo}}$	Vertical stress acting on the base of the silo
σ_v	Vertical stress above the tunnel crown
φ'	Effective friction angle
K_{wedge}	Wedge lateral earth pressure coefficient
K_a	Active earth pressure coefficient
K_{silo}	Silo lateral earth pressure coefficient

1 Introduction

1.1 Motivation and objectives

1.1.1 Motivation

In recent years, the expansion of cities and urban areas has resulted in a rising demand for underground transportation systems. The construction of the transportation tunnels represents a viable solution to minimize the volume of traffic on the ground surface.

The excavation of tunnels is frequently done with a mechanized Tunnel Boring Machine (TBM). The stability problem of the tunnel face refers to the support pressure which is applied at the face of the TBM as it moves forward. This support pressure must be large enough to prevent the soil from failing into the tunnel (active collapse failure), but small enough in order not to cause the soil to be pushed up from the excavated tunnel face, which would lead to a heave of the soil at the ground surface (passive failure).

The adequate tunnel face pressure to avoid face instability depends on various factors such as soil properties (e.g., shear strength, permeability, unit weight), tunnel geometry (e.g., diameter, cover depth) and location of the ground water table.

As the tunnel excavation advances, the soil above the excavation face tends to move downward. Meanwhile, the moving soil is resisted by stationary soil leading to the development arching in the soil (vertical arching), see Fig. 1.1 (a). Furthermore, the soil at the front of the tunnel face tends to yield towards the excavation face. However, this tendency is resisted at the boundaries of the tunnel face. As a result, horizontal arching is developed around the tunnel face, see Fig. 1.1 (b). This vertical and horizontal arching has significant influence on the tunnel face support pressure.

Another important aspect requires more attention when evaluating a safe support pressure in case that a slurry TBM is used to excavate the tunnel in a water-saturated soil. In that case the support medium will flow out from the tunnel face into the surrounding soil and will lead to an increase of pore water pressure at the front of the tunnel face.

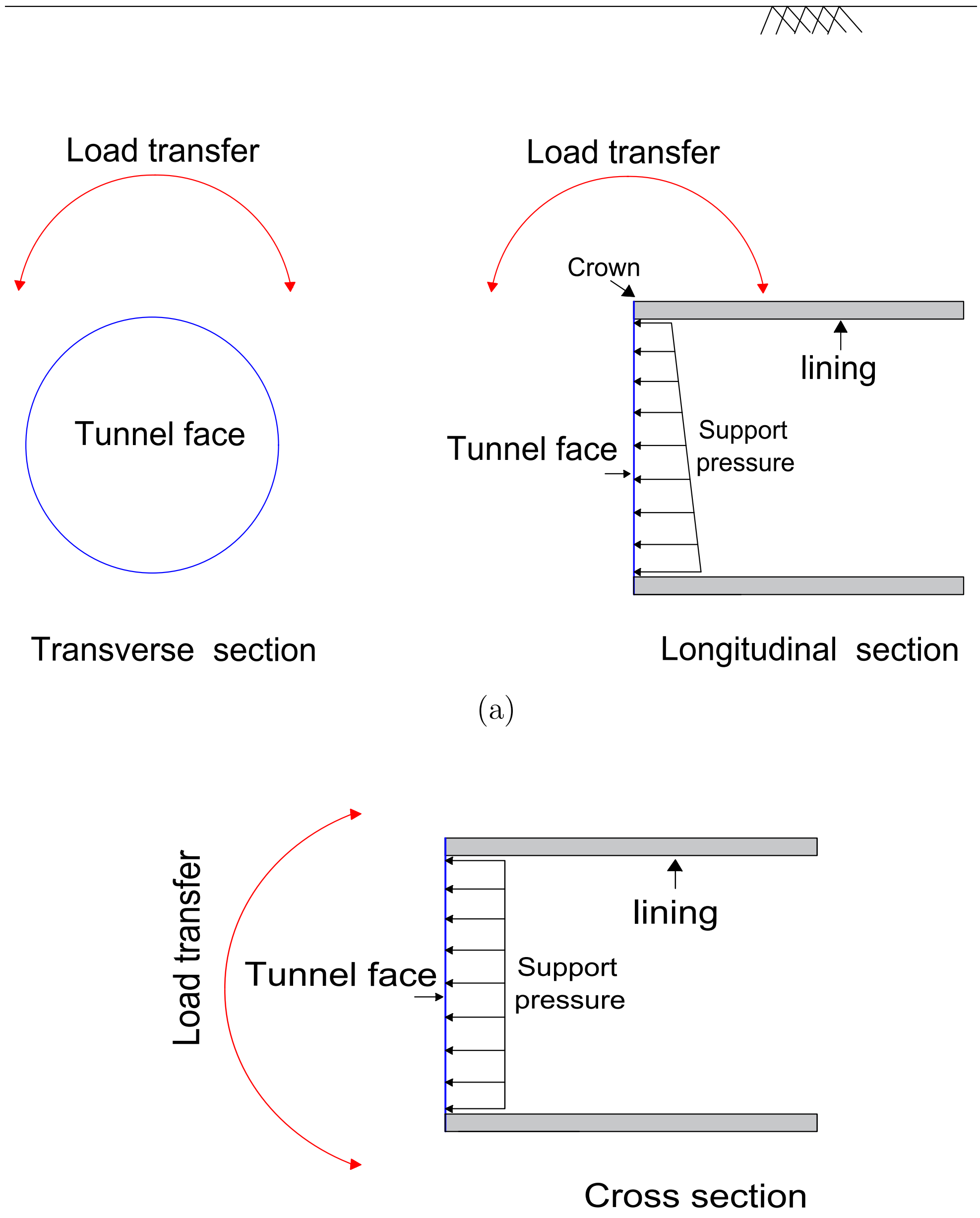
Load transfer
Load transfer
Crown
Tunnel face
lining
Tunnel face
Support
pressure
Transverse section
Longitudinal section
Load transfer
lining
Tunnel face
Support
pressure
Cross section

(a)

(b)

Figure 1.1: Vertical and horizontal arching during excavation of the tunnel: (a) vertical arching above the tunnel face; (b) horizontal arching at the front of the tunnel face

The increase of the pore water pressure at the front of the tunnel face is associated with a hydraulic gradient between the mixing chamber of the TBM and the surrounding soil. The hydraulic gradient results in seepage forces in the soil near the tunnel face leading to a local reduction of effective stress and thus shear strength of the soil. The reduction of shear strength is a consequence of the reduction of effective normal stress acting on potential sliding planes. Nevertheless, only limited attention has been given to the effect of the excess pore pressure distribution on the required support pressure in previous investigations (e.g., Broere, 2001; Dias & Bezuijen, 2016).

Analytical approaches such as the Limit Equilibrium Method (LEM) (e.g., Horn, 1961; Jancsecz & Steiner, 1994; Anagnostou & Kovari, 1994; Broere, 2001; Kirsch & Kolymbas, 2005) or the Limit Analysis Method (LAM) (e.g., Leca & Dormieux, 1990; Mollon et al., 2010; Tang et al., 2014; Ibrahim et al., 2015) are used to assess the stability of the tunnel face assuming various failure mechanisms. However, the results are quite different. The Finite Element Method (FEM) (e.g., Peila, 1994; Ng & Lee, 2002; Mayer et al., 2003; Sterpi & Cividini, 2004; Kim & Tonon, 2010), the Discrete Element Method (DEM) (e.g., Maynar & Rodriguez, 2005; Funatsu et al., 2008; Zhang et al., 2011) and the Finite Difference Method (FDM) (e.g., Li et al., 2009; Dias, 2011; Senent & Jimenez, 2015) may be effective tools for analyzing the stability of the tunnel face too, considering the stress-strain relationship of the soil and thus incorporating soil behavior more realistically. However, the simulation of the tunnel face failure using three dimensional DEM, FEM or FDM model is very time consuming.

Inspite of the importance of a stable tunnel face, specific recommendations or technical standard for calculating the support pressure are limited (e.g., DAUB, 2016). In practice, the estimation of the support pressure to be applied at the tunnel face is based on the experience acquired in the field. This support pressure is chosen in dependence of the soil conditions and the working parameters of the tunnel boring machine.

On the other hand, on real projects the tunnel engineer needs to find a simple calculation model in the literature, which can be transformed into a spread sheet or simple design charts that can be used to quickly estimate the support pressure (for preliminary design studies).

To enhance the state of the art of this topic, within this dissertation a new 3D approach is developed to investigate the stability of the tunnel face. Using KEM (Kinematical Element Method), different 3D failure mechanisms are studied. The proposed 3D KEM models are initially developed for homogeneous soil and consider the effect of hydrostatic and excess pore pressures. Consideration is given for different soil strength parameters (e.g. cohesion and friction angle) and the geometry of the tunnel that influence the stability of the tunnel face. The investigation of the 3D failure mechanisms delivers minimum support pressure (in case of closed face tunneling) or the factor of safety (in case of open face tunneling). For quantifying the effect of 3D silo arching on the support pressure, a feasible approach in calculating the three-dimensional lateral earth pressure coefficient (K_{3D}) is proposed. Within this approach, a 3D active earth pressure acting on the vertical silo slip surfaces is assumed.

Based on the KEM models, design charts and equations are proposed to be used by practical engineers in the preliminary stages of tunnel design. They deliver a safe operating support pressure that should be applied to the excavation face by a tunnel boring machine.

1.1.2 Objectives

The overall aim of this research is to develop a new 3D model to investigate the stability of the tunnel face which initially developed for deal with homogenous and incorporates the effect of hydrostatic and excess pore water pressure on the minimum support pressures to be applied at the tunnel face by a TBM. In particular, the following objectives are addressed:

- Objective 1: To use the principle of KEM to investigate the stability of the tunnel face in dry or water-saturated for homogeneous soil.
- Objective 2: To perform a systematic comparison between the results of the KEM models and those of existing approaches in the literature, which have been developed to investigate the stability of the tunnel face.
- Objective 3: To evaluate the safety factor for the tunnel face stability in open-face tunneling.
- Objective 4: To investigate the influence of hydrostatic and excess water pore pressures on the stability of the tunnel face during tunnel construction
- Objective 5: To develop design equations and stability charts, which can be used in practice (for preliminary design studies) and enable a quick calculation for tunnel engineers.

To achieve the previous objectives, the guiding methodology of the proposed research is presented within Fig. 1.2 and Fig. 1.3. In Fig. 1.3, it should be clearly noted that the minimum support pressure in dry soil condition has been obtained as described by

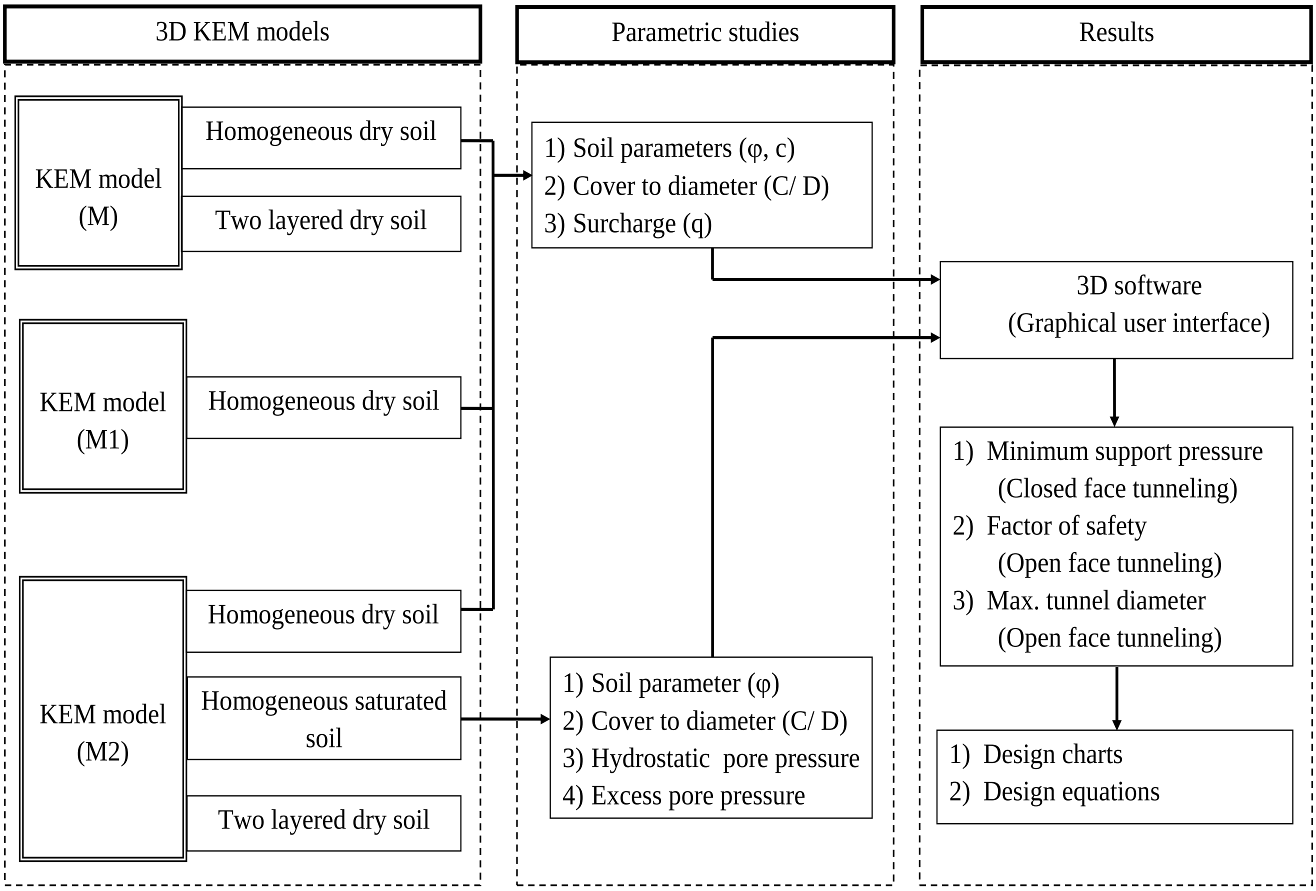
3D KEM models
Parametric studies
Results
KEM model (M)
Homogeneous dry soil
Two layered dry soil
KEM model (M1)
Homogeneous dry soil
KEM model (M2)
Homogeneous dry soil
Homogeneous saturated soil
Two layered dry soil
1) Soil parameters (φ, c)
2) Cover to diameter (C/ D)
3) Surcharge (q)
1) Soil parameter (φ)
2) Cover to diameter (C/ D)
3) Hydrostatic pore pressure
4) Excess pore pressure
3D software (Graphical user interface)
1) Minimum support pressure (Closed face tunneling)
2) Factor of safety (Open face tunneling)
3) Max. tunnel diameter (Open face tunneling)
1) Design charts
2) Design equations

Figure 1.2: Guiding methodology for the proposed research using KEM models

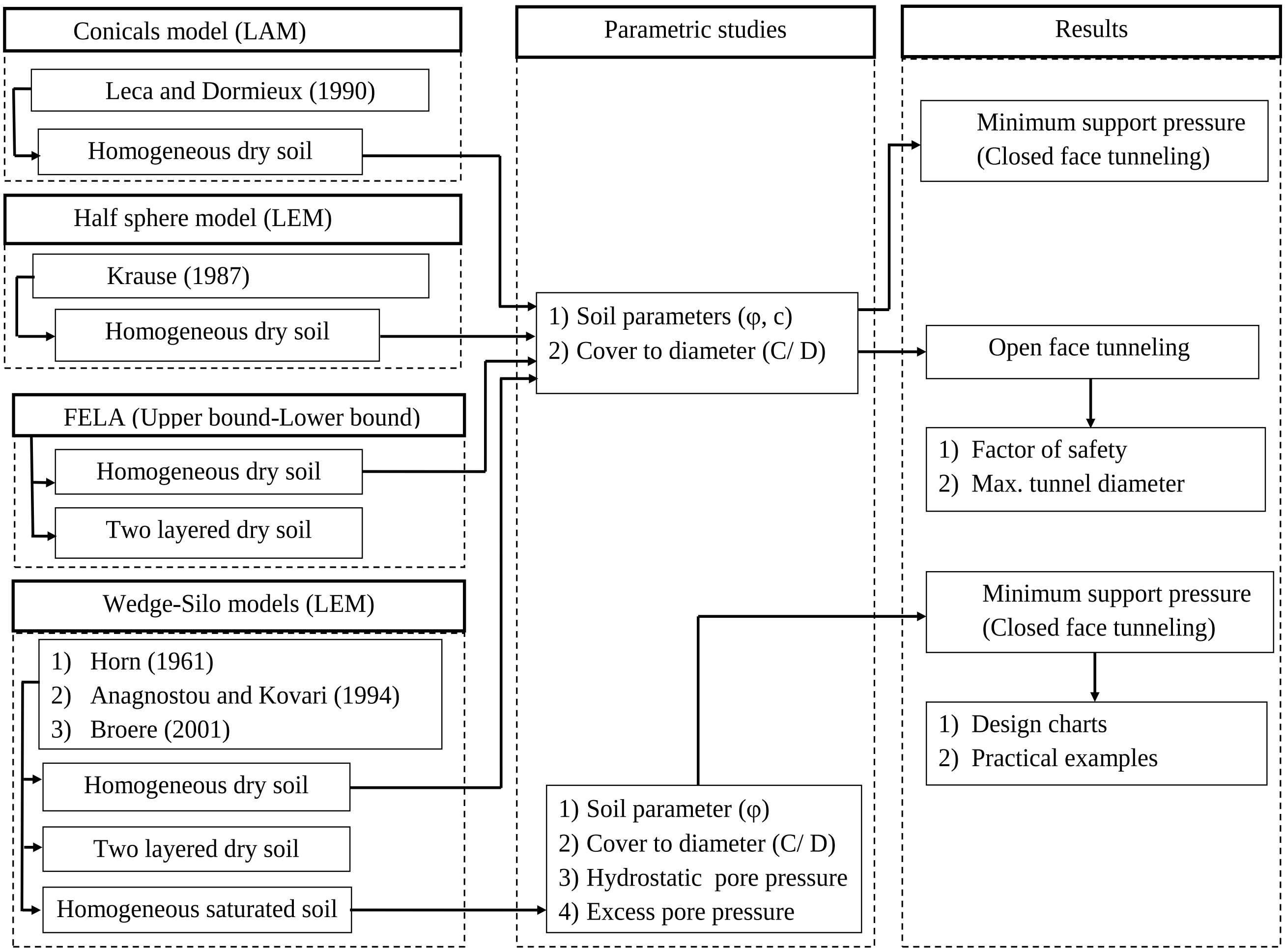
Conicals model (LAM)
Leca and Dormieux (1990)
Homogeneous dry soil
Half sphere model (LEM)
Krause (1987)
Homogeneous dry soil
FELA (Upper bound-Lower bound)
Homogeneous dry soil
Two layered dry soil
Wedge-Silo models (LEM)
1) Horn (1961)
2) Anagnostou and Kovari (1994)
3) Broere (2001)
Homogeneous dry soil
Two layered dry soil
Homogeneous saturated soil
Parametric studies
1) Soil parameters (φ, c)
2) Cover to diameter (C/ D)
1) Soil parameter (φ)
2) Cover to diameter (C/ D)
3) Hydrostatic pore pressure
4) Excess pore pressure
Results
Minimum support pressure (Closed face tunneling)
Open face tunneling
1) Factor of safety
2) Max. tunnel diameter
Minimum support pressure (Closed face tunneling)
1) Design charts
2) Practical examples

Figure 1.3: Guiding methodology for the existing approaches

original authors. Within this thesis some of these existing approaches have been extended to investigate the stability of the tunnel face in two-layered soils and to evaluate the factor of safety in open-face tunneling. Furthermore, the existing approaches have been extended, to study the effect of hydrostatic and excess pore water pressure on the stability of the tunnel face.

1.2 Contents of the thesis

This thesis consists of seven chapters, the content of each chapter can be briefly summarized as:

- Chapter 1: Introduction

  This chapter introduces the motivation, objectives and the organization of this thesis.

- Chapter 2: State of the art

  In this chapter, an overview on various tunneling excavation methods is presented, particularly on mechanized methods. Furthermore, this chapter contains a review of the literature regarding previous investigations on the tunnel face stability.

- Chapter 3: Kinematical Element Method (KEM)

  Within this chapter, the Kinematical Element Method (KEM), its main assumptions and the necessary optimization method are described.

- Chapter 4: KEM model M for tunnel face stability stability

  In this chapter, the fundamental assumptions of KEM model (M) and the failure mechanism for the stability analysis of the tunnel face are introduced. Also, the calculation procedure for estimating the 3D lateral earth pressure coefficient is explained. The results of KEM calculations are presented and discussed. A comparison between the results of KEM model (M), existing approaches in the literature and finite element limit analysis solutions is undertaken.

- Chapter 5: Modified KEM models (M1 and M2)

  In this chapter, two modified failure mechanisms are studied using KEM to estimate the minimum support pressure of the tunnel face. The results obtained with KEM model (M2) are compared to other solutions available from the literature. For an open-face tunneling, the safety factor are calculated using the strength reduction technique.

- Chapter 6: Effect of excess pore pressure on the stability of the tunnel face

  In this chapter, the influence of the excess pore pressure, generated in the soil by a slurry shield TBM, on the effective and total support pressure during tunnel excavation is discussed. As a result of the analysis, a number of design graphs that can be used to evaluate the operational face support pressure is proposed.

- Chapter 7: Conclusions and future work

  This chapter provides a summary of the research, done within this thesis. The most important findings of this study are addressed. Furthermore, an outlook on possible future work is given.

2 State of the art

2.1 Introduction

The main key to a successful tunnel construction is the appropriate selection of the tunnel excavation technique. The choice is based on the known or expected ground conditions as well as the adaptability of the excavation technique to variability of the ground conditions. There are many different tunnel excavation methods (e.g., cut and cover, conventional and mechanized tunneling) to suit a range of different project conditions. In case of mechanized tunneling, adequate support pressure (e.g., compressed air, slurry or earth pressure support) at the tunnel face is required to counterbalance the pressure generated by the soil, water and overlying infrastructures and thus stabilize the tunnel face.

Several analytical methods are used in evaluating the required support pressure which differ in their calculation assumptions, required computing time and calculation efficiency. The analytical approaches can basically be divided into two groups, namely, Limit Equilibrium Method (LEM) and Limit Analysis Method (LAM). The limit equilibrium method has been widely used for analyzing the stability of the tunnel face (e.g., Horn, 1961; Jancsecz & Steiner, 1994; Anagnostou & Kovari, 1994; Broere, 2001). In the limit equilibrium method the static equilibrium between the forces acting on the soil masses involved in the collapse mechanism is considered.

The second group of analytical methods is based on the so-called the upper bound theory (e.g., Leca & Dormieux, 1990; Mollon et al., 2010; Tang et al., 2014; Ibrahim et al., 2015), which states that the work done by external loads in an increment of displacements for a kinematically admissible mechanism equals the energy dissipated by internal stresses.

The application of numerical methods with advanced constitutive models improved substantially the analysis of the tunnel face stability, considering the various 3D aspects. The Finite Element Method (FEM), the Discrete Element Method (DEM) and the Finite Difference Method (FDM) are useful tools in simulating the stability of the tunnel face were performed (e.g., Peila, 1994; Ohta & Kiya, 2001; Vermeer et al., 2002; Kirsch, 2009).

However, the simulation of the tunnel face failure using three dimensional DEM, FEM or FDM models is very time consuming.

For investigating the soil deformations caused by tunneling, various physical model tests were conducted. Either centrifuge (ng) model tests or small scale (1g) model tests were performed (e.g., Chambon & Corte, 1994; Takano et al., 2006; Kirsch, 2009; Idinger et al., 2011). The physical models provide a beneficial information about ground surface settlement, the required face support and insight into the 3D arching at the front of the tunnel face. Moreover, the results of the physical model tests can be used to validate the numerical and the analytical models.

2.2 Overview on various tunnel excavation methods

A tunnel construction consists of three main processes, namely excavation, mucking and primary support. Tunnel excavation is the procedure of removing soil from the tunnel face. Mucking is the process of removing the spoil from the tunnel. Throughout the years, many different techniques for tunnel face excavation have been developed. The appropriate method of tunnel excavation depends on many factors such as geological soil conditions, the impact of the excavation on the surrounding environment, time/cost considerations, the ground water conditions, the length and diameter of the tunnel, the depth of the tunnel and the final use of the tunnel (Chapman et al., 2017).

Basically, two types of tunnel excavation methods are used:

- Conventional method
- Mechanized method

2.2.1 The conventional method

Conventional tunneling is a method for excavating a tunnel using conventional machinery (e.g., tracked loaders, excavators, locomotives, dump trucks) without removing the buildings or interrupting the possible activities (e.g., transportation) at the ground surface. The excavation is preliminarily supported by ground improvement (e.g., grouting, jet grouting, soil freezing) or permanent support system (e.g., reinforcement, steel pipes, forepole). The conventional method is basically composed of three main construction (ITA, 2009) steps, that are continuously repeated 1) excavation, 2) mucking, 3) installation of temporary and permanent support systems. The conventional tunneling is a

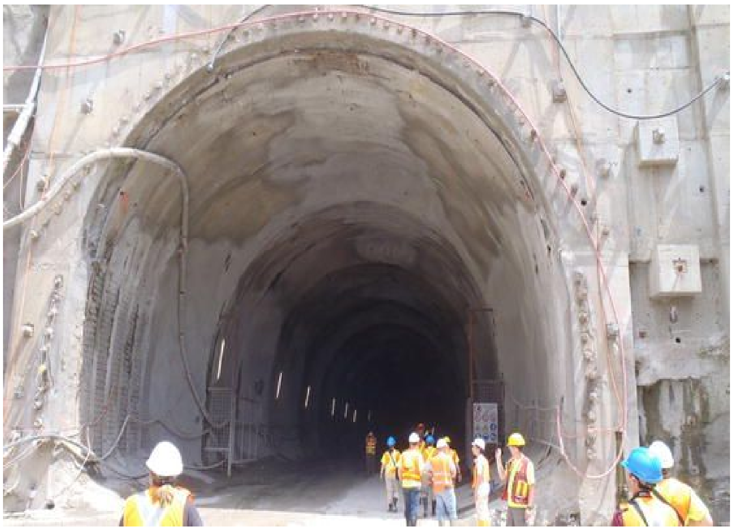

Figure 2.1: Tunnel San Fedele, Switzerland (tunnelingonline, 2019)

flexible excavation process in which many changes can be easily applied during tunnel construction (e.g., change the diameter of the tunnel, ground improvement).

As an example of the application of the conventional excavation method, the tunnel San Fedele (Roveredo Bypass Project) in Switzerland with a maximum of 25 m overburden is shown in Fig. 2.1.

2.2.2 Mechanized method

Mechanized tunneling summarizes all techniques where excavation is performed mechanically by means of teeths, picks or disks (ITA, 2009). The first attempt to utilize the mechanized tunneling was made by an American engineer Charles Wilson in 1851, which is considered as a successful continuous borer for the rock. Wilson's machine was trialled on the East portal of the Hoosac tunnel in Massachusetts. The general idea was that the machine would cut into the rock and then that cut rock could be blasted out. Since then, the technological development for mechanized tunneling has made a great progress. Mechanized tunneling is performed by Tunnel Boring Machines (TBM). These machines do not only carry out the excavation of the ground, but they also provide a support against the surrounding soils. Fig. 2.2 shows a typical Earth Pressure Balance TBM.

The mechanized tunneling is mainly divided into two types, namely open face tunneling and closed face tunneling. In open face tunneling, the tunnels are constructed without applying permanent support to the tunnel face. Whereas, in closed face tunneling, the face support is continuously applied e.g. by a pressurized slurry, earth pressure balance or compressed air.

2.2.2.1 Open face tunneling

In open face tunneling, there is no permanent support pressure applied at the tunnel face during the excavation process. The stability of the tunnel face must be guaranteed by the shear strength of the soil or by a temporary support e.g. by means of shortcrete and anchors. The open face tunneling is widely used for tunnel construction in soils with high shear strength (Moller, 2006).

Regarding the process of excavation in case of open face tunneling two techniques can be distinguished: conventional open face tunneling, and open face shield tunneling. In conventional open face tunneling, the tunnel is excavated using the typical digging machines and the excavation is preliminarily supported by ground improvement or reinforcement. The conventional open face tunneling allows either full-face or partial excavation of the tunnel cross section, while in open face shield tunneling, fully mechanized heading machines are used to create a cavity and then segmental lining is inserted to secure the cavity. The choice of one of these techniques depends on several factors including tunnel sizes, structural analysis and geotechnical aspects (Moller, 2006).

2.2.2.2 Closed face tunneling

The principle of closed face tunneling is that an active pressure is continuously applied at the tunnel face in order to reduce the ground deformation and control the tunnel face stability. This method is used when the geological conditions are so unfavorable that the tunnel face becomes unstable without instant application of support pressure.

The concept of using a closed face shield was introduced by Marc Brunel in 1825 during construction of the underpass river Thames in London (Beaver, 1972). Also, at that time Lord Cochrane suggested to use compressed air to stabilize soft or loose soil for the tunneling excavation. In 1874, James Greathead designed a compressed air shield that was intended for the construction of the Woolwich Tunnel in Great Britain (Hemphill, 2012).

There are four typical shield tunnel machines with different types of support that are widely used; mechanical support, compressed air, earth pressure balance and slurry support. In the following each type of shield tunnel machine will be described briefly:

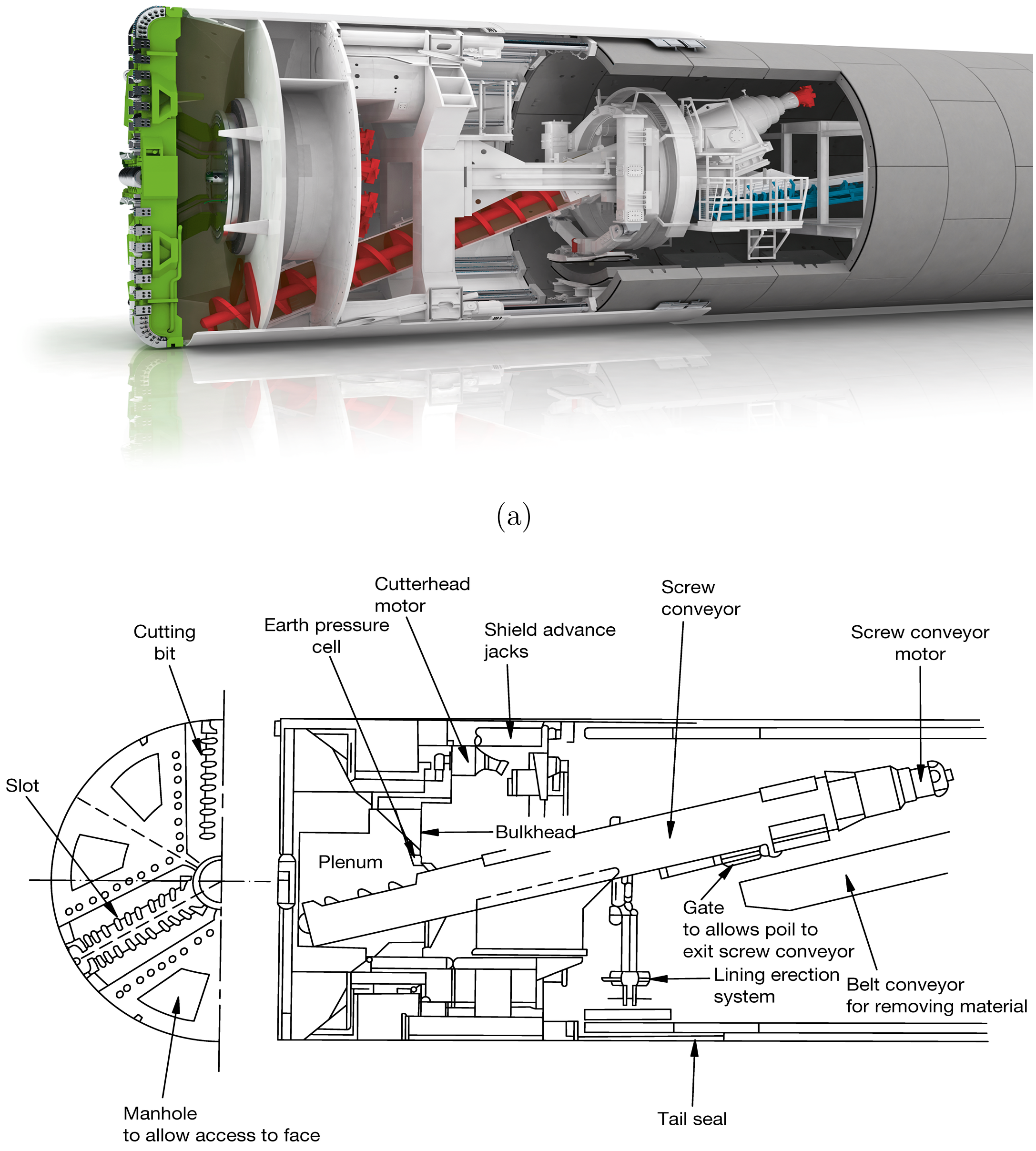
(a)

(b)
Cutterhead
motor
Screw
conveyor
Earth pressure
cell
Cutting
bit
Shield advance
jacks
Screw conveyor
motor
Slot
Bulkhead
Plenum
Gate
to allows poil to
exit screw conveyor
Lining erection
system
Belt conveyor
for removing material
Manhole
to allow access to face
Tail seal

Figure 2.2: Earth Pressure Balance TBM, Chapman et al. (2017): (a) 3D schematic representation of EPB; (b) longitudinal section through an EPB

1. Mechanical support TBM

   Mechanical support TBM has a full face cutterhead which provides face support by constantly pushing the excavated material ahead of the cutterhead against the surrounding ground.

2. Compressed air TBM

   Compressed air TBM is a tunnel boring machine where compressed air is used to counteract the hydrostatic and pressure exerted on the tunnel face. The compressed air pressure is practically uniform over the full height of the tunnel face. However, the distribution of pressure due to water and earth pressure along depth of the excavated tunnel face is trapezoidal, which means there are differences in the balancing of pressure at the tunnel face. This problem is solved by compressing the air to balance the water and earth pressures at the lowest point of the tunnel face. A compressed air TBM is specially suited for an excavation in stable soils of low permeability with the presence of water (AFTES, 2000).

3. Slurry shield TBM

   A slurry shield TBM has a full face cutterhead. The cutterhead acts as the means of excavation, whereas face support is provided by slurry counter pressure. The slurry is a suspension composed of bentonite clay and water. The bentonite suspension penetrates into the soil, forming a thin impermeable film (filter cake) which guarantees the transfer of counter pressure to the excavation face. This type of TBM is particularly suitable for use in soils with low permeability (e.g., clayey soil, silt) and heterogeneous soft ground (AFTES, 2000).

4. Earth Pressure Balance shield (EPB)

   The Earth Pressure Balance shield (EPB) has a full face cutterhead. The confinement is achieved by pressurizing the excavated material in the cutterhead chamber. Muck is extracted from the chamber continuously by a pressure discharge system. The excavated soil is removed from the cutterhead chamber with its increased pressure towards the tunnel where the ambient pressure is acting. The face support counterbalances the ground water and the earth pressure is obtained by means of the material excavated by the cutting wheel, which serves as support medium itself. EPB is particularly suitable for soils which are capable to transmit the pressure in the cutterhead chamber (e.g., silt, fine clayey sand, soft chalk, marl) (AFTES, 2000).

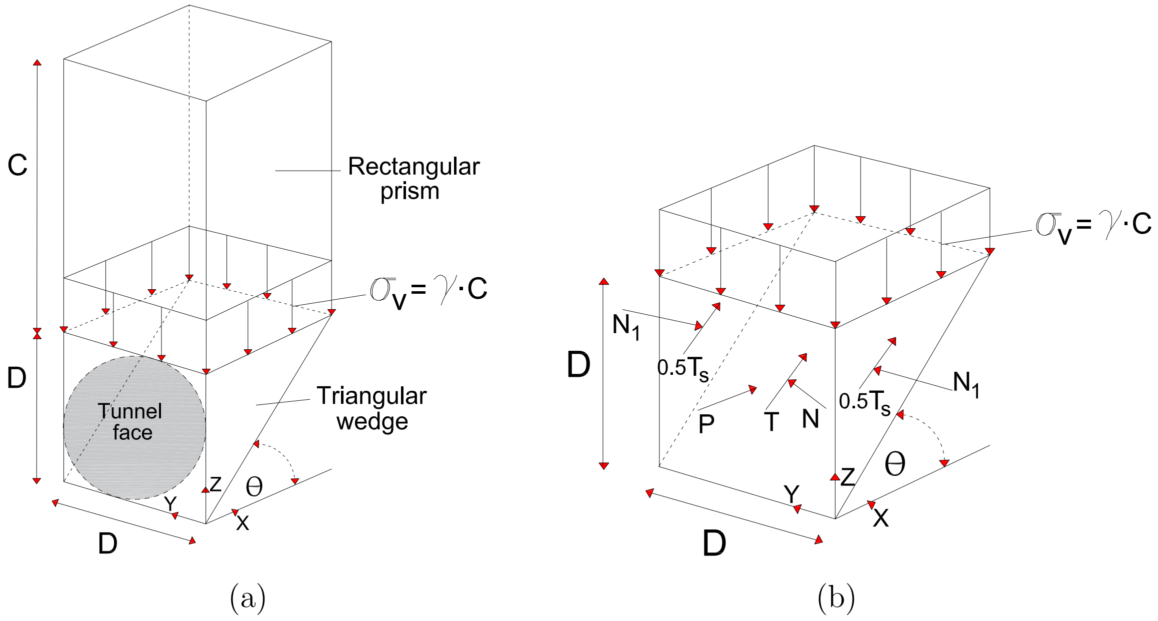

Figure 2.3: 3D Horn's model, Horn (1961): (a) Horn's failure mechanism; (b) forces acting on the wedge

2.3 Overview on tunnel face stability analysis models

As mentioned before, a variety of modeling strategies have been introduced by researchers for simulating the stability of the tunnel face. Analytical approaches, numerical methods and experimental model tests have been applied for that purpose. The research activities for each method are briefly summarized in the following subsections.

2.3.1 Tunnel face stability analysis in case of frictional or frictional-cohesive soil

2.3.1.1 Limit Equilibrium Method (LEM)

The limit equilibrium method is widely used as analysis technique for the stability of geotechnical problems. It applies the static equilibrium between the acting forces on the soil mass for the assumed collapse mechanism.

Based on the limit equilibrium method, various tunnel face stability models have been established. The most popular one is the wedge-silo model.

The first systematic study for the 3D stability of the tunnel face was performed by Horn in 1961. Horn (1961) presented a 3D failure mechanism replacing the circular shape of the tunnel face with a square shape as shown in Fig. 2.3. Horn's failure mechanism consists of a triangular prism wedge and a vertical rectangular prism above the wedge. The triangular prismatic wedge is loaded by a vertical force resulting from the full weight of the rectangular prism, i.e. no arching effect at the rectangular prism is taken into account when calculating the vertical stress ($\sigma_v(C) = C \cdot \gamma$) acting on the top of the wedge. In Horn's failure mechanism no shear forces are taken into account between the surfaces of the rectangular prism and the adjoining soil, as well as no shear force on the horizontal plane between the rectangular prism and the wedge.

Horn (1961) presumed a linear distribution of vertical stress along the sides of the wedge, see Fig. 2.5. Furthermore, the horizontal stress σ_h is assumed to be linearly dependent on the vertical stress σ_v by the coefficient of lateral earth pressure for the wedge K_{wedge}. Horn (1961) used $K_{wedge} = K_0$ with $K_0 = 1 - \sin\varphi$, according to *Jaky* (1944). The vertical stress along the sides of the wedge is calculated as follows:

$$\sigma_{v_{wedge}}(v) = (D - z) \cdot \gamma + C \cdot \gamma \quad (0 \leq z \leq D) \tag{2.1}$$

where z is the distance from the bottom of the tunnel, see Fig. 2.5. The shear stress (τ_{wedge}) acting on the sides of the wedge is obtained as follows:

$$\tau_{wedge}(z) = c + \sigma_h(z) \cdot \tan\varphi \tag{2.2}$$

The shear forces (T_s) acting on the sides of the wedge (Fig. 2.6) can be determined as follows:

$$T_s = 2 \cdot \int_0^D \tau_{wedge}(z) \cdot b(z)\, dz \tag{2.3}$$

where $b(z)dz$ denotes the width of the wedge at elevation z. Eq. (2.3) leads to

$$T_s = D^2 \cdot \tan\theta \cdot \left[c + K_0 \cdot \tan\varphi \cdot \left(\frac{1}{3} \cdot \gamma \cdot D + \frac{2}{3} \cdot C \cdot \gamma\right)\right] \tag{2.4}$$

According to the Mohr-Coulomb criterion, the shear force acting on the inclined sliding surface is obtained as follows:

$$T = N \cdot \tan\varphi + \frac{c \cdot D^2}{\sin\theta} \tag{2.5}$$

By equilibrating the static forces on the wedge, the equations of equilibrium can be written as:

$$\sum F_x = 0, \quad P + T \cdot \cos\theta + T_s \cdot \cos\theta - N \cdot \sin\theta = 0 \tag{2.6}$$

$$\sum F_z = 0, \quad G_s + G_w - T \cdot \sin\theta - T_s \cdot \sin\theta - N \cdot \cos\theta = 0 \tag{2.7}$$

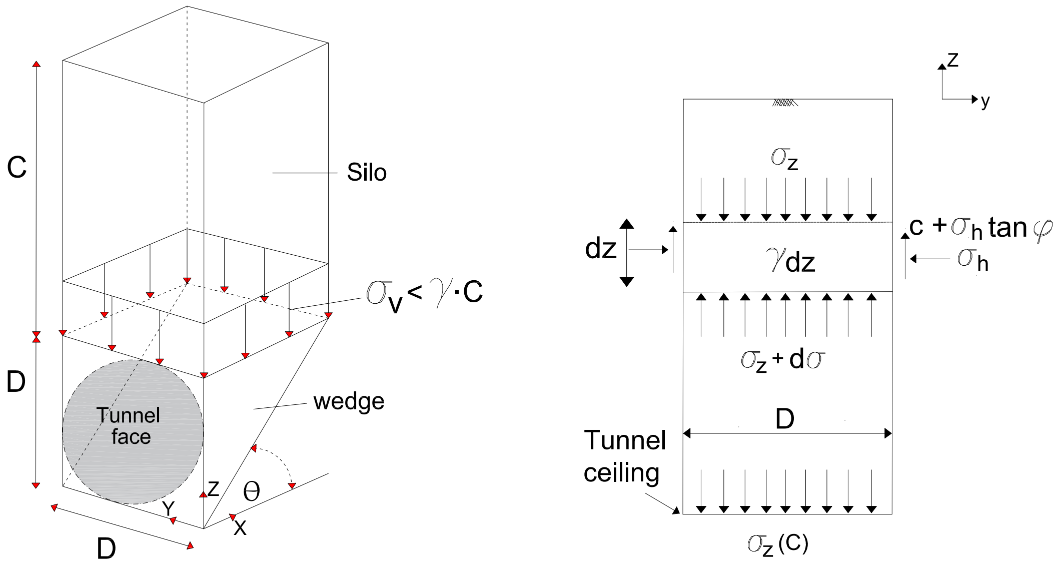
C
Silo
D
σv < γ·C
wedge
Tunnel face
Z
Θ
Y
X
D
z
y
σz
dz
c + σh tan φ
γdz
σh
σz + dσ
D
Tunnel ceiling
σz (C)

(a) (b)

Figure 2.4: 3D limit equilibrium model: (a) failure mechanism of wedge-silo model; (b) a strip of soil in arching silo

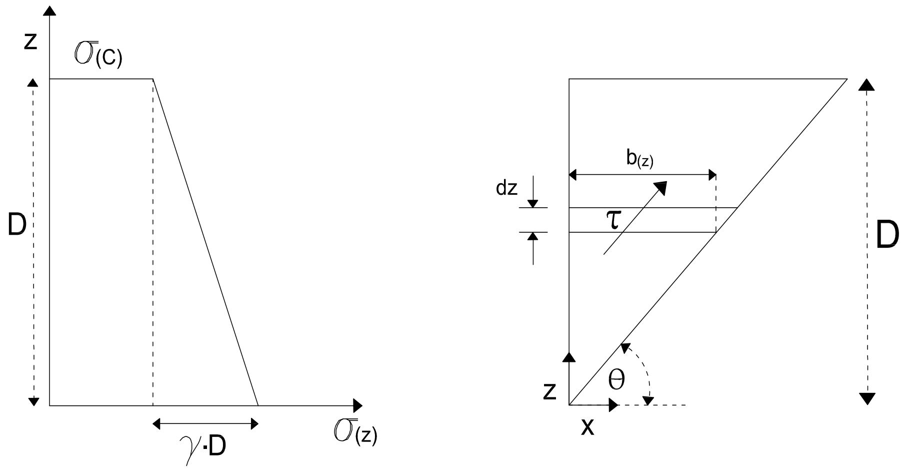
z
σ(C)
D
γ·D
σ(z)
b(z)
dz
τ
D
Θ
z
x

(a) (b)

Figure 2.5: Vertical and shear stress distribution on the wedge: (a) vertical stress; (b) shear stress

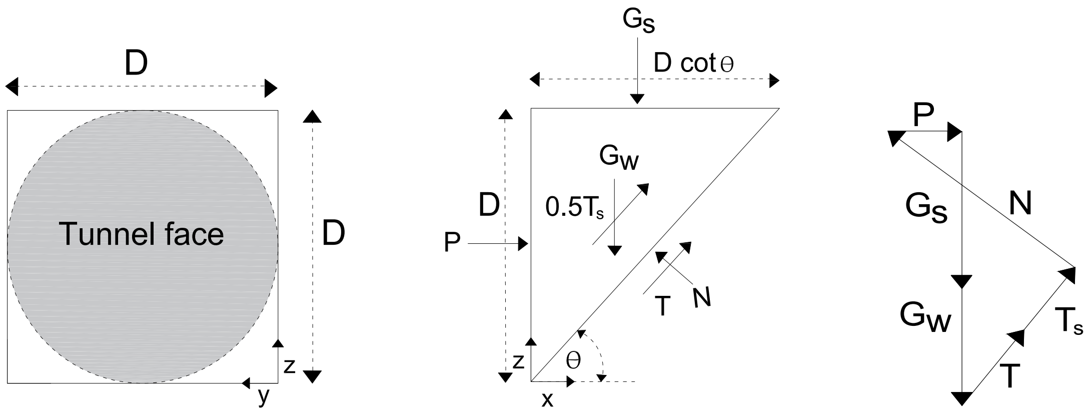

(a) (b) (c)

Figure 2.6: (a) Circular tunnel face approximated by a square and the force equilibrium on wedge; (b) forces acting on the wedge; (c) force polygon

where the weight of the wedge is

$$G_w = 0.5 \cdot \gamma \cdot D^3 \cdot \cos\theta \tag{2.8}$$

and the vertical force on the top of the wedge is

$$G_s = C \cdot \gamma \cdot D^2 \cdot \cot\theta \tag{2.9}$$

By combining Eq. (2.6) and Eq. (2.7) and eliminating the forces N and T, the required support force P can be calculated from the following equation:

$$P = \frac{G_s + G_w}{\cot(\theta + \varphi)} - \frac{T_s + c \cdot (\frac{D^2}{\sin\theta})}{\sin\theta \cdot (\cot\theta + \tan\varphi)} \tag{2.10}$$

The critical inclination angle θ is determined by maximizing the support force P:

$$\frac{dP}{d\theta} = 0 \tag{2.11}$$

where $0^o < \theta < 90^o$

The minimum support pressure is assumed to be uniformly distributed across the tunnel face and thus given by

$$p = \frac{P}{D^2} \tag{2.12}$$

Latterly, Horn's failure mechanism is called wedge-silo model. Using Horn's failure mechanism, different approaches for the distribution of vertical stress with depth have been proposed. The wedge-silo model has been used by several researchers as a basis for further development.

Based on Limit Equilibrium Method, Anagnostou & Kovari (1994), Jancsecz & Steiner (1994), Broere (2001) and Anagnostou (2012) proposed 3D tunnel face stability models based on Horn's failure mechanism including the effect of soil arching in the silo by using Janssen's silo theory (1895), see Fig. 2.4.

The silo theory leads to the following equation for the vertical stress acting on the base of the silo:

$$\sigma_{v_{silo}}(z) = \frac{a \cdot \gamma - c}{K_{silo} \cdot \tan\varphi}(1 - e^{-\frac{z}{a} \cdot K_{silo} \cdot \tan\varphi}) \tag{2.13}$$

where γ is the unit weight of the soil, φ is the friction angle, c is cohesion of the soil, a is the ratio of the area over circumference of horizontal plane of the silo, K_{silo} is the coefficient of lateral pressure and z is the soil depth measured from the ground surface.

Two assumptions are adopted in the wedge-silo model based on Janssen's analysis of soil arching. The first assumption is that the lateral earth pressure coefficient of the soil in the silo is assumed in advance, and that it is constant over the tunnel depth. The second assumption is that the vertical stresses are uniformly distributed across any horizontal section of the silo as well at the base of the silo. In addition to the previous assumptions, the shear force on the horizontal plane between the silo and the wedge is omitted in the equilibrium of forces.

Different assumptions have been made by various researchers for K_{silo}. Anagnostou & Kovari (1994) assumed $K_{silo} = 0.8$. Jancsecz & Steiner (1994) used a 2D active earth pressure coefficient for the silo, $K_{silo} = K_a$ with $K_a = \tan^2(45 - \varphi/2)$, Broere (2001) used the lateral earth pressure coefficient at rest (K_0) proposed by Jaky (1944). Anagnostou (2012) suggested $K_{silo} = 1.0$.

Fig. 2.7 shows the values of K_{silo} and K_{wedge} proposed by different researchers as functions of different friction angles. K_{wedge} is further discussed below. According to Jancsecz & Steiner (1994) and Broere (2001) models, the K_{silo} and K_{wedge} values decrease with an increase in friction angle. In contrast, in the models of Anagnostou & Kovari (1994) and Anagnostou (2012), K_{silo} and K_{wedge} are assumed to be constant, that means independent of friction angle. As evident in Fig. 2.7 (a), the value of K_{silo} obtained from Anagnostou (2012) model is larger than the other models for the same friction angle. Whereas, the value of K_{silo} obtained from Jancsecz & Steiner (1994) model is lower than the other models.

Once the vertical stress on the top of the wedge is calculated using the silo theory, the next step is to assume the distribution of vertical stresses and the accompanying horizontal

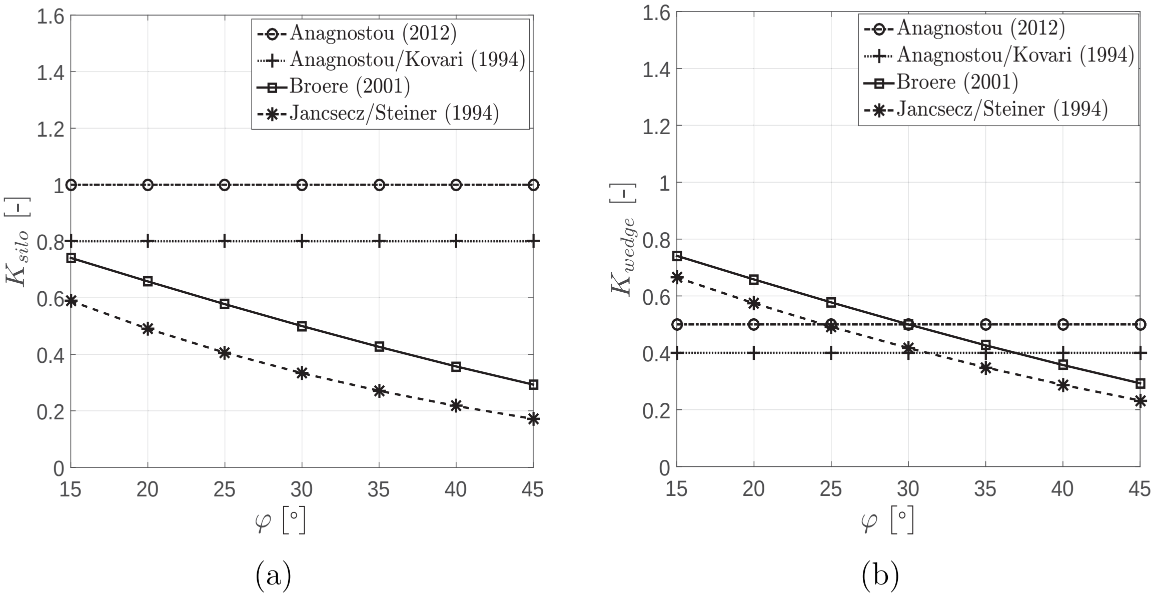

(a) (b)

Figure 2.7: K_{silo} and K_{wedge} assumed by various approaches: (a) variation of K_{silo} with friction angle; (b) variation of K_{wedge} with friction angle

stresses acting on the wedge. Two possible options for estimating the distribution of vertical stresses along the sides of the wedge are as follows:

1. Assuming a linear vertical stress distribution along the depth of the tunnel, where $\sigma_{v_{wedge}} = D \cdot \gamma$
2. Using the infinitesimal slices method in the wedge which is consistent with silo theory.

Following the first option for estimating the distribution of vertical stress, Anagnostou & Kovari (1994) and Jancsecz & Steiner (1994) assumed linear proportionality between the horizontal stress $\sigma_h(z)$ and the vertical stress $\sigma_v(z)$ along the sides of the wedge, see Fig. 2.5. The vertical stress along the sides of the wedge is calculated as follows:

$$\sigma_{v_{wedge}}(z) = (D - z) \cdot \gamma + \sigma_{v_{silo}}(C) \quad (0 \leq z \leq D) \tag{2.14}$$

where $\sigma_{v_{silo}}(C)$ is calculated based on the silo theory (Eq. (2.13)).

The shear force (T_s) acting on both sides of the wedge is determined as follows:

$$T_s = D^2 \cdot \tan\theta \cdot \left[c + K_0 \cdot \tan\varphi \cdot \left(\frac{1}{3} \cdot \gamma \cdot D + \frac{2}{3} \cdot C \cdot \gamma\right)\right] \tag{2.15}$$

where the weight of the wedge is

$$G_w = 0.5 \cdot \gamma \cdot D^3 \cdot \cos\theta \tag{2.16}$$

and the vertical force on the top of the wedge is

$$G_s = \sigma_{v_{silo}}(C) \cdot D^2 \cdot \cot\theta \tag{2.17}$$

The required support force P is calculated from the following equation:

$$P = \frac{G_s + G_w}{\cot(\theta+\varphi)} - \frac{T_s + c\cdot(\frac{D^2}{\sin\theta})}{\sin\theta\cdot(\cot\theta+\tan\varphi)} \tag{2.18}$$

The critical inclination angle θ is determined by maximizing the support force P:

$$\frac{dP}{d\theta} = 0 \tag{2.19}$$

where $0^o < \theta < 90^o$

The minimum support pressure is assumed to be uniformly distributed along the tunnel face and thus given by

$$p = \frac{P}{D^2} \tag{2.20}$$

A number of authors have suggested different values for K_{wedge} based on practical experience. Anagnostou & Kovari (1994) assumed $K_{wedge} = 0.4$. Jancsecz & Steiner (1994) suggested the lateral earth pressure coefficient for the wedge as the average of K_a and K_0 with $K_0 = 1 - \sin\varphi$ according to Jaky (1944), $K_{wedge} = (K_a + K_0)/2$, see Fig. 2.7 (b)). Jancsecz & Steiner (1994) described the relation between horizontal and vertical stress at the tunnel axis by a 3D earth pressure coefficient. The minimum support pressure (p) at the tunnel axis is calculated as:

$$p = K_{3D} \cdot \sigma_v(D) \tag{2.21}$$

The 3D earth pressure coefficient K_{3D} is expressed by Eq. (2.22).

$$K_{3D} = \frac{\sin\theta\cdot\cos\theta - \cos^2\theta\cdot\tan\varphi - \frac{K\cdot\alpha}{1.5}\cdot\cos\theta\cdot\tan\varphi}{\sin\theta\cdot\cos\theta + \sin^2\theta\cdot\tan\varphi} \tag{2.22}$$

where

$$K = \frac{1 - \sin\varphi + \tan^2(45 - \frac{\varphi}{2})}{2} \tag{2.23}$$

and

$$\alpha = \frac{1 + 3\cdot\frac{C}{D}}{1 + 2\cdot\frac{C}{D}} \tag{2.24}$$

Broere (2001) and Anagnostou (2012) used the infinitesimally small slices method in the wedge, described by Walz & Prager (1978) for slurry-filled trenches. The wedge is subdivided into small horizontal slices i (i is the number of each slice), possibly enabling

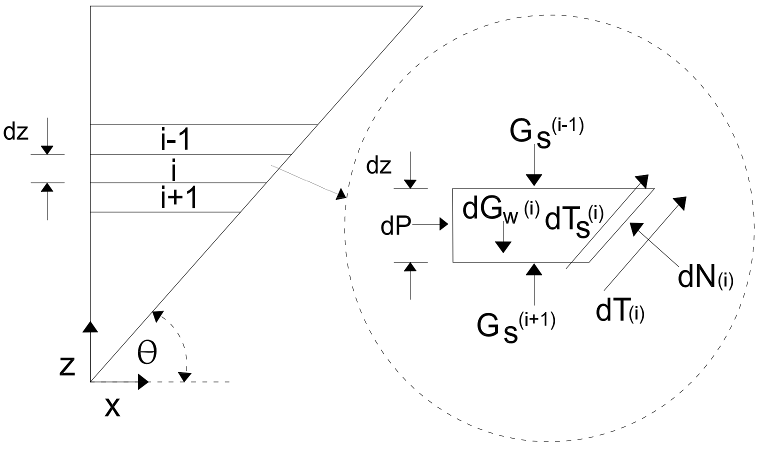

Figure 2.8: Forces acting on infinitesimally small slices on the wedge

the consideration of different soil conditions, see Fig. 2.8. The force equilibrium on each horizontal slice is formulated. The minimum support pressure is calculated based on integrating the horizontal and vertical forces over the whole wedge for each horizontal slice. The method of slices assumes a linearly proportional relationship between the horizontal stress ${\sigma_h}^{(i)}$ and the vertical stress ${\sigma_h}^{(i)}$.

$$ {\sigma_h}^{(i)}(z) = K_{wedge}^{(i)} \cdot {\sigma_v}^{(i)}(z) \tag{2.25} $$

Broere (2001) proposed $K_{wedge}^{(i)}$ $=K_0$. Anagnostou (2012) assumed $K_{wedge}^{(i)} = 0.5$. The vertical stress distribution and the failure mechanism for different arching implementations are shown in Fig. 2.9, the results in Fig. 2.9 are obtained for the maximum value of the minimum support pressure.

Chen et al. (2015) improved the 3D wedge-silo model by considering the height of the silo on the basis of physical model test results (Fig. 2.10). The effective height (H_v) is calculated as:

$$ H_v = \min\left\{C, \frac{2D}{\tan\theta}\right\} \tag{2.26} $$

They proposed a new analytical method for calculating the lateral earth pressure coefficient in silo by considering the rotation of the maximum principle stress which occurs in the arching zone above the wedge:

$$ K_{silo} = \frac{\cos^2\theta_0 + K_a \cdot \sin^2\theta_0}{\frac{1}{3}\cdot(1-K_a)\cdot\sin^2\theta_0 + K_a} \tag{2.27} $$

where $\theta_0 = \frac{\pi}{4} + \frac{\varphi}{2}$ and $K_a = \tan^2(45 - \varphi/2)$.

Liu et al. (2019) proposed a new 3D model for face stability analysis with a dual failure mechanism, see Fig. 2.11. The failure mechanism consists of two parts: a rotational failure

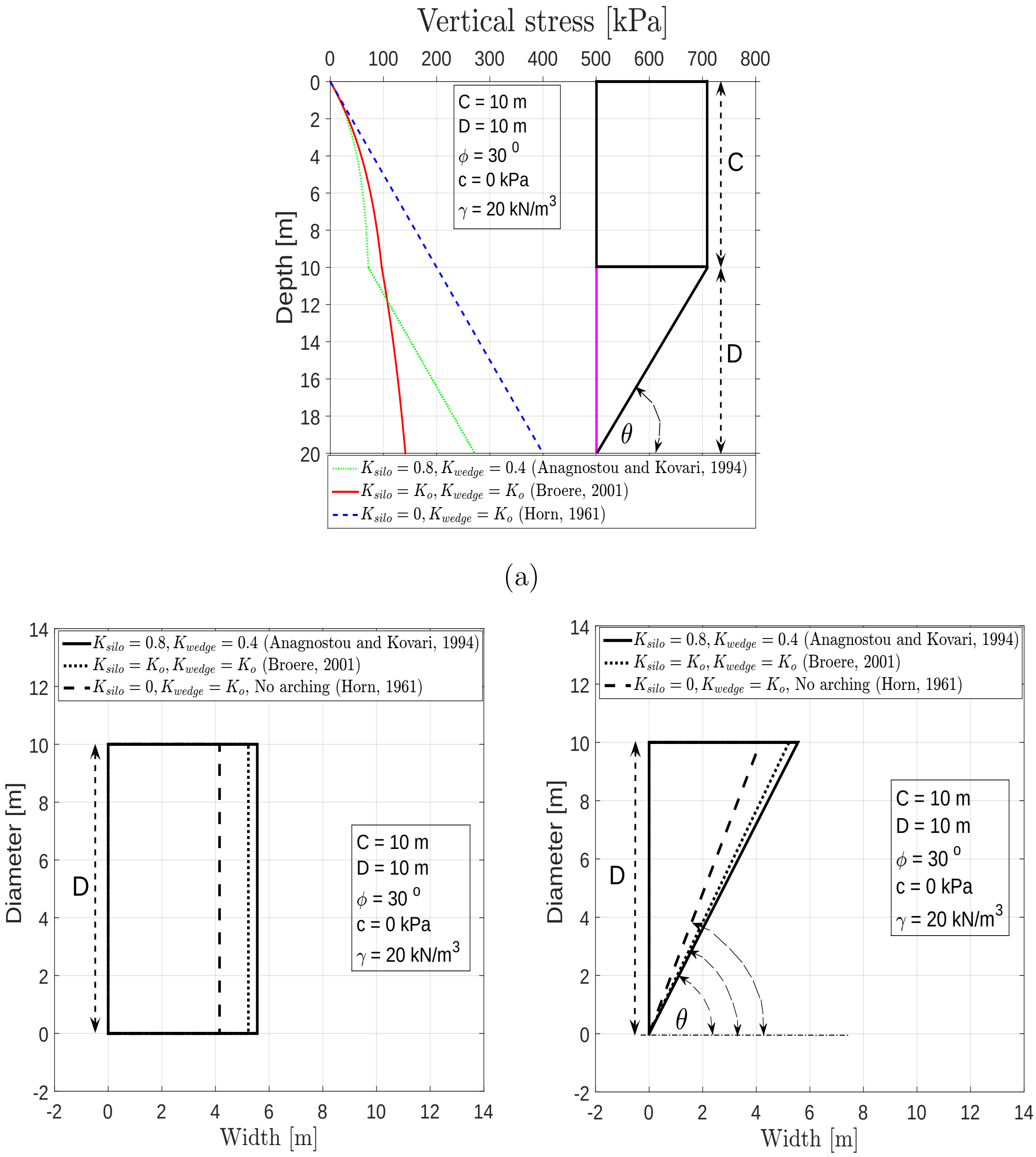

(a)

(b)

(c)

Figure 2.9: Vertical stress distribution for different approaches, either considering arching or not: (a) vertical stress distribution; (b) top view of failure mechanism; (c) side view of failure mechanism

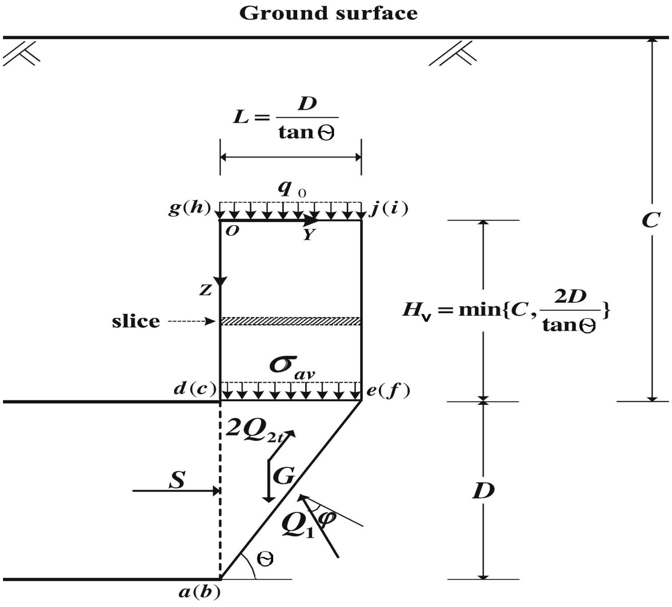

Figure 2.10: Improved wedge-silo model, Chen et al. (2015)

zone (lower zone) and a gravitational failure zone (upper zone). The rotational failure zone is bounded by a log spiral shaped slip surface and tends to rotate to the tunnel face. The vertical distributed force loads acting on the top (wedge) of the rotational failure zone is obtained from an analysis of the gravitational failure zone using the silo theory with $K_{silo} = K_0$.

The wedge-silo model has been investigated by several researchers considering the excess pore pressure at the tunnel face (Broere, 2001; Bezuijen, 2002) and the influence of slurry infiltration process (Broere & van Tol, 2000; Bezuijen, 2002). The effect of excess pore pressure and slurry infiltration on the minimum support pressure will be discussed in more detail in Chapter 6.

Unlike the wedge-silo models, Krause (1987) established three models considering the internal stability of the soil at the front of the tunnel face. The 3D failure mechanisms are respectively a half cylinder, a quarter of a circle and a half sphere, see Fig. 2.12. The shear and cohesion forces along the sliding surface set up the resistance against a collapse. Based on the equilibrium of forces of the 3D failure mechanisms, Krause (1987) derived the following expressions for the minimum support pressure p.

1. Half cylinder

$$p = \frac{1}{\tan\varphi} \cdot \left(\frac{1}{6} \cdot D \cdot \gamma - 0.5 \cdot \pi \cdot c\right) \tag{2.28}$$

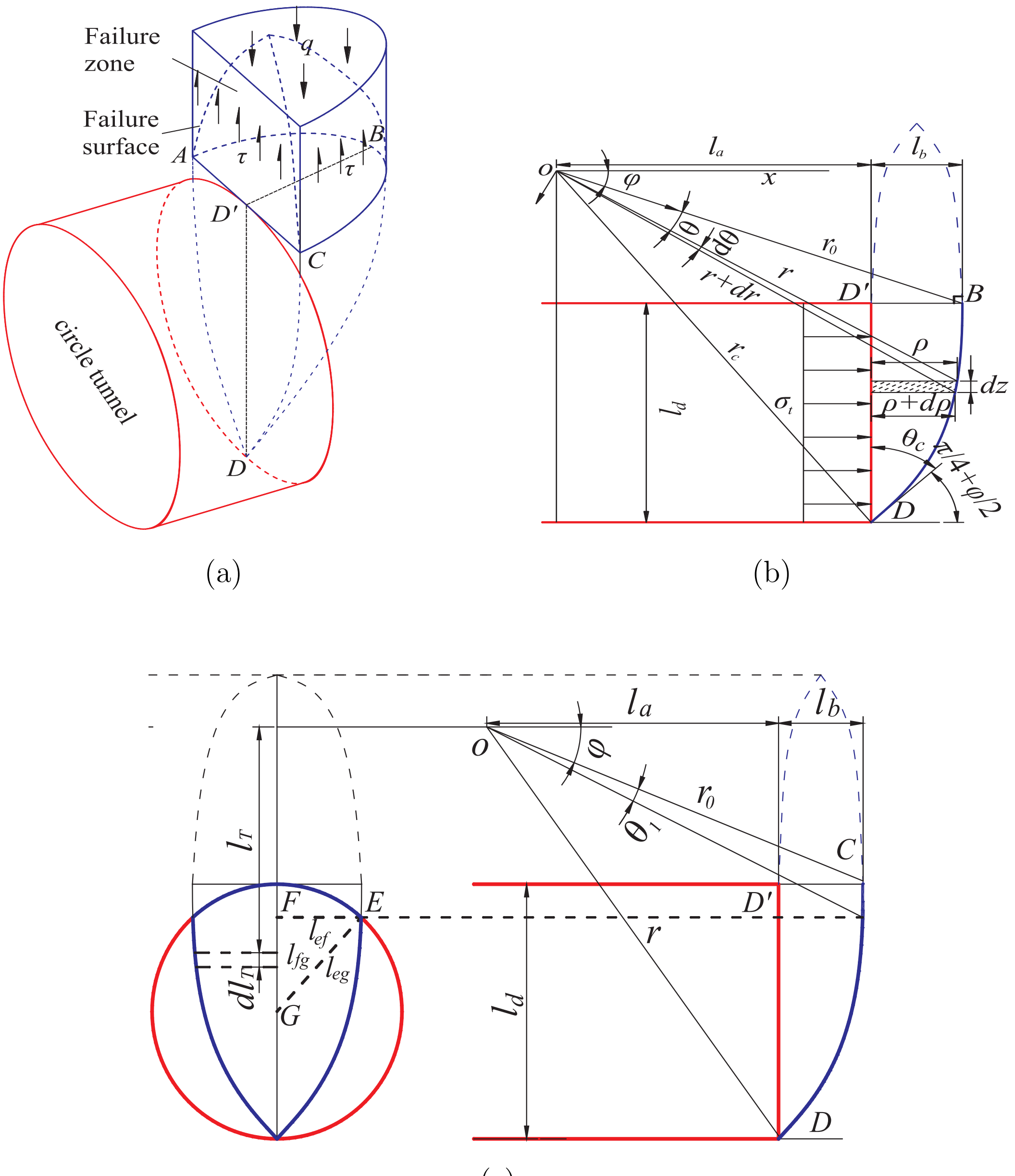
Failure zone
Failure surface
q
τ
τ
A
B
C
D′
D
circle tunnel
o
φ
l_a
l_b
x
θ
dθ
r_0
r
r+dr
D′
B
r_c
l_d
$σ_t$
ρ
dz
ρ+dρ
$θ_c$
π/4+φ/2
D
l_a
l_b
o
φ
r_0
$θ_1$
C
l_T
F
E
D′
r
l_{ef}
l_{fg}
l_{eg}
dl_T
G
l_d
D

(a) (b)

(c)

Figure 2.11: 3D model for tunnel face stability, Liu et al. (2019): (a) 3D failure mechanism; (b) Rotational failure zone; (c) geometric relationships between the slip surface and tunnel face

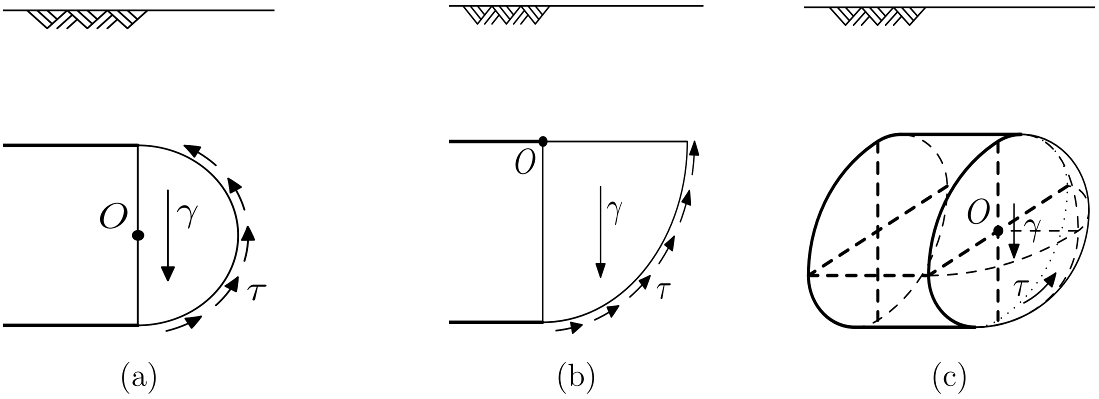

Figure 2.12: Failure mechanisms at the front of tunnel face, Krause (1987): (a) half cylinder; (b) quarter circle; (c) half sphere

2. Quarter circle

$$p = \frac{1}{0.5 + \tan\varphi} \cdot \left(\frac{1}{3} \cdot D \cdot \gamma - 0.5 \cdot \pi \cdot c\right) \tag{2.29}$$

3. Half sphere

$$p = \frac{1}{\tan\varphi} \cdot \left(\frac{1}{9} \cdot D \cdot \gamma - 0.5 \cdot \pi \cdot c\right) \tag{2.30}$$

2.3.1.2 Limit Analysis Method (LAM)

The limit analysis theorem is applied to materials which can be idealized as perfectly plastic with associated plastic flow rule. The concept of limit analysis is based on the theorems of plasticity developed by Drucker et al. (1951), namely the lower and upper bound theorem. By using the lower and upper bound theorems, the range in which true collapse load is expected, can be found.

The upper bound theorem states that the work done by external load in an increment of displacement for a kinematically admissible mechanism equals the energy dissipated by internal stresses. These external loads are not lower than the true collapse loads. For that reason these loads represent an upper bound on the actual solution. The lowest possible upper bound solution is determined with an optimization scheme by trying various possible kinematically admissible failure mechanisms.

The lower bound theorem states that if an internal stress field is in equilibrium with external loads without overcoming the yield criterion in the soil mass. These external loads are not higher than the true collapse loads. The highest possible lower bound solution can be determined by trying different possible statically admissible stress fields.

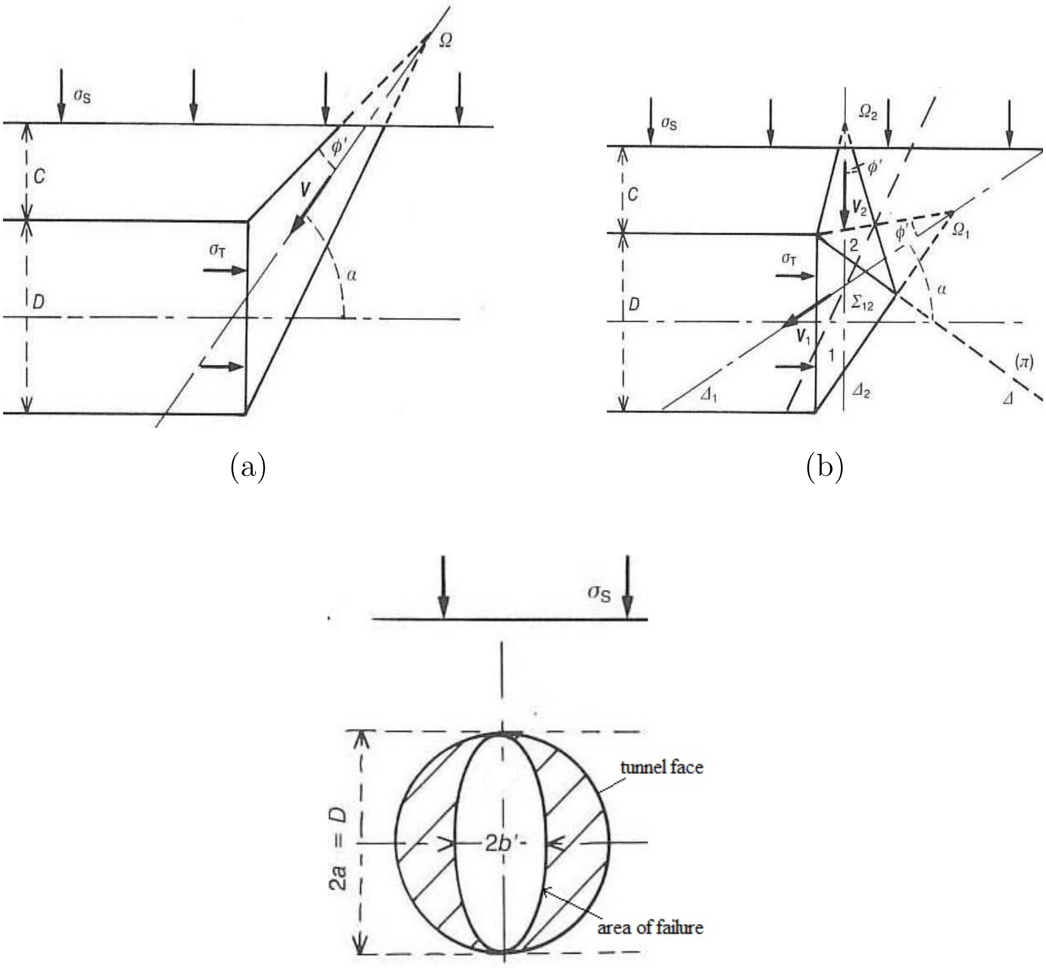
σS
C
D
σT
φ'
V
Ω
α
Ω2
Ω1
V2
V1
2
1
Σ12
Δ1
Δ2
Δ
(π)
tunnel face
2b'
2a = D
area of failure

(a) (b)

(c)

Figure 2.13: Upper bound failure mechanisms, Leca & Dormieux (1990): (a) one conical failure mechanism; (b) two conical failure mechanisms; (c) cross section of the tunnel face

Many researchers have also used the upper bound method to examine the stability of the tunnel face. A number of authors has assumed different shapes of the failure mechanism to obtain the upper bound solution for calculating the minimum support pressure.

Leca & Dormieux (1990) proposed two mechanisms for the failure zone at the front of the tunnel face; one consists of a single conical block and the other is composed of two solid conical wedges with elliptic cross sections at the intersection with the tunnel face, see Fig. 2.13. Both failure mechanisms are characterized by only one parameter, namely, the angle α between the axis of the cone and the horizontal tunnel axis.

Leca & Dormieux (1990) assumed the velocity of each rigid block to be collinear with the axis of each linked cone. This implies that the plastic energy dissipation along the discontinuities obeys the associated flow rule. Also, the two-blocks mechanism given by Leca & Dormieux (1990) is constrained by the normality condition required by plasticity theory. However, this condition does not allow the three-dimensional slip surfaces to develop more freely.

The minimum support pressure at the tunnel axis is expressed by the following equation:

$$p = N_s \cdot q_s + N_\gamma \cdot \gamma \cdot D \tag{2.31}$$

where N_s and N_γ are the non-dimensional coefficients and q_s is the surcharge pressure. Leca & Dormieux (1990) present two sets of graphs for the coefficients N_s and N_γ with respect to friction angle.

An improved failure mechanism composed of several rigid conical blocks was proposed by Mollon et al. (2010). This failure mechanism is an extension of the 3D failure mechanism developed by Leca & Dormieux (1990), see Fig. 2.14. Mollon et al. (2010) found that the total number of five block is sufficient to calculate the minimum support pressure. The improvement of the solution by Mollon et al. (2010) is due to the increase in the degree of freedom of the failure mechanism. Moreover, the failure mechanism proposed by Mollon et al. (2010) is able to account the whole circular tunnel face.

The results obtained by Leca & Dormieux (1990) and Mollon et al. (2010) indicated that for a cohesionless or a frictional-cohesive soil with a friction angle greater than or equal to 20°, the minimum support pressure is independent of the tunnel cover depth.

More recently, the upper bound model used by Leca & Dormieux (1990) was evolved for investigating the effect of layered soil on the minimum support pressure. Tang et al. (2014) amended the solution of Leca & Dormieux (1990) to be applicable in a layered soil. Tang et al. (2014) studied the influence of soil properties of the crossed layered soil

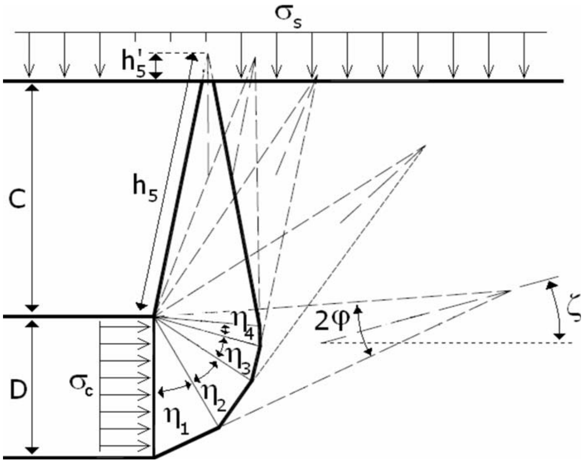
σ_s
h'_5
h_5
C
D
σ_c
η_1
η_2
η_3
η_4
2φ
ζ

Figure 2.14: Conical multiblocks failure mechanism, Mollon et al. (2010)

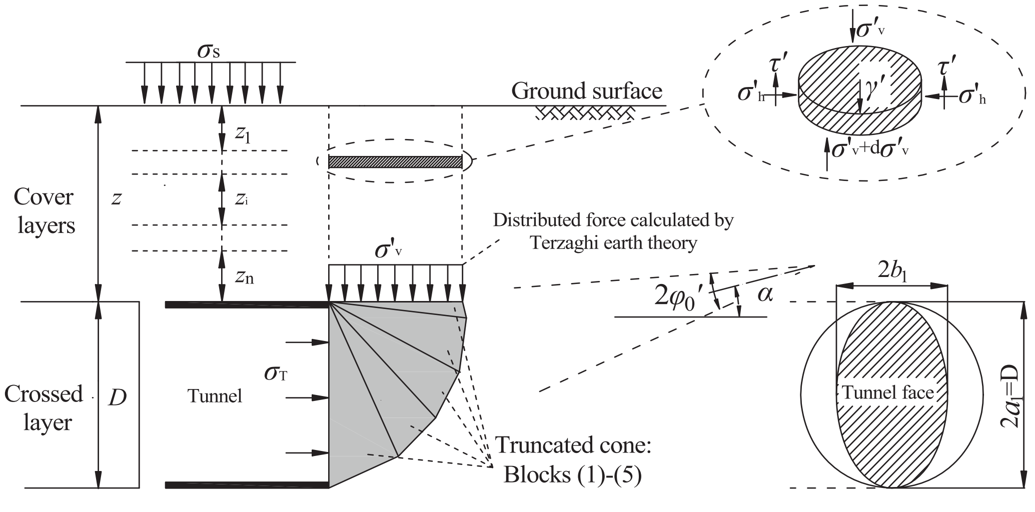
σ_s
Ground surface
z_1
z_i
z_n
z
Cover layers
Crossed layer
D
Tunnel
σ_T
σ'_v
Distributed force calculated by Terzaghi earth theory
Truncated cone: Blocks (1)-(5)
$2\varphi_0'$
α
$2b_1$
$2a_1$=D
Tunnel face
σ'_v
τ'
τ'
γ'
σ'_h
σ'_h
$\sigma'_v+d\sigma'_v$

Figure 2.15: Combined multiblocks failure mechanism, Han et al. (2016)

and the cover layered soil on the minimum support pressure. Their results indicated that the minimum support pressure is highly influenced by the shear strength of crossed soil, while the shear strength of the cover soil is less important.

Ibrahim et al. (2015) improved the 3D failure mechanism of Mollon et al. (2010) to compute the minimum support pressure in dry multilayered purely frictional soil. The improved 3D failure mechanism can consider two or three soil layers.

Senent & Jimenez (2015) extended the solution of Mollon et al. (2010) to study the possibility of partial collapse in layered soils. The proposed model by Senent & Jimenez (2015) examined the influence of soil properties of the crossed soil and the cover soil on the minimum support pressure.

Khezri et al. (2015) investigated the effect of linear variation of cohesion with depth from the ground surface to the base of the tunnel face ($C + D$) on the minimum support pressure. Their results show that adopting the mean value of soil cohesion as a cohesion that does not vary with depth, would lead to conservative predictions for the tunnel face support pressure. However, adopting the cohesion determined for the centreline of the tunnel underestimate the tunnel face support pressure and leads to an unsafe design.

Han et al. (2016) proposed a 3D multiblocks failure mechanism for multilayered cohesive-frictional soils, see Fig. 2.15. Their failure mechanism combines the silo theory (upper part) with the upper bound solution (lower part). The failure mechanism is composed of five truncated cones in the wedge. The distributed load acting on top of the truncated cone is calculated using silo theory with $K_{silo} = K_0$. The minimum support pressure is obtained as an upper bound solution in failure of the wedge.

Lee & Nam, 2004 included the effect of seepage forces emerging from the groundwater flow in the upper bound solution. They found that the minimum support pressure for the face stability is equal to the sum of the effective support pressure obtained from the upper bound solution and the seepage pressure acting on the tunnel face.

2.3.1.3 Finite Element Limit Analysis (FELA)

The Finite Element Limit Analysis (FELA) was developed at the university of Newcastle and was first established by Sloan (1988). FELA couples the lower and upper bound theorems of plasticity theory (Drucker et al., 1951) with the concept of finite element method to provide rigorous bounds on collapse load. FELA utilizes the capabilities of the finite element method to discretize the soil mass and the boundary conditions in combination with the plastic bound theorem to limit the true load by upper bound and lower

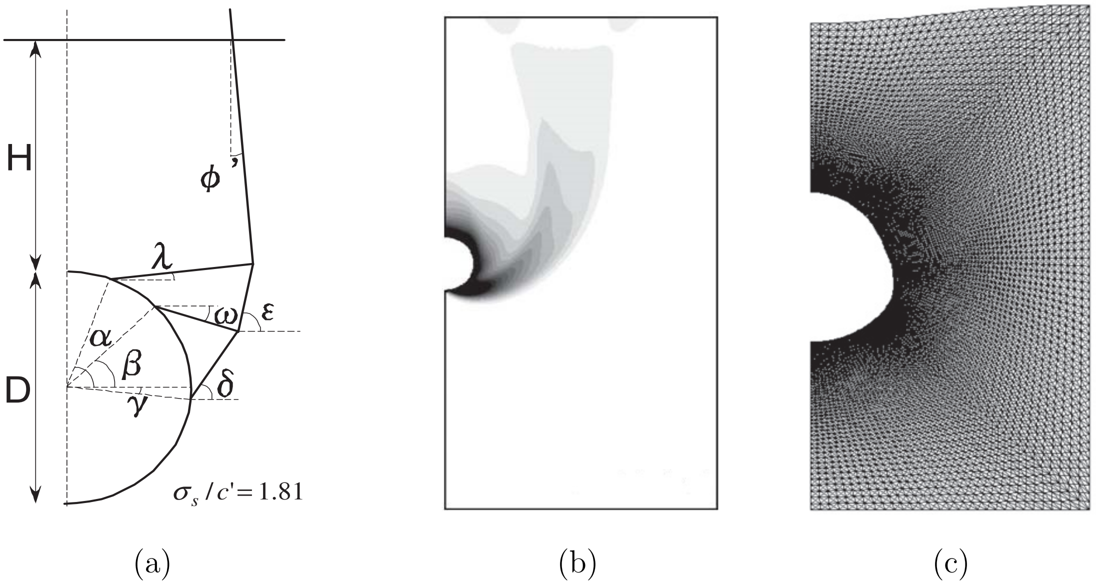

Figure 2.16: Comparison of rigid block mechanism with finite element limit analysis, Yamamoto et al. (2011): (a) rigid block mechanism; (b) power dissipation; (c) deformed mesh

bound solutions. The computational efficiency is achieved by an optimization technique in mathematical programming (e.g., linear programming).

To date, no intensive studies have been published for the 3D tunnel face stability problem have used FELA. Most recent researches are developed on two-dimensional FELA, leading to a number of research papers have been subsequently published.

Lyamin & Sloan (2000) investigated the stability of a plane strain circular model of a tunnel in frictional-cohesive soil using FELA with the nonlinear programming technique. The results are presented in the form of dimensionless stability charts.

Yamamoto et al. (2011) investigated the stability of a single shallow tunnel in frictional-cohesive soils subjected to surcharge loading. Rigorous lower and upper bound solutions for the ultimate surcharge loading are obtained from the simulations. The upper and lower bound results obtained through the finite element limit analysis were compared to results obtained by upper bound rigid block mechanisms, see Fig. 2.16. It was found that the upper and lower bound results from the finite element limit analysis were in very good agreement with the upper bound solution results.

Yamamoto et al. (2013) studied the stability of dual circular tunnel in frictional-cohesive soils subjected to surcharge loading. For a series of tunnel cover to diameter ratios and material properties (φ, c and γ) lower and upper bound solutions for the ultimate sur-

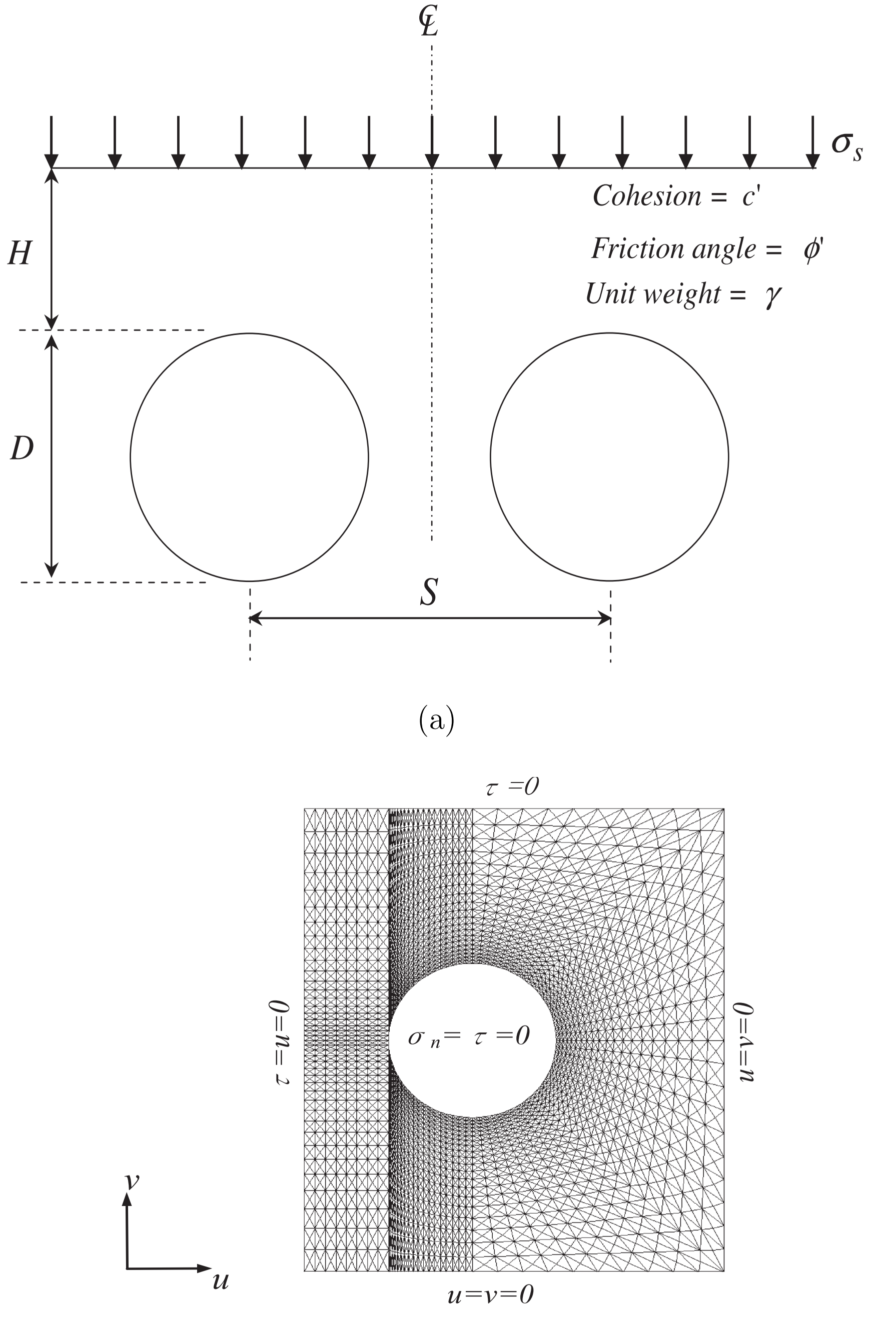
℄
σ_s
Cohesion = c'
Friction angle = ϕ'
Unit weight = γ
H
D
S
(a)
τ =0
u=τ=0
σ_n= τ =0
u=v=0
v
u
u=v=0
(b)

Figure 2.17: Finite Element Limit Analysis for the stability of dual circular tunnel, Yamamoto et al. (2013): (a) plane-strain dual circular tunnels in cohesive-frictional soil; (b) finite element mesh for $C/D = 1$, showing boundary conditions for numerical limit analysis

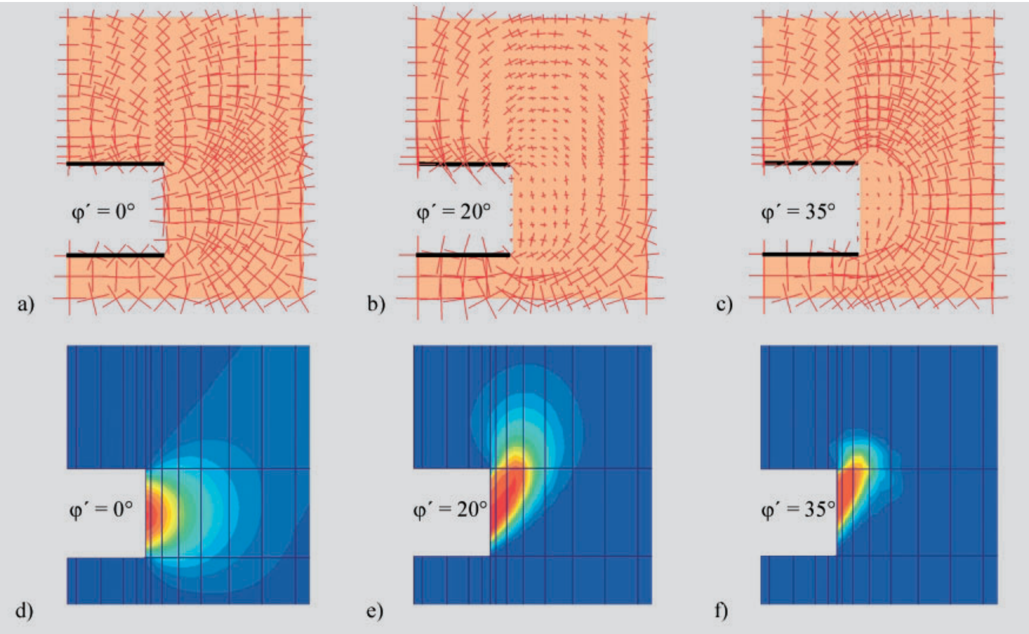

Figure 2.18: Principal stresses (a-c) and incremental displacements (d-f) at failure, C/D = 5 (The graded shades from blue to red describe the increase amount of displacement finite element simulations of Vermeer et al. (2002))

charge loading are obtained, see Fig. 2.17. Their results indicated that the center to center distance between the dual circular tunnel appears as a new problem parameter and plays a key role in tunnel face stability.

2.3.1.4 Numerical methods

Using numerical analysis and computer modeling, many studies have been made to estimate the necessary support pressure and evaluate the tunnel face stability. Numerical modeling can be used to study complex scenarios such as unsaturated soil conditions, layered soil and seepage flow. For numerical modeling, a suitable constitutive model for the soil must be chosen (e.g. elastoplasticity with Mohr-Coulomb yield condition, hypoplasticity or hardening soil model). However, a verification of the numerical models with physical model tests or simulation results of other authors is always necessary.

Based on 3D calculations with the finite element method (FEM), Vermeer et al. (2002) investigated the effect of friction angle and cohesion on the minimum support pressure (Fig. 2.18). The soil was modeled with elastic-perfectly plastic Mohr-Coulomb constitutive model. The FEM models were established for homogeneous dry/drained soil conditions. The results of FEM calculations indicated that for $c = 0$ kPa, $\varphi \geq 20^o$ and $C/D \geq 1$,

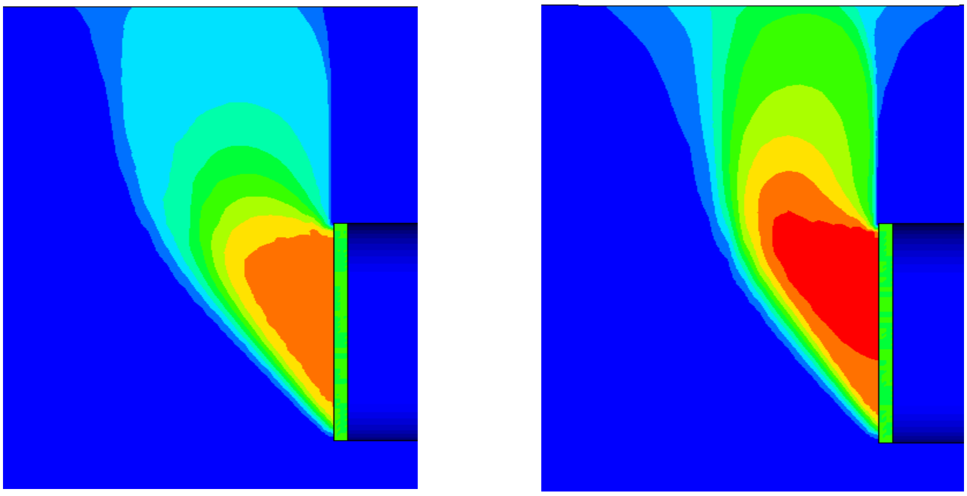

(a) (b)

Figure 2.19: Numerical results of incremental displacements for $C/D = 1$, Kirsch (2010*b*): (a) Mohr-Coulomb model; (b) hypoplastic model

the minimum support pressure only depends on the friction angle and not on the cover depth of the tunnel. Besides, for frictional-cohesive soil and $C/D \geq 2$, the cover depth has no influence of the minimum support pressure. The results of Vermeer et al. (2002) are expressed by the following formula for the minimum support pressure:

$$p_u = \gamma \cdot D \cdot N_\gamma - c \cdot N_c \tag{2.32}$$

where the non-dimensional coefficients N_γ and N_c are formulated as function of friction angle of the soil

$$N_\gamma = \frac{1}{9 \cdot \tan\varphi} - 0.05 \qquad (\varphi \geq 20^o, C/D \geq 1) \tag{2.33}$$

$$N_c = \frac{1}{\tan\varphi} \qquad (\varphi \geq 20^o, C/D \geq 2) \tag{2.34}$$

A numerical study with FEM was performed by Kirsch (2010*b*), who studied the stability of the tunnel face in sand. He compared the numerical results with the results of physical model tests. In his simulations Kirsch (2010*b*) two different material models is used: elastoplasticity with Mohr-Coulomb failure criterion and the hypoplastic model (Fig. 2.19). The results of both the simulations with the Mohr-Coulomb and the hypoplastic model showed good agreement with the support pressures measured in the tests. Kirsch (2010*b*) also found that the cover to diameter ratio has a marginal influence on the minimum support pressure.

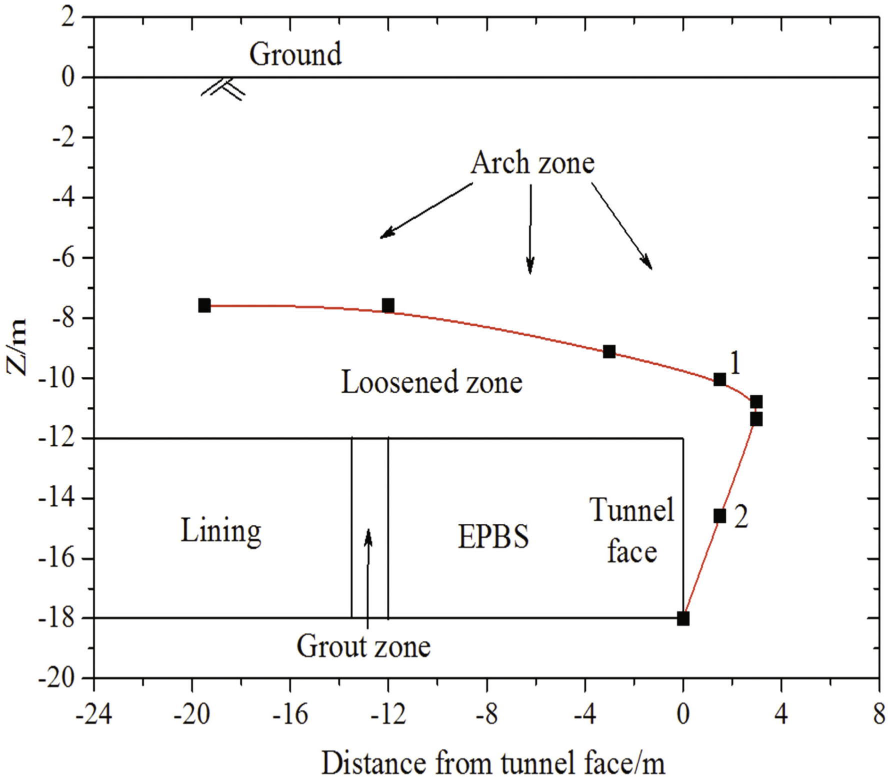

Figure 2.20: Approximated extension of soil arching zone around a tunnel, Lin et al. (2018)

Ohta & Kiya (2001) used the Finite Difference Method (FDM) to examine the influence of the soil properties and groundwater level on the stability of the tunnel face. Ohta & Kiya (2001) established a relationship between the minimum support pressure at the tunnel face and the ground water level for different values of Young's modulus of the soil.

Lin et al. (2018) investigated the development of soil arching during tunnel excavation with earth-pressure balanced shield (EPBS) in dry sand using FEM. Their results indicated that the area ahead of the tunnel face forms a loosened zone due to the lack of the support pressure. The vertical stress is significantly reduced in the loosened zone. Due to the influence of the support pressure, the volume loss and the grouting pressure on the soil surrounding the tunnel, the arching zone gradually develops upward until segments are installed.

In addition to the aforementioned numerical studies, several numerical simulations of the tunnel face stability problem were conducted by other researchers, through FEM (e.g., Peila, 1994; Ng & Lee, 2002; Mayer et al., 2003; Sterpi & Cividini, 2004; Kim & Tonon, 2010), FDM (e.g., Li et al., 2009; Dias, 2011; Senent & Jimenez, 2015) and DEM (e.g., Maynar & Rodriguez, 2005; Funatsu et al., 2008; Zhang et al., 2011).

2.3.1.5 Physical model tests

To assess the required tunnel face support pressure, the failure mechanism and the evolution of soil arching resulting from tunnel excavation, physical models have been extensively used in the laboratory. The physical model tests can be conducted under 1g conditions or at increased g-level (ng) using a geotechnical centrifuge.

Chambon & Corte (1994) performed a series of ng-tests to determine the minimum support pressure in dry sand. Their results indicated that the same failure geometry is observed with different soil densities. The arching effect was found to occur in the upper part of the failure zone, see Fig. 2.21 (a). On the other hand, the minimum support pressure was reported to be affected by the changes in the cover depth ratio (e.g., $C/D = 0.5$, 1, 2 and 4) as well as by the density of the soil.

Takano et al. (2006) performed 1g tests using X-ray in order to evaluate the effect of overburden on arching. They compared the three-dimensional failure zones for the different heights of overburden (e.g., $C/D = 1$, 2 and 4). They found that the arching effect occurs at an overburden of 2D or more. Moreover, according to the tests of Takano et al. (2006), a semicircular slip surface is generated behind the tunnel face, and the failure zone extends straightly upward with an elliptic cross-sectional shape above the tunnel.

Messerli et al. (2010) carried out 1g-tests on the stability of a tunnel face in sand in order to study the effects of cover depth and unsupported span on the support pressure. The tunnel face was supported by either a rigid movable or a flexible face. The unsupported span was introduced by a latex membrane with very low stiffness. It was found that the value of the support pressure measured at the face agrees well with the results of limit equilibrium calculations (Anagnostou & Kovari, 1994). Furthermore, the rigid face test confirmed clearly the failure mechanism proposed by Horn (1961), see Fig. 2.21 (b).

Kirsch (2010*b*) studied the support pressure in dense and loose sands by using 1g-tests. The results indicated that the minimum support pressure is independent of the initial density of the soil. In dense sand the failure zone developed in the vicinity of the tunnel face and propagated stepwise towards the ground surface. Furthermore, in dense sand a chimney wedge type collapse mechanism could be observed. On the other hand, for loose sand, the soil movements immediately reached up to the ground surface, see Fig. 2.21 (c).

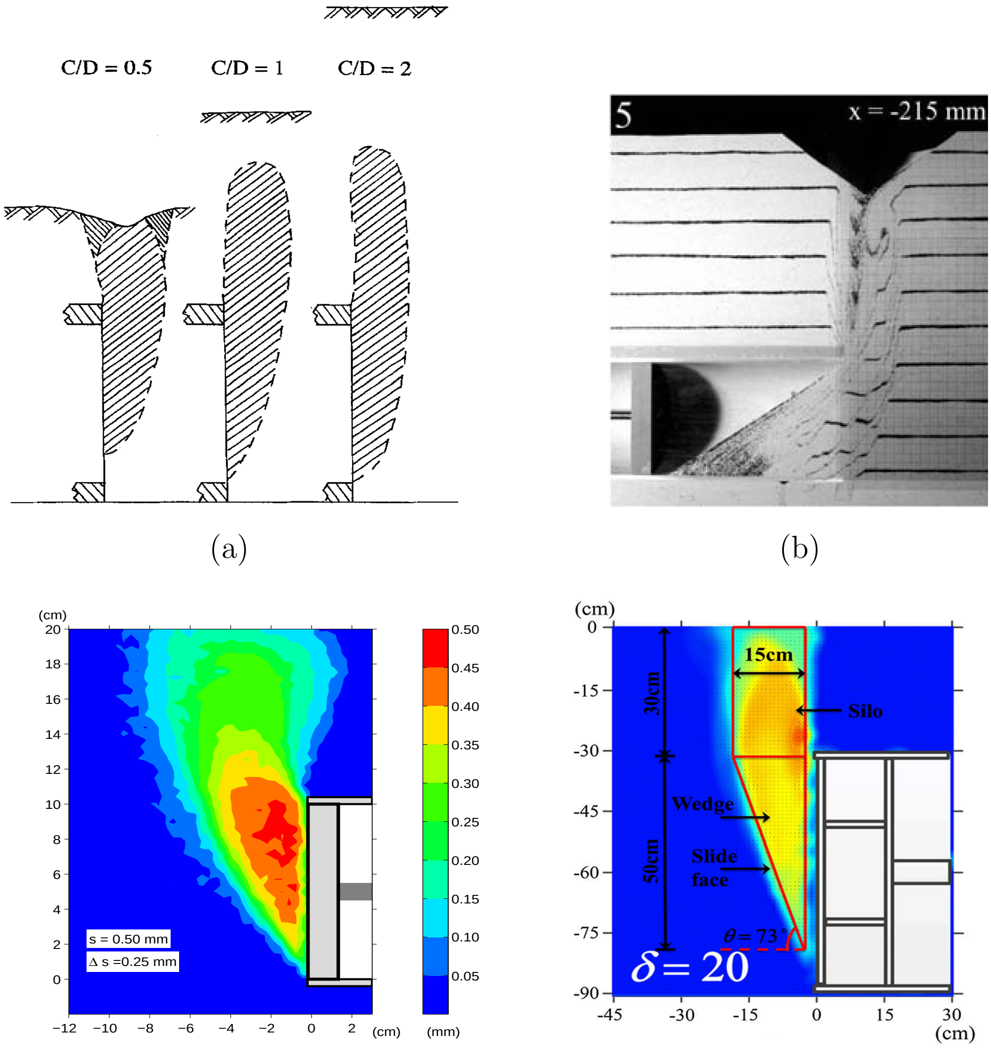

(a) (b)

(c) (d)

Figure 2.21: Shape of the failure mechanism observed in physical model tests: (a) observed failure mechanism for different C/D ratios, Chambon & Corte (1994); (b) observed failure mechanism in dense sand, Messerli et al. (2010); (c) observed failure mechanism in loose sand, Kirsch (2009); (d) observed failure mechanism in low-speed case, Liu et al. (2018)

Idinger et al. (2011) performed ng-tests using dry sand. The influence of the overburden was examined for three cover to diameter ratios (e.g., C/D = 0.5, 1, and 1.5). They observed that the failure mechanism took the form of a narrow chimney extending from the tunnel face to the ground surface. The slip surfaces arised from the bottom of the tunnel face and propagated at an angle of about $45°+\varphi/2$ to the horizontal until it turned more or less vertical reaching the ground surface.

Chen et al. (2013) conducted a set of 1g-tests for various cover to diameter ratios to investigate the evolution of soil arching during face failure in dry sand. Their results indicated a chimney-like failure mechanism. The measured minimum support pressure increased with the increase of the C/D ratio.

Liu et al. (2018) studied the stability of the tunnel face for shallow tunnels in dry sand using 1g large scale model tests. They investigated the influence of moving face speed on the support pressure and the geometry of the failure mechanisms. The test results showed that when the moving speed is relatively high, the minimum support pressure is lower than in the case with relatively low moving speed. In both cases of speed, the observed failure zone was similar to that in the wedge-silo model. However, for the low-speed case the inclination angle of the sliding surface with respect to the horizontal plane θ was much higher than $45°+\varphi/2$ and close to $45°+\varphi$, see Fig. 2.21 (d). Furthermore, for the high-speed case the inclination angle (θ) was slightly higher than $45°+\varphi/2$. The effective width of the failure zone was approximately $2D/3$.

Date et al. (2008), Hisatake & Ohno (2008) and Juneja et al. (2010) performed series of physical model tests to investigate the effect of a pre-supporting system (so-called forepoling) on the stability of the tunnel face and the maximum possible unsupported length during tunnel excavation.

Other physical model tests were reported by Lunardi et al. (1992), Al Hallak et al. (2000) and Kamata and Mashimo (2003) to investigate the distribution and length of the vertical face reinforcement on the stability of the tunnel face.

2.3.2 Tunnel face stability analysis in case of purely cohesive soils

The first study of the stability of tunnels in soft ground was conducted by Broms & Bennermark (1967). This early work was performed on the stability of unsupported circular vertical openings in an undrained cohesive soil, see Fig. 2.22. Their stability solution was expressed in term of the stability number N. The stability number was

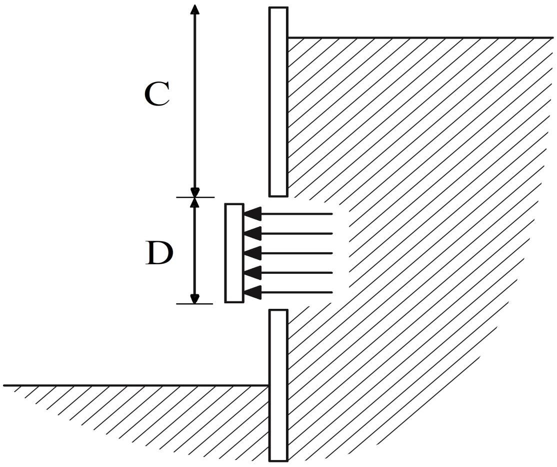

Figure 2.22: Unsupported circular vertical opening, Broms & Bennermark (1967)

defined to be equal to the difference between the stress resulting from the weight of the overburden including uniform surcharge pressure σ_s and the applied support pressure σ_t divided by the undrained shear strength c_u:

$$N = \frac{\sigma_s + \gamma \cdot (C + D/2) - \sigma_t}{c_u} \tag{2.35}$$

where C is the cover depth and D is the tunnel diameter.

The support pressure at the axis of the tunnel face can be calculated with the following expression:

$$\sigma_t = \gamma \cdot (C + D/2) + \sigma_s - N \cdot c_u \tag{2.36}$$

According to the method of Broms & Bennermark (1967) method, the collapse of the tunnel face occurs if the vertical pressure is higher than $6c_u$.

The ranges of stability number corresponding to different states of ground surface deformation are presented in Table 2.1. Following the concept of the stability number, a large number of research papers have been subsequently published in the area of the tunnel face stability.

Using the limit theorems of plasticity (lower and upper bound theorems), Davis et al. (1980) investigated the stability of the tunnel face in cohesive soil. They considered three different shapes of shallow underground opening using the lower bound solution.

The first solution referred to a plane strain unlined circular tunnel which represents an infinitely long tunnel (Fig. 2.23 (a)). The second solution presented a plane strain heading which approximates an infinitely long and unlined wide tunnel (Fig. 2.23 (b)). The third

Table 2.1: Relation between the stability number and deformation, according to Broms & Bennermark (1967)

N	Deformation
< 1	Negligible
$1 - 2$	Elastic
$2 - 4$	Elastic-plastic
$4 - 6$	Plastic
> 6	Collapse

solution is that for a circular tunnel heading for fully lined tunnels where $P/D = 0$ (P is the unlined length), see Fig. 2.23 (c).

The corresponding stability numbers are respectively:

$$N = 2 \cdot \ln\left(\frac{2 \cdot C}{D} + 1\right) \qquad \text{(Fig. 2.23 } (a)\text{)} \tag{2.37}$$

$$N = 2 + 2 \cdot \ln\left(\frac{2 \cdot C}{D} + 1\right) \qquad \text{(Fig. 2.23 } (b)\text{)} \tag{2.38}$$

$$N = 4 \cdot \ln\left(\frac{2 \cdot C}{D} + 1\right) \qquad \text{(Fig. 2.23 } (c)\text{)} \tag{2.39}$$

Also, Davis et al. (1980) introduced four upper bound solutions with different failure mechanisms (mechanisms A-D) for the stability of a plane strain cylindrical cavity, as shown in Fig. 2.24.

Mechanism A is composed of a single sliding block which is deduced from failure mechanisms observed in centrifuge model tests (Cairncross, 1973; Mair, 1979). Mechanism B is composed of two sliding blocks, with an isosceles triangle and a trapezoid on the longitudinal tunnel cross section. Mechanism C consists of three sliding blocks with four variable angles describing the failure planes. Mechanism C and includes mechanisms A and B as special cases. Mechanism D is composed of five sliding blocks, with three variable angles.

Finally, Davis et al. (1980) assessed the possibility of a local failure of the tunnel face, studying 3D circular heading at the front of the tunnel face where the support pressure is not dependent on the cover of the tunnel. The tunnel face is stable against local collapse for the following value of the undrained shear strength:

$$c_u \geq \frac{D \cdot \gamma}{5.63} \tag{2.40}$$

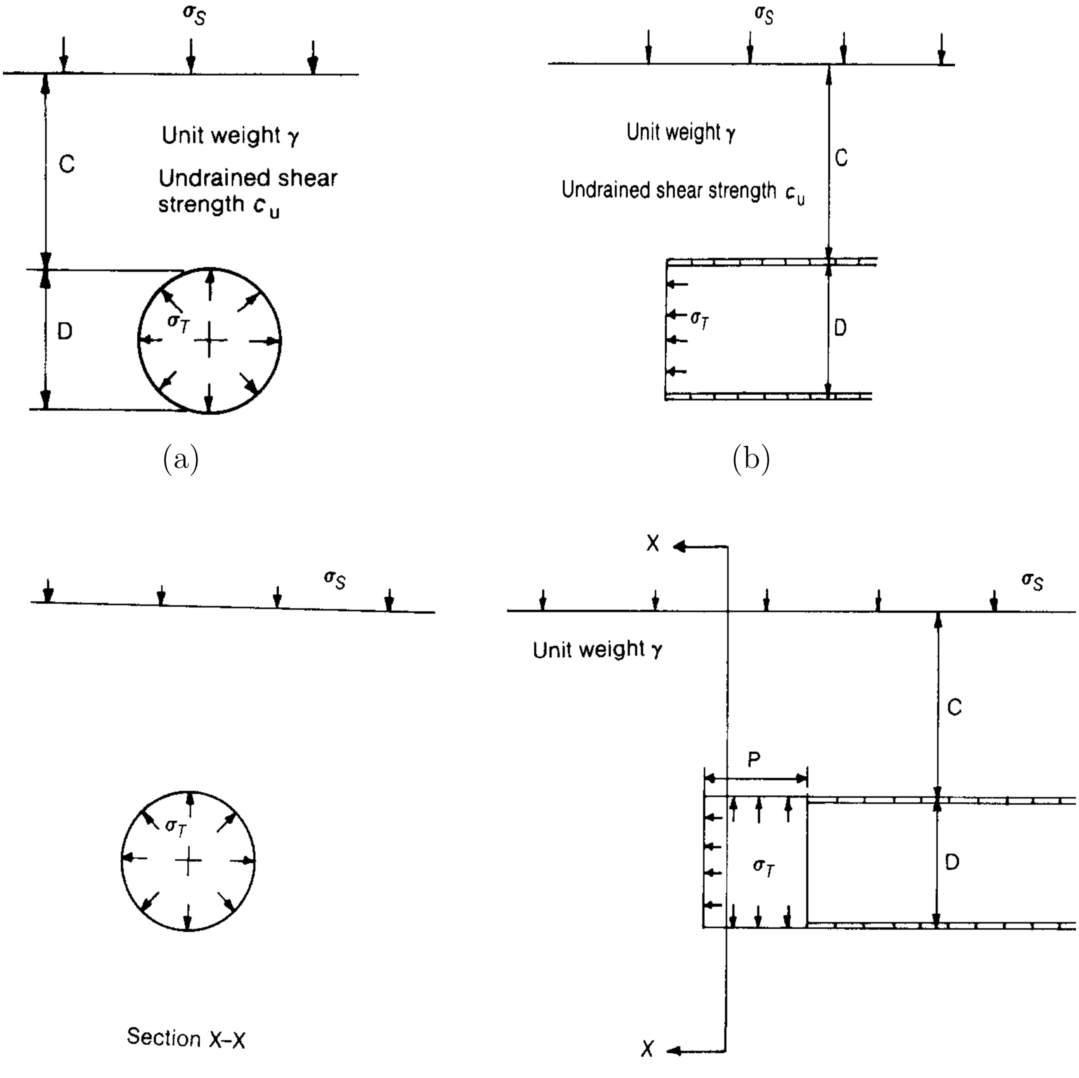
σS
C
D
Unit weight γ
Undrained shear strength cu
σT
X
P
Section X-X

(a) (b)

(c)

Figure 2.23: Lower bound solution for tunnel heading, Davis et al. (1980): (a) plane strain circular tunnel; (b) plane strain tunnel heading; (c) circular tunnel heading for fully lined tunnels

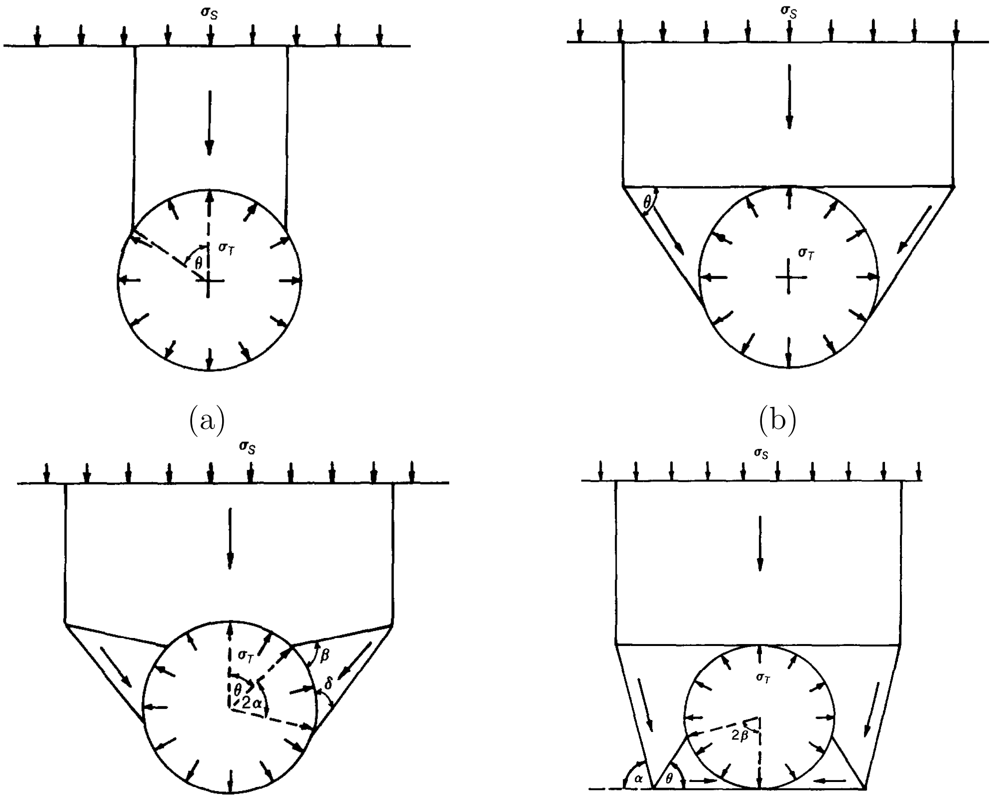

(a) (b)

(c) (d)

Figure 2.24: Upper bound mechanisms, Davis et al. (1980): (a) mechanism A; (b) mechanism B; (c) mechanism C; (d) mechanism D

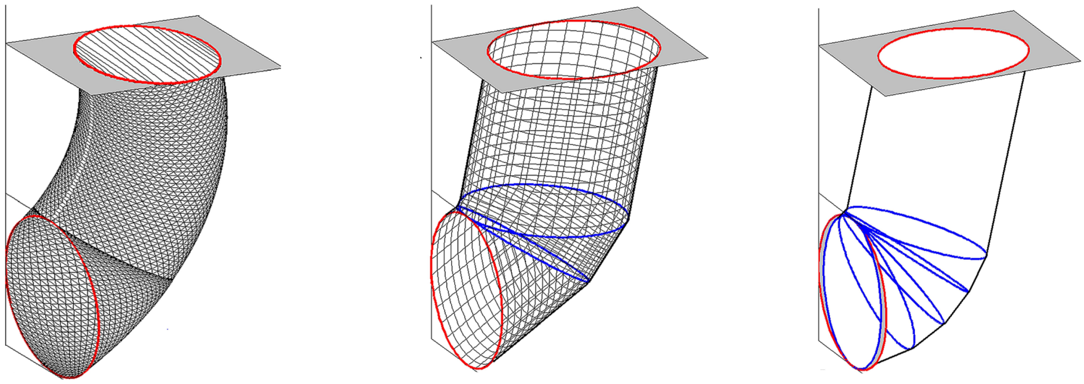

(a) (b) (c)

Figure 2.25: 3D collapse mechanisms based on upper bound solution, Mollon et al. (2012): (a) two blocks failure mechanism; (b) three blocks failure mechanism; (c) five blocks failure mechanism

Kimura & Mair (1981) conducted centrifuge model tests with clay. Their test results suggested a wider range for the stability number between 5 and 10, depending on the ratio of the cover depth to the tunnel diameter (C/D) and the unlined length of the tunnel. They indicated that the stability number increases with increasing cover to diameter ratio and decreases with the unsupported length of the tunnel head.

Osman et al. (2006) performed upper bound calculations of collapse loads in tunnels using distributed shear deformation mechanism. Within the plastic deformation mechanism, the soil is idealized as an elastic perfectly plastic material with cohesion equal to c_u. Outside this mechanism the soil is assumed to be rigid. This failure mechanism does not incorporate slip surfaces and displacement discontinuities.

Sloan (1989), Sloan & Assadi (1993) and Sloan (1994) were the first who applied the Finite Element Limit Analysis (FELA) to investigate the stability of a plane-strain circular tunnel in cohesive soil using linear programming technique. In these research works a wide range of geometrical tunnel profiles including circular, square, rectangular and twin circular tunnel. Furthermore, these authors considered the shear strength of the soil to vary linearly with depth. Their stability number is expressed as a function of two parameters as follows:

$$N = \frac{\sigma_s - \sigma_t}{c_u} = f\left(\frac{C}{D}, \frac{\gamma D}{c_u}\right) \tag{2.41}$$

where $\frac{C}{D}$ is the depth ratio and $\frac{\gamma D}{c_u}$ is the shear strength ratio.

Klar et al. (2007) suggested a new kinematical approach in limit analysis theory for the 2D and 3D stability analysis of circular tunnels in purely cohesive soil. They substituted the plastic velocity field for the elastic displacement field to study the tunnel stability in clay ground.

Mollon et al. (2012) established an upper bound solution for purely cohesive soils. Based on the normality condition of the kinematical theorem of limit analysis, they introduced three failure mechanisms involving multiple rigid-blocks motions, see Fig. 2.25.

The minimum support pressure is assessed by the following equation:

$$p = D \cdot \gamma \cdot N_\gamma - c \cdot N_c + \sigma_s \cdot N_s \tag{2.42}$$

where N_γ, N_c and N_s are non-dimensional coefficients of purely cohesive soil and expressed as follows:

$$N_\gamma = C/D + 0.5 \tag{2.43}$$

$$N_s = 1 \tag{2.44}$$

$$N_c = N \tag{2.45}$$

Mollon et al. (2012) proposed a set of graphs for the stability number N in Eq. (2.42).

2.4 Comments on the wedge-silo model

2.4.1 Failure mechanism and failure zone

Based on the results of the physical model tests (e.g., Kirsch, 2010*b*; Chen et al., 2013; Liu et al., 2018), it can be concluded that the cover to diameter ratio C/D has a significant effect on the geometry of the failure mechanism. If C/D is low (e.g., $C/D = 0.5$), the failure zone reaches the ground surface leading to the development of a global failure zone, see Fig. 2.26 (a and c). The global failure zone is divided into two sub-zones with different mechanisms: the lower and the upper sub-zone. The soil in the lower sub-zone tends to yield and rotate towards the tunnel face. This action is due to insufficient support and weight of the soil (i.e. gravity). However, this tendency is resisted by friction forces at the slip surface. The rotation trend was also observed by Kirsch (2010*b*), Idinger et al. (2011) and Chen et al. (2013). The upper sub-zone is shaped by soil gravity. The soil arching action is the main factor that defines the shape of the upper sub-zone. If C/D is high (e.g., $C/D = 1$ or 2), a bulb-shaped failure zone consisting of a vertical chimney above the tunnel crown and confined by a curved envelope forming a local failure zone, see Fig. 2.26 (b and d).

According to the proposed failure mechanism of the wedge-silo model (e.g., Jancsecz & Steiner, 1994; Anagnostou & Kovari, 1994; Broere, 2001), the height of the silo is assumed to be identical to the whole cover depth above the tunnel crown. For different C/D ratio, the failure mechanism of wedge-silo model assumes a globe failure zone. Therefore, to incorporate the arching effect on failure mechanism of the wedge-silo model, the weight of the soil in the silo is reduced by activating the shear forces along the sliding surfaces of the silo. This reduced vertical stress is applied at the top of the wedge. Furthermore, the shear forces acting on the flanks of the prismatic wedge are taken into account in the static equilibrium of the forces.

In the wedge-silo model, the equilibrium of the forces needs an estimation of the shear forces acting at the slip surfaces. However, the value of shear forces/stresses depends on

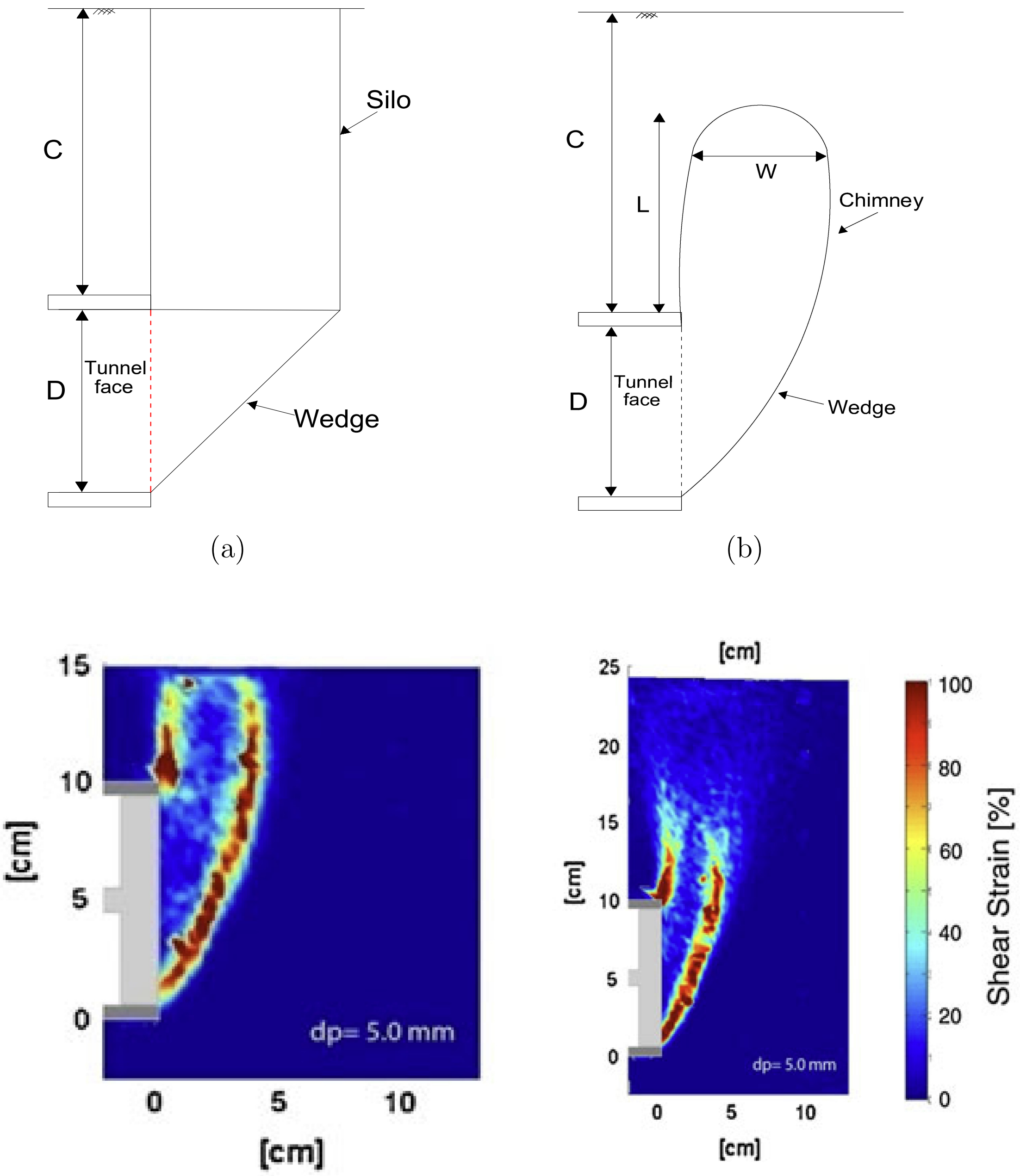
C
Silo
D
Tunnel face
Wedge
C
L
W
Chimney
D
Tunnel face
Wedge
15
10
5
0
[cm]
0
5
10
[cm]
dp= 5.0 mm
[cm]
25
20
15
10
5
0
[cm]
0
5
10
[cm]
dp= 5.0 mm
100
80
60
40
20
0
Shear Strain [%]

(a) (b)

(c) (d)

Figure 2.26: Comparison of failure geometries in physical model tests and wedge-silo model: (a) wedge-silo model failure mechanism; (b) schematic diagram of failure mechanism, Local collapse; (c) global collapse ($C/D = 0.5$), Idinger et al. (2011); (d) local collapse ($C/D = 1.5$), Idinger et al. (2011)

Table 2.2: Comparison of the failure geometry in wedge-silo model with physical model tests

Models	Author	C/D	Mode of failure	L^*	W^+	$p_u/(\gamma \cdot D)$
ng test	Chambon & Corte (1994)	0.5	Global failure	C	$0.41D$	0.044
		2	Local failure	0.84D	0.60D	0.049
LEM	Anagnostou & Kovari (1994)	0.5	Global failure	C	$0.38D$	0.072
	Anagnostou & Kovari (1994)	2	Global failure	C	$0.4D$	0.075
LEM	Horn (1961)	0.5	Global failure	C	$0.32D$	0.084
	Horn (1961)	0.5	Global failure	C	$0.30D$	0.239

L^* is the height of the silo
W^+ is the width of the silo
LEM (Limit Equilibrium Method)

the horizontal stresses which cannot be calculated from equilibrium conditions (Anagnostou, 2012). Thus, to overcome this statically indeterminate task, the horizontal stress σ_h is assumed proportionally dependent on the vertical stress σ_v. The ratio between the horizontal stress to corresponding vertical stress represents the coefficient of lateral earth pressure. This value of the lateral earth pressure coefficient must be assumed in advance.

As shown in Table 2.2, the comparison between the results of physical model tests with the results of the wedge-silo model (Horn, 1961; Anagnostou & Kovari, 1994) indicate a larger silo height and a smaller width of the silo in the failure mechanism of the wedge-silo model. Also, Table 2.2 shows that Horn (1961) gives a higher value of support pressure compared to the results of Anagnostou & Kovari (1994) and physical model tests (Chambon & Corte (1994)). This can be expected as in the model of Horn (1961), the vertical force acting on the top of the wedge is the full weight of the silo (no arching).

2.4.2 Shape of tunnel cross section

In the wedge-silo model, the circular tunnel cross section A_c can be approximated in three different ways. In the first case, the tunnel face is approximated by a square A_s having the same area as the tunnel face (e.g., Horn, 1961; Anagnostou & Kovari, 1996; Kirsch & Kolymbas, 2005), as illustrated in Fig. 2.27 (a). However, to achieve a coincidence of the location of the centers of gravity of the circular and the square area, the cover depth C and the diameter D must be modified to the equivalent cover-depth C_e and the equivalent

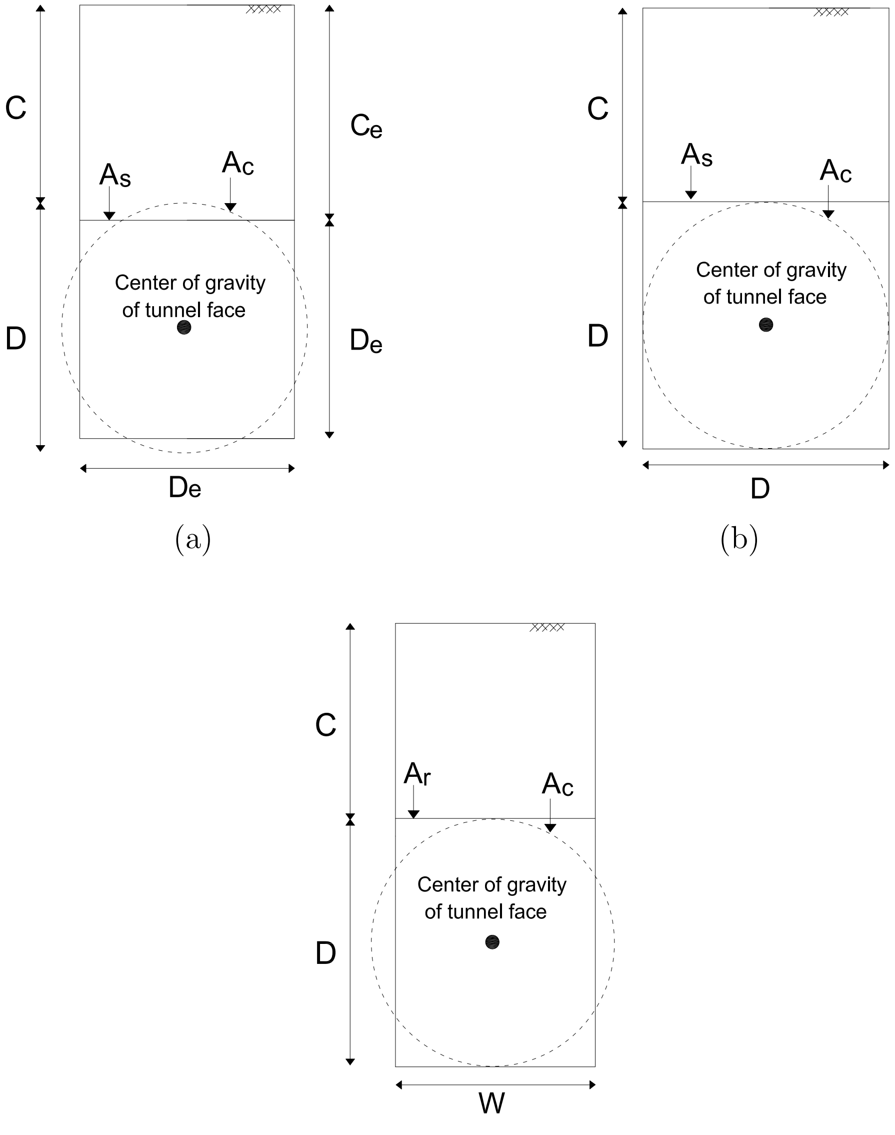
C
Ce
As
Ac
Center of gravity
of tunnel face
D
De
De
C
As
Ac
Center of gravity
of tunnel face
D
D
C
Ar
Ac
Center of gravity
of tunnel face
D
W

(a) (b) (c)

Figure 2.27: Different approximations of the circular tunnel cross-section by either a square or a rectangle in the wedge-silo model: (a) $A_c = A_s$; (b) $A_c < A_s$; (c) $A_c = A_r$

Table 2.3: Calculated support pressure using different tunnel cross-sections

	Support pressure (kPa)			Decreasing percentage (%)	
φ	$A_c = A_s$	$A_c < A_s$ (Reference)	$A_c = A_r$	$A_c = A_s$	$A_c = A_r$
15^o	100.36	106.84	102.99	6.45	3.63
20^o	70.93	76.89	72.86	8.34	5.24
25^o	49.57	54.55	50.66	10.04	7.13
30^o	34.2	38.08	34.52	11.34	9.30
35^o	22.99	26.09	23,037	12.19	10.04

tunnel diameter D_e as follows:

$$C_e = C + 0.057D \tag{2.46}$$

$$D_e = \frac{\sqrt{\pi}}{2}D \tag{2.47}$$

It is important to mention that Anagnostou & Kovari (1996) and Kirsch & Kolymbas (2005) neglected the portion $0.057D$ in Eq. (2.46) and assumed $C_e = C$ for calculating the support pressure.

Within the second case, the tunnel face is assumed to be a square area, as shown in Fig. 2.27 (b). In that case the height H and the width W of the wedge are equal to the diameter D of the tunnel face (e.g., Anagnostou & Kovari, 1994; Broere, 2001), leading to a square area which is about 21.5 % larger than the area of the circular tunnel face.

In the third case, a rectangular area A_r is assumed which has the same sectional area as the circular tunnel face. In that case the height H of the wedge is equal to the diameter D of the tunnel face, whereas the width is smaller than the diameter D, as shown in Fig. 2.27 (c). The width W of the wedge is calculated as follows:

$$W = 0.785D \tag{2.48}$$

To address the effect of the three possible case of the assumed area on the support pressure, the minimum support pressure for the face of the tunnel in dry cohesionless soil ($\gamma = 18$ kN/m^3, $c = 0$ kPa, $D = 10$ m and $C = 10$ m) has been calculated for all three cases using Anagnostou & Kovari (1994). The results are compared in Table 2.3. The minimum support pressure calculated from the second case ($A_c < A_s$) is taken as reference value, see Table 2.3.

From Table 2.3, it can be seen that the second case ($A_c < A_s$) which replaces the circular tunnel face by an equivalent square leads to a higher support pressure than the other

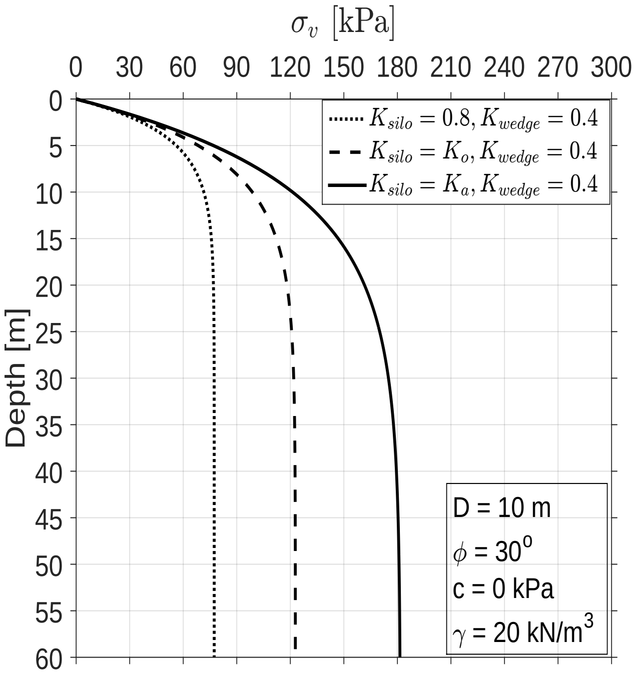

Figure 2.28: Vertical stress distribution with different values of K_{silo}

two choices. In addition, the differences are more significant for larger friction angles. However, the differences between the support pressures calculated with the three different assumptions do not exceed 15%.

Therefore, it can be concluded that in calculations with the wedge-silo model, the assumed shape of the tunnel cross-section has little influence on the minimum support pressure.

2.4.3 Effect of K_{silo} on the vertical stress

Based on Janssen's silo theory (1895), the vertical stress at the base of the silo increases exponentially with silo depth and reaches asymptotically to a constant value. The rate of approach to the asymptotic value of the vertical stress depends on the value of K_{silo} (if all other parameters and dimensions are identical). This can be seen clearly in Eq. (2.13), where K_{silo} is the variable of the natural exponential function. Meanwhile, the asymptotic value of the vertical stress is dependent on the value of K_{silo}, where K_{silo} is placed in the denominator of the first term in Eq. (2.13).

To study the effect of K_{silo} on the vertical stress, the vertical stress distribution is illustrated in Fig. 2.28 for three possible choices of K_{silo} ($K_{silo} = K_a$, $K_{silo} = K_0$, and $K_{silo} = 0.8$) in Eq. (2.13). The soil is assumed to be homogeneous. The dry unit weight is set to $\gamma = 20$ kN/m^3, the friction angle is $\varphi = 30^o$, the cohesion $c = 0$ kPa and the tunnel diameter $D = 10$ m. For simplicity, the surcharge is neglected ($q = 0$ kPa).

It is obvious from Fig. 2.28 that the vertical stress decreases with increasing value of K_{silo}, from $K_{silo} = K_a$ ($K_a = 0.33$) to $K_{silo} = K_0 = 0.5$ by about 32 % and from $K_a = 0.33$ to $K_{silo} = 0.8$ by about 55 %. Meanwhile, the asymptotic value is reached at lower depth with increasing value of $K_{silo} = 0.8$. For $K_{silo} = 0.8$, the vertical stress reaches its asymptotic value by a depth of about one times the diameter. For $K_{silo} = K_0$, the corresponding depth is about two times of the diameter, while it is four times the diameter for $K_{silo} = K_a$.

Therefore, it can be inferred that the value of vertical stress and the depth of arching is significantly influenced by the choice of K_{silo}, which means that the value of support pressure is significantly affected by the choice of K_{silo}.

2.5 Conclusions

This chapter presents a review on analytical and numerical models as well as physical model tests which have been used to analyze the stability of the tunnel face for dry frictional, frictional-cohesive and pure cohesive soil. The following main conclusions can be drawn:

1. Due to the assumed failure mechanism of the wedge-silo model, the stability of tunnel face using the limit equilibrium method (LEM) is a statically indeterminate problem. In order to solve this problem, some assumptions have to be made regarding the distribution of the vertical stress. Furthermore, the horizontal stress σ_h is assumed to be linearly dependent on the vertical stress σ_v by the coefficient of lateral earth pressure (e.g., Jancsecz & Steiner, 1994; Anagnostou & Kovari, 1994; Anagnostou & Kovari, 1996; Broere, 2001; Kirsch & Kolymbas, 2005).

2. To use Janssen's solution, it is required to choose an explicit value for the lateral earth pressure coefficient of the silo. However, the values of K_{silo} used in the literature vary in a wide range. Thus, the choice of an appropriate value for both the lateral earth pressure coefficient of the silo K_{silo} and the wedge K_{wedge} remains an open question for further research.

3. For shallow tunnels, the observed failure mechanisms in the physical model tests are similar to the wedge-silo type failure mechanism described by Horn (1961). However,

the slip surface arising from the bottom of the tunnel face observed in the model tests is curved instead of a straight sloped line assumed in the models (e.g., Idinger et al., 2011; Kirsch, 2010*a*).

4. As the tunnel excavation proceeds, the soil at the front of the tunnel face tends to yield towards the excavation face. However, this tendency is resisted by shear stresses in the soil near the tunnel face. As a result, horizontal soil arching develops around the tunnel face. This soil arching must be considered in a similar way as that of the silo response over the face of the tunnel.

5. Using the limit theorems of plasticity a series of stability models has been proposed for purely cohesive soil. Thes minimum support pressure predicted by these models depends solely on the undrained shear strength c_u. These model are based on the stability number and the corresponding states of deformation of the soil.

Although many researchers have proposed different approaches for the analysis of the tunnel face stability, there are still considerable efforts for calculating the support pressure more accurately. Within this thesis, the tunnel face stability is analyzed with the Kinematical Element Method (KEM) models are presented. The KEM models provide a convenient estimation of the required support pressure for tunnels with a circular face in frictional-cohesive soils. In addition, the KEM models overcomes the assumptions that have been adopted in previous studies presented in the literature. A feasible method for calculating the lateral earth pressure acting on the silo (K_{silo}) based on a KEM model is proposed, which can be easily applied to the failure mechanism and does not need any further assumptions. The proposed KEM models are able to consider the effect of horizontal arching action at the front of the tunnel face. The KEM failure mechanisms can be easily adapted to take into account pore water pressures either under hydrostatic or seepage conditions.

3 Kinematical Element Method (KEM)

3.1 General

The Kinematical Element Method (KEM) was presented for the first time by Gussmann (1982). KEM is an advanced and computationally straightforward procedure to determine the collapse loads in geotechnical stability problems, i.e. the loads that lead to the failure of the soil mass.

In KEM, slip surfaces (shear bands) divide the soil mass into rigid blocks (kinematic elements). Each element i moves with displacement $\mathrm{v_i}$. A set of a specific number of kinematic elements is called failure mechanism. By assuming a displacement $\mathrm{v_1}$ for one of the kinematic elements, it is possible to determine the displacement of all remaining kinematic elements with the aid of kinematic compatibility conditions. Only tangential translations between the kinematic elements are allowed. A rotation is not allowed and a possible dilatancy in the shear band is not taken into account.

The forces acting between the elements are found by including an external unknown force S in the static equilibrium analysis, which is interpreted as reserved load causing the failure of the rigid blocks. At the failure state, the soil resistance is fully mobilized along the slip surfaces. Plastic deformations occur only within the shear bands, whereas the blocks are considered to be rigid. Within the shear bands the shear stress τ and the normal stress σ satisfy the Mohr-Coulomb failure yield criterion.

To determine the direction of the shear force along the edge of each kinematic element, the relative displacements between the kinematic elements are calculated with the condition $S \cdot \mathrm{v_1} > 0$. The external unknown force is a function of the chosen failure mechanism, which will be varied using an optimization technique until the external unknown force S is found. The optimization can involve a maximization or minimization process depending on the geotechnical stability problem.

A KEM calculation is composed of three types of analysis, namely the kinematic analysis, the static analysis and the optimization process.

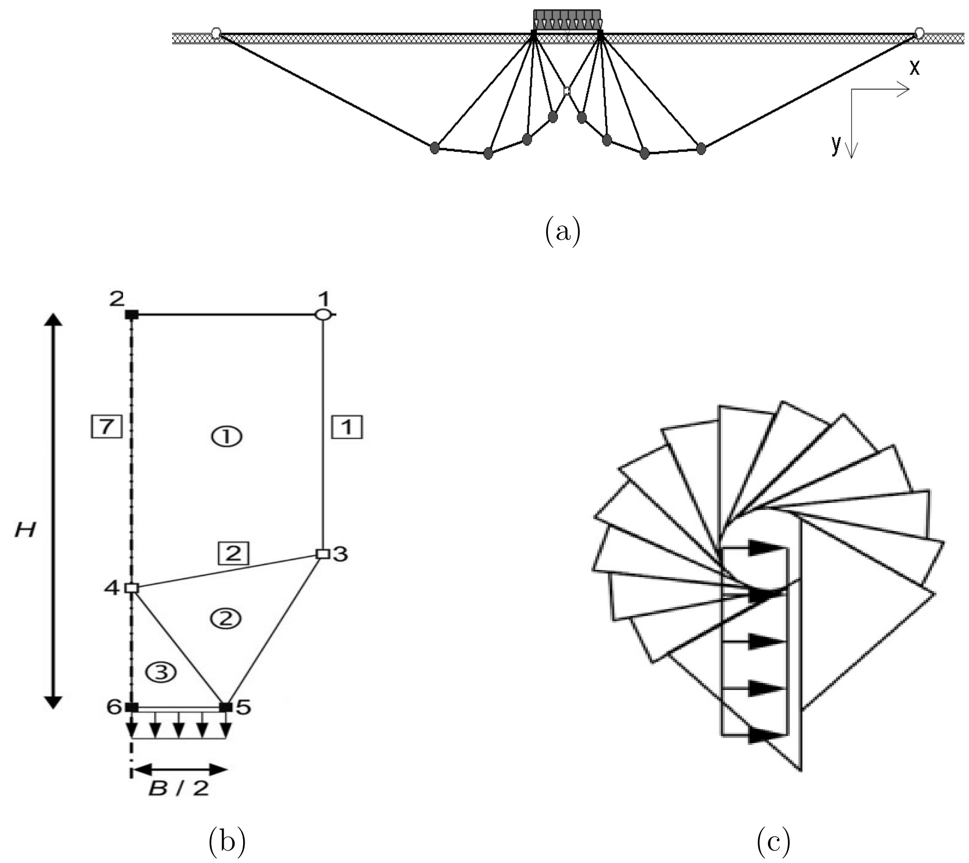

(a)

(b)

(c)

Figure 3.1: KEM models for different geotechnical stability problems, Gussmann et al. (2016): (a) bearing capacity of footing; (b) trapdoor problem; (c) vertical anchor plate

3.2 Application of KEM in geotechnical problems

KEM provides a computer implemented solution for rigid body failure mechanisms including optimization tools to determine the most relevant failure mechanism. KEM can be applied to analyze the bearing capacity of footings (Fig. 3.1 (a)), the active and passive earth pressure, as well as the slope stability in 2D and 3D model analysis. This method has been also applied to more complex geotechnical problems such as the trap door problem (Fig. 3.1 (b)) or to determine the ultimate load of plate anchors (Fig. 3.1 (c)) and soil nails. In addition, KEM can be used to study more complex soil conditions such as soil with pore water pressure, either hydrostatic or due to seepage flow, with drained or undrained conditions as well as unsaturated soil conditions.

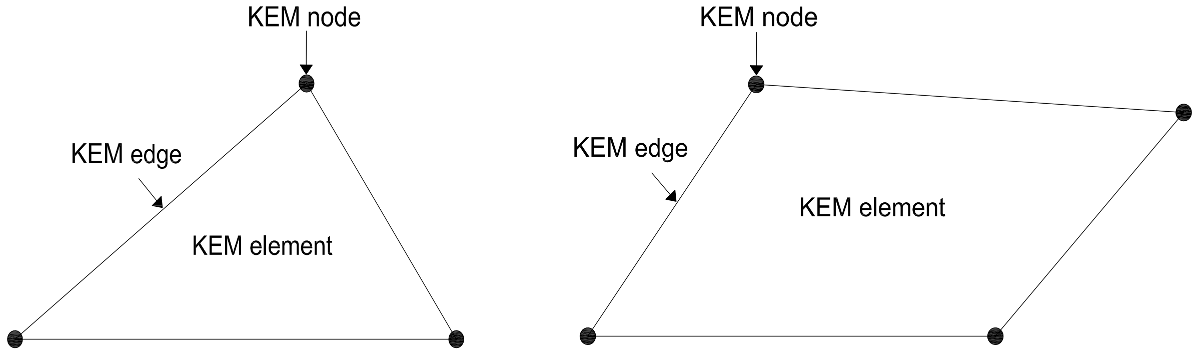
KEM node
KEM edge
KEM element
KEM node
KEM edge
KEM element

(a) (b)

Figure 3.2: Basic element of KEM 2D model: a) triangle element; b) irregular polygon element

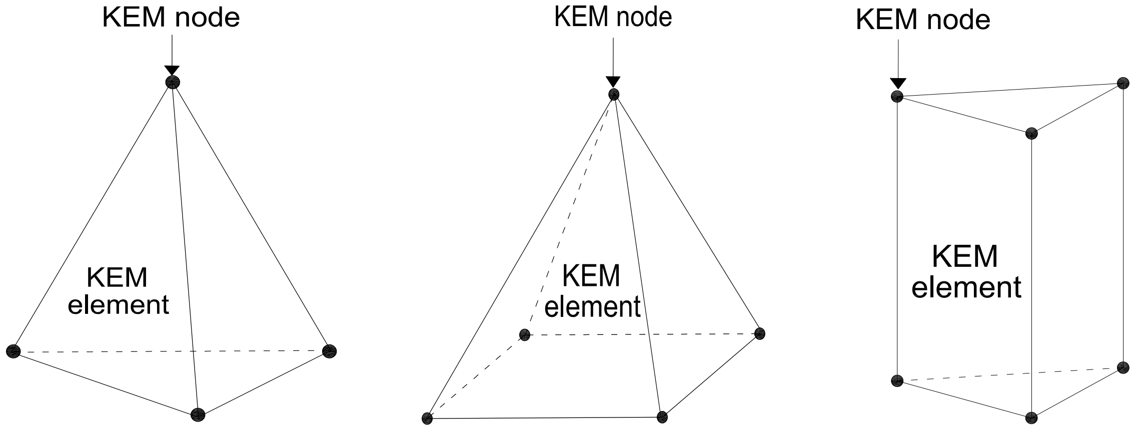
KEM node
KEM element
KEM node
KEM element
KEM node
KEM element

(a) (b) (c)

Figure 3.3: Basic element of KEM 3D model: (a) tetrahedron element; (b) pyramid element; (c) triangular prism

3.3 Geometry

In KEM 2D or 3D analysis, the chosen failure mechanism consists of a number of rigid blocks with a certain shape and plane boundaries, as shown in Fig 3.1. In case of two-dimensional elements blocks, the soil mass is divided into convex polygons which are bounded by straight line segments. These segments are called the edges or the boundaries. Triangles and quadrilaterals are examples of polygons which can be considered as appropriate 2D rigid blocks (Fig. 3.2).

For three dimensional blocks, all convex polyhedrons whose faces are perfectly planar polygons (e.g., tetrahedron, pyramid and triangular prism) can be used (Fig. 3.3). Each 3D block has its faces, edges (boundaries) and vertices. The vertices of the polygons or the polyhedron are called kinematic nodes (Fig. 3.4), which can be either fixed or free nodes. The sliding edges (2D) or surfaces (3D) of the mechanism are separated by contact joint edges (2D) or surfaces (3D).

There are four plane boundary conditions in KEM (Figs. 3.5):

1. Inner boundary: boundary between two rigid blocks being in contact.
2. Flexible boundary: boundary with pre-known displacement.
3. Outer boundary: boundary between the rigid block and the soil at the rest.
4. Free boundary: boundary with no constraints.

In the case of a 3D KEM model, the method of vector analysis provides relatively simple formulations to determine all the relevant features of each block including its volume, the area of the faces and the positions of its vertices. The Cartesian coordinate system x, y, and z is selected as global coordinate system and defined by the orthonormal unit vectors $\{e_x, e_y, e_z\}$ with $e_x = [1, 0, 0], e_y = [0, 1, 0]$ and $e_z = [0, 0, 1]$. The failure surfaces are represented by m vertices $[P_1, P_2, ..., P_m]$ and n surfaces, $[F_1, F_2, ..., F_n]$ with the coordinates of the nodes $[(x_1, y_1, z_1), (x_2, y_2, z_2), ..., (x_m, y_m, z_m)]$, see Fig. 3.4.

The vector from point $P_1(x_1, y_1, z_1)$ to point $P_2(x_2, y_2, z_2)$ is determined as follows:

$$P_1P_2 = (x_1 - x_2)e_x + (y_1 - y_2)e_y + (z_1 - z_2)e_z \tag{3.1}$$

The matrix of direction cosine on the surface of the element spanned by the two vectors (P_1P_2, P_2P_3) expressed by

$$[\cos\lambda, \cos\beta, \cos\alpha] = \frac{P_1P_2 \times P_2P_3}{|P_1P_2 \times P_2P_3|} \tag{3.2}$$

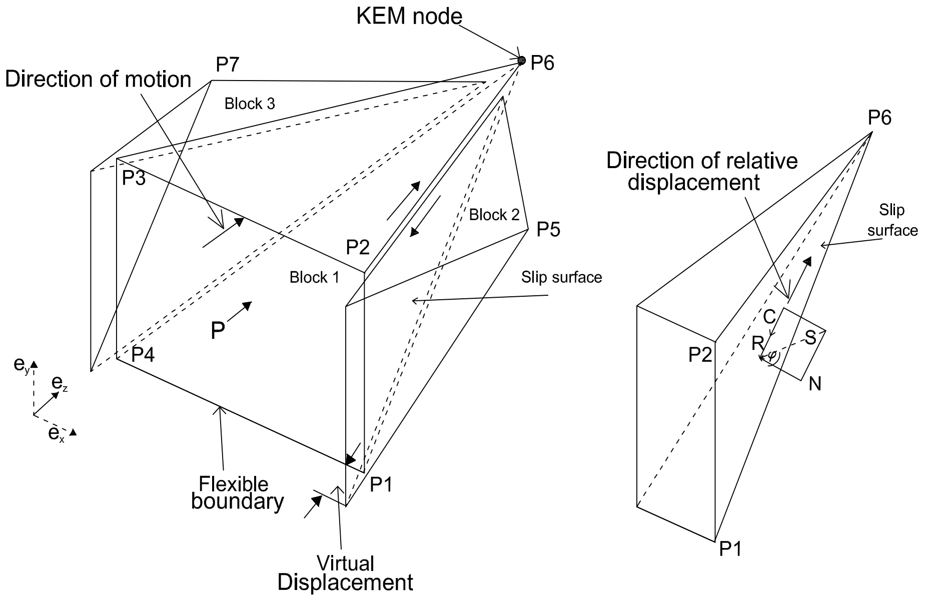
KEM node
P6
Direction of motion
P7
Block 3
P3
P2
Block 2
P5
Block 1
Slip surface
P
P4
e_y
e_z
e_x
Flexible boundary
P1
Virtual Displacement
P6
Direction of relative displacement
Slip surface
C
S
R
φ
N
P2
P1

Figure 3.4: KEM model for 3D passive earth pressure (modified from Gussmann (1986))

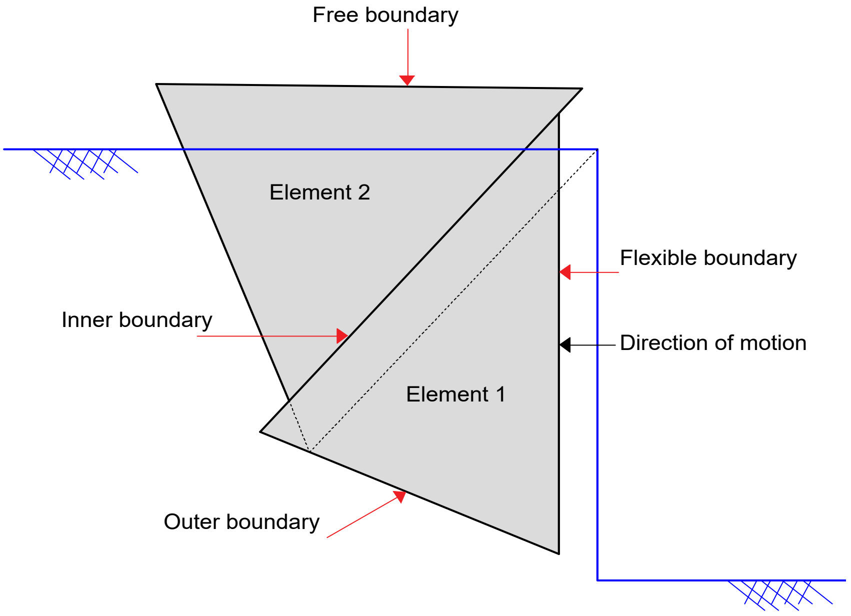
Free boundary
Element 2
Flexible boundary
Inner boundary
Direction of motion
Element 1
Outer boundary

Figure 3.5: Boundary conditions and kinematics for KEM 2D passive earth pressure problem

The distance from point $P_m(x_m, y_m, z_m)$ to point $P_{m+1}(x_{m+1}, y_{m+1}, z_{m+1})$ is calculated as follows:

$$d_{(x,y,z)}^{((m+1),m)} = \sqrt{(x_{m+1} - x_m)^2 + (y_{m+1} - y_m)^2 + (z_{m+1} - z_m)^2} \tag{3.3}$$

where

$x_{((m+1),m)} = x_{m+1} - x_m$

$y_{((m+1),m)} = y_{m+1} - y_m$

$z_{((m+1),m)} = z_{m+1} - z_m$

In order to determine the volume of the polyhedron blocks (e.g. pyramid element, triangular prism) and the areas of its faces, a subdivision of the polyhedron block into a number of tetrahedron blocks is applied.

The volume of a tetrahedron block can be computed from:

$$\text{volume} = \frac{1}{6}\begin{vmatrix} x_1 & y_1 & z_1 & 1 \\ x_2 & y_2 & z_2 & 1 \\ x_3 & y_3 & z_3 & 1 \\ x_4 & y_4 & z_4 & 1 \end{vmatrix} \tag{3.4}$$

where x_i, y_i and z_i (i=1, 2 , 3, 4) are the coordinate of the corner points of the tetrahedron block.

The area of triangular face of a block in a 3D space is

$$\text{area} = \frac{1}{2}\sqrt{\begin{vmatrix} y_1 & z_1 & 1 \\ y_2 & z_2 & 1 \\ y_3 & z_3 & 1 \end{vmatrix}^2 + \begin{vmatrix} z_1 & x_1 & 1 \\ z_2 & x_2 & 1 \\ z_3 & x_3 & 1 \end{vmatrix}^2 + \begin{vmatrix} x_1 & y_1 & 1 \\ x_2 & y_2 & 1 \\ x_3 & y_3 & 1 \end{vmatrix}^2} \tag{3.5}$$

where x_i, y_i and z_i (i = 1, 2, 3) are the coordinates of the corner points.

3.4 Kinematic analysis

Based on KEM assumptions, the rigid blocks can only slide tangentially along inner and outer contact surfaces, and the rotation is not allowed. The outer contact surfaces are located between the blocks and the surrounding soil, while the inner contact surfaces are lying between the blocks. The kinematic process starts by initiating a pre-known displacement v (virtual displacement) on a flexible boundary, $V = \mathrm{v}e_1$, as shown in Fig. 3.4. The flexible boundary is chosen based on the direction of the external (unknown) force which causes the failure of the mechanism. The given virtual displacement induces a displacement of each block i (i is the number of blocks). Each block moves along the shear band with a global displacement $V_i = [V_{ix}, V_{iy}, V_{iz}]$. The soil at the rest O is considered as fixed rigid block with a zero displacement $V_O = [0, 0, 0]$.

By considering the compatibility conditions for the movable rigid blocks, a linear set of equations for the kinematic system of the blocks can be written as follows:

$$[K_v]_{j\times n} \cdot [V]_{n\times 1} + [\hat{V}]_{j\times 1} = 0 \tag{3.6}$$

$$[V]_{n\times 1} = -[K_v]^{-1}_{j\times n} \cdot [\hat{V}]_{j\times 1} \tag{3.7}$$

where n denotes the number of contact surfaces and j the number of degrees of freedom of the rigid blocks, in which j = 3 · i (i is the number of blocks), j should be equal to n for a normal condition. $[K_v]$ is the kinematics matrix which contains the direction cosine of the unit normal vectors of each surface with respect to the global coordinates system, $[V]$ is the vector of unknown (virtual) displacements values of each block and $[\hat{V}]$ is the vector of the pre-known displacement on the flexible boundary, which causes the displacements of the kinematic system.

By solving Eq. (3.7), the global displacements of each block are obtained and the relative tangential displacements between any adjacent blocks can be determined.

The directions of the relative tangential displacements between any adjacent blocks and between the blocks with the surrounding soil are calculated as follows:

$$\Delta V^{((i+1)-i)}_{(x,y,z)} = V^{(i+1)}_{(x,y,z)} - V^{(i)}_{(x,y,z)} \tag{3.8}$$

$$\Delta V^{((i+1)-i)}_{(x,y,z)} = \left[\left(V^{(i+1)}_{(x)} - V^{(i)}_{(x)}\right), \left(V^{(i+1)}_{(y)} - V^{(i)}_{(y)}\right), \left(V^{(i+1)}_{(z)} - V^{(i)}_{(z)}\right)\right] \tag{3.9}$$

$$\Delta V^{(i-o)}_{(x,y,z)} = V^{(i)}_{(x,y,z)} - V^{(o)}_{(x,y,z)} \tag{3.10}$$

$$\Delta V^{(i-o)}_{(x,y,z)} = \left[\left(V^{(i)}_{(x)} - 0\right), \left(V^{(i)}_{(y)} - 0\right), \left(V^{(i)}_{(z)} - 0\right)\right] \tag{3.11}$$

It must be noted that v is a virtual displacement and not a real displacement. The values of the relative displacements do not influence the results. They are only necessary to define the shear forces directions, which are determined by the sign of the displacements.

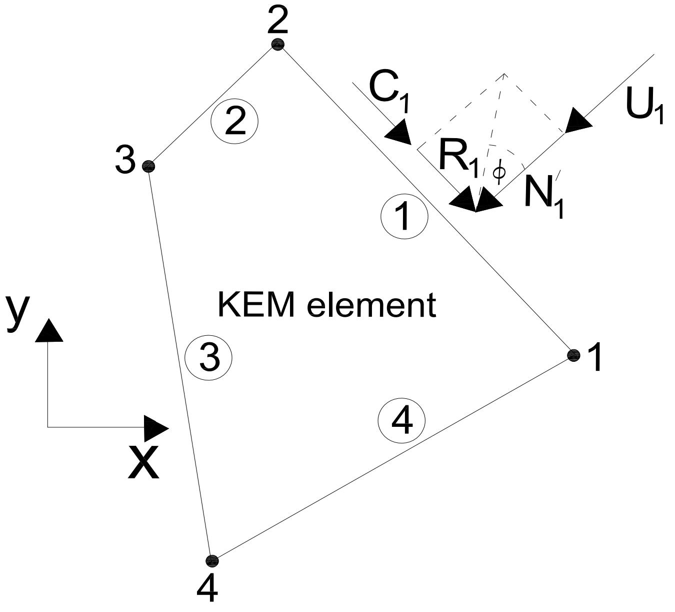

Figure 3.6: Forces acting on the edge of 2D KEM element

3.5 Static analysis

By including an external normal force (unknown) in the equilibrium equations of the forces, it is possible to find the normal forces acting between the blocks. Within the shear bands the shear stress τ and the normal stress σ satisfy the Mohr-Coulomb failure criterion.

$$\tau = \sigma \cdot \tan \varphi + c \tag{3.12}$$

The normal forces acting on each contact surface (see Fig. 3.6) are the effective normal force N'_n and the pore water pressure force U_n. The total normal force N_n can be calculated as follows:

$$N_n = N'_n + U_n \tag{3.13}$$

The frictional shear forces R_n and the total shear forces T_n along each sliding surfaces are calculated as follows:

$$R_n = N'_n \cdot \tan \varphi_n \tag{3.14}$$

$$T_n = R_n + C_n \tag{3.15}$$

where C_n is the cohesion force.

The direction of the shear forces is opposite to the relative tangential movement of the blocks, which have been determined in the preceding analysis of the kinematics.

The force equilibrium equations for each rigid block along the x, y and z-axis and the resultant (S_i) of all forces are given by

$$S_i = (\sum_{i=1}^{n} S_{ix}, \sum_{i=1}^{n} S_{iy}, \sum_{i=1}^{n} S_{iz}) \tag{3.16}$$

By assembling the force equilibrium equations over all rigid blocks taking the normal forces acting at the contact surfaces and the virtual force at the flexible boundary as unknowns, the equilibrium equations are represented in matrix form as follows:

$$[K_s]_{j\times n} \cdot [N]_{n\times 1} + [F]_{j\times 1} = 0 \tag{3.17}$$

where $[K_s]$ is the static coefficient matrix, [N] is the normal vector of unknown forces and [F] is the vector of known forces containing inertia forces, surface loads, cohesion forces etc.

3.6 Optimization process

The aim of the optimization process in KEM is to find the critical geometry of the failure mechanism with respect to specific boundary conditions. The geometry of the block system is expressed by contact surfaces which are defined by the nodes. Therefore, the optimization process for the geometry is can be done in terms of the coordinates of the nodes. The coordinates of the free kinematic nodes will be varied until the critical failure mechanism is found. To do so, the algorithm of particle swarm optimization (PSO) (Kennedy & Eberhart, 1995) is applied for finding a proper geometry of the failure mechanism.

Particle Swarm Optimization (PSO) is a computational method that can be used to solve different kinds of engineering optimization problems. In 1995, Kennedy and Eberhart were introduced PSO as a new metaheuristic search method. It was inspired by the social behavior of individuals living together in groups such as bird flocking, and swarm of insects. The population of particles occurs in the n-dimensional searching space. Each particle will move about the searching space according to a certain amount of knowledge. Each particle has some inertia and will continue to have a component of motion in the direction in which it is moving. It also keeps track of the best solution for all the particles achieved so far, as well as the best solution achieved so far by each particle. After each iteration, every particle will modify its direction such that it has additional components towards its own best position and towards the overall best position. The flowchart for the PSO algorithm is shown in Fig. 3.7.

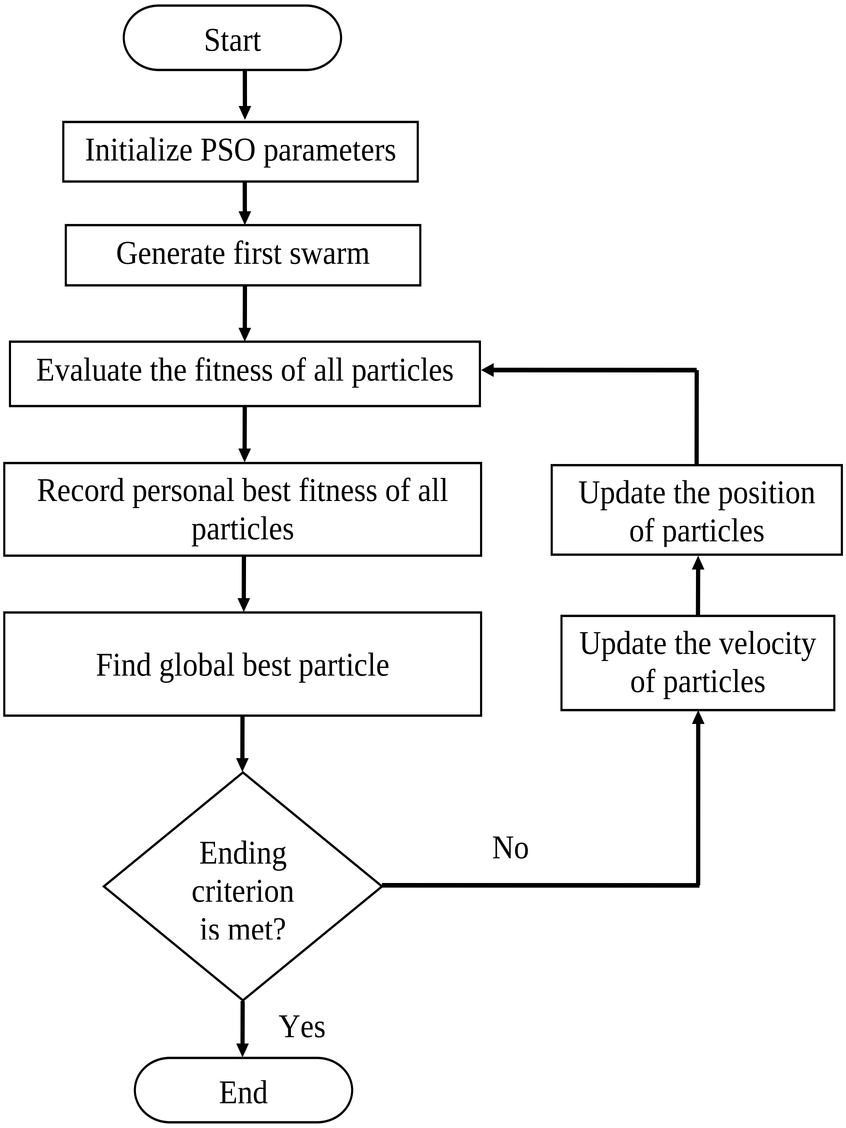
Start
Initialize PSO parameters
Generate first swarm
Evaluate the fitness of all particles
Record personal best fitness of all particles
Find global best particle
Ending criterion is met?
No
Yes
Update the velocity of particles
Update the position of particles
End

Figure 3.7: Flowchart for PSO algorithm

Table 3.1: PSO parameters

PSO parameter	Symbol	Parameter value
No. of particles	P_{size}	25
Maximum velocity	v_{max}	0.2
Minimum velocity	v_{min}	-0.2
First acceleration parameter	c_1	0.50
Diversity of the population maintenance	c_2	1.25
Maximum number of iterations	T_{max}	250

The velocity of each particle is updated using the following equation:

$$v_{id}(t+1) = \underbrace{wv_{id}(t)}_{\text{momentum}} + \underbrace{c_1 r_1 \left(p_{id}(t) - x_{id}(t)\right)}_{\text{cognitive component}} + \underbrace{c_2 r_2(t) \left(p_{gd}(t) - p_{id}(t)\right)}_{\text{social component}} \tag{3.18}$$

$$w = [(T_{max} - G) \cdot (0.9 - 0.4)/T_{max}] + 0.4 \tag{3.19}$$

The position of particle x_i is then updated according to the following equation:

$$x_{id}(t+1) = x_{id}(t) + v_{id}(t+1) \tag{3.20}$$

where t is current step time, $x_{id}(t)$ is the current position of each particle at site d, $v_{id}(t)$ is the current velocity at site d, $p_{id}(t)$ is the best position found so far at a certain site d, $p_{gd}(t)$ is the neighborhood best state found so far at site d, r_1 and r_2 are two independent random numbers in the range [0:1] and c_1 and c_2 are cognitive and social parameters, respectively, w is an inertia weight parameter and G is the current iteration number. The PSO parameters are used in the simulations of this thesis listed in Table 3.1.

PSO reaches its objective if it meets the termination criteria. The termination criteria can be set as follows:

1. Reaching the maximum number of iterations.
2. Finding the best solution.
3. Achieving a constant fitness for a certain number of iterations.

4 KEM model (M) for tunnel face stability

4.1 Introduction

One of the major aspects for the mechanized tunneling process is to adequately support the soil at the tunnel face during tunnel construction. To prevent the tunnel face from collapse a minimum pressure at the tunnel face is required.

Within this chapter the Kinematical element method (KEM) will be applied to analyze the stability of a circular tunnel face. The 3D KEM model (M) is introduced. The KEM model (M) consists of two rigid blocks, a tetrahedron wedge block (lower part) and triangular prism block (upper part). The results obtained with KEM model (M) are compared with the results of analytical and numerical approaches as well as physical model tests available in the literature. To further validate KEM model (M), numerical simulations using the Finite Element Limit Analysis (FELA) have been performed and compared with the results of KEM model (M).

4.2 KEM model (M) for tunnel face stability

4.2.1 Geometry of the failure mechanism

The failure mechanism consists of two parts (see Fig. 4.1). The soil wedge block (lower part) is enclosed by four surfaces: The tunnel face, two outer contact surfaces and the inner contact surface with the upper silo block. The silo block (upper part) raises from the crown of the tunnel to the ground surface enclosed by five surfaces: the ground surface, the inner contact surface with the wedge block, and three vertical outer contact surfaces to the adjacent soil. The positions of the nodes (P1, P2, P3, P6, P7) in the Cartesian coordinate system depends on chosen cover height (C) and diameter (D) of the tunnel.

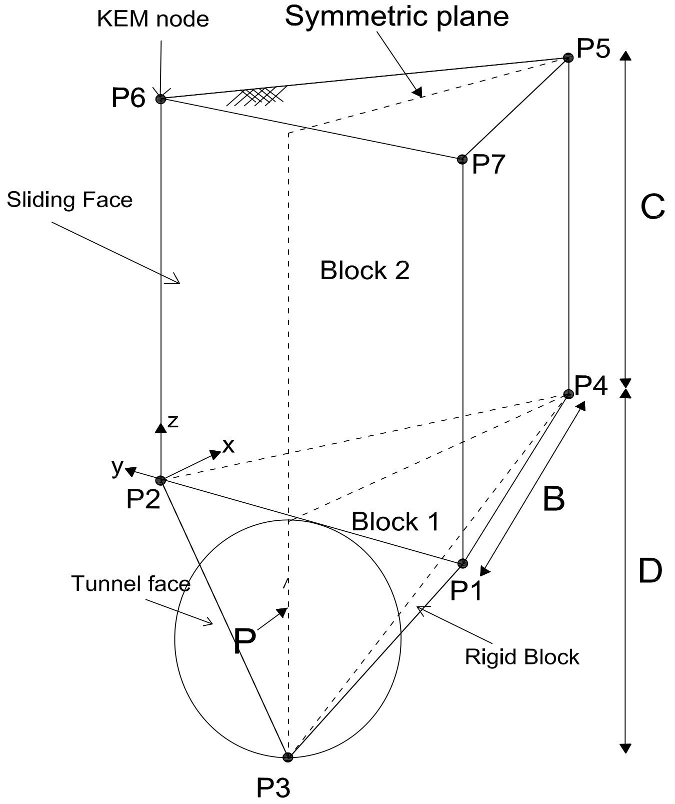
KEM node
Symmetric plane
P5
P6
P7
Sliding Face
C
Block 2
P4
z
x
y
P2
B
Block 1
Tunnel face
P1
D
P
Rigid Block
P3

Figure 4.1: Geometry of the failure mechanism

Based on the results of physical model tests (Chambon & Corte, 1994; Kirsch, 2010*b*; Chen et al., 2013) and numerical calculations (Kirsch, 2010*b*; Lin et al., 2018), the failure zone for the tunnel face collapse consists of two failure zones. The first failure zone above the tunnel crown occurs in a vertical band and ends at the ground surface. The second failure zone at the front of the tunnel face occurs with a semicircular slip surface. Therefore, the degrees of freedom for each node of KEM model M during the optimization process to find the relevant geometry of the failure mechanism is chosen as follows:

1. The nodes P1, P2, P3, P6 and P7 are fixed in x, y and z direction.
2. The node P4 is fixed in y and free in x and z direction.
3. The node P5 is fixed in y and z direction and is bounded to the node P4 in x direction.

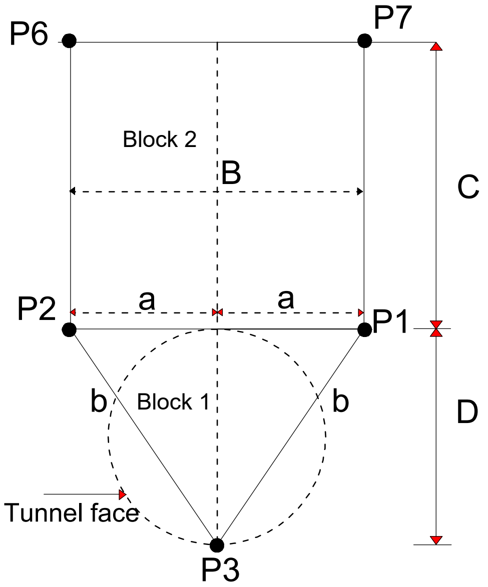

Figure 4.2: Geometry of the triangle

4.2.2 Equivalent area of the tunnel face

The tunnel face is approximated by triangle with two equal sides (b) (see Fig. 4.2), the area of triangle is same area as the tunnel face. The sides a and b of the equilateral triangle are calculated as follows:

$$a = 0.25 \cdot \pi \cdot D \tag{4.1}$$

$$b = \sqrt{D^2 + a^2} \tag{4.2}$$

where D is the diameter of the tunnel.

The width B between the nodes (P1, P2) for the outer contact surface (P1, P2, P6, P7) (see Fig. 4.2) is calculated as follows:

$$B = 2 \cdot a \tag{4.3}$$

$$B = 0.5 \cdot \pi \cdot D \tag{4.4}$$

4.2.3 Half of KEM model (M)

The KEM model (M) can be further simplified considering the symmetry of the failure mechanism (see Fig. 4.3). The simplified model considers only one half of the problem. The following assumptions are made:

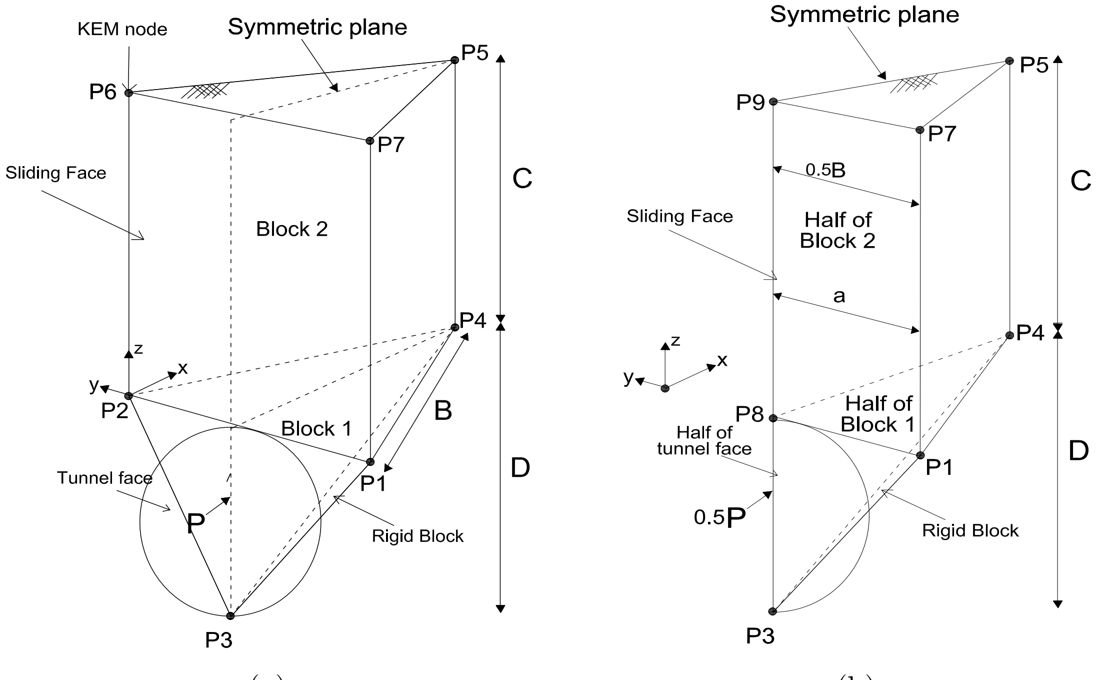
KEM node
Symmetric plane
P5
P6
P7
Sliding Face
Block 2
C
P4
z
x
y
P2
Block 1
B
Tunnel face
P1
D
P
Rigid Block
P3
Symmetric plane
P9
P5
P7
0.5B
C
Sliding Face
Half of Block 2
a
P4
z
x
y
P8
Half of Block 1
Half of tunnel face
P1
D
0.5P
Rigid Block
P3

(a) (b)

Figure 4.3: Geometry of the failure mechanism: (a) KEM model (M); (b) KEM model (M) considering the symmetry of the failure mechanism

1. The circular tunnel face is modeled with the half area of an equilateral triangle, see Fig. 4.4.
2. No displacement in y direction over the symmetric plane.
3. No shear forces along the symmetric plane.
4. The normal forces on the symmetric plane are taken into account.

4.2.4 Kinematic analysis

The kinematic process will start by initiating unit displacement v (virtual displacement) on the face of the tunnel V = -ve_1 (see Fig. 4.5). Each block i moves with a global displacement $V_i = [V_{ix}, V_{iy}, V_{iz}]$ with respect to the soil at rest O. The soil at rest is considered as an element with zero displacement $V_O = [0, 0, 0]$. The relative displacement of each block is determined by a hodograph, as shown in Fig. 4.6.

The directions of the relative tangential displacements between any adjacent blocks and between the blocks and the surrounding soil are determined according to Eqs. (3.9) and (3.11), respectively (Chapter 3).

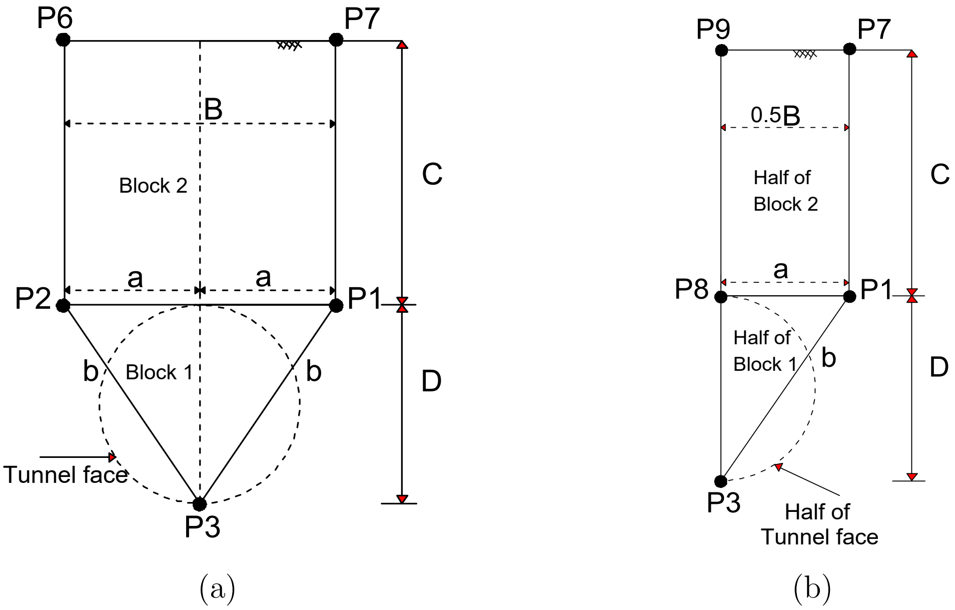
P6
P7
B
Block 2
C
a
a
P2
P1
b
Block 1
b
D
Tunnel face
P3
(a)
P9
P7
0.5B
Half of
Block 2
C
a
P8
P1
Half of
Block 1
b
D
P3
Half of
Tunnel face
(b)

Figure 4.4: Approximated shape of the tunnel face: (a) KEM model (M); (b) half of KEM model

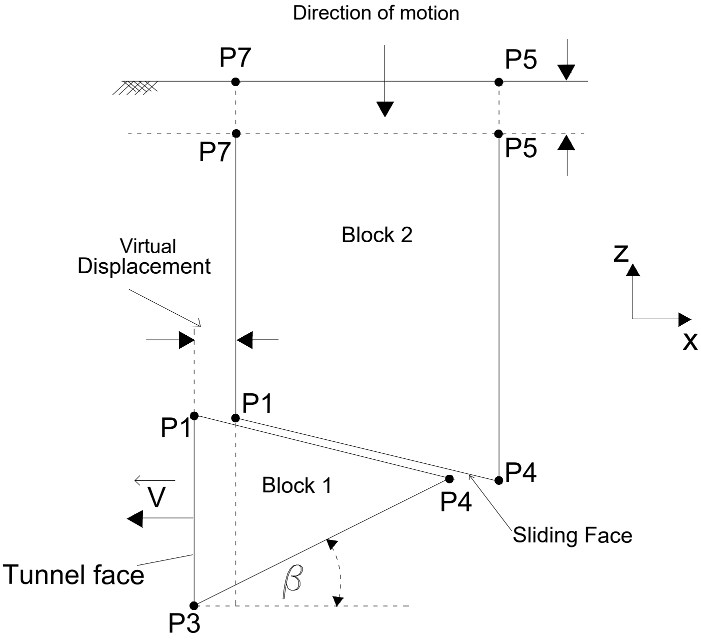
Direction of motion
P7
P5
P7
P5
Block 2
Virtual
Displacement
z
x
P1
P1
P4
Block 1
P4
V
Sliding Face
Tunnel face
β
P3

Figure 4.5: Kinematic of the blocks

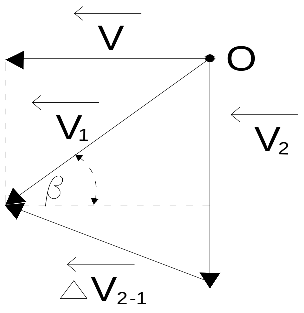

Figure 4.6: Displacement hodograph with respect to the soil at rest O

4.2.5 Acting forces

Fig. 4.7 presents the external and the internal forces acting on each block for the total system and the symmetric half of KEM model (M). These forces are defined as follows:

1. For the total system of KEM model (M) (Fig. 4.7 (a))
    a) Acting forces
        i. W_i : The weight of each block.
        ii. Q : The surcharge load acting on the ground surface.
    b) Reaction forces
        i. N_n : The normal forces on each of the slip surfaces (n = 2 .....7).
        ii. $R_n = N_n \cdot \tan \varphi_n$: The frictional shear forces for each of the slip surfaces (n is the number of slip surface).
        iii. C_n : The cohesion forces on each of the slip surfaces (n = 2 .....7).
    c) P (N_1) : The support force on the tunnel face.
2. For symmetric half of KEM model (M) (Fig. 4.7 (b))
    a) Acting forces
        i. $0.5 \cdot W_i$: The weight of each block.
        ii. $0.5 \cdot Q$: The surcharge load acting on the ground surface.
    b) Reaction forces
        i. N_n : The normal forces on each of the slip surfaces (n = 2, 4, 5, 6).
        ii. $N_7{}^*$: The normal force on symmetric plane (silo).

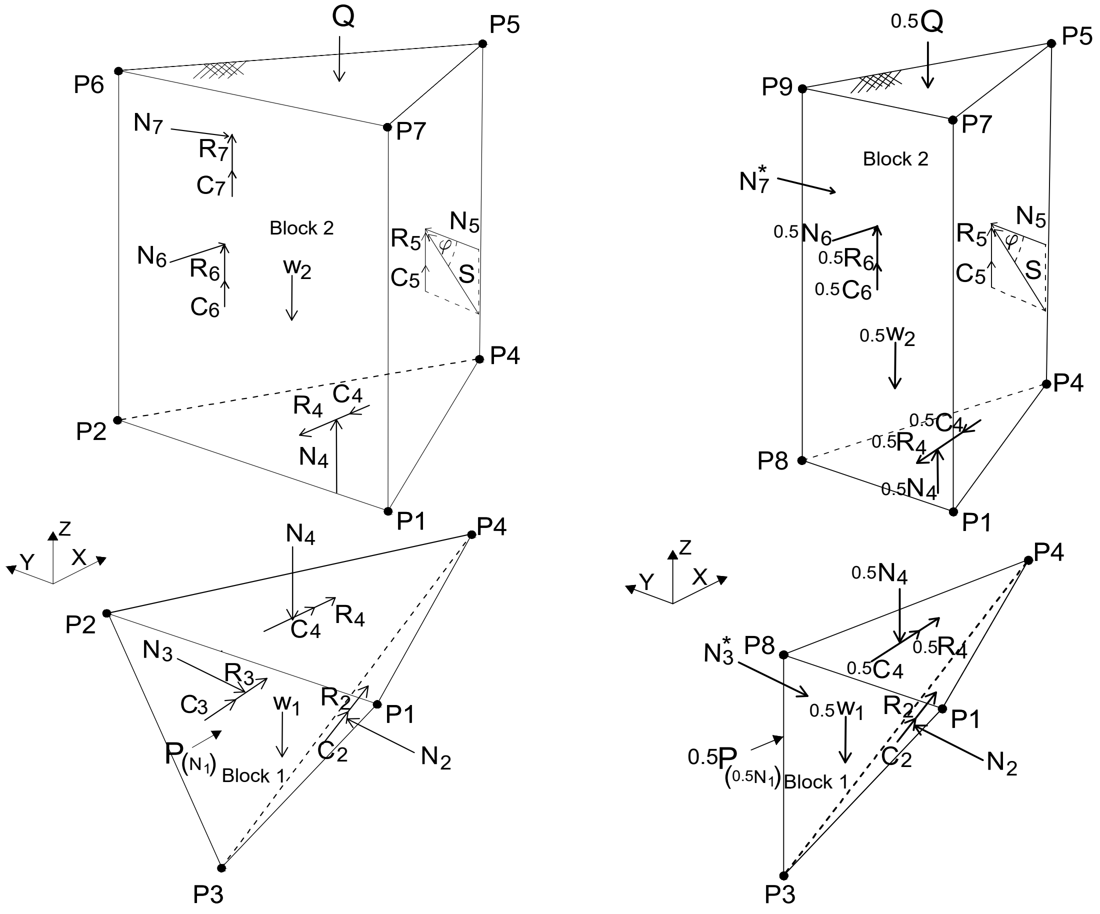
Q
P5
P6
P7
N7
R7
C7
Block 2
N6
R6
C6
w2
R5
C5
N5
φ
S
P4
P2
R4
C4
N4
P1
Z
Y
X
N4
C4
R4
P4
P2
N3
R3
C3
w1
R2
P1
C2
N2
P(N1)
Block 1
P3
0.5Q
P5
P9
P7
Block 2
N7*
0.5N6
0.5R6
0.5C6
R5
C5
N5
φ
S
0.5w2
P4
0.5C4
0.5R4
P8
0.5N4
P1
Z
Y
X
0.5N4
P4
N3*
P8
0.5R4
0.5C4
0.5w1
R2
P1
0.5P
(0.5N1)
Block 1
C2
N2
P3

(a) (b)

Figure 4.7: The free-body diagram: (a) KEM model (M); (b) half of KEM model (M)

iii. ${N_3}^*$: The normal force on symmetric plane (wedge).

iv. $R_n = N_n \cdot \tan \varphi_n$: The shear forces for each of the slip surfaces (n = 2, 4, 5, 6).

v. ${R_7}^*$: The frictional shear force on the symmetric plane (silo), ${R_7}^* = 0$.

vi. ${R_3}^*$: The shear force on the symmetric plane (wedge), ${R_3}^* = 0$.

vii. C_n : The cohesion forces on each of the slip surfaces (n = 2, 4, 5, 6).

viii. ${C_7}^*$: The cohesion force on the symmetric plane, ${C_7}^* = 0$.

ix. ${C_3}^*$: The cohesion force on the symmetric plane (wedge), ${C_3}^* = 0$.

c) 0.5·P (0.5·N$_1$) : The support force on the tunnel face.

4.2.6 Problem of indeterminacy

The static system-matrix for the half of KEM model (M) is formulated as follows:

$$[K_s]_{6\times 7} \cdot [N]_{7\times 1} + [F]_{6\times 1} = 0 \tag{4.5}$$

From Eq. (4.5), it is obvious that the system is statically indeterminate: the number of unknowns is greater than the number of available equations. Hence, equilibrium equations alone are insufficient for obtaining a solution. In order to solve the problem, using the physical model tests and the numerical results, one can estimate the lateral stresses imposed on the silo delivering the one unknown force of the system. The problem is discussed more detail in the following section.

4.2.7 Setting up the static system

According to the observations from physical model tests (Chambon & Corte, 1994; Messerli et al., 2010; Chen et al., 2013), for low cover to diameter ratios (e.g., C/D = 0.5) silo mechanism forms directly above the tunnel face and sinkhole develops at the ground surface (global failure), see Fig. 4.8 (a). However at larger values of cover depth (e.g., C/D = 2) a bulb-shaped failure zone is observed above the tunnel face (local failure), while there is no obvious settlement on the ground surface.

The outcomes of the physical model tests demonstrate that the soil mass bounding the silo mechanism moves slightly in the direction to the silo, allowing the soil mass to expand horizontally. This small movement of the surrounding soil allows a reduction in the horizontal stress acting on the silo. This reduction of horizontal stress in the soil surrounding the silo is observed in the physical model tests (Chen et al., 2013, Fig. 4.8 (b)) and numerical results (Chen et al., 2011), as shown in Fig. 4.8 (c, d).

Clearly, the moving soil mass inside the silo must support the surrounding soil mass by a minimum pressure to avoid extending the collapse. With the relaxation in the surrounding soil mass, the horizontal stress around the silo is less than at rest (Chen et al., 2011; Chen et al., 2013). Besides, the horizontal stresses around the silo cannot drop below their active values.

Based on the earth pressures and failure patterns of tunnel face observed in physical model tests, Chen et al. (2013) concluded that the surrounding soil mass is brought into active state.

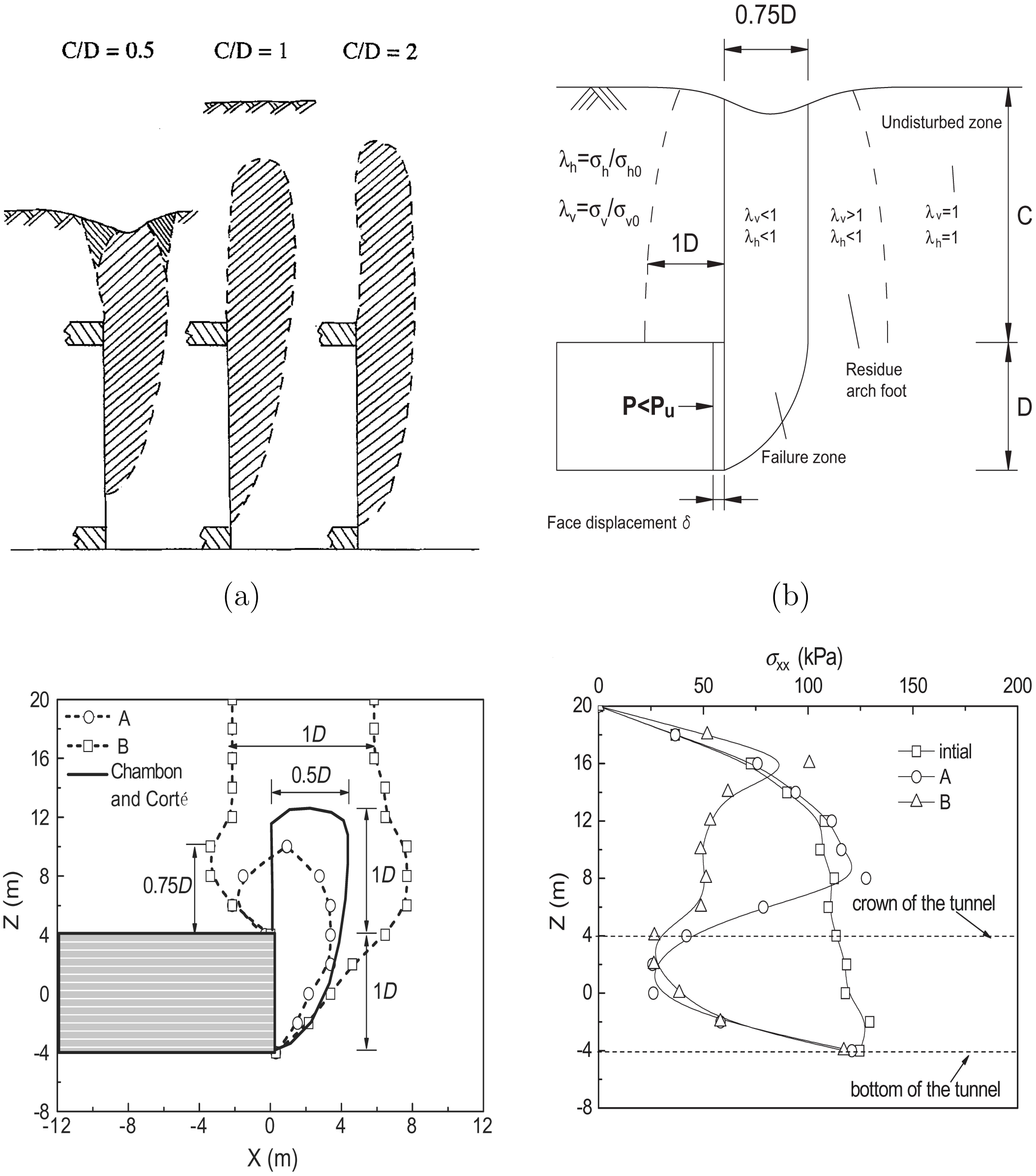

(a) (b)

(c) (d)

Figure 4.8: Shape of the failure mechanism observed in physical model tests and numerical simulations: (a) observed failure mechanism for different C/D ratios, Chambon & Corte (1994); (b) distribution of stress concentration, Chen et al. (2013); (c) failure zone from DEM simulations, Chen et al. (2011) (A: limited displacement of tunnel face displacement/diameter = 0.043, B: elevated displacement of tunnel face displacement/diameter = 0.269); (d) variation of horizontal stress, Chen et al. (2011) (A: limited displacement of tunnel face displacement/diameter = 0.043, B: elevated displacement of tunnel face displacement/diameter = 0.269)

From the previous discussion two assumptions can be made to solve the problem of indeterminacy as follows:

1. It is assumed that 3D active earth pressure acts on the outer contact surface F_6 (P1, P2, P6, P7) (see Fig. 4.1) of the silo which is located above the tunnel face. Since only half of the KEM model (M) is used in calculating the support force, only half of 3D active earth pressure is assumed to act on the half of outer contact surface F_6 (P1, P7, P8, P9) (see Figs. 4.3 and 4.9).
2. The pre-given normal virtual displacement differs from zero for the 3D KEM model active earth pressure. However, the displacements of the outer sides of the silo are assumed zero when coupling the 3D KEM model for active earth pressure (half of the model) with the half of the outer contact surface F_6 (P1, P7, P8, P9) in KEM model (M).

The influence of two previous assumptions for the forces acting on the two other outer contact surfaces F_5 (P1, P4, P5, P7) and F_7 (P2, P4, P5, P6) will be discussed later.

Since the process of finding a minimum support pressure (maximum force) at the tunnel face is linked to a technique for finding the minimum factor of safety, it could consider the process as an optimization problem.

4.3 3D lateral earth pressure coefficient

Within this section, the procedure for calculating the 3D lateral earth pressure coefficient (K_{3D}) using KEM is described and validated. In the following part, the results of the KEM model (Fig. 4.10) for 3D active earth pressure are presented and discussed.

The horizontal normal force of the 3D KEM model for the active earth pressure problem is defined by:

$$N_6 = 0.5 \cdot K_{3D} \cdot \gamma \cdot C^2 \cdot B \tag{4.6}$$

Therefore, the calculated 3D active earth pressure coefficient (K_{3D}) is

$$K_{3D} = \frac{N_6}{0.5 \cdot \gamma \cdot C^2 \cdot B} \tag{4.7}$$

Fig. 4.11 shows the comparison of the present solution with the methods of Huder (1972) derived from the silo theory, Walz & Prager (1978) based on the theory of element slices

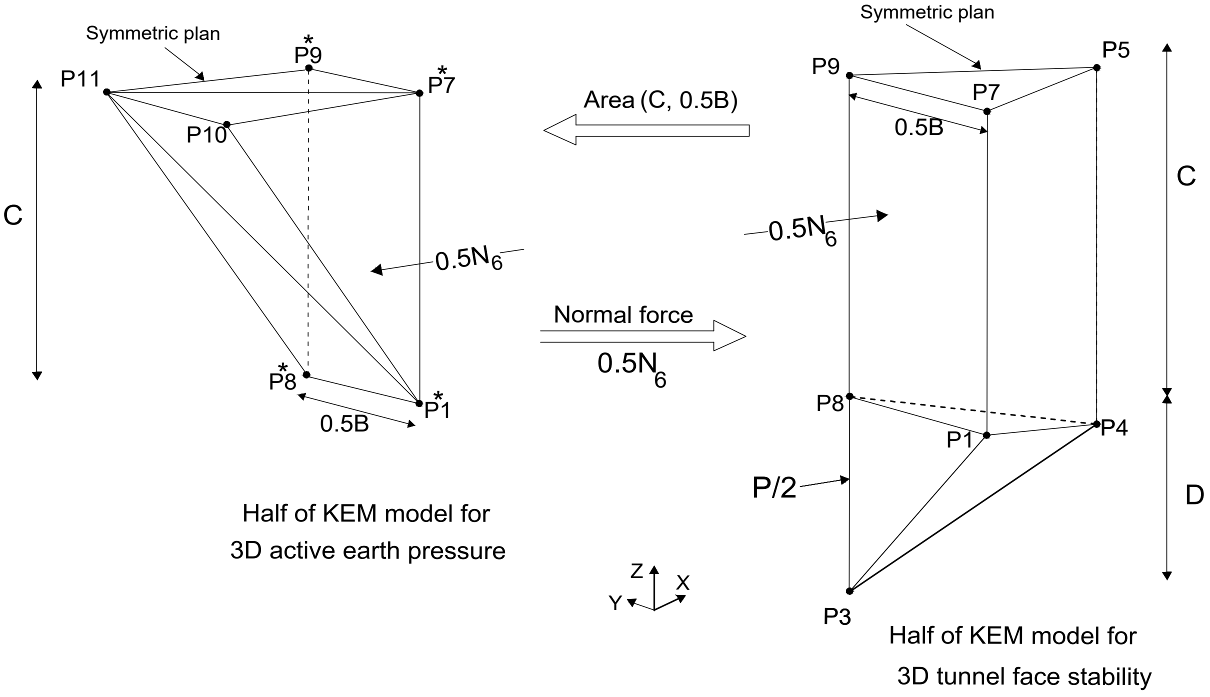
Symmetric plan
P11
P9*
P7*
P10
C
0.5N6
P8*
P1*
0.5B
Half of KEM model for
3D active earth pressure
Area (C, 0.5B)
Normal force
0.5N6
Z
X
Y
Symmetric plan
P9
P5
P7
0.5B
C
0.5N6
P8
P1
P4
P/2
D
P3
Half of KEM model for
3D tunnel face stability

Figure 4.9: Forces transferred from 3D active earth pressure model to tunnel face stability model

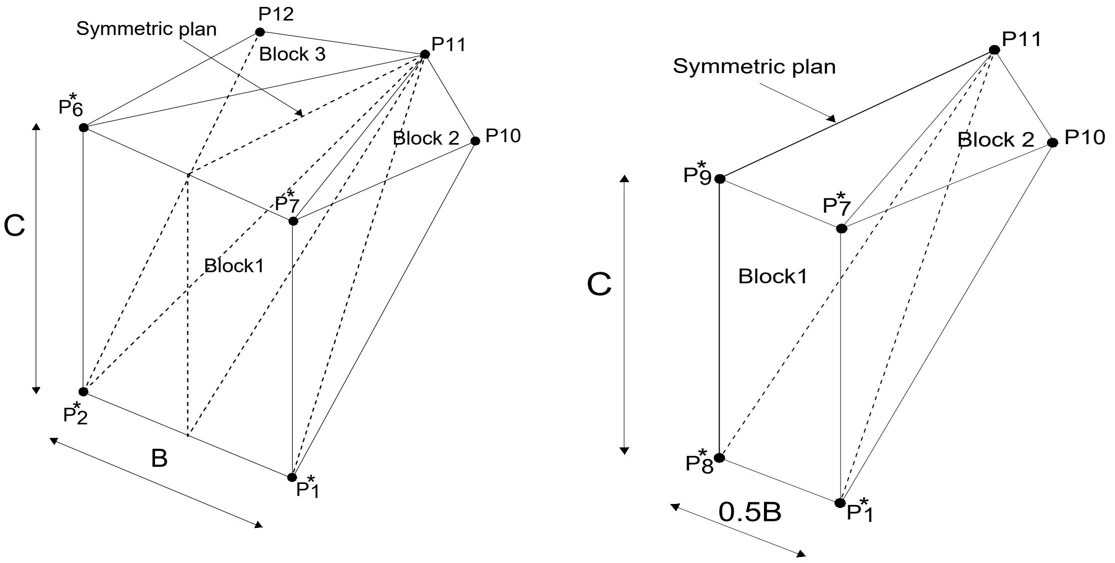
Symmetric plan
P12
Block 3
P11
P6*
Block 2
P10
C
P7*
Block1
P2*
B
P1*
P11
Symmetric plan
Block 2
P10
P9*
P7*
C
Block1
P8*
0.5B
P1*

(a) (b)

Figure 4.10: KEM model for 3D active earth pressure problem: (a) geometry of the failure mechanism; (b) half of KEM model

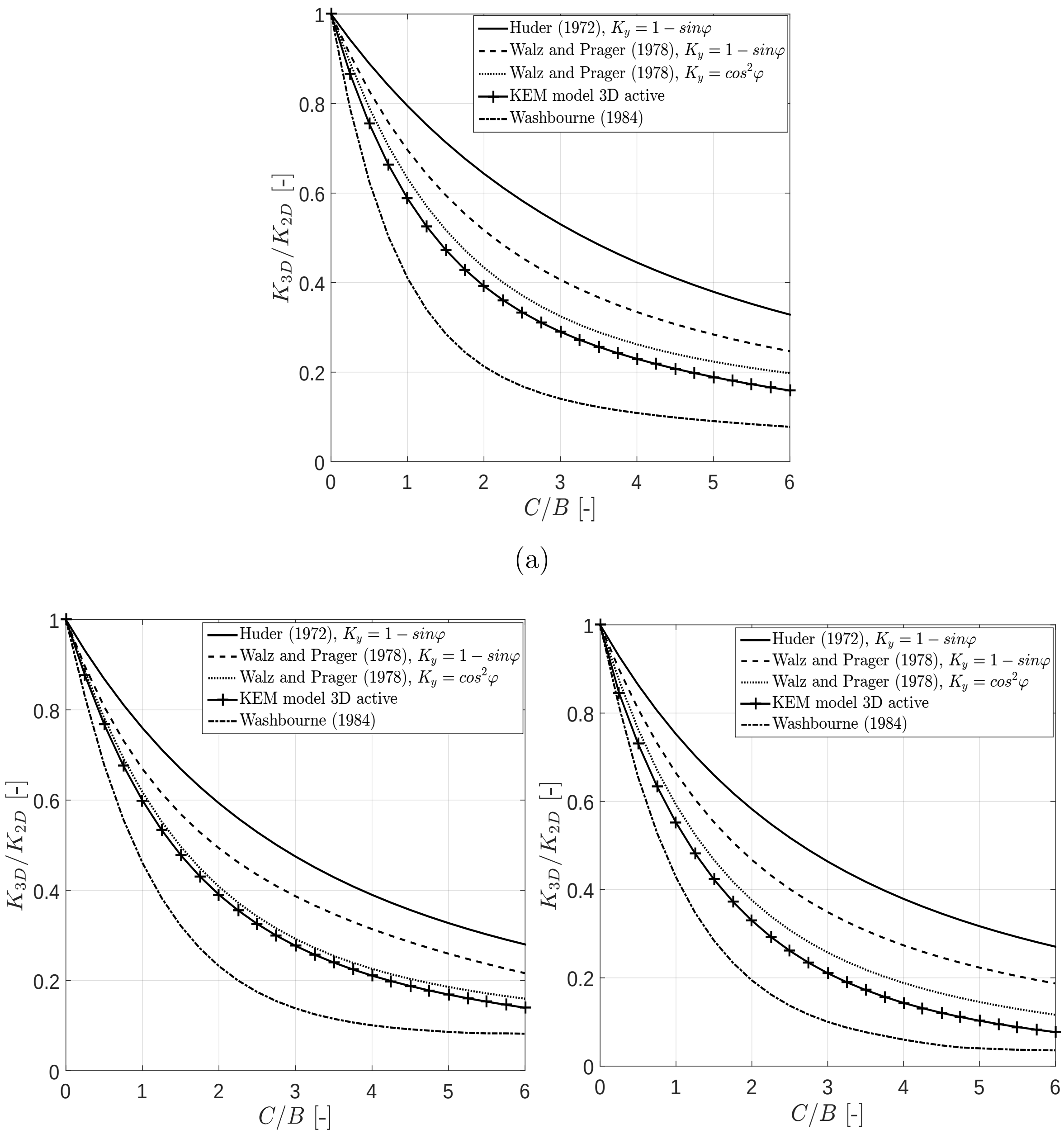

(a)

(b)

(c)

Figure 4.11: Comparison of K_{3D} value obtained from different methods with results from KEM model for 3D active earth pressure problem; (a) $\varphi = 20^o, \delta = 0^o$; (b) $\varphi = 30^o, \delta = 0^o$; (c) $\varphi = 40^o, \delta = 0^o$

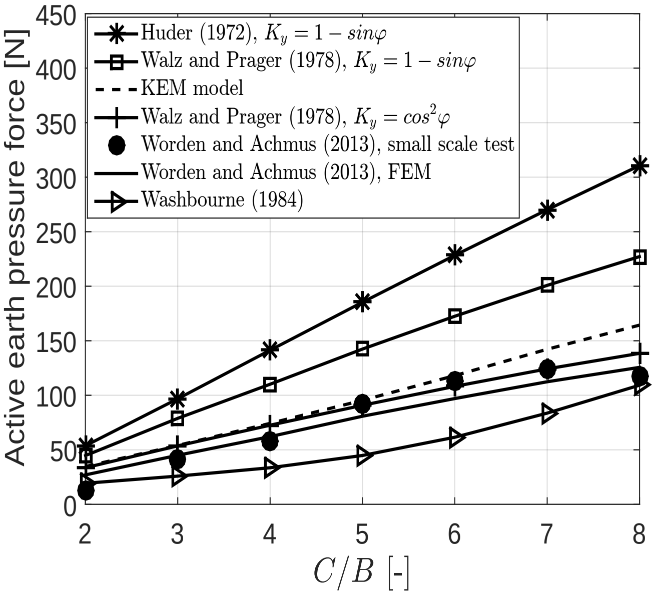

Figure 4.12: Comparison of experimental and numerical results with results from KEM model (M), $\varphi = 31.7^o$

and Washbourne (1984), who modified the shape of the sliding wedge, assuming the wedge as triangular prism sliced by plane. Walz & Prager (1978) suggested the value of earth pressure coefficient (K_y) to lie within the range $K_c \leq K_y \leq K_o$, where $K_0 = 1 - \sin\varphi$ and $K_c = \cos^2\varphi$. Fig. 4.11 represents the value of the K_{3D}/K_{2D} ratio as a function of C/B ratio (see Fig. 4.10). Where the 2D active earth pressure coefficient (K_{2D}) is calculated as follows:

$$K_{2D} = \frac{1 - \sin\varphi}{1 + \sin\varphi} \tag{4.8}$$

The results indicate that the K_{3D}/K_{2D} ratio decreases with increasing C/B ratio. It can also be observed that the K_{3D}/K_{2D} ratio for a specific C/B ratio decreases with increasing friction angle of the soil. Furthermore, the KEM model (3D active) gives almost identical or slightly smaller K_{3D}/K_{2D} values than the theory of Walz & Prager (1978) ($K_y = \cos^2\varphi$), which again are lie below the values obtained by Huder (1972) and Walz & Prager (1978) with $K_y = 1 - \sin\varphi$. The K_{3D}/K_{2D} values of Washbourne (1984) are significantly lower than those of all other approaches.

In Fig. 4.12, the small scale test results and the numerical results given by tom Wörden & Achmus (2013) are used for the validation of KEM (3D active) model. The best agreement with the numerical and experimental results of tom Wörden & Achmus (2013) is obtained with KEM model (3D active earth pressure) and the approach of Walz & Prager (1978) using $K_y = \cos^2\varphi$.

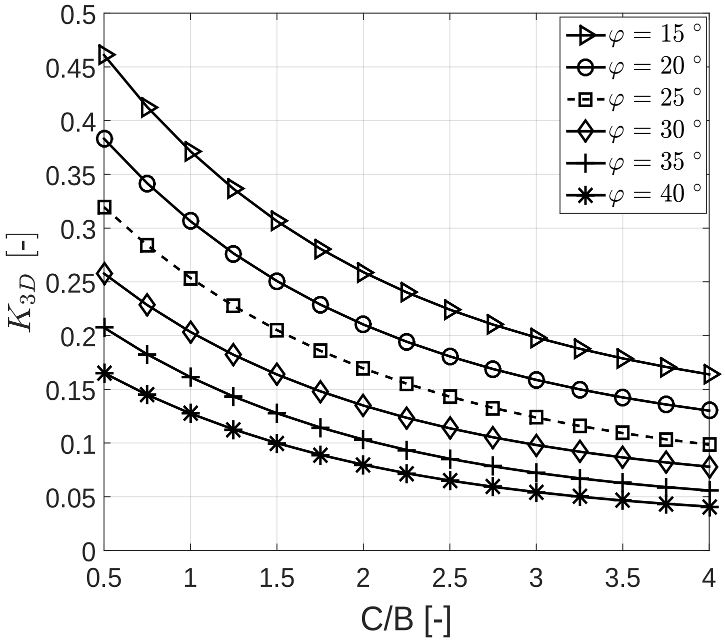

Figure 4.13: 3D lateral earth pressure coefficient K_{3D} for different friction angles (φ) obtained from KEM model

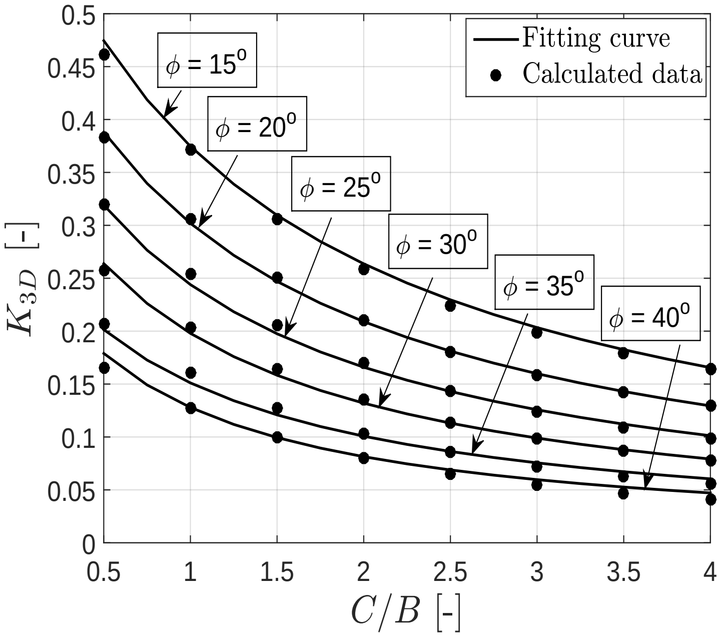

Figure 4.14: 3D lateral earth pressure coefficient K_{3D} obtained from KEM model and its approximation by Eq. (4.9)

The values of the 3D lateral earth pressure coefficient K_{3D} obtained from the KEM model are given as a function of C/B ratio for different values of the friction angles are presented in Fig. 4.13. An equation for calculating K_{3D} as a function of C/B ratio and φ has been developed as follows:

$$K_{3D} = \frac{2 \cdot e^{-0.054 \cdot \varphi}}{1.75 + C/B - (0.025 \cdot \varphi)} \tag{4.9}$$

The 3D lateral earth pressure coefficients obtained from the KEM model or from Eq. (4.9), respectively, are presented in Fig. 4.14.

4.4 Optimization procedure

Searching for critical failure mechanism is a problem of maximization. Fig. 4.15 presents the flow chart for optimization algorithm of calculating minimum support pressure. The iterative optimization algorithm is started by specifying input data for the soil parameters (φ, γ and c), the diameter of the tunnel (D), the cover depth (C) and also by defining the surcharge load acting on the ground surface (Q), see Figs 4.1 and 4.7.

After setting up initial input data, the cover depth (C) and the half length between nodes (P1, P2) (0.5B) are switched from the subroutine "tunnel face stability" to the subroutine "3D active earth pressure", as shown in Fig. 4.9. Thereafter, randomly selected values for the x-coordinate of the nodes P10 and P11 as well as for y-coordinate of node P10 are initiated. An iterative procedure using PSO is implemented to the subroutine "3D active earth pressure" to find the maximum normal force ($0.5N_6$) for 3D active earth pressure failure.

The value of maximum normal force ($0.5N_6$) is transferred to the subroutine "tunnel face stability". This force acts at the slip surface between the nodes (P1, P7, P8, P9). Subsequently, in the subroutine "tunnel face stability", the value of the shear force at the slip surface between the nodes (P1, P7, P8, P9) is computed as $0.5N_6 \cdot tan\varphi$. Then, from the static equilibrium equations, the support pressure is calculated using Eq. (4.5). To continue searching for the maximum support force in the subroutine "tunnel face stability", new coordinates for free nodes (P4, P5) are chosen based on their current position finding the most adequate failure mechanism described by the x-coordinate of the nodes P4 and P5 and by the z-coordinate of the node P4. The optimization procedure is terminated, when PSO in the subroutine "tunnel face stability" reaches a termination criteria, that can be either when a predefined maximum number of iterations is reached

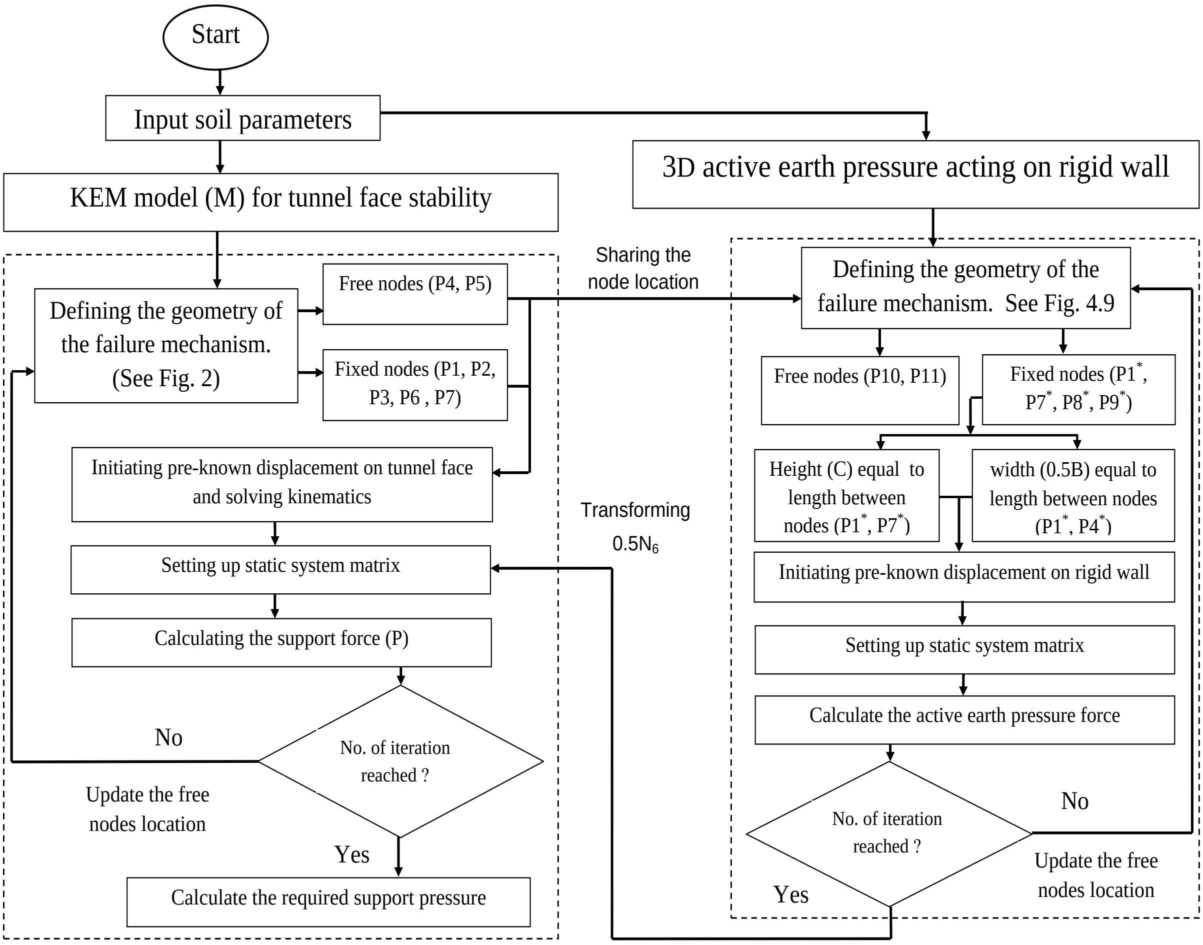
Start
Input soil parameters
KEM model (M) for tunnel face stability
3D active earth pressure acting on rigid wall
Defining the geometry of the failure mechanism. (See Fig. 2)
Free nodes (P4, P5)
Fixed nodes (P1, P2, P3, P6 , P7)
Sharing the node location
Initiating pre-known displacement on tunnel face and solving kinematics
Setting up static system matrix
Calculating the support force (P)
No
No. of iteration reached ?
Update the free nodes location
Yes
Calculate the required support pressure
Transforming 0.5N6
Defining the geometry of the failure mechanism. See Fig. 4.9
Free nodes (P10, P11)
Fixed nodes (P1*, P7*, P8*, P9*)
Height (C) equal to length between nodes (P1*, P7*)
width (0.5B) equal to length between nodes (P1*, P4*)
Initiating pre-known displacement on rigid wall
Setting up static system matrix
Calculate the active earth pressure force
No. of iteration reached ?
No
Update the free nodes location
Yes

Figure 4.15: Flow chart for the procedure of calculating the support pressure in KEM model (M)

Table 4.1: Selected physical model tests for verification of KEM model (M)

Author	Model	Tested material	φ [^{o}]	c [kPa]	C/D [$-$]
Chen et al.(2013)	1g test	Yangtze River sand	37	0.5	0.5, 1, 2
Chambon and Corte (1994)	ng test	Fontainebleau sand	$38 - 42$	$0 - 5$	0.5, 1, 2, 4
Kirsch (2009)	1g test	Ottendorf-Okrilla sand	32.5	0	0.5, 0.75, 1, 1.5, 2

or when a constant value of support pressure for a certain number of iterations. Finally, minimum support pressure is calculated based on the support force.

4.5 Development of failure mechanism by optimization process

The development of the geometry of the failure mechanism, the minimum support pressure, and the lateral earth pressure coefficient at surface F_5 (P1, P4, P5, P7) during the iterations of the optimization process is shown in Fig. 4.16. In this, the final value of the inclination of the bottom surface (β) of the wedge is about $\beta = 55^o$, which is close to the slip surface angle for the 2D active state ($\theta_a = 45^o + \varphi/2$) Rankine's theory (Rankine, 1857). The final value of the lateral earth pressure coefficient acting on the surface F_5 (P1, P4, P5, P7) of the silo part is about 0.39, which is close to the 3D active earth pressure value calculated by KEM model (3D active) for the surface F_6 (P1, P2, P6, P7) which is 0.37. For all geometrical parameters as well as for the support pressure the final values have been reached after about 50 iterations, starting from specific initial geometries. Of course the shape of the curves and the number of iterations to reach final values depends on the initial geometry.

4.6 Verification by physical model tests

Three series of physical model tests from literature have been chosen to verify the accuracy of KEM model (M) for predicting the minimum support pressure. The specifications of the physical model tests are summarized in Table 4.1.

Fig. 4.17 presents the comparison of normalized support pressure ($p_u/(\gamma D)$) calculated by the KEM model (M) with the results from Chambon & Corte (1994), Kirsch (2009) and Chen et al. (2013).

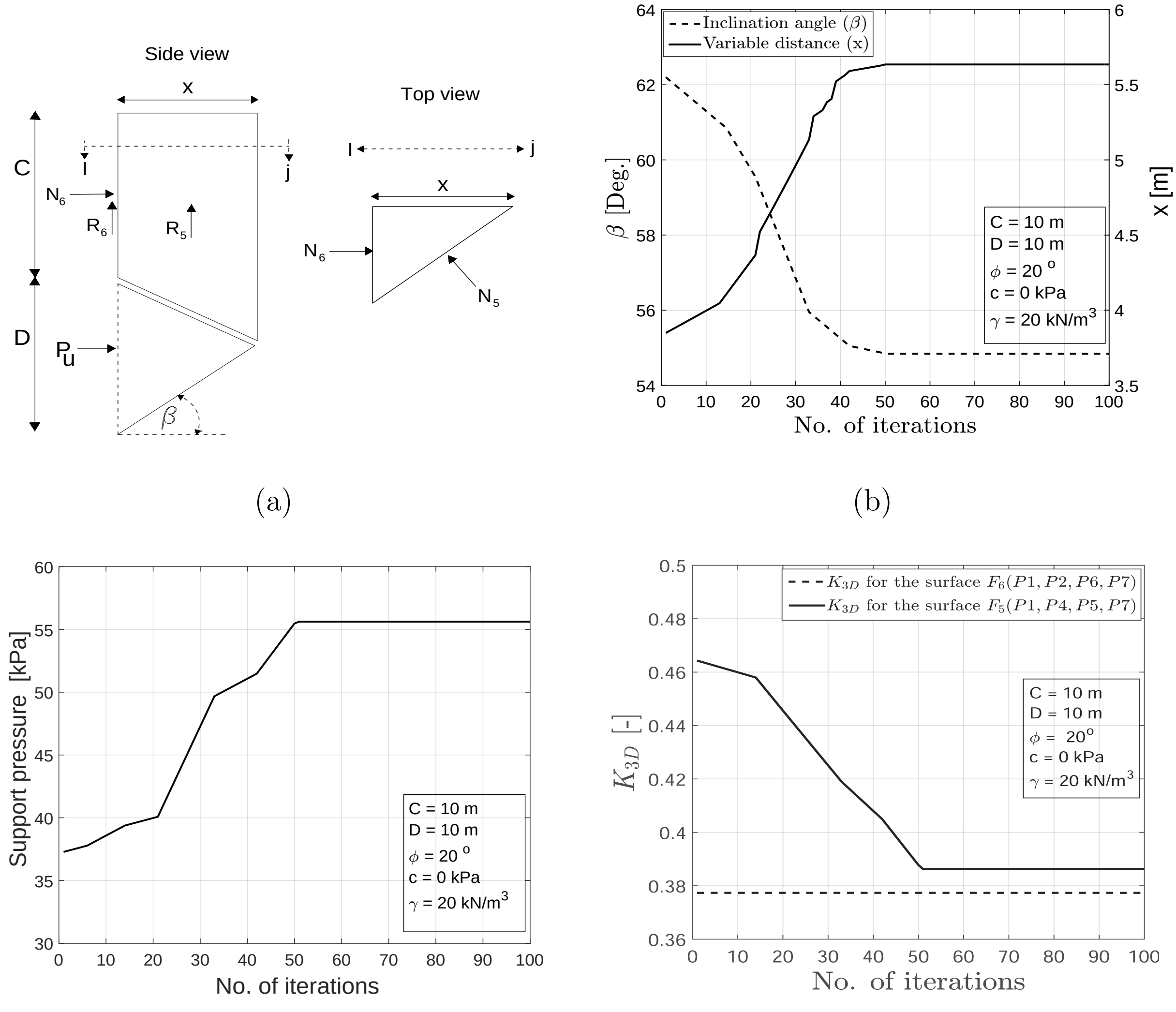

(a) (b)

(c) (d)

Figure 4.16: Iteration steps in the optimization process: (a) the failure mechanism; (b) development of the failure mechanism; (c) minimum support pressure; (d) 3D active earth pressure coefficient

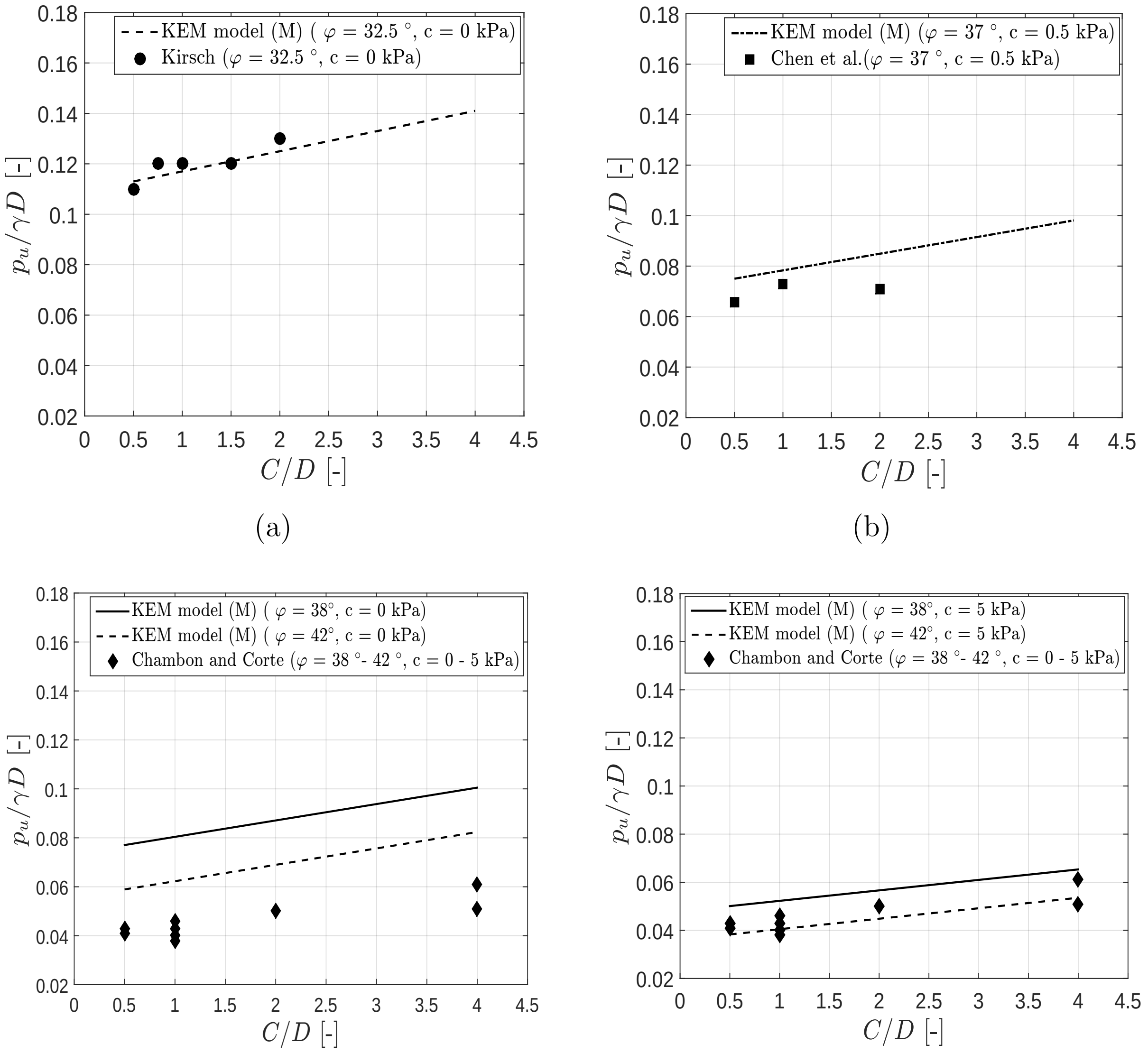

(a) (b)

(c) (d)

Figure 4.17: Comparison of $p_u/(\gamma D)$ value obtained from the KEM model (M) with physical model tests: (a) $p_u/(\gamma D)$ obtained from KEM model (M) compared to ng tests of Kirsch (2009); (b) $p_u/(\gamma D)$ obtained from KEM model (M) compared to ng tests of Chen et al. (2013); (c) $p_u/(\gamma D)$ obtained from KEM model (M) (c = 0 kPa) compared to ng tests of Chambon & Corte (1994); (d) $p_u/(\gamma D)$ obtained from KEM model (M) ($c = 5$ kPa) compared to ng tests of Chambon & Corte (1994)

From Fig. 4.17, it can be seen that the normalized minimum support pressure obtained from the ng tests of Chambon & Corte (1994), Chen et al. (2013) and the 1g tests of Kirsch (2009) increases slightly with the increase in the C/D ratio. This tendency is reproduced by KEM model (M). This dependency of the minimum support pressure on the C/D ratio was also detected by Anagnostou & Kovari (1994), Anagnostou1994 and Chen et al. (2011).

The values of normalized support pressure calculated by KEM model (M) show a good agreement with the results obtained by Kirsch (2009). Furthermore, when the results of KEM model (M) are compared with normalized support pressures obtained from Chen et al. (2013), the difference between the $p_u/(\gamma D)$ values vary between 6.5 % and 16.4 % only.

The soil used in the ng tests of Chambon & Corte (1994) is reported to have a little cohesion, which is given as the range $c = 0$ - 5 kPa. The values of $p_u/(\gamma D)$ obtained from the ng tests of Chambon & Corte (1994) are less than those predicted by KEM model (M) if a cohesionless soil ($c = 0$ kPa) is assumed. However, if a cohesion $c = 5$ kPa is considered, the KEM model (M) predicts a minimum support pressure much closer to the ng test results.

As a conclusion, it can be inferred that the minimum support pressure calculated by KEM model (M) approximates the physical model test results very well.

4.7 Comparison of the KEM model (M) results with other approaches

Analogous to the method proposed by Terzaghi (1943) for bearing capacity analysis, the minimum support pressure (p_u) is often represented by the following form in the literature (Vermeer et al., 2002; Mollon et al., 2010; Anagnostou, 2012):

$$p_u = \gamma \cdot D \cdot N_\gamma - c \cdot N_c + q \cdot N_q \tag{4.10}$$

where the contribution of different loads and soil parameters including self-weight (γ), cohesion (c) and surface surcharge (q) are expressed by sum of three terms incorporating the the non-dimensional bearing capacity coefficients N_γ, N_c and N_q which are functions of the internal friction angle φ of the soil. Due to the active conditions around the tunnel face the cohesion is reducing the necessary support pressure.

Within this section, Eq. (4.10) is adopted to express the minimum support pressure. In KEM calculations with $c = 0$ kPa and $q = 0$ kPa, the soil unit weight coefficient (N_γ) is obtained. Furthermore, setting $\gamma = 0$ kN/m^3 and $q = 0$ kPa, the cohesion coefficient N_c is calculated. In addition, with $\gamma = 0$ kN/m^3 and $c = 0$ kPa, the surcharge load coefficient N_q can also be obtained.

The minimum support pressure computed from Terzaghi's bearing capacity formula (Eq. 4.10), which is based on the superposition principle is not a rigorous solution. It delivers an approximate solution of the minimum support pressure and it includes an error due to the superposition effect. However, Mollon et al. (2010) reported that this error is quite small and can be neglected.

To validate the results of the KEM model (M), the non-dimensional coefficients N_γ and N_c were examined individually in simulations with KEM model (M) and compared with the results of other available approaches in literature. Also, an additional check is made by comparing the KEM model (M) results with finite element limit analysis (upper and lower bound solutions) results.

4.7.1 Comparison of the KEM model (M) results with the existing approaches

Fig. 4.18 compares the value of the non-dimensional coefficient N_γ calculated by the KEM model (M) with those given by the approaches of other researchers as a function of friction angle, for a C/D ratio equal to 1.

It can be seen from Fig. 4.18 that the results of Vermeer et al. (2002) obtained by FEM calculations and Anagnostou (2012) derived from a modified wedge model based on the infinitesimally thin slices method and Mollon et al. (2010) using the upper bound method give N_γ values lying close to the results of KEM model (M), while the differences are larger for the other models. The method of Anagnostou (2012) and the KEM model (M) are taking into account the contribution of horizontal arching action over the tunnel face, which leads to similar results calculated by both methods.

The results given by Krause (1987) lie above those of KEM model (M). In that model the soil conditions above the tunnel face are not taken into account in calculating the support pressure. The solution of Anagnostou & Kovari (1994) using limit equilibrium method significantly overestimates the value of N_γ compared to the other solutions. This is due to the simplified way of considering the vertical stress distribution (linear distribution)

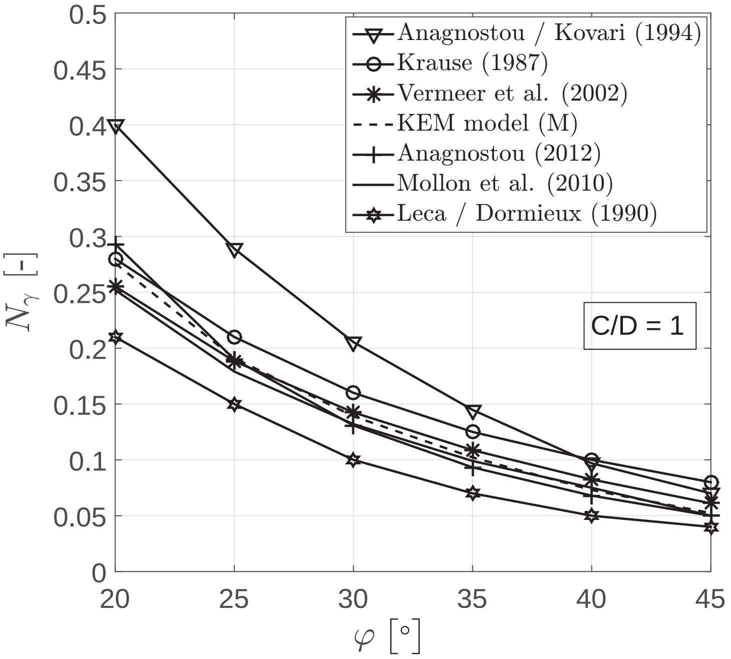

Figure 4.18: Comparison of N_γ values obtained from different approaches in the literature for different friction angles with the results of KEM model (M)

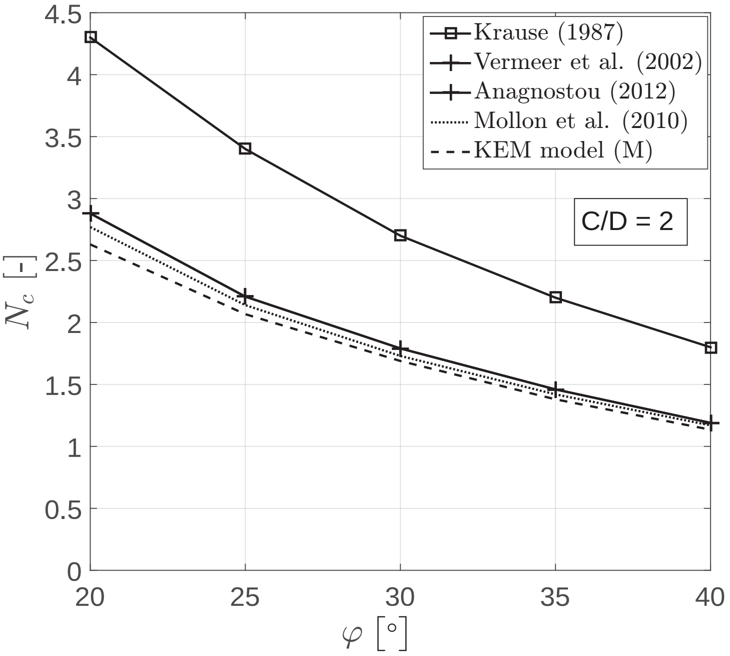

Figure 4.19: Comparison of N_c value obtained from the theoretical methods using different friction angles with KEM model (M)

which disregards the arching effect in the calculation of the horizontal stress at the sides of the wedge.

The non-dimensional coefficients N_γ obtained from Leca & Dormieux (1990) using the upper bound method are clearly lower than the results given by the others approaches. This is due to that the shape of the tunnel face is considered as an elliptic cross section inscribed to the circular face (the elliptic cross section and the circular tunnel face do not have the same area). Furthermore, the two-blocks mechanism given by Leca & Dormieux (1990) is constrained by the normality condition, required by plasticity theory. The velocity vector must enclose an angle φ with the discontinuity surfaces along the sliding surfaces. However, this condition restricts the development of the three-dimensional slip surfaces.

As can be seen in Fig. 4.19, where C/D ratio is 2, the results of Vermeer et al. (2002) and Anagnostou (2012) for N_c are the same. The non-dimensional coefficients N_c obtained by KEM model (M) are slightly lower than those of Vermeer et al. (2002), Anagnostou (2012) and Mollon et al. (2010). However, Krause's results for N_c are extremely conservative.

As shown in Figs. 4.18 and 4.19, the minimum support pressure predicted by KEM model (M), replacing the circular shape of the tunnel face by a isosceles triangle of equivalent area, is very close to the minimum support pressure given by Anagnostou (2012), who substituted the circular shape of the tunnel face with a square area. Also the solution of Vermeer et al. (2002) and Mollon et al. (2010), who used a circular shape of the equivalent area, are very close to the KEM results. Therefore, it can be concluded that the shape of the equivalent area of the tunnel face has little influence on the calculated minimum support pressure. In addition, the data in Figs. 4.18 and 4.19 reveal that, the values of N_γ and N_c obtained from KEM model (M) as well as all other approaches from the literature increase strongly with a decrease in friction angle.

4.7.2 Comparison of KEM model (M) with Finite Element Limit Analysis (FELA) results

4.7.2.1 Modeling of tunnel face stability in OptumG3

In this section, Finite Element Limit analysis (FELA) using the commercial software (Krabbenhoft et al., 2015) OptumG3 ware employed to investigate the stability of the tunnel face. Due to the symmetry of the problem, the numerical model encompasses only half of the domain as shown in Fig. 4.20. A circular tunnel with diameter (D) was

Table 4.2: Soil parameters and tunnel geometry

Parameter	Value	Unit
Tunnel diameter (D)	10	[m]
Cover depth (C)	5-20	[m]
Friction angle (φ)	$15-45$	[^{o}]
Dry unit weight(γ)	18	[kN/m^3]
Cohesion (c)	0	[kPa]
Surcharge (q)	0	[kPa]

modeled by a half cylinder. Any effect of the tunneling process was neglected. The tunnel has a cover depth (C) measured from the ground surface. In order to investigate the stability of the tunnel face in frictional-cohesive soil, the stress-strain behavior of the soil was modeled as perfectly plastic Mohr-Coulomb material with associated flow rule and a dilatancy angle (ψ) equal to the friction angle (φ) of the soil.

The boundary conditions of the symmetric plane were defined such that the normal displacements at the plane were zero, while the displacements in the other remaining directions were free allowed. The nodes of the bottom plane were fixed in all directions, while displacement conditions at the vertical boundary planes were the same as those of the symmetric plane. The soil was assumed to be homogeneous in dry condition. The geometry of the tunnel and the soil strength parameters are summarized in Table 4.2. The size of the model was chosen so that these restraints had very little effect on the results.

4.7.2.2 Results and discussion

Five adaptive steps were selected to obtain an accurate solution, where an initial mesh with 2000 elements was automatically adapted to a final mesh with about 20000 elements. It can be seen from Fig. 4.21 that little mesh refinement occurs in the vicinity of the model boundaries, meaning that the boundaries have no noticeable impact on the results. The shear strains for the collapse failure mechanism obtained with OptumG3 are shown in Fig. 4.22.

The results obtained using the OptumG3 are rigorous upper and lower bounds solutions. An approximate estimation of the collapse load can be simply calculated as the mean value (p_m) of the upper and lower bound solutions as follows:

$$p_m = \frac{p_{up} + p_{lw}}{2} \tag{4.11}$$

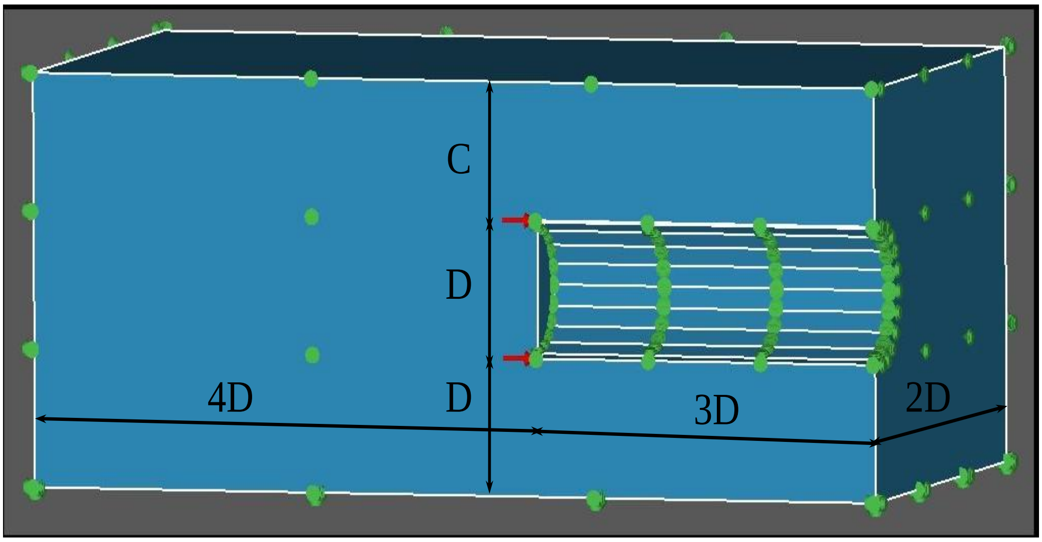

Figure 4.20: Geometry the boundary conditions of tunnel for the 3D model

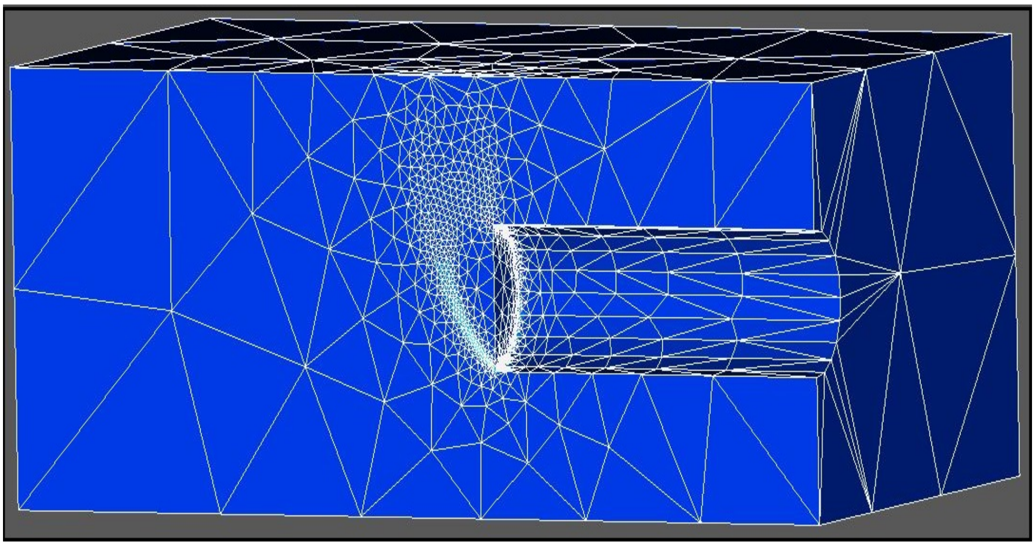

Figure 4.21: Finite element mesh with mesh adaptivity

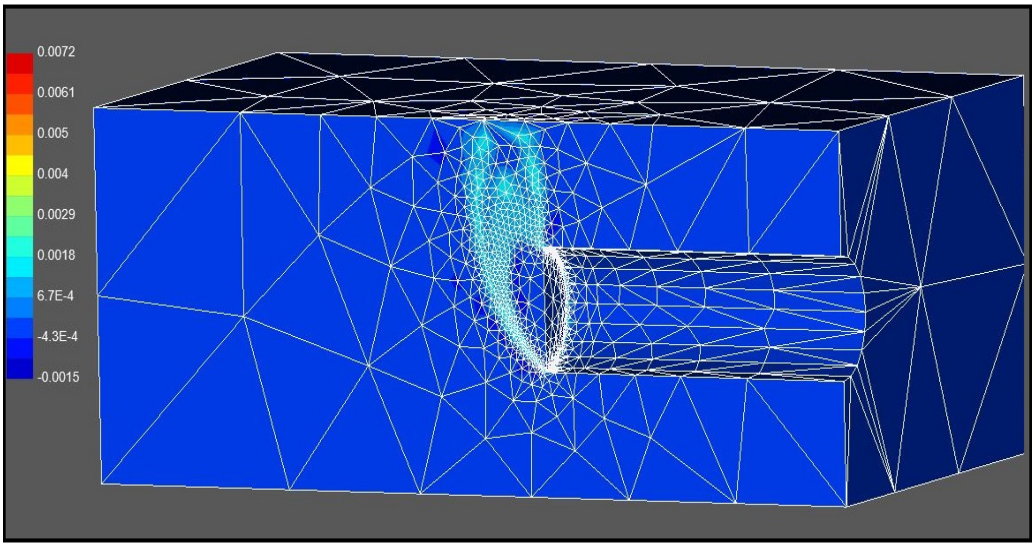
0.0072
0.0061
0.005
0.004
0.0029
0.0018
6.7E-4
-4.3E-4
-0.0015

Figure 4.22: Upper bound results of 3D FELA model showing shear strain

Table 4.3: Comparison of the minimum support pressures obtained from KEM model (M) and FELA for $C/D = 1$

φ	FELA (LB)	FELA (UB)	FELA (Mean value)	KEM model (M)
15^o	76.07	74.03	75.05	74.52
20^o	51.10	49.51	50.30	49.68
25^o	36.19	34.81	35.50	34.38
30^o	26.57	25.45	26.01	25.02
35^o	19.89	18.99	19.44	18.36
40^o	14.98	14.12	14.55	13.14
45^o	10.50	10.27	10.38	9.36

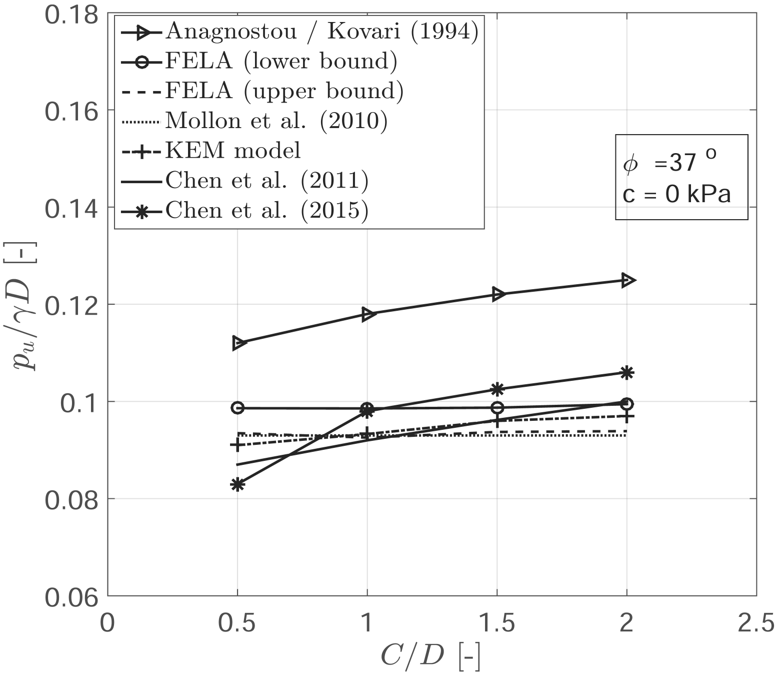

Figure 4.23: Comparison of normalized support pressure as a function of C/D ratio obtained from KEM model (M), FELA (lower and upper bound solutions) and different approaches from the literature

where p_{up} is the upper bound solution of the collapse support pressure, while p_{lw} is its lower bound solution. Table 4.3 shows a comparison between the results of KEM model (M) and those of FELA for $C/D = 1$ and various values of friction angles. The results of FELA were obtained with the final adaptive meshes. The comparison indicates a good agreement of the KEM results with the mean values of the upper and lower bounds solutions.

From Fig. 4.23, it can be seen that the KEM model (M) results show a slight increase of $p_u/(\gamma D)$ with an increase of C/D. Similar trends are observed in different types of wedge-silo models (Anagnostou & Kovari, 1994; Chen et al., 2015) and DEM simulations (Chen et al., 2011). Meanwhile, the results of the FELA simulations and the upper bound solution Mollon et al. (2010) show that C/D has almost no effect on $p_u/(\gamma D)$.

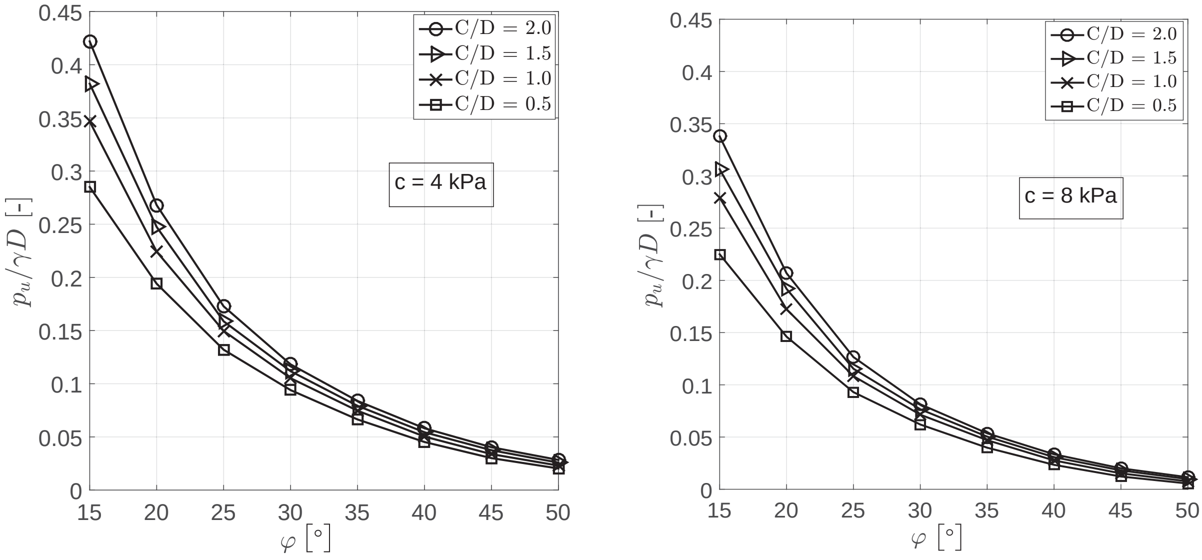

(a) (b)

Figure 4.24: Influence of friction angle on normalized support pressure for two different values of cohesion and different values of C/D ratio; results obtained with KEM model (M): (a) $c = 4$ kPa; (b) $c = 8$ kPa

4.8 Parametric studies with the KEM model (M)

4.8.1 Influence of friction angle

For two different values of cohesion ($c = 4$ and 8 kPa), the influence of friction angle (φ) on normalized support pressure ($p_u/(\gamma D)$) for different C/D ratios is shown in Fig. 4.24. It is obvious that the normalized support pressure for the same C/D ratio is decreasing non-linearly with the increase of the friction angle approaching to 0 (no support pressure is needed) for higher friction angles $\varphi \geq 50^o$. It is interesting to note that the effect of C/D ratio on normalized support pressure is more pronounced at lower friction angles $\varphi \leq 35^o$.

4.8.2 Influence of the cohesion

The influence of cohesion on normalized support pressure is further studied based on the simulation results presented in Fig. 4.25. C/D ratio was assumed to be either 1 or 2. The friction angle was set to $\varphi = 20^o$, 25^o, 30^o, 35^o and 40^o, while the cohesion was varied from 0 kPa to 10 kPa. Examining the trend of the curves in Fig. 4.25, it appears

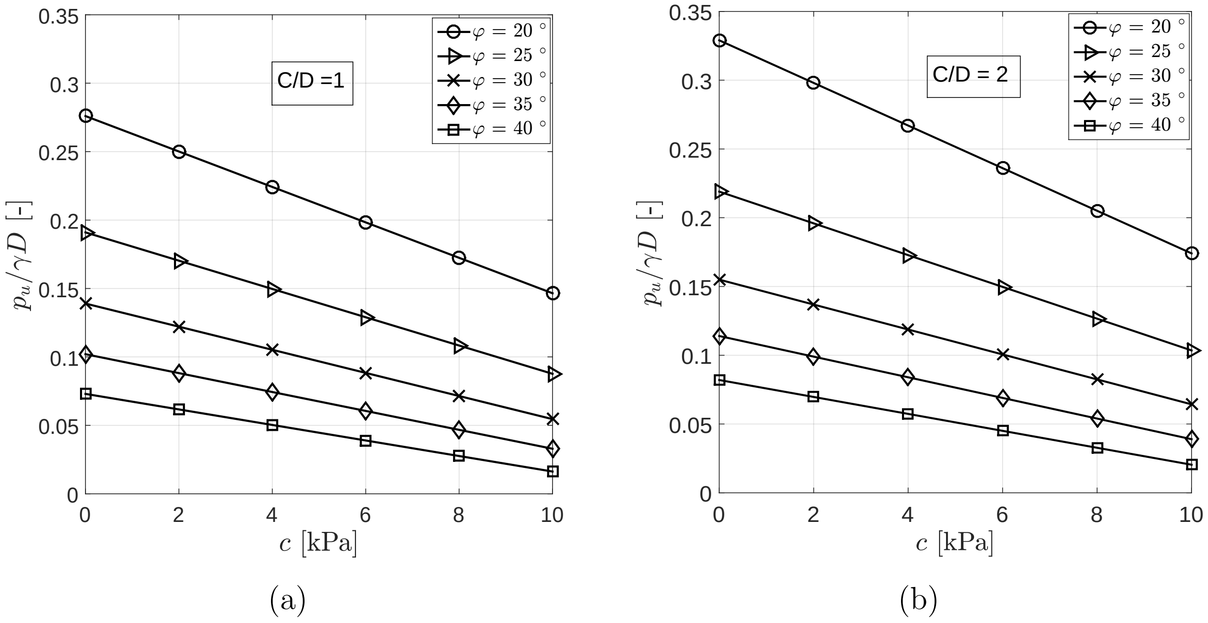

Figure 4.25: Influence of cohesion on normalized support pressure for two different values of cohesion and different values of C/D ratio; results obtained with KEM model (M): (a) $C/D = 1$; (b) $C/D = 2$

that the normalized support pressure is decreasing linearly with increasing cohesion. The smaller φ, large is the rate of support pressure decrease. Thus, it can be concluded that the cohesion affects the normalized support pressure more significantly for lower friction angles. This applies to both studied with different C/D ratios.

4.8.3 Influence of cover depth to diameter ratio (C/D)

The analysis of influence of the C/D ratio on the normalized support pressure is conducted for cohesion ($c = 4$ kPa and $c = 8$ kPa) within a common range of C/D ratios (0.5 - 2.5). The results in Fig. 4.26 illustrate that for the friction angles $\varphi = 20^o$ and $\varphi = 25^o$, the normalized support pressure is significantly influenced by the C/D ratio and grows non-linearly with increasing the C/D. For higher friction angle $\varphi = 30^o$, the normalized support pressure increases almost linearly with increasing C/D ratio. It is evident in Fig. 4.26 that the influence of C/D becomes less pronounced with increasing friction angle.

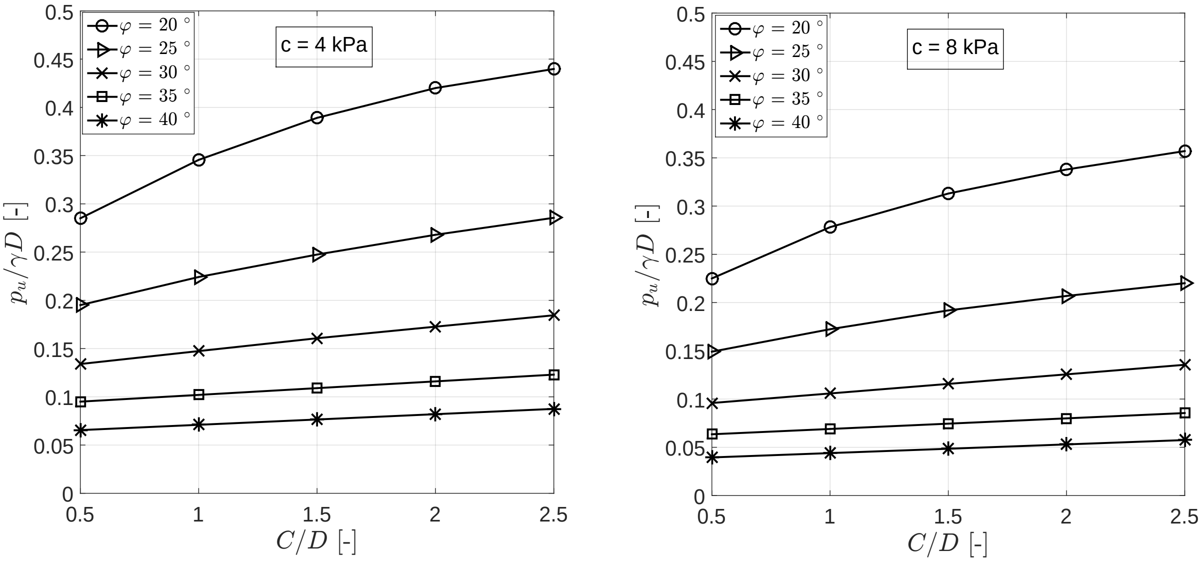

(a) (b)

Figure 4.26: Influence of cover to diameter ratio C/D on normalized support pressure for two different values of cohesion and different friction angles for the results obtained with KEM model (M): (a) $c = 4$ kPa; (b) $c = 8$ kPa

4.9 Development of design equations

Figs. 4.27 and 4.28 show the non-dimensional coefficients N_γ and N_c obtained with the KEM model as functions of friction angles and C/D ratios. As the friction angle decreases, the effect of C/D ratio becomes more prominent and the inclination of the N_γ-φ and N_c-φ curves higher.

The N_q - φ curves in Fig. 4.29 and the values in Table 4.4 demonstrate that N_q becomes zero for C/D ratios greater than or equal to 1.5 for $\varphi \geq 15^o$. The same applies to friction angles $\varphi = 40^o$ at $C/D = 0.5$ as well as for $\varphi = 30^o$ at $C/D = 1$.

Based on a fitting of the results of Figs. 4.27, 4.28 and 4.29 the following equations approximating the N_γ, N_c and N_q values have been developed for $\varphi \geq 15°$:

$$N_\gamma \approx a_1 \cdot (\tan\varphi)^{-b_1} \tag{4.12}$$

$$a_1 = 0.055 + 0.007 \cdot C/D \tag{4.13}$$

$$b_1 = 1.50 \cdot (C/D - 0.37)^{0.044} \tag{4.14}$$

$$N_c \approx (\tan\varphi)^{-b_2} \tag{4.15}$$

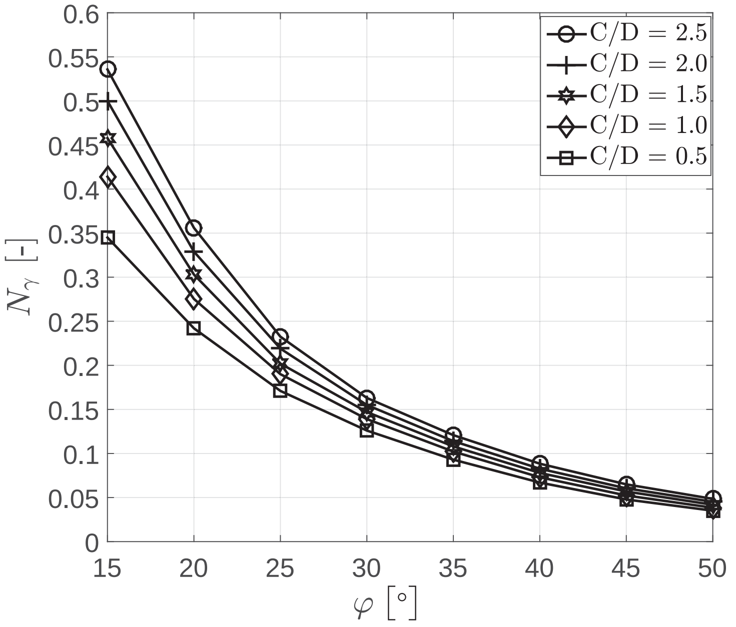

Figure 4.27: N_γ as function of the soil friction angle, KEM model (M)

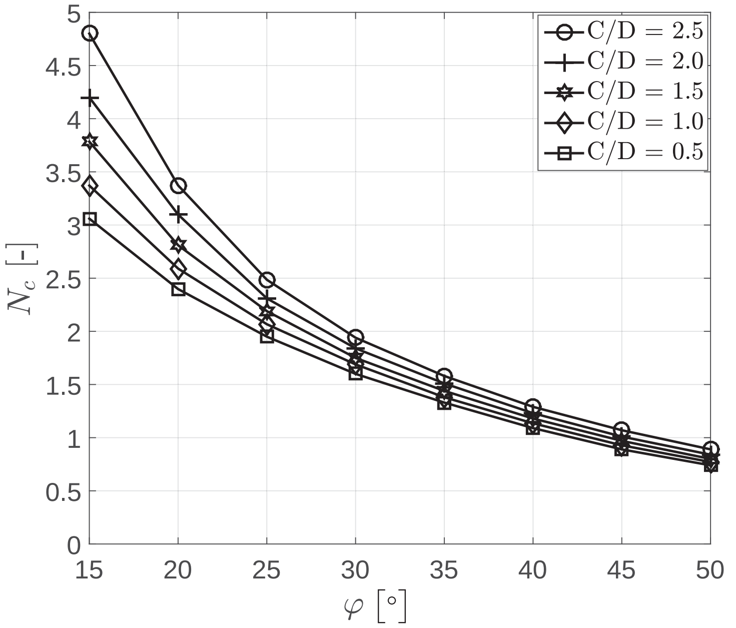

Figure 4.28: N_c as function of the soil friction angle, KEM model (M)

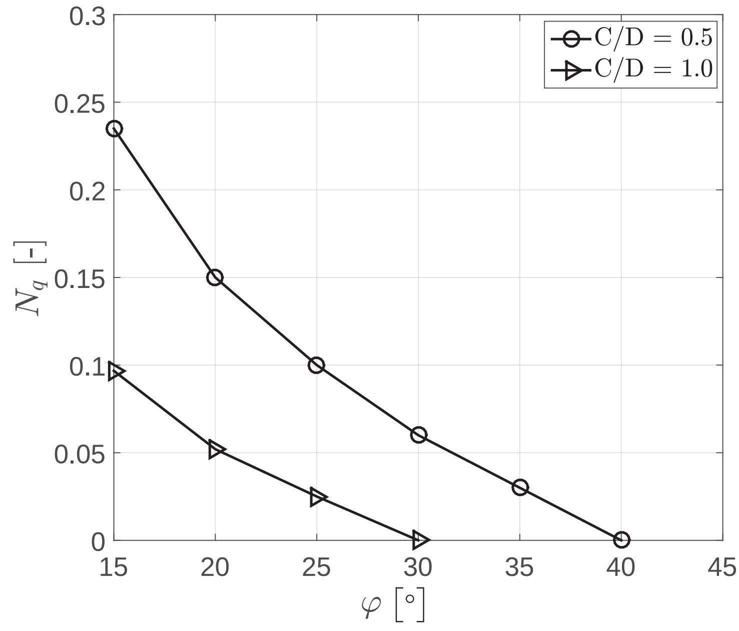

Figure 4.29: N_q as function of the soil friction angle, KEM model (M)

Table 4.4: Values of N_γ, N_c and N_q for various internal friction angles and C/D ratios; results obtained with KEM model (M)

	N_γ					N_c					N_q				
								C/D							
φ	0.5	1	1.5	2	2.5	0.5	1	1.5	2	2.5	0.5	1	1.5	2	2.5
15^o	0.345	0.414	0.457	0.506	0.536	3.100	3.371	3.784	4.203	4.811	0.235	0.091	0.000	0.000	0.000
20^o	0.242	0.276	0.304	0.329	0.356	2.398	2.590	2.820	3.099	3.373	0.150	0.052	0.000	0.000	0.000
25^o	0.171	0.191	0.202	0.219	0.233	1.950	2.067	2.161	2.310	2.485	0.100	0.025	0.000	0.000	0.000
30^o	0.126	0.139	0.147	0.155	0.163	1.601	1.689	1.770	1.814	1.940	0.060	0.000	0.000	0.000	0.000
35^o	0.093	0.102	0.108	0.114	0.121	1.330	1.382	1.442	1.501	1.580	0.030	0.000	0.000	0.000	0.000
40^o	0.067	0.073	0.078	0.082	0.088	1.092	1.135	1.181	1.232	1.290	0.000	0.000	0.000	0.000	0.000
45^o	0.047	0.052	0.057	0.060	0.065	0.891	0.928	0.971	1.02	1.080	0.000	0.000	0.000	0.000	0.000
50^o	0.037	0.041	0.045	0.048	0.052	0.741	0.771	0.802	0.841	0.891	0.000	0.000	0.000	0.000	0.000

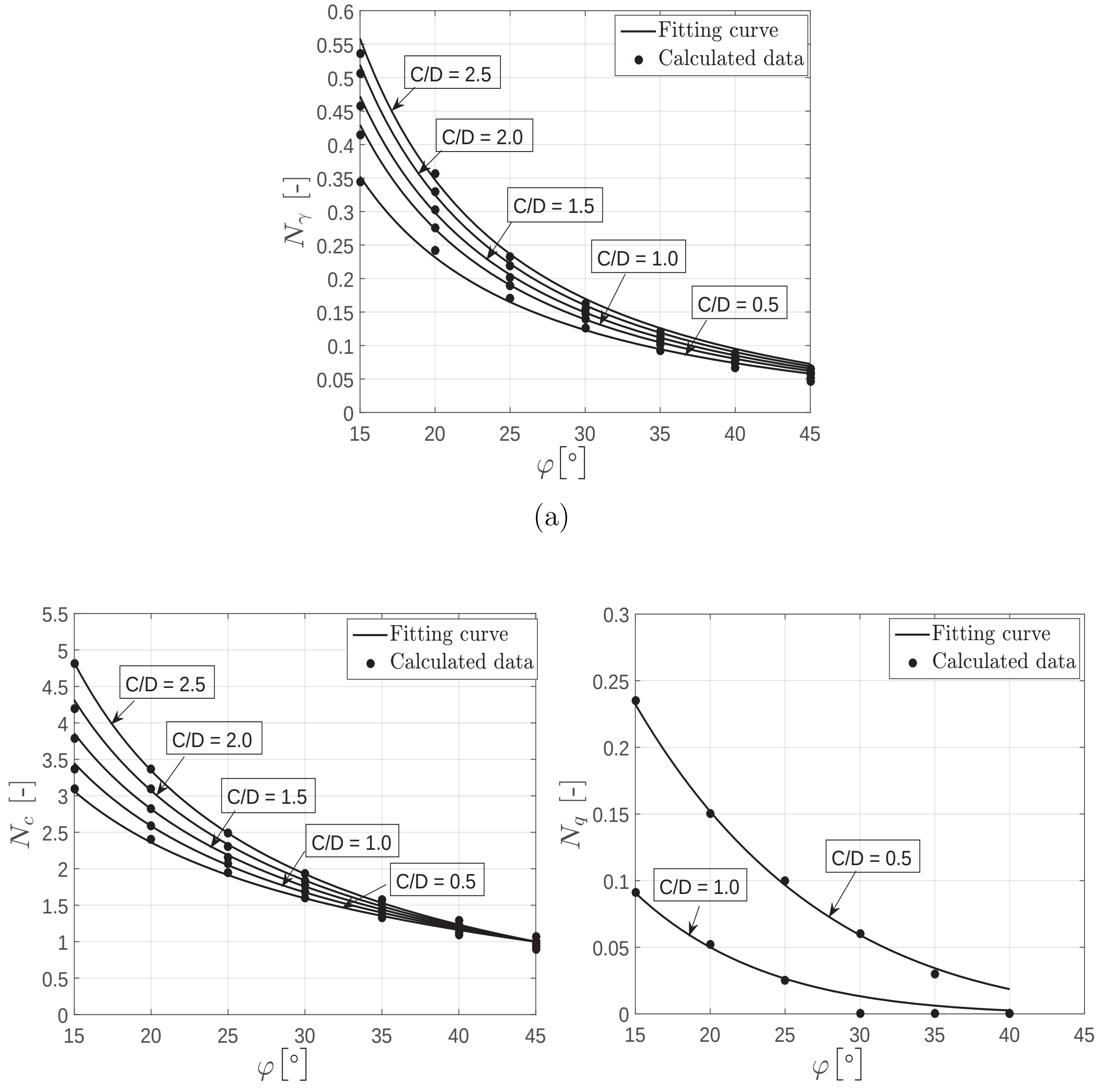

(a)

(b) (c)

Figure 4.30: Fitting curves for the approximated equations of (a) N_γ, (b) N_c, (c) N_q

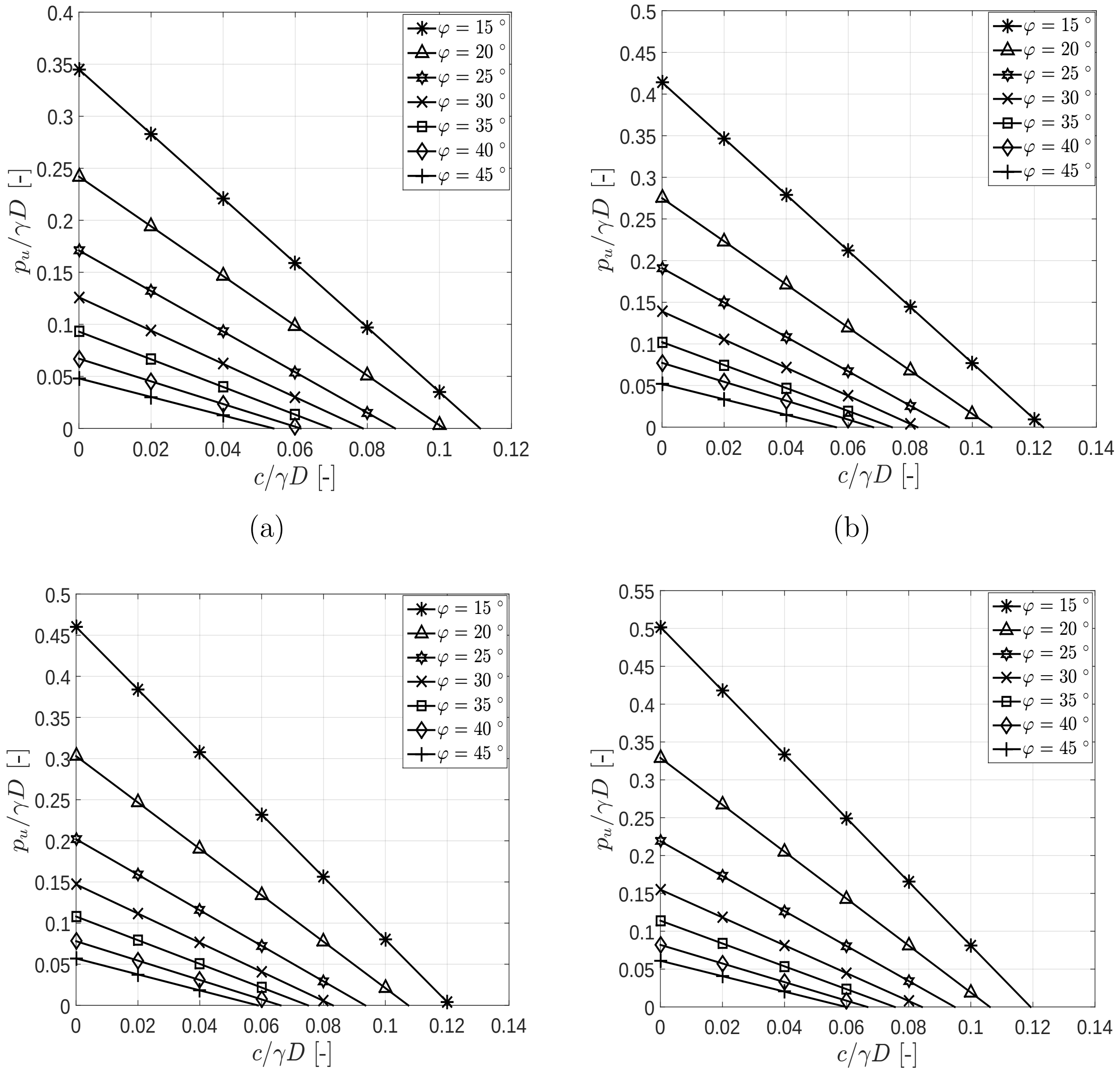

(a) (b)

(c) (d)

Figure 4.31: Design charts for the minimum support pressure, KEM model (M) ($q = 0$ kPa): (a) $C/D = 0.5$; (b) $C/D = 1$; (c) $C/D = 1.5$; (d) $C/D = 2$

$$b_2 = 0.77 + 0.17 \cdot C/D \tag{4.16}$$

$$N_q \approx a_2 \cdot b_3^{\tan\varphi)} \quad \text{(C/D} \leq 1.0) \tag{4.17}$$

$$a_2 = 1.04 - 0.56 \cdot C/D \tag{4.18}$$

$$b_3 = 0.0022 - 0.0019 \cdot C/D \tag{4.19}$$

These equations can be applied in combination with Eq. (4.10) to predict the minimum support pressure Fig. 4.30 shows the comparison between the N_γ N_c and N_q and values obtained from the KEM simulations (circles) for different friction angles and C/D ratios, confirming a good agreement.

For a practical application Table 4.4 provides the values of N_γ, N_c and N_q for different values of friction angle and C/D ratio. Furthermore, a design charts giving the normalized support pressure $p_u/(\gamma D)$ as a function of the normalized cohesion $c/(\gamma D)$ for different friction angles and C/D ratios.

4.10 Limitations of KEM model (M)

The comparison between the KEM model (M) and the other existing approaches indicates that the KEM solution gives reasonable results for tunnel face stability calculations in frictional and frictional-cohesive soil under simple conditions. A ground water table and seepage flow around the tunnel face have not been studied yet. However, based on the investigations done so far the limitations of this KEM model can be noted as follows.

1. KEM model (M) simplifies the geometry of the tunnel face by replacing the circular shape of the tunnel with an equivalent triangle having the same cross-sectional area. However, the location of the centroid of the circular area does not coincide with centroid of the triangle (see Fig 4.32). Therefore, if KEM model (M) is applied to saturated soil conditions, the hydrostatic pore pressure at the centroid of the triangle will be lower than the that at the centroid of the circular tunnel face.

2. In the case of the hypothetic case $\varphi = 0$, $c = 0$ kPa (material properties of water) and for $C/D = 0.5$, in wedge silo model the normalized support pressure $p_u/(\gamma D)$ converges to 1, while in KEM model (M) it approaches to 0.833. This is due to the shape of the tetrahedron wedge block (lower part) in KEM model (M), which leads to a reduction of the volume of the "wedge" block by 0.167 compared to the wedge-silo model, see Fig 4.33.

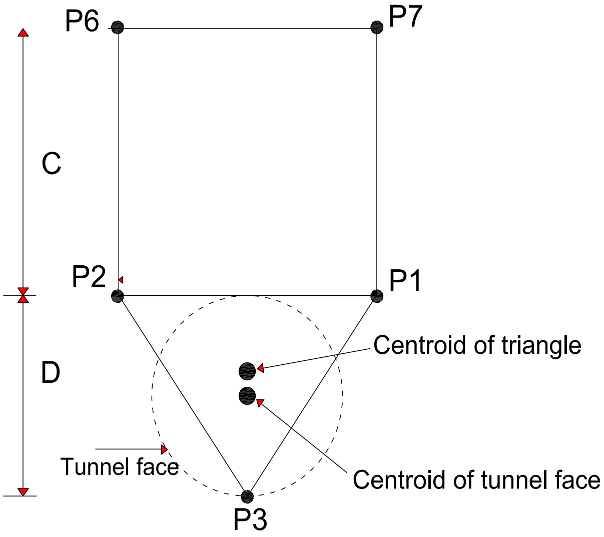
P6
P7
C
P2
P1
D
Centroid of triangle
Tunnel face
Centroid of tunnel face
P3

Figure 4.32: Geometry of the tunnel face in KEM model (M)

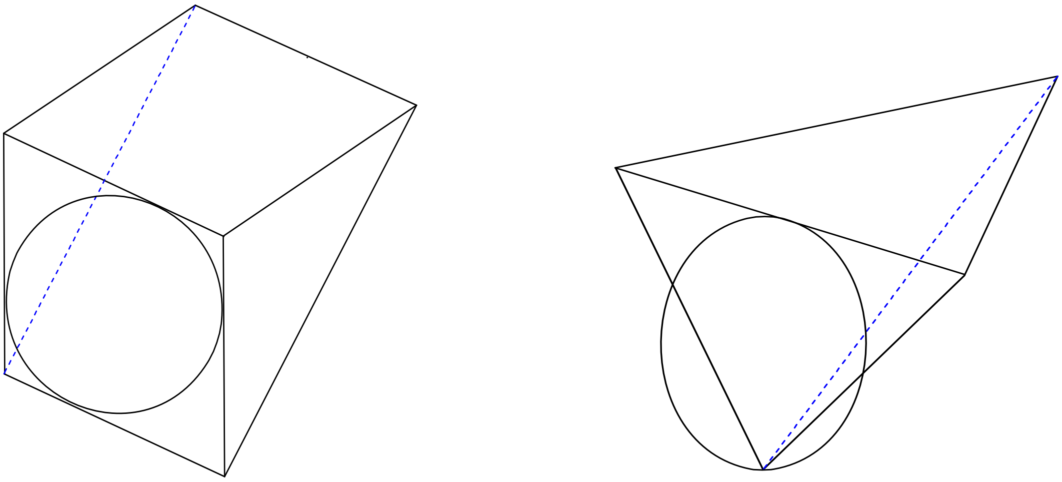

(a)

(b)

Figure 4.33: Shape of the wedge in wedge-silo model and KEM model (M): (a) wedge-silo model; (b) KEM model (M)

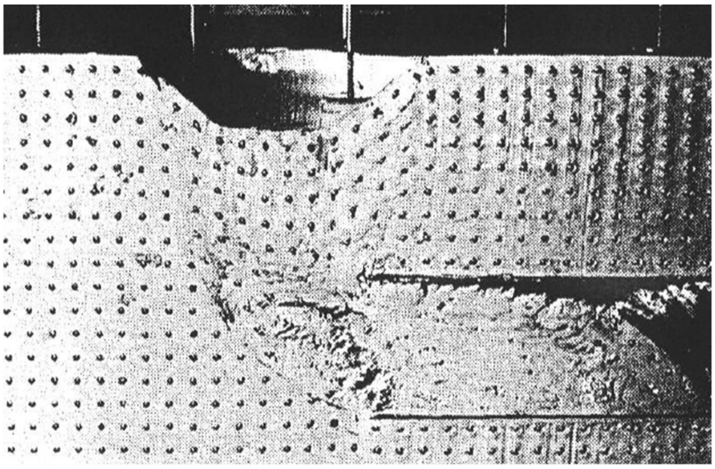

Figure 4.34: Tunnel face collapse in undrained clays, Schofield (1980)

3. Based on the centrifuge tests performed by Schofield (1980) and Kimura & Mair (1981), the collapse of the tunnel face in undrained clays does not involve the motion of rigid blocks, but a continuous deformation of the soil (see Fig 4.34). The soil mass tends to yield and rotate towards the tunnel face. In that case, a significant discrepancy exists between the failure mechanism assumed in KEM model (M) and those obtained from centrifuge tests. To consider such failure mechanism, KEM model (M) needs to be modified by increasing the number of elements in the wedge. Therefore, the slip surface of the wedge will become curved.

Due to these limitations or shortcomings of the KEM model (M), the modifications described in Chapter 5 were undertaken.

4.11 KEM 3D tunnel face stability software (KEM-3D-T)

Based on the Kinematical Element Method (KEM), a software for calculating the minimum support force necessary for the tunnel face stability has been developed, named KEM-3D-T. The computer program is written using Matlab language with graphical user interface which can be easily applied by non expert users. When the program is opened by the user, a screen similar to the one shown in Fig. 4.35 is presented.

Three different KEM models have been implemented in KEM-3D-T, namely the models (M), (M1) and (M2). Models (M1) and (M2) will be presented in Chapter 5.

In KEM-3D-T, the first step is to model the geometry of the tunnel. The geometry tab contains a number of options such as the coordinate of the ground level, the overburden

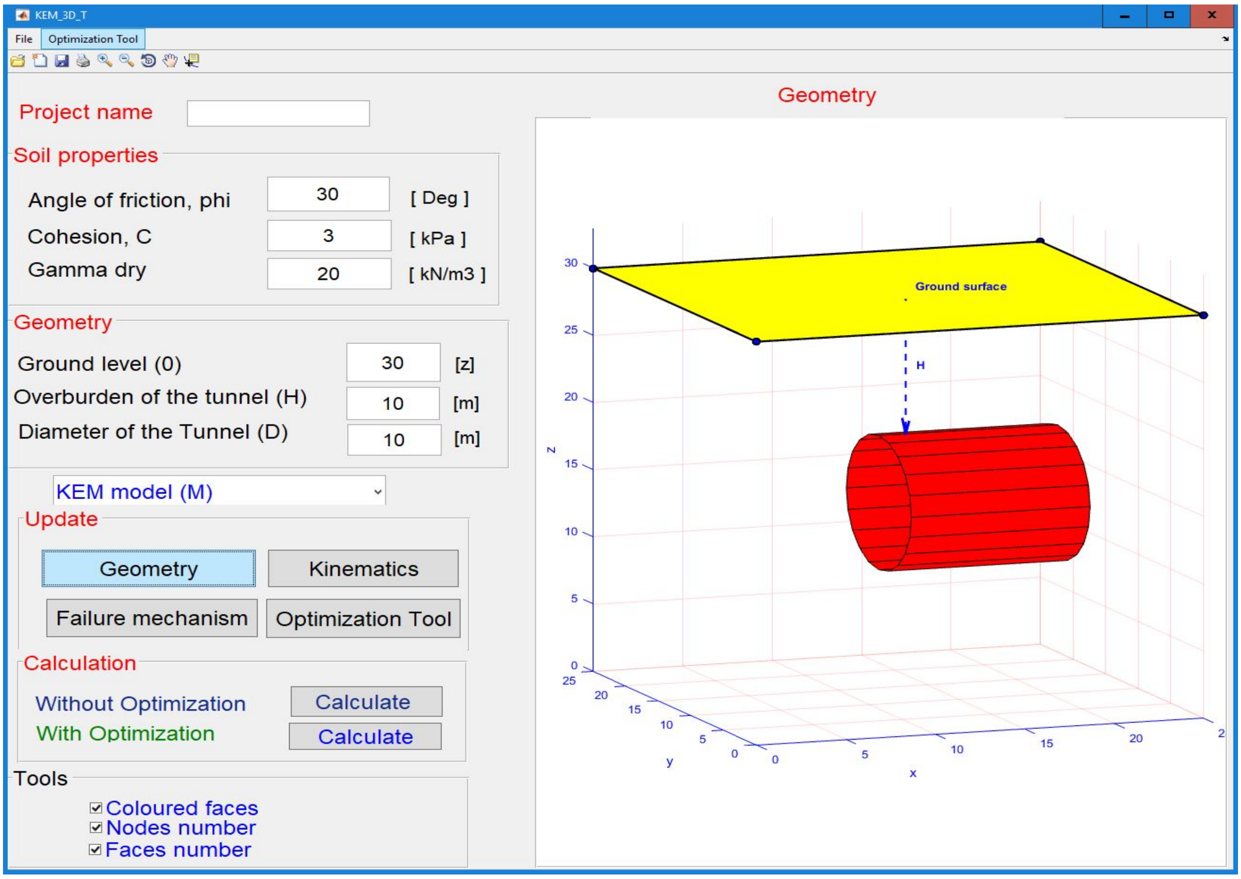
Project name

Soil properties

Angle of friction, phi: 30 [Deg]

Cohesion, C: 3 [kPa]

Gamma dry: 20 [kN/m3]

Geometry

Ground level (0): 30 [z]

Overburden of the tunnel (H): 10 [m]

Diameter of the Tunnel (D): 10 [m]

KEM model (M)

Tools

☑ Coloured faces

☑ Nodes number

☑ Faces number

KEM_3D_T
File
Optimization Tool
Update
Geometry
Kinematics
Failure mechanism
Optimization Tool
Calculation
Without Optimization
Calculate
With Optimization
Calculate
Geometry
Ground surface
H
z
30
25
20
15
10
5
0
y
25
20
15
10
5
0
x
0
5
10
15
20
2

Figure 4.35: KEM-3D-T opening screen

and the diameter of the tunnel. Once the model geometry has been established, the soil properties can be specified.

The next step is to run the analysis. The results of the analysis are presented by the maximum support force on the tunnel face and the relative displacements of each block.

Some useful tools have been added to the software. For example, the button in the foreground gives the user the ability to select zoom in or out. The drop-down box is used to select the type of the KEM models (M), (M1) or (M2). The check boxes on the left side can be used to display the color of the face of the blocks, the number of the node and the number of each face.

Figs 4.36 to 4.43 demonstrate the input of the model geometry and the results of different KEM models using different tools.

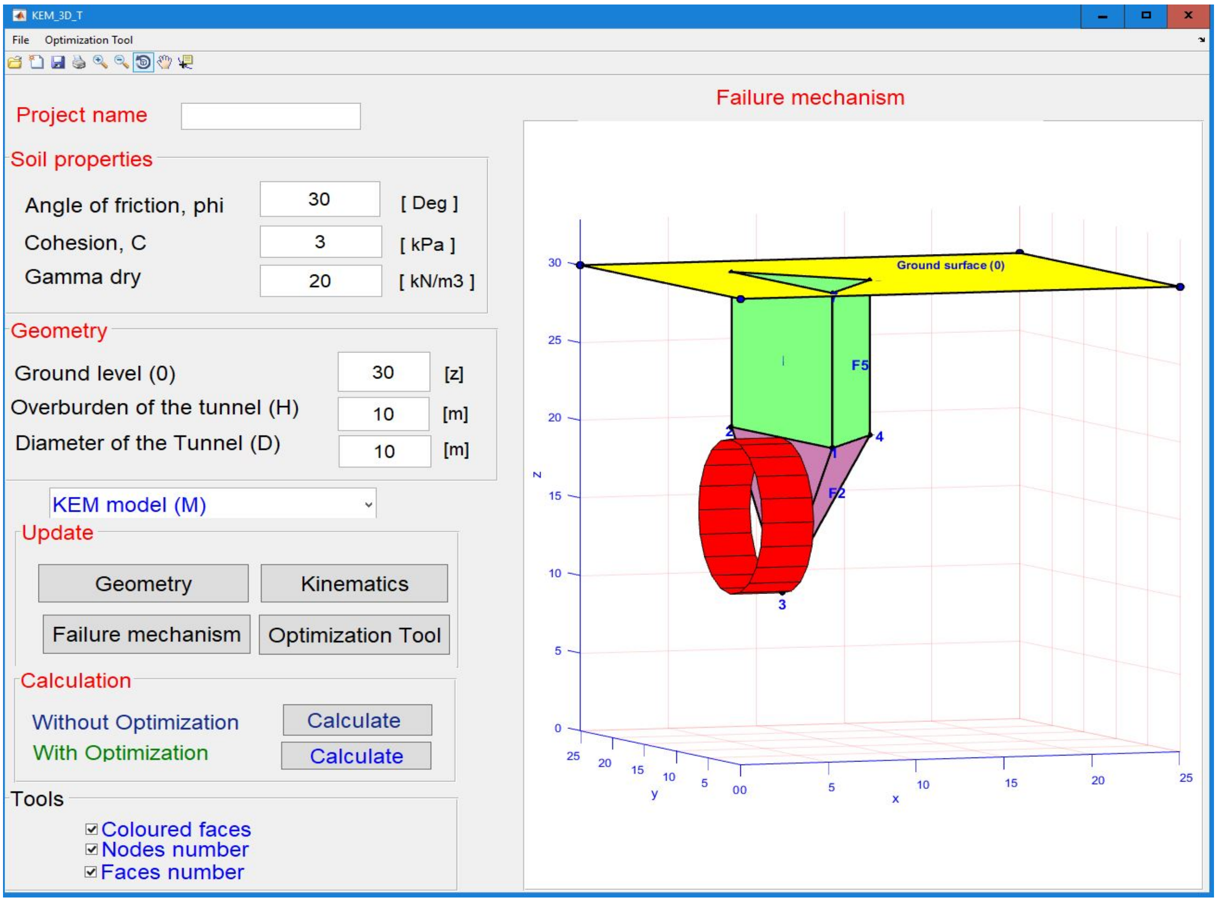
KEM_3D_T
File
Optimization Tool
Update
Geometry
Kinematics
Failure mechanism
Optimization Tool
Calculation
Without Optimization
Calculate
With Optimization
Calculate
Tools
Failure mechanism
Ground surface (0)
F5
F2
1
2
3
4
z
0
5
10
15
20
25
30
y
25
20
15
10
5
0
x
0
5
10
15
20
25

Project name

Soil properties

Angle of friction, phi 30 [Deg]
Cohesion, C 3 [kPa]
Gamma dry 20 [kN/m3]

Geometry

Ground level (0) 30 [z]
Overburden of the tunnel (H) 10 [m]
Diameter of the Tunnel (D) 10 [m]

KEM model (M)

☑ Coloured faces
☑ Nodes number
☑ Faces number

Figure 4.36: KEM-3D-T shows the failure mechanism for KEM Model (M)

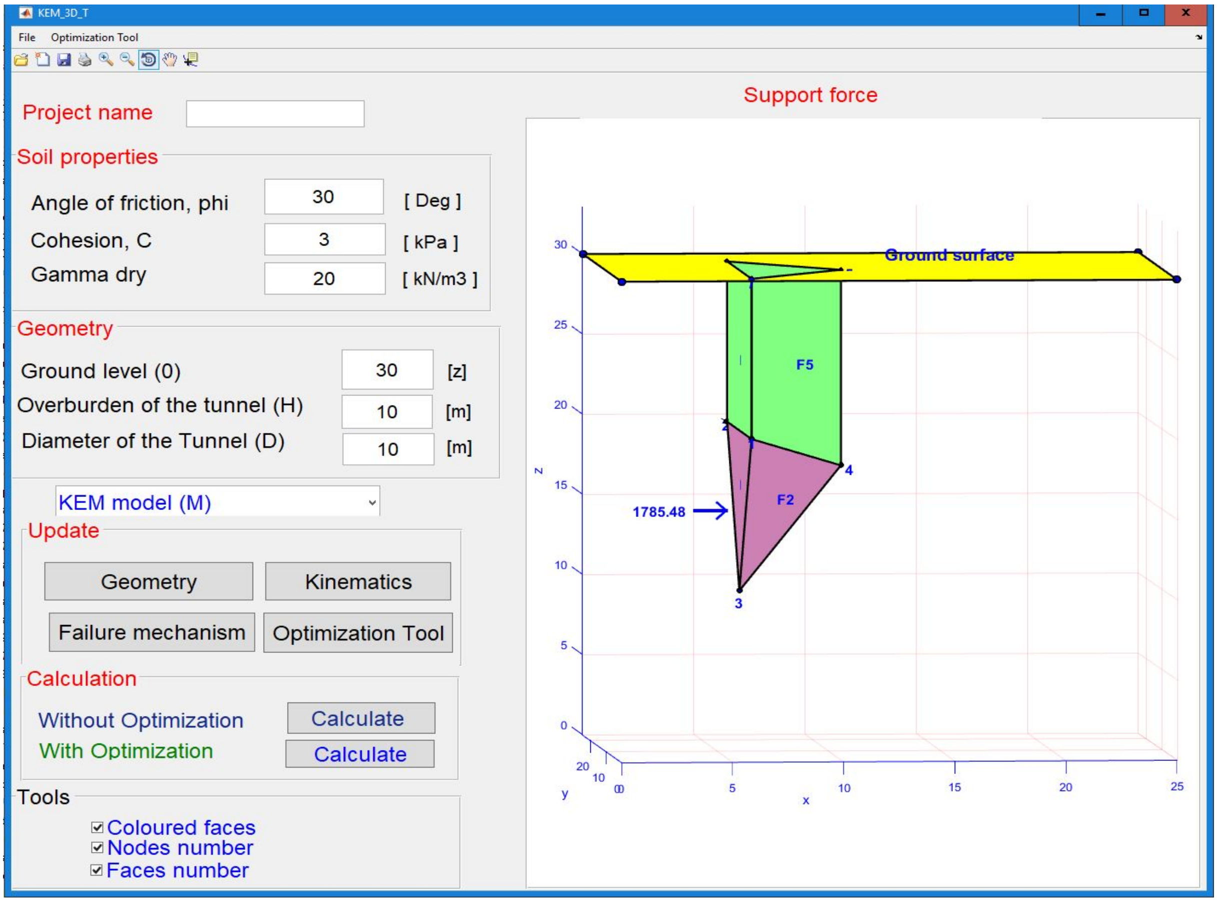

Project name

Soil properties

Angle of friction, phi 30 [Deg]
Cohesion, C 3 [kPa]
Gamma dry 20 [kN/m3]

Geometry

Ground level (0) 30 [z]
Overburden of the tunnel (H) 10 [m]
Diameter of the Tunnel (D) 10 [m]

KEM model (M)

Tools

☑ Coloured faces
☑ Nodes number
☑ Faces number

KEM_3D_T
File
Optimization Tool
Update
Geometry
Kinematics
Failure mechanism
Optimization Tool
Calculation
Without Optimization
Calculate
With Optimization
Calculate
Support force
Ground surface
F5
F2
1785.48
1
2
3
4
z
30
25
20
15
10
5
0
x
0
5
10
15
20
25
y
20
10
0

Figure 4.37: KEM-3D-T shows the support force for KEM Model (M)

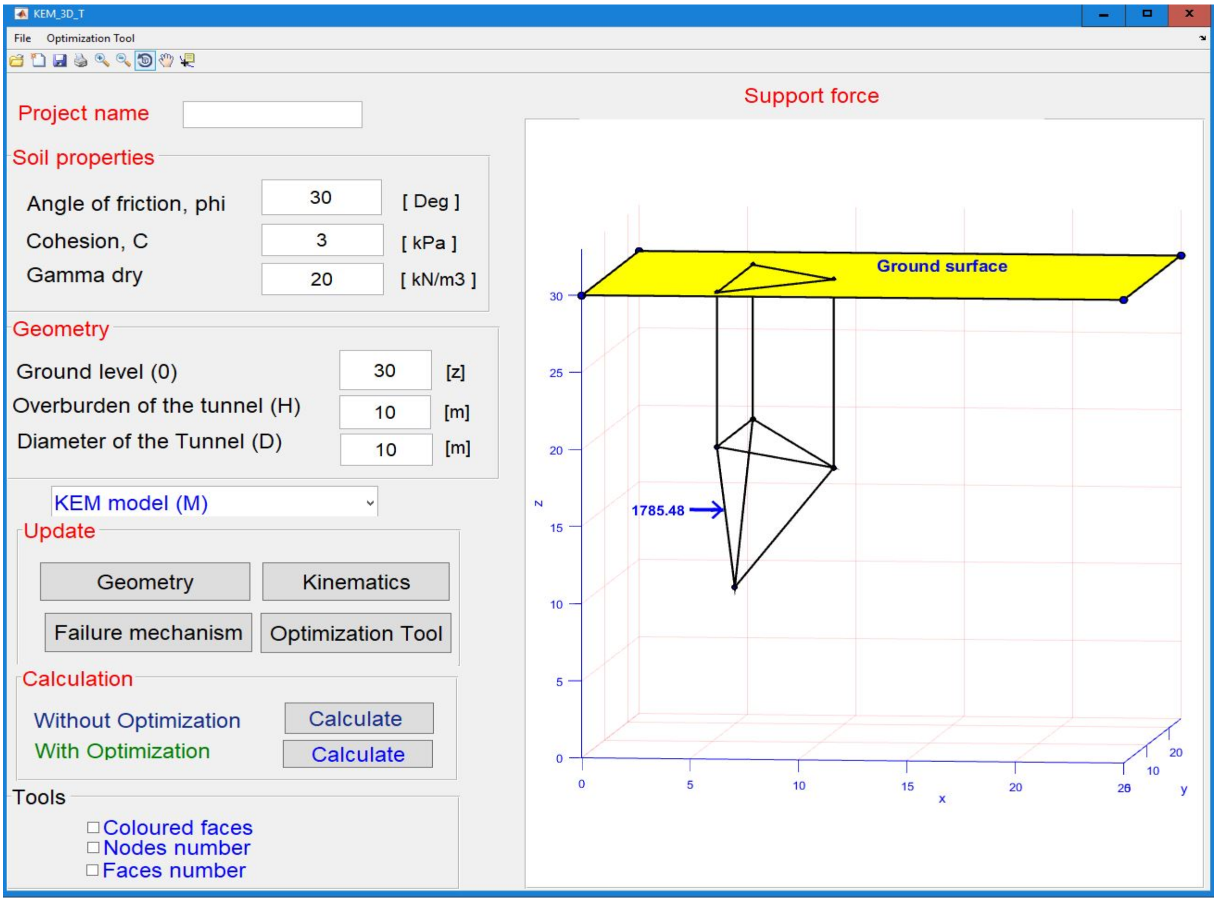
KEM_3D_T
File
Optimization Tool
Support force
Ground surface
1785.48
30
25
20
15
10
5
0
z
0
5
10
15
20
25
x
10
20
y
Update
Geometry
Kinematics
Failure mechanism
Optimization Tool
Calculation
Calculate
Calculate

Project name

Soil properties

Angle of friction, phi 30 [Deg]

Cohesion, C 3 [kPa]

Gamma dry 20 [kN/m3]

Geometry

Ground level (0) 30 [z]

Overburden of the tunnel (H) 10 [m]

Diameter of the Tunnel (D) 10 [m]

KEM model (M)

Without Optimization

With Optimization

Tools

☐ Coloured faces
☐ Nodes number
☐ Faces number

Figure 4.38: KEM-3D-T shows the support force for KEM Model (M) without displaying the color and the number of the nodes

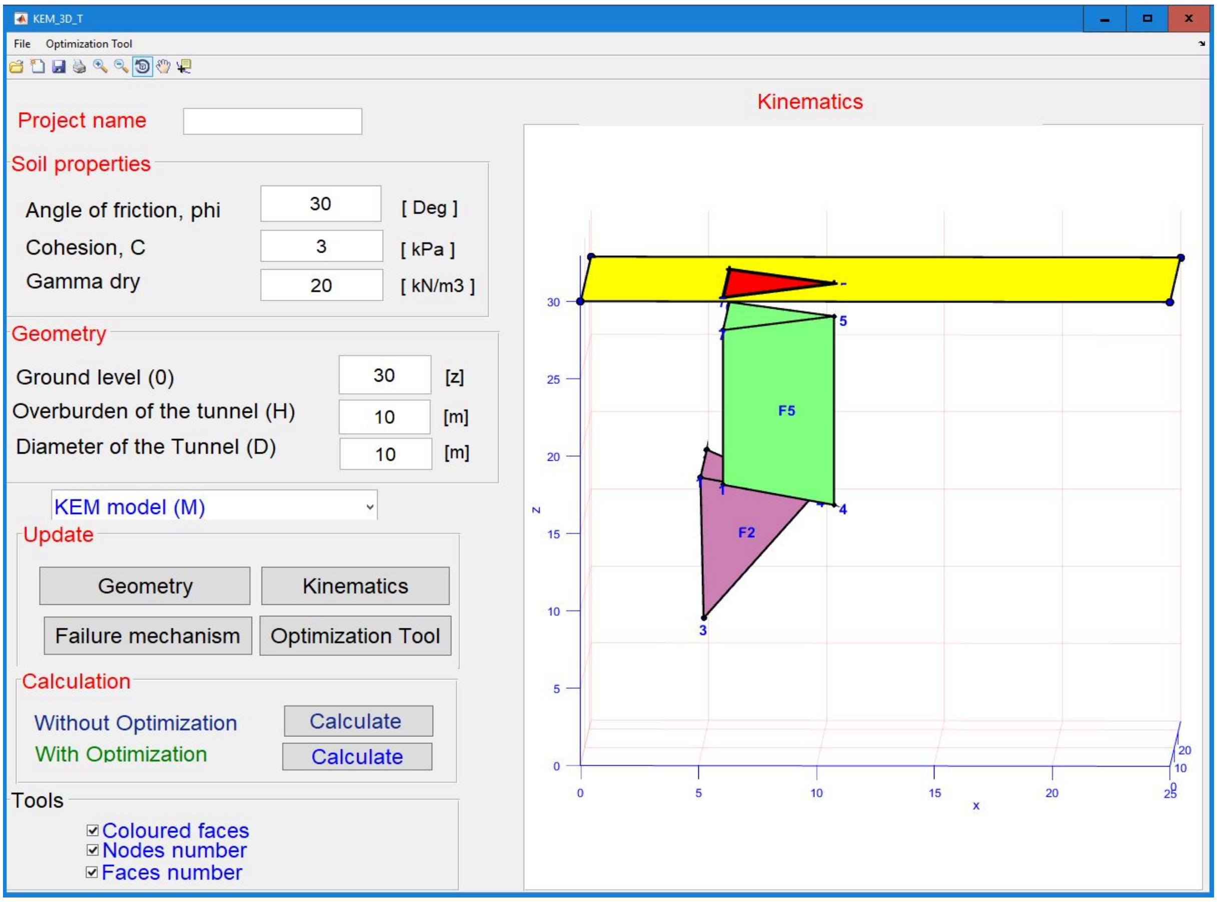
KEM_3D_T
File
Optimization Tool
Update
Geometry
Kinematics
Failure mechanism
Optimization Tool
Calculation
Without Optimization
Calculate
With Optimization
Calculate
Tools
Kinematics
F5
F2
1
2
3
4
5
z
x
0
5
10
15
20
25
30
0
10
20

Project name

Soil properties

Angle of friction, phi 30 [Deg]

Cohesion, C 3 [kPa]

Gamma dry 20 [kN/m3]

Geometry

Ground level (0) 30 [z]

Overburden of the tunnel (H) 10 [m]

Diameter of the Tunnel (D) 10 [m]

KEM model (M)

Tools

☑ Coloured faces

☑ Nodes number

☑ Faces number

Figure 4.39: KEM-3D-T shows the virtual displacements for KEM Model (M)

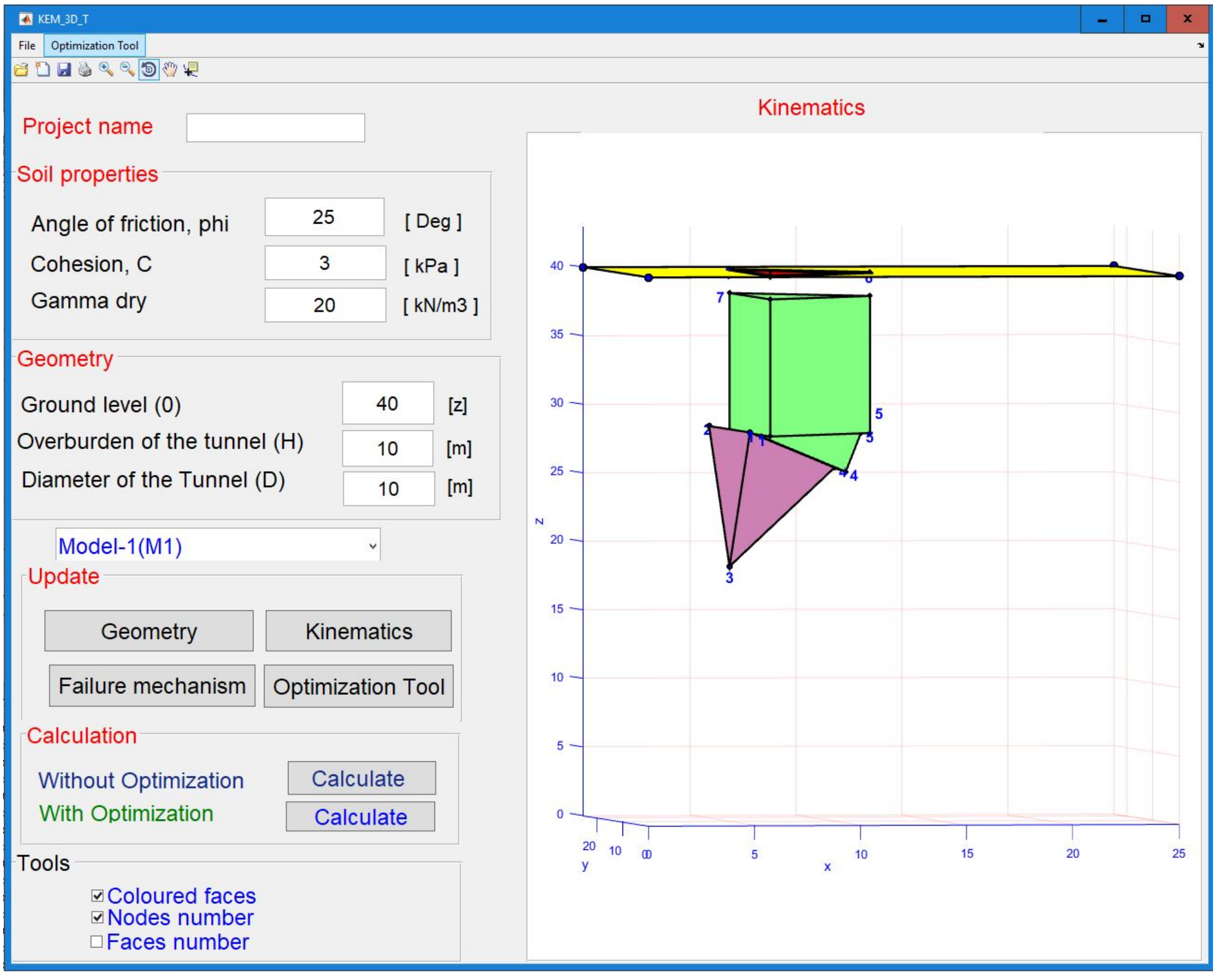

Project name

Soil properties

Angle of friction, phi 25 [Deg]
Cohesion, C 3 [kPa]
Gamma dry 20 [kN/m3]

Geometry

Ground level (0) 40 [z]
Overburden of the tunnel (H) 10 [m]
Diameter of the Tunnel (D) 10 [m]

Model-1(M1)

Tools

☑ Coloured faces
☑ Nodes number
☐ Faces number

KEM_3D_T
File
Optimization Tool
Update
Geometry
Kinematics
Failure mechanism
Optimization Tool
Calculation
Without Optimization
Calculate
With Optimization
Calculate
Kinematics
z
40
35
30
25
20
15
10
5
0
y
20
10
0
x
5
10
15
20
25
1
2
3
4
5
6
7

Figure 4.40: KEM-3D-T shows the virtual displacements for KEM Model (M1) with three elements

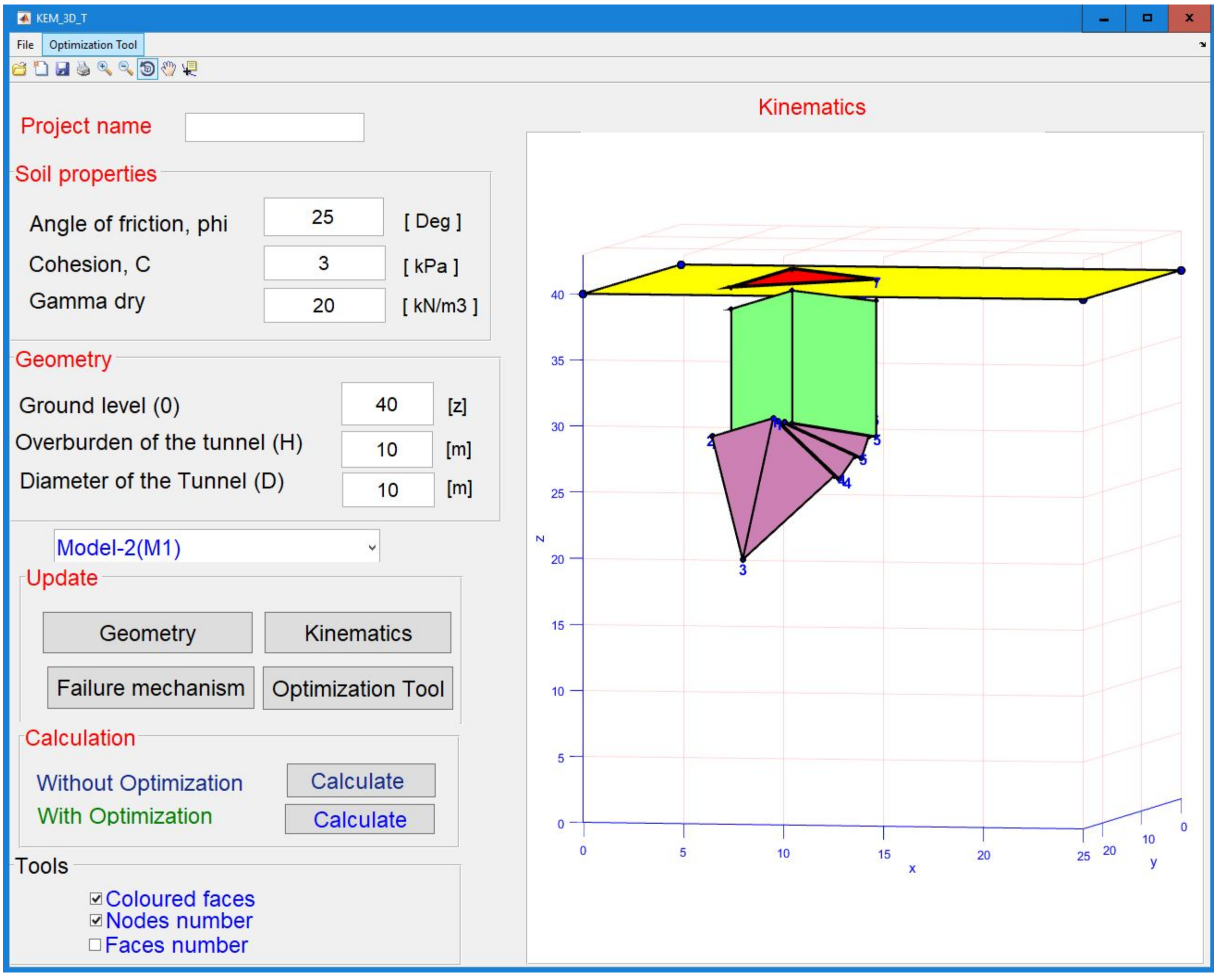

Project name

Soil properties

Angle of friction, phi 25 [Deg]

Cohesion, C 3 [kPa]

Gamma dry 20 [kN/m3]

Geometry

Ground level (0) 40 [z]

Overburden of the tunnel (H) 10 [m]

Diameter of the Tunnel (D) 10 [m]

Model-2(M1)

Calculation

Without Optimization

With Optimization

Tools

☑ Coloured faces

☑ Nodes number

☐ Faces number

KEM_3D_T
File
Optimization Tool
Update
Geometry
Kinematics
Failure mechanism
Optimization Tool
Calculate
Calculate
Kinematics
z
0
5
10
15
20
25
30
35
40
x
0
5
10
15
20
25
y
20
10
0
2
3
4
5
7

Figure 4.41: KEM-3D-T shows the virtual displacements for KEM Model (M1) with four elements

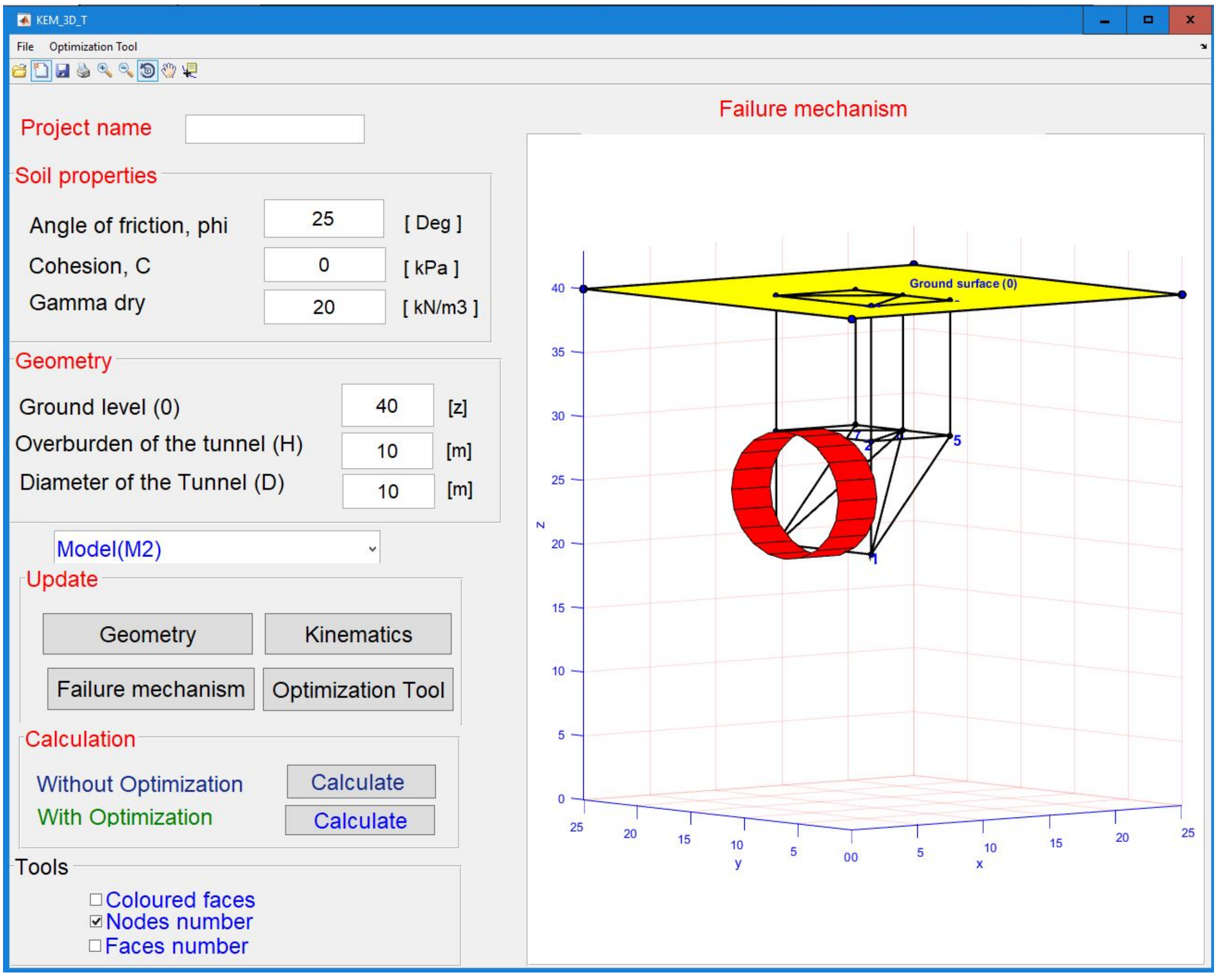
KEM_3D_T
File
Optimization Tool
Failure mechanism
Ground surface (0)
40
35
30
25
20
15
10
5
0
z
25
20
15
10
5
00
y
5
10
15
20
25
x
1
2
5
7
Update
Geometry
Kinematics
Failure mechanism
Optimization Tool
Calculation
Calculate
Calculate
Tools

Project name

Soil properties

Angle of friction, phi 25 [Deg]
Cohesion, C 0 [kPa]
Gamma dry 20 [kN/m3]

Geometry

Ground level (0) 40 [z]
Overburden of the tunnel (H) 10 [m]
Diameter of the Tunnel (D) 10 [m]

Model(M2)

Without Optimization
With Optimization

☐ Coloured faces
☑ Nodes number
☐ Faces number

Figure 4.42: KEM-3D-T shows the failure mechanism of KEM Model (M2)

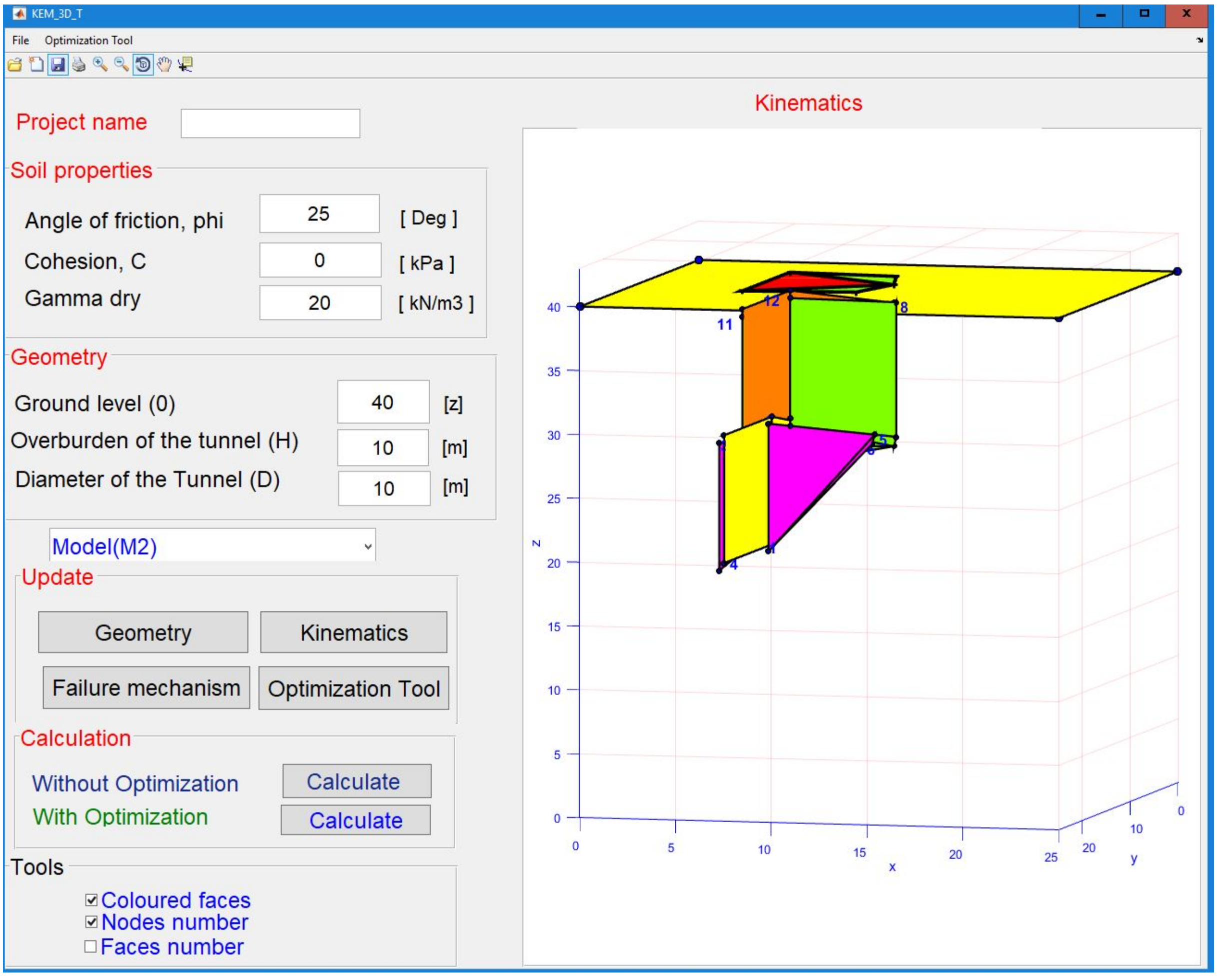
KEM_3D_T
File
Optimization Tool
Kinematics
Update
Geometry
Kinematics
Failure mechanism
Optimization Tool
Calculation
Calculate
Calculate
Tools
11
12
8
4
z
x
y
40
35
30
25
20
15
10
5
0
0
5
10
15
20
25
20
10
0

Project name

Soil properties

Angle of friction, phi 25 [Deg]

Cohesion, C 0 [kPa]

Gamma dry 20 [kN/m3]

Geometry

Ground level (0) 40 [z]

Overburden of the tunnel (H) 10 [m]

Diameter of the Tunnel (D) 10 [m]

Model(M2)

Without Optimization

With Optimization

☑ Coloured faces
☑ Nodes number
☐ Faces number

Figure 4.43: KEM-3D-T shows the virtual displacements for KEM Model (M2)

4.12 Summary

In this chapter the KEM is applied to estimate the minimum support pressure being necessary for stabilizing the tunnel face in dry frictional and frictional-cohesive soil. 3D KEM model (M) is developed which consists of two rigid blocks, the tetrahedron wedge block (lower part) and the triangular prism block (upper part, silo part). In order to incorporate the influence of 3D soil arching in the silo part a 3D active earth pressure acting on the vertical slip surfaces of the prism from the surrounding soil is presumed. The results for the minimum support pressure obtained with the KEM model (M) are compared with the results of numerical simulations and analytical approaches, as well as physical model tests available in the literature. Similar to Terzaghi's superposition method commonly used in bearing capacity analysis, the minimum support pressure is expressed as the sum of cohesion (c), surcharge load (q) and weight of the soil along the tunnel diameter D ($\gamma \cdot D$) multiplied by non-dimensional coefficients N_c, N_q and N_γ. Simple formulas have been developed for calculating the non-dimensional coefficients as a function of cover depth to tunnel diameter ratio (C/D) and internal friction angle of the soil (φ). To further validate the proposed KEM model (M), numerical simulations using Finite Element Limit Analysis (FELA) have been performed The upper and lower bound solutions obtained from the FELA simulations were compared with the KEM model (M) results. The KEM model (M) gives good results in terms of minimum support pressure compared to physical model test results, various analytical and numerical solutions as well as FELA for the tunnel face stability analysis in homogenous soils. The results of the simulations with KEM model (M) are presented in design charts using the normalized support pressure ($p_u/(\gamma D)$) and normalized cohesion ($c/(\gamma D)$) on the axes.

5 Modified KEM models (M1 and M2)

5.1 Introduction

In geotechnical engineering, the result of a stability analysis is significantly dependent on the chosen failure mechanism. The selection of a proper failure mechanism is thus of great importance in estimating the collapse load.

Michalowski (1997) proposed a multi-wedge discretization system for estimating the bearing capacity of a strip footing. He concluded that the multiblock mechanism significantly improves the solutions given by the two-blocks failure mechanism. This is due to the increase in the number of degrees of freedom offered by the multiblock mechanism to compered to two-blocks mechanism.

Latterly, the multiblock failure mechanism was applied for the analysis of three-dimensional passive earth pressure (Soubra & Regenass, 2000) and bearing capacity of square and rectangular footings (Michalowski, 2001).

Based on the upper bound method, a number of authors has also applied the multiblock failure mechanism to investigate the stability of the tunnel face. Mollon et al. (2010), Zhang et al. (2015) and Han et al. (2016) improved the two solid conical failure mechanism proposed by Leca & Dormieux (1990) using 3D failure mechanisms composed of several rigid blocks.

In Chapter 4, the proposed failure mechanism consists of two rigid blocks (KEM model (M)) offering two degrees of freedom for the wedge (see Figs. 4.1 and 4.3). In order to improve the solution efforts are undertaken within this chapter to refinement the two-blocks mechanism by increasing the number of blocks in the failure mechanism of KEM model (M). To verify the accuracy of the modified KEM models (M1 and M2), a comparative calculations are carried out between KEM models (M1 and M2) and different approaches i literature. The results are presented in charts demonstrating the influence of internal friction angle of the soil (φ) and cohesion (c) on the normalized support pressure ($p_u/(\gamma D)$).

Furthermore, the strength reduction method is used to calculate the safety factor of the tunnel face, as well as the maximum diameter in open-face tunneling.

5.2 Multiblocks failure mechanism (M1)

5.2.1 Geometry

The M1 failure mechanism is an extension of two-blocks failure mechanism. Fig. 5.1 shows the failure mechanism (M1) using KEM 3D tunnel face stability software (KEM-3D-T). The first modified model (M1) is multiblocks composed of five rigid blocks in which the wedge block is divided into a sequence of four blocks. In general, the geometrical construction of this mechanism is similar to that of the two-blocks failure mechanism i.e., the silo block is a triangular prism block ranging from the crown of the tunnel to the ground surface. The tunnel face is approximated by a equilateral triangle with the same area as the tunnel face as shown in Fig. 5.2.

5.2.2 Kinematic analysis

The stationary soil mass outside the failure mechanism is identified as region O with a zero displacement $V_O = [0, 0, 0]$. To start the kinematic process a unit displacement is initiated on the face of the tunnel with displacement $V_1 = [1, 0, 0]$. In this model all elements move as rigid blocks in the downward direction (see Fig. 5.3). The directions of the relative tangential displacements between any adjacent blocks are determined according to Eq. (3.9) (Chapter 3).

5.2.3 Static analysis

The static system-matrix for one half of KEM model (M1) is written as follows :

$$[K_s]_{15\times16} \cdot [\mathrm{N}]_{16\times1} + [\mathrm{F}]_{15\times1} = 0 \tag{5.1}$$

From Eq. (5.1), the system has 16 unknown reaction normal forces, while there are only 15 equations of equilibrium. To solve the system of equations an additional equation or one reaction force is needed.

As discussed in Chapter 4, the load acting from the adjoining soil of the silo is considered as a 3D active earth pressure exerting on the vertical slip surface of the silo. The 3D lateral

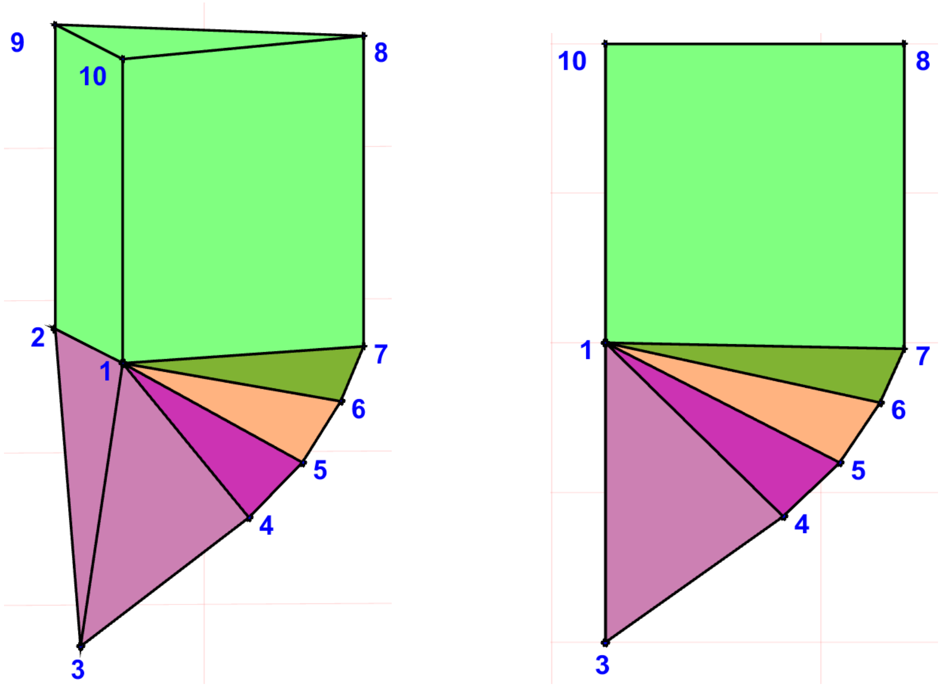
9
10
8
2
1
7
6
5
4
3
10
8
1
7
6
5
4
3

Figure 5.1: Geometry of the failure mechanism, KEM model (M1) using KEM-3D-T

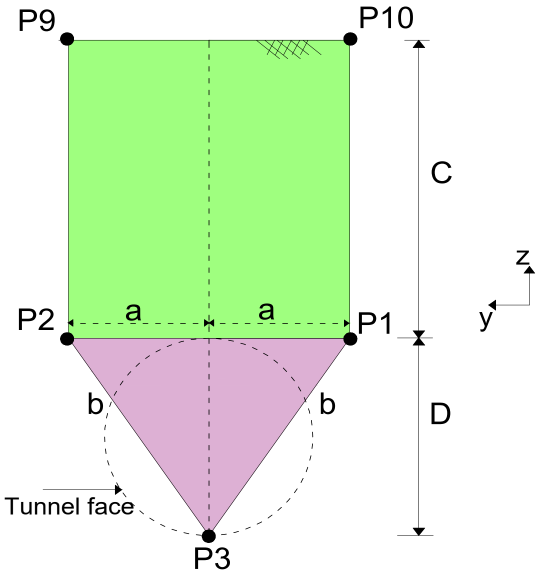
P9
P10
C
z
y
P2
a
a
P1
b
b
D
Tunnel face
P3

Figure 5.2: Geometry of equilateral triangle for KEM model (M1)

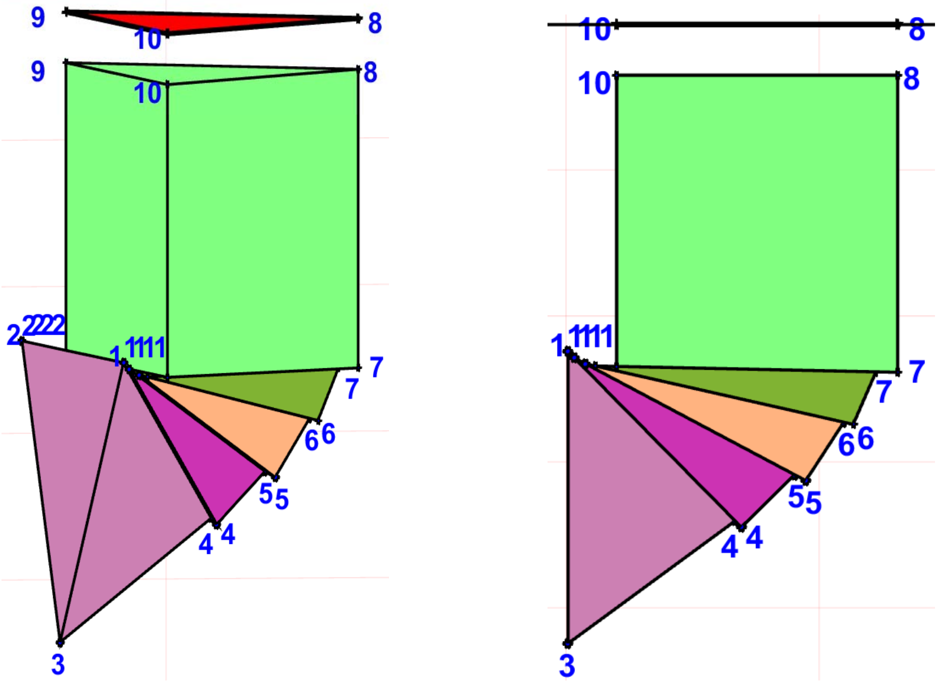

Figure 5.3: Kinematic of the blocks for KEM model (M1) using KEM-3D-T

earth pressure coefficient between the silo and the adjoining soil is calculated according Eq. (4.9) (Chapter 4) leading to an estimate of one unknown force of the system.

5.2.4 Discussion and comments on KEM model (M1)

Beside the failure mechanism with five rigid blocks, also the failure mechanisms with two, three and four elements shown in Figs 5.4 and 5.5 have been included in the analysis. Table 5.1 presents the values of the minimum support pressure for different the numbers of the rigid blocks, varying from two to five, considering both cohesionless and frictional-cohesive soils. The percent of improvement in the support pressure corresponding to a given number of blocks is calculated with reference to the failure mechanism (M) composed of two blocks.

From Table 5.1, it can be seen that the improvement in the minimum support pressure increases with the increase in the number of blocks. However, this increase of accuracy is rather small. For instance as shown in Fig. 5.6, when using five instead of two rigid blocks, an improvement of 4.34 % is achieved for a cohesionless soil with a friction angle of 25^o. The variation of the inclination angle (θ) for the silo and the width of the silo (x) with the number of blocks is shown in Fig. 5.7. When the number of blocks increases, the inclination angle of the surface at the bottom of the silo decreases, while, the the width

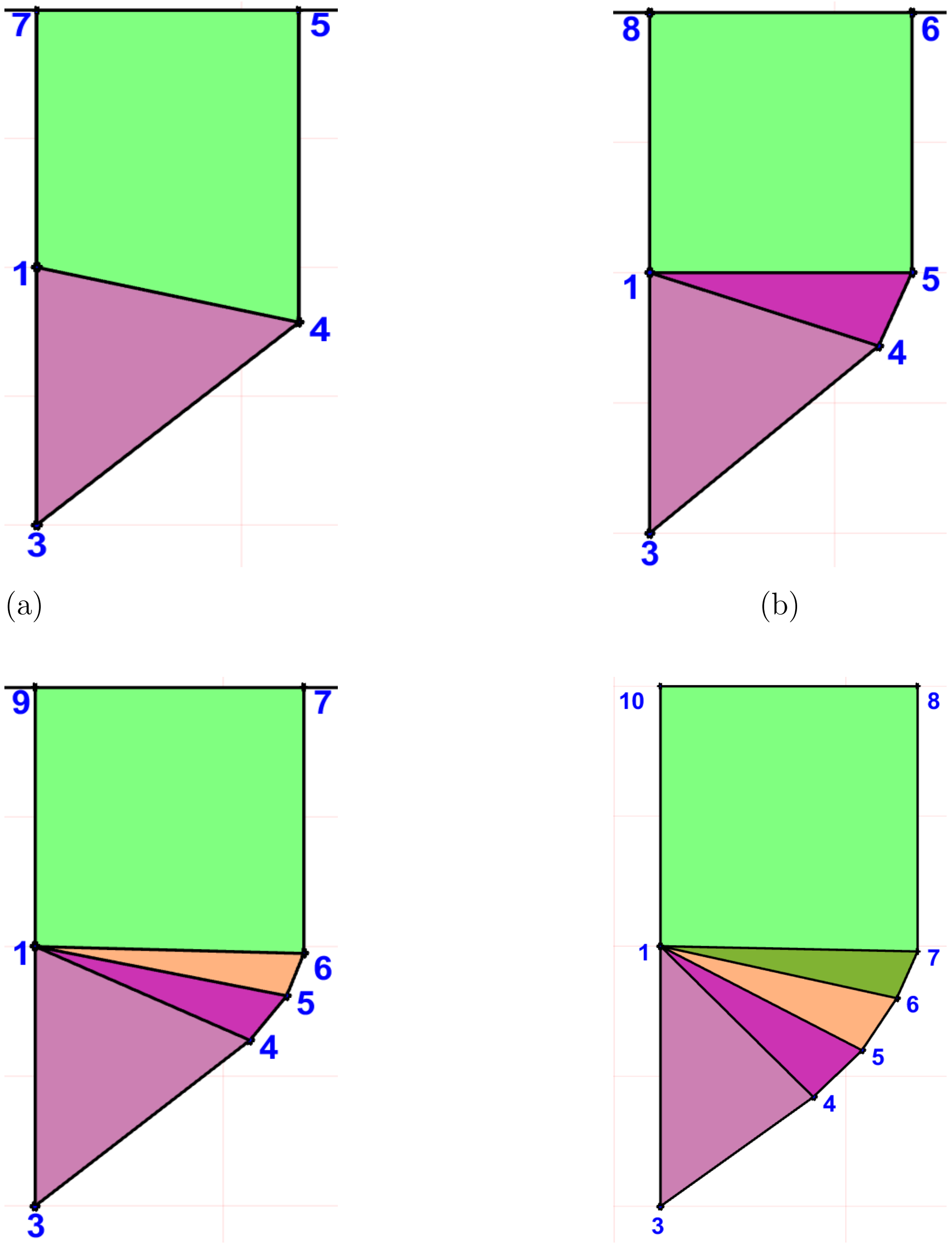
7
5
1
4
3
8
6
1
5
4
3
9
7
1
6
5
4
3
10
8
1
7
6
5
4
3

(a) (b)

(c) (d)

Figure 5.4: Failure mechanism for different numbers of elements for KEM model (M1) using KEM-3D-T with $\varphi = 25^o$, $c = 0$ kPa: (a) 2 elements; (b) 3 elements; (c) 4 elements; (d) 5 elements

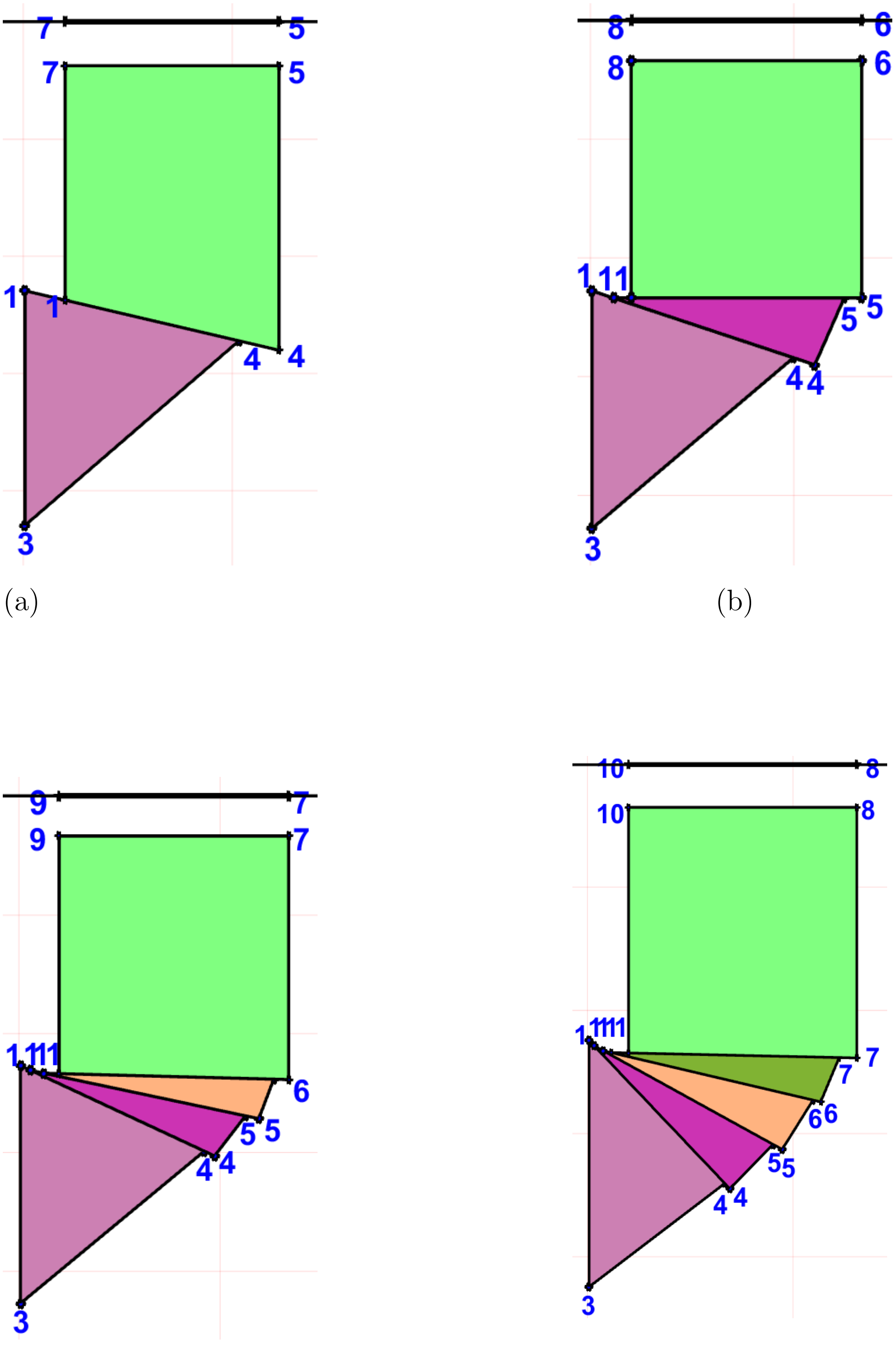
7
5
7
5
1
1
4
4
3
8
6
8
6
1
11
5
5
4
4
3
9
7
9
7
1
111
6
5
5
4
4
3
10
8
10
8
1
1111
7
7
6
6
5
5
4
4
3

(a) (b)

(c) (d)

Figure 5.5: Kinematics for different numbers of elements using KEM-3D-T with $\varphi = 25^o$, $c = 0$ kPa: (a) 2 elements; (b) 3 elements; (c) 4 elements; (d) 5 elements

Table 5.1: Influence of the number of blocks on the minimum support (C/D = 1 and γ = 18 kN/m^3)

	Cohesionless soils			
	$\varphi = 25^o$, $c = 0$ kPa		$\varphi = 35^o$, $c = 0$ kPa	
Number of blocks	Minimum support pressure pressure (kPa)	Improvement (%)	Minimum support pressure (kPa)	Improvement (%)
2	34.53		18.35	
3	35.38	2.41	18.48	0.65
4	35.80	3.54	18.57	1.13
5	36.10	4.34	18.71	1.87
	Frictional-cohesive soils			
	$\varphi = 25^o$, $c = 5$ kPa		$\varphi = 35^o$, $c = 2$ kPa	
Number of blocks	Minimum support pressure pressure (kPa)	Improvement (%)	Minimum support pressure pressure (kPa)	Improvement (%)
2	24.04		14.26	
3	24.10	0.23	14.291	0.20
4	24.23	0.77	14.37	0.76
5	24.40	1.47	14.42	1.10

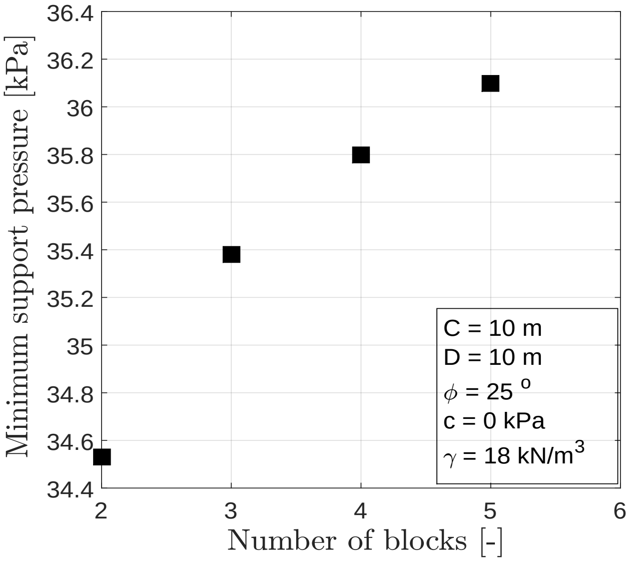

Figure 5.6: Improvement of support pressure versus number of blocks for model (M1)

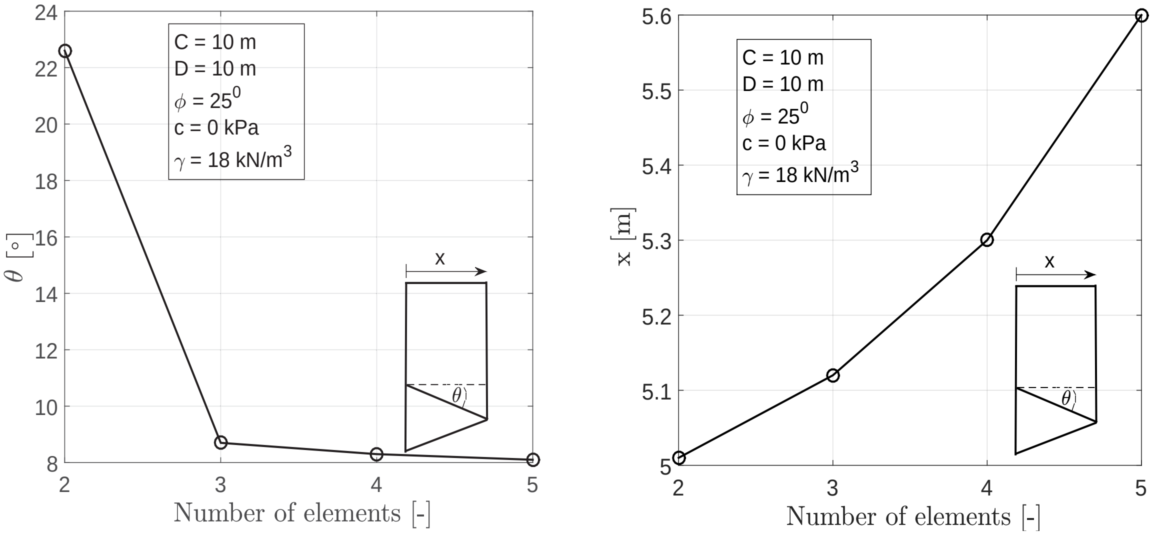

(a) (b)

Figure 5.7: Variation of the inclination angle θ of the surface at the bottom of the silo: (a) inclination angle for the silo (θ) with the number of blocks; (b) width of the silo (x) with the number of blocks

of the silo increases. By using KEM model (M1), the approximation of the geometry of the failure mechanism within the wedge comes closer to reality. With increasing number of blocks the slip surface of the wedge approaches a curved surface (see Figs. 5.4 and 5.5) which is similar to the semicircular slip surfaces observed in physical model tests (e.g., Idinger et al., 2011; Kirsch, 2010*a*).

5.3 Multiblocks failure mechanism (M2)

5.3.1 Geometry

The modified KEM model (M2) consists of two domains (see Fig. 5.8), the wedge (lower part) and the silo (upper part). The wedge is divided into three rigid blocks. Two outer tetrahedron blocks have scalene triangles at each of its faces. The inner rigid block is a three-dimensional rectangle-based pyramid having one square face (tunnel face), while the other faces are triangles with a common vertex. The silo is divided into three triangular prisms, each of them with two triangular faces at the top and the bottom and three rectangular faces at the sides. In this model the circular tunnel face is approximated by a square area (A_s) with side length equal to the diameter (D) of the tunnel face as shown in Fig. 5.8 (b).

$$A_s = D \cdot D \tag{5.2}$$

5.3.2 Kinematic analysis

By initiating a unit displacement v (virtual displacement) on the face of the tunnel V = -ve_1, the rectangle-based pyramid wedge moves downward with displacement vector $V_i = [1, 0, V_{iz}]$. The downward movement of the square pyramid wedge (P_1, P_2, P_6, P_{14}, P_{15}) is accommodated by the movement of adjacent and above tetrahedron blocks. The two triangular prisms of the silo are translating vertically with different displacements. The left-hand side wedge moves with displacements $V_i = [V_{ix}, 0, V_{iz}]$. In general, the directions of the relative tangential displacements between any adjacent blocks are determined according to Eq. (3.9) (Chapter 2).

5.3.3 Static analysis

The static system-matrix for one half of KEM model (M2) is written as follows:

$$[K_s]_{12\times 13} \cdot [\mathrm{N}]_{13\times 1} + [\mathrm{F}]_{12\times 1} = 0 \tag{5.3}$$

From Eq. (5.3), it becomes clear that the system has 13 unknown reaction normal forces, while there are only 12 equations of equilibrium (statics), indicating that the number of unknown reaction normal forces exceeds the number of in equilibrium equations by one.

In order to solve this statically indeterminate problem a 3D active earth pressure acting on the vertical slip surface (P2, P12, P13, P14) of the prism is assumed. The value of maximum normal ($0.5N_{13}$) and shear ($0.5R_{13}$) force is transferred from the subroutine "3D active earth pressure" to the subroutine "tunnel face stability", see Fig. 5.9. Based on the results of the calculations shown in Fig. 5.10 the following equation for calculating K_{3D} as a function of C/B ratio and friction angle φ has been developed for cohesionless soils:

$$K_{3D} = \frac{2.47 \cdot e^{-0.062\cdot\varphi}}{0.78 - (0.0375 \cdot \varphi) + (0.00039 \cdot \varphi^2) + C/B} \tag{5.4}$$

The good approximation of the numerical K_{3D} data by Eq. (5.4) is demonstrated by the curves in Fig. 5.11.

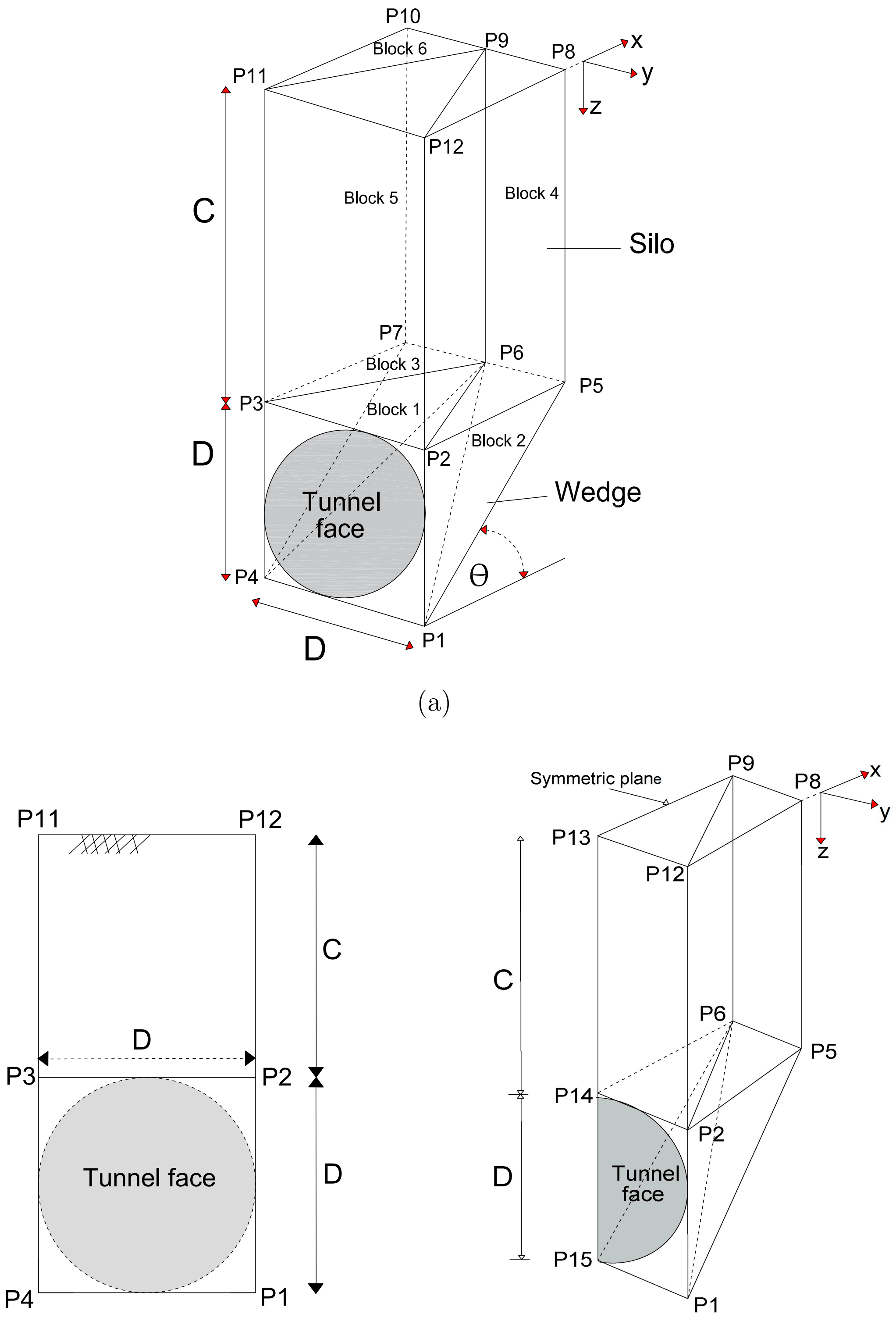
P10
Block 6
P9
P8
x
y
z
P11
P12
C
Block 5
Block 4
Silo
P7
Block 3
P6
P5
P3
Block 1
Block 2
D
P2
Tunnel face
Wedge
θ
P4
D
P1
P11
P12
C
D
P3
P2
Tunnel face
D
P4
P1
Symmetric plane
P9
P8
x
y
z
P13
P12
C
P6
P5
P14
P2
D
Tunnel face
P15
P1

(a)

(b)

(c)

Figure 5.8: KEM model (M2): (a) geometry of the failure mechanism; (b) geometry of the tunnel face; (c) half of the model

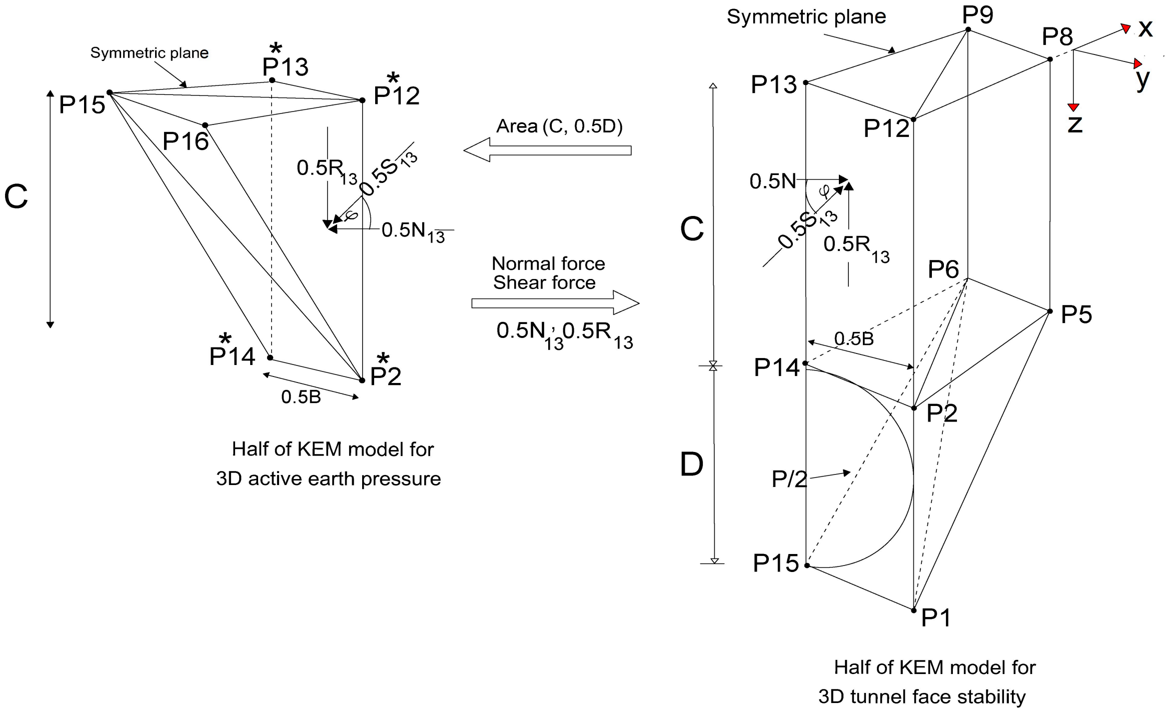
Symmetric plane
P13*
P12*
P15
P16
C
0.5R13
0.5S13
φ
0.5N13
P14*
P2*
0.5B
Half of KEM model for
3D active earth pressure
Area (C, 0.5D)
Normal force
Shear force
0.5N13, 0.5R13
Symmetric plane
P9
P8
x
y
z
P13
P12
0.5N
φ
0.5S13
0.5R13
C
P6
P5
P14
0.5B
P2
D
P/2
P15
P1
Half of KEM model for
3D tunnel face stability

Figure 5.9: Forces transferred from 3D active earth pressure model to tunnel face stability model (M2)

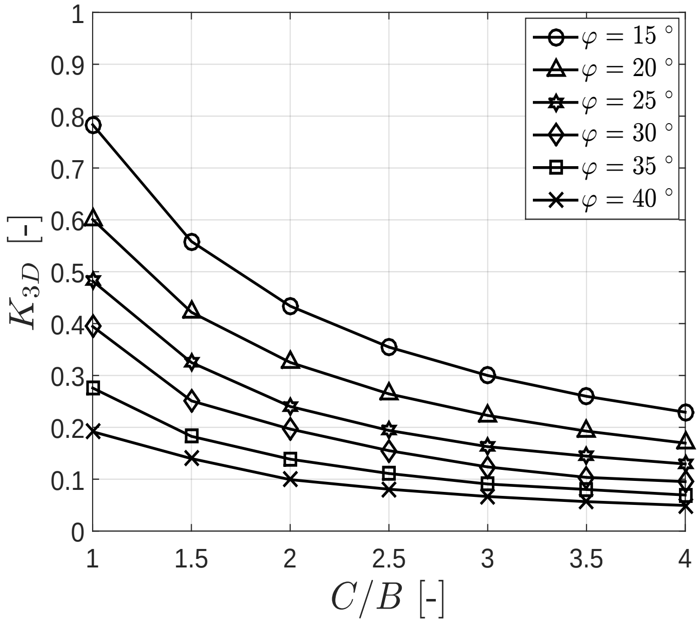

Figure 5.10: 3D lateral earth pressure coefficient (K_{3D}) as a function of C/D different friction angles (φ) used for KEM model (M2)

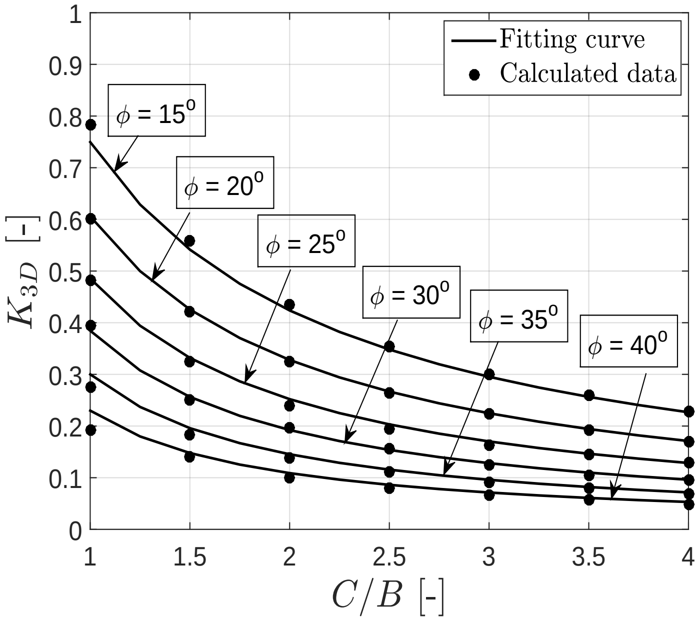

Figure 5.11: 3D lateral earth pressure coefficient (K_{3D}) obtained from the KEM simulations fitted by Eq. (5.4)

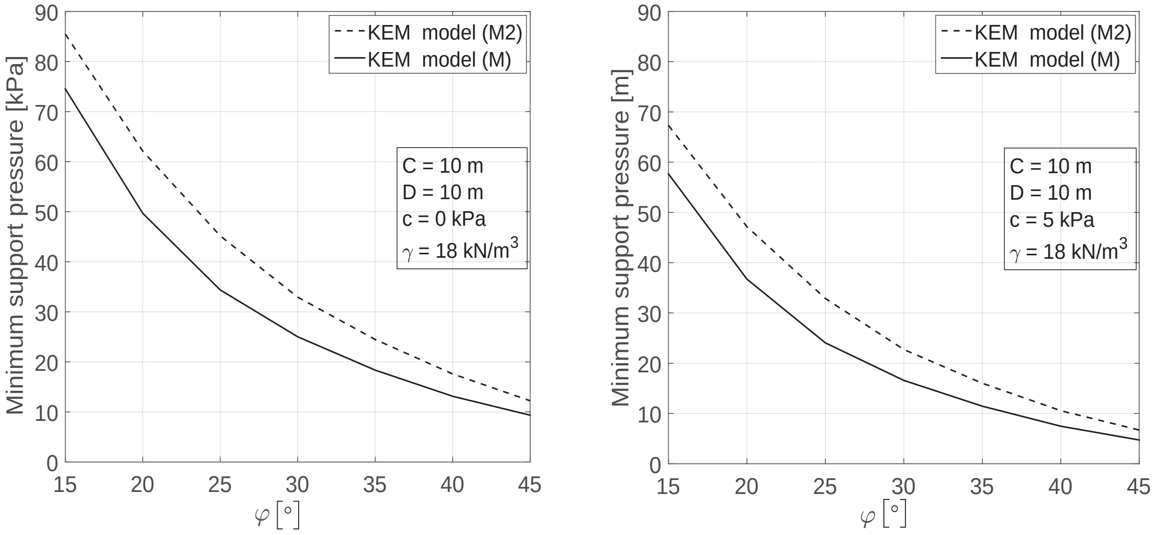

(a) (b)

Figure 5.12: Comparison of KEM model (M) with KEM model (M2) for (a) cohesionless soil and (b) frictional-cohesive soil

5.4 Comparison of KEM model (M) with KEM model (M2)

Fig. 5.12 presents a comparison between the results of KEM model (M) and KEM model (M2) results for frictional and frictional-cohesive soil. It can be concluded that KEM model (M2) delivers a larger in minimum support pressure. The increase of the minimum support pressure of KEM model (M2) with respect to KEM model (M) lies in the range 12 - 23 % in case of cohesionless soil and 14 - 25 % for frictional-cohesive soil.

5.5 Comparison with other existing approaches

5.5.1 Homogeneous soil

To evaluate the validity of KEM models (M and M2), the effect of friction angle (φ) and cohesion (c) on normalized support pressure ($p_u/(\gamma D)$) is investigated by these two models and compared with five models from the literature covering two different approaches, Limit Equilibrium Method (LEM) and Limit Analysis Method (LAM). The soil is assumed to be homogeneous. The dry unit weight is set to $\gamma = 18$ kN/m^3, the tunnel diameter $D = 10$ m and C/D ratio is assumed to be 1. The surcharge is neglected ($q = 0$ kPa).

Fig. 5.13 presents the relationship between the normalized support pressure ($p_u/(\gamma D)$) and normalized cohesion ($c/(\gamma D)$) for two different values of friction angle, $\varphi = 20^o$ and 40^o.

Fig. 5.13 shows that for $\varphi = 20^o$ and $\varphi = 40^o$, the slope of the line representing the solution of Krause (1987) is higher than that of the other solutions, indicating that cohesion has much more effect on the support pressure compared to the other approaches. In contrast, the slopes of the lines resulting from the solutions of Broere (2001), Anagnostou & Kovari (1994), Anagnostou (2012), KEM model (M) and KEM model (M2) are quite similar. Therefore, the effect of cohesion on the minimum support pressure is described in a similar way by all these models.

It can be seen in Fig. 5.13 that for $\varphi = 20^o$, the solution of Anagnostou & Kovari (1994) using limit equilibrium method predicts higher values $p_u/(\gamma D)$ than the other approaches. However, at $\varphi = 40^o$, the solution of Broere (2001) exceeds the solution of Anagnostou & Kovari (1994). This can be attributed to two reasons; firstly, the simplified way of considering the vertical stress distribution along the sides of the wedge, i.e. linear vertical

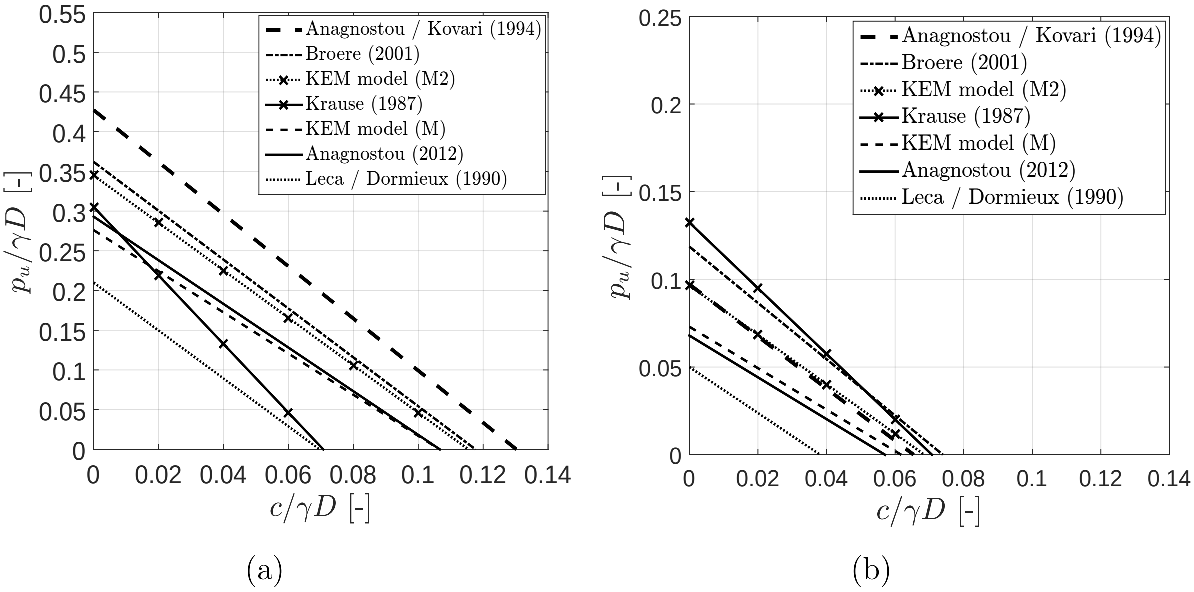

(a) (b)

Figure 5.13: Normalized support pressure ($p_u/(\gamma D)$) as function of normalized cohesion ($c/(\gamma D)$), comparison of results of KEM models (M1) and (M2) with other approaches from the literature: (a) $\varphi = 20^o$ and $C/D = 1$; (b) $\varphi = 40^o$ and $C/D = 1$

stress distribution in the model of Anagnostou & Kovari (1994). Secondly, for $\varphi > 35^o$ Anagnostou & Kovari (1994) assumed $K_{wedge} = 0.4$ which is higher than the value of set into approach by Broere (2001) ($K_{wedge} = K_0$). Consequently, in Anagnostou & Kovari (1994) model, the vertical stress and the frictional resistance acting on the wedge are considerably higher than the corresponding values used in the Broere (2001) model. Finally, at $\varphi = 40^o$, the combination of the two previous reasons leads to lower the minimum support pressures prediction by Anagnostou & Kovari (1994) model compared to the model of Broere (2001).

For $\varphi = 20^o$, the values of $p_u/(\gamma D)$ obtained from KEM model (M2) are close to the prediction by Broere (2001) model. The difference in $p_u/(\gamma D)$ between these two methods is less than 5 %. Meanwhile, for $\varphi = 40^o$, the values of $p_u/(\gamma D)$ obtained from the model of Anagnostou & Kovari (1994) and KEM model (M2) are almost identical.

According to Fig. 5.13, for both studied two friction angles ($\varphi = 20^o$ and 40^o), the results of Anagnostou (2012) which are based on the infinitesimally thin slices method and the results of KEM model (M) using a two-blocks mechanism are located between the results of KEM model (M2) and the upper bound solution of Leca & Dormieux (1990).

For both friction angles ($\varphi = 20^o$ and 40^o), the values of $p_u/(\gamma D)$ obtained from Leca & Dormieux (1990) using the upper bound method are clearly below the results given by

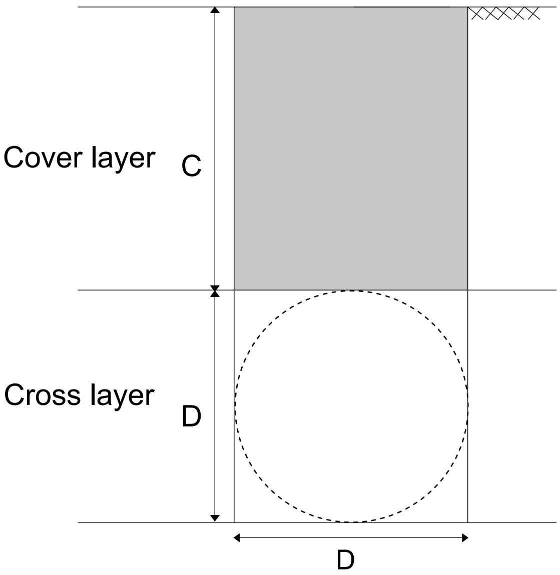

Figure 5.14: Model considering two layers of soil

the other approaches. This is due to that the shape of the tunnel face is considered as an ellipse inscribed to the circular tunnel face. Furthermore, the two-blocks mechanism given by Leca & Dormieux (1990) is constrained by the normality condition, required by plasticity theory. The velocity vector must enclose an angle φ with discontinuity surfaces along the sliding surfaces. However, this condition prevents the three-dimensional slip surfaces from developing more freely.

5.5.2 Layered soil

In this section, the tunnel face stability in layered soils is investigated using different approaches, the model considers two layers (cover and cross layer) of the soil is shown in Fig. 5.14. The cover and the cross layer are assumed to be located above the groundwater table. The soil strength parameters and geometry of the tunnel are described in Table 5.2.

The effect of the soil parameters of the cover layer on the minimum support pressure is investigated by varying the friction angle of the cover layer, while the soil properties of the cross layer are kept constant. The variation of the normalized minimum support pressure with the friction angle of the cover layer is shown in Fig. 5.15.

It is clear from Fig. 5.15 that the results obtained from the different approaches are quite different. It can be noticed that the wedge-silo models (Jancsecz & Steiner, 1994; Anagnostou & Kovari, 1994; Broere, 2001) give much larger support pressures than the KEM models (M and M2), the limit analysis models and the FELA models. The results of

Table 5.2: Soil parameters and tunnel geometry (soil with two layers)

Model description	Parameter	Value	Unit
Cover layer	Cover depth (C)	9	[m]
	Friction angle (φ)	15-45	[^{o}]
	Unit weight(γ)	18	[kN/m^3]
	Cohesion (c)	2.5	[kPa]
Cross layer	Tunnel diameter (D)	6	[m]
	Friction angle (φ)	20	[^{o}]
	Unit weight(γ)	18	[kN/m^3]
	Cohesion (c)	2.5	[kPa]

Han et al. (2016) are slightly below the upper and lower bound results of FELA. This can be attributed to the fact that the 3D failure mechanism of Han et al. (2016) is composed of five truncated cones which offers much more degrees of freedom. However, in the failure mechanism assumed by Han et al. (2016), the shape of the tunnel face is considered as an ellipse. This ellipse and the circular tunnel face do not have the same cross-sectional area. Furthermore, the soil arching effect above the cones is considered by a vertical force according to Janssen's silo theory. The results of KEM model (M2) are above the results of KEM model (M). In addition, the results obtained using KEM model (M) slightly exceed the results obtained using FELA upper and lower bound solutions. The upper bound solution of Tang et al. (2014) gives significantly smaller values than the other approaches. This can be explained by the fact that the upper bound solution of Tang et al. (2014) is based on the mechanism composed of two cones proposed by Leca & Dormieux (1990), which is restricted in the number of the degrees of freedom.

Furthermore, it can be seen from Fig. 5.15 that the minimum support pressure decreases with increasing friction angle in case of the upper bound solution of Han et al. (2016), both KEM models, the FELA results and the Anagnostou & Kovari (1994) model. The steepest trend is predicted by the model of Anagnostou & Kovari (1994). Surprisingly, applying the solution of Broere (2001), the minimum support pressure decreases up to a minimum value at $\varphi = 40^o$ before increasing again with further increase of φ. A similar trend is obtained from the approach of Jancsecz & Steiner (1994). In that case the minimum support pressure decreases slightly to the minimum value at $\varphi = 30^o$, while it increases subsequently.

The trends of the support pressure predicted by the wedge-silo models (Jancsecz & Steiner, 1994; Anagnostou & Kovari, 1994; Broere, 2001) can be explained as follows. From silo

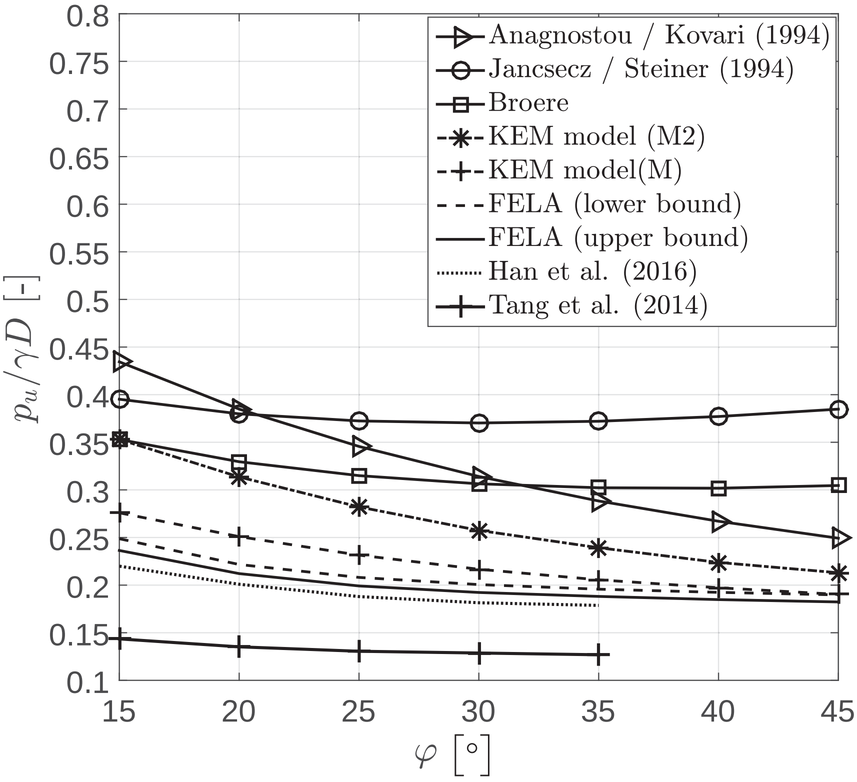

Figure 5.15: Minimum support pressure as a function of different friction angles

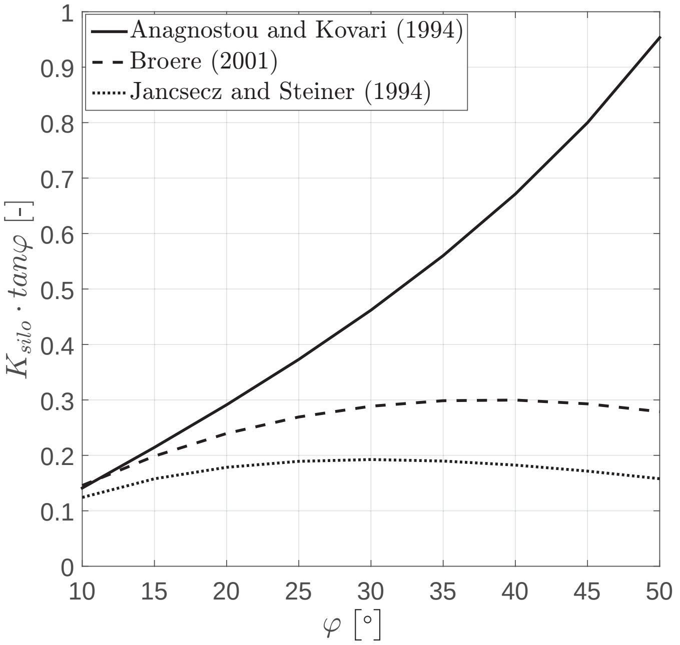

Figure 5.16: $K_{silo} \cdot \tan\varphi$ as a function of the friction angle of the cover layer obtained from different approaches

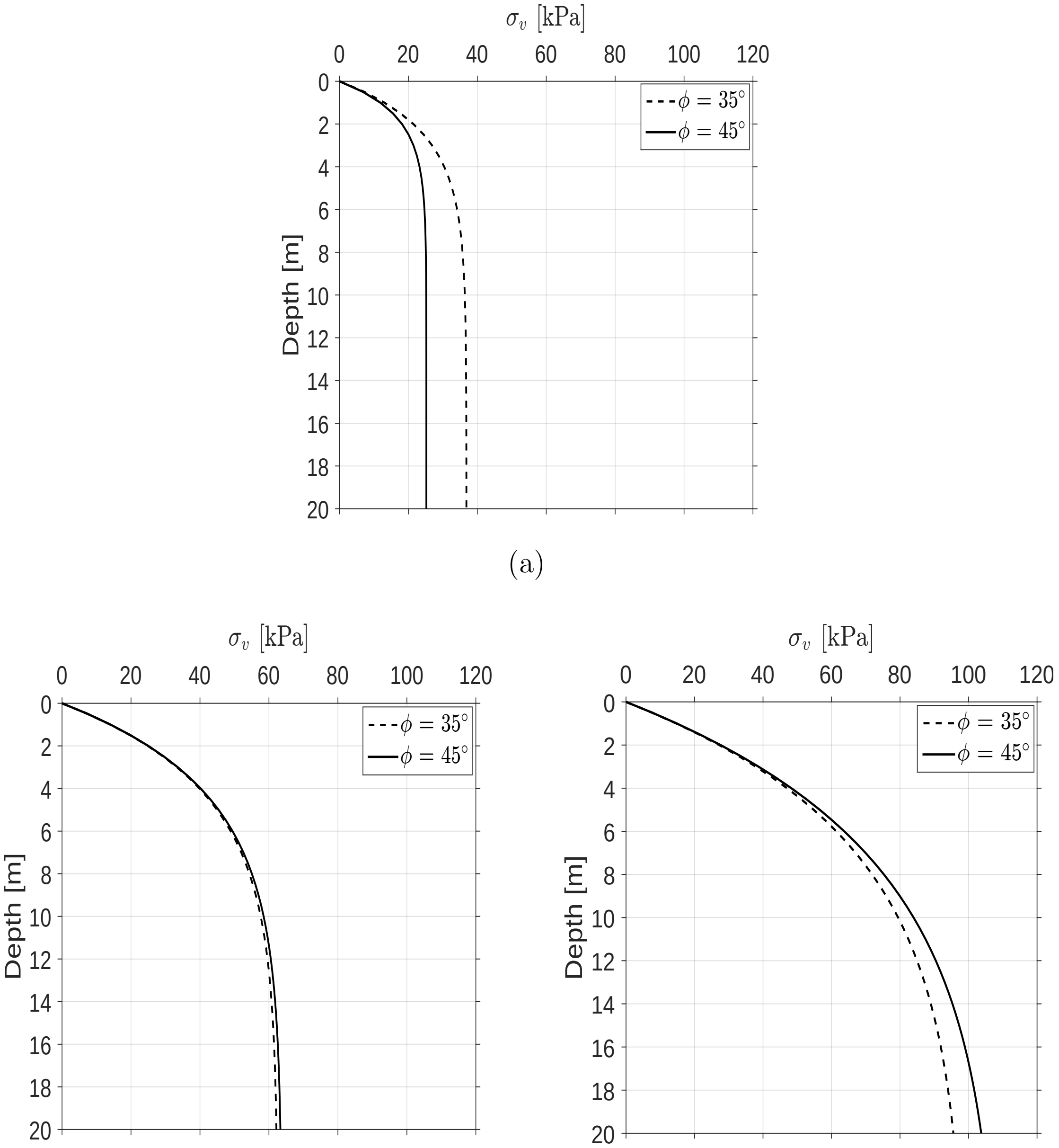

(a)

(b)

(c)

Figure 5.17: Vertical stress distribution in different models: (a) Anagnostou & Kovari (1994) model; (b) Broere (2001) model; (c) Jancsecz & Steiner (1994) model

theory (Eq. (2.13), Chapter 2), the value of vertical stress above the tunnel crown is mainly dependent on the value of $K_{silo}\cdot$ tanφ (for the same soil strength parameters). For the model of Anagnostou & Kovari (1994) model this value will be $0.8 \cdot \tan\varphi$, for the Broere (2001) solution it will be (1-sinφ)·tanφ, and for the Jancsecz & Steiner (1994) solution ($\tan^2(45 - \varphi/2)$)·tanφ. As shown in Fig. 5.16, the value of $K_{silo} \cdot \tan\varphi$ in the solution of Anagnostou & Kovari (1994) increases exponentially. According to the approach of Broere (2001), the value of $K_{silo}\cdot$ tanφ increases up to a maximum value at $\varphi = 40^o$ before it decreases again. The same trend is obtained for the equations of Jancsecz & Steiner (1994), where the maximum value is reached at $\varphi = 30^o$.

The effect of $K_{silo} \cdot \tan\varphi$ on the vertical stress distribution in the different model is shown in Fig. 5.17. From those diagrams one it conclude that in the models of Jancsecz & Steiner (1994) and Broere (2001), the vertical stress for $\varphi = 45^o$ is close or slightly higher than that for $\varphi = 35^o$ at any depth. In contrast, in the approach of Anagnostou & Kovari (1994), the vertical stress for $\varphi = 35^o$ is always higher than that for $\varphi = 45^o$.

Based on the previous results it can be concluded that for the set of soil parameters and geometry of the tunnel used in this study (see in Table 5.2) the approaches of Jancsecz & Steiner (1994) and Broere (2001) predict a trend of the minimum support pressure with friction angle which contradicts practical experience. The discrepancies between the support pressure predicted by the different approaches are obvious in Fig. 5.15.

5.6 Development of design equations based on KEM model (M2) simulations

Figs. 5.18 to 5.20 give the non-dimensional coefficients N_γ, N_c and N_q derived from simulations with the KEM model (M2) for different friction angles and C/D ratios. The results reflect the expected the decrease in N_γ, N_c and N_q values as friction angle increases for a constant C/D ratio. Table 5.3 provides the values of N_γ, N_c and N_q for different ranges of friction angle and C/D ratio. The results of N_q in fig 5.20and Table 5.3 show that the value of N_q becomes equal to zero for C/D ratios greater than or equal to 1.5 for any friction angle.

Based on a fitting of the data shown in Fig. 5.21, simple relationships for calculating N_γ, N_c and N_q have been developed as follows:

$$N_\gamma \approx a_3 \cdot (b_4)^{\tan\varphi} \quad (\varphi \geq 15^o) \tag{5.5}$$

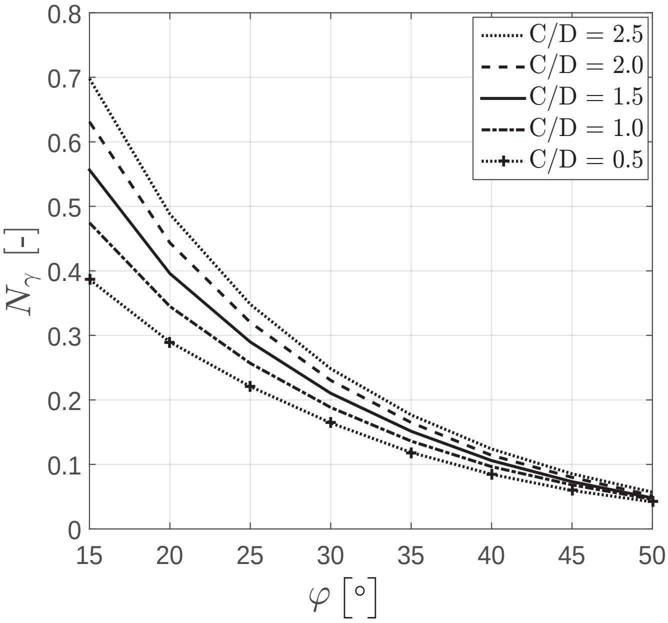

Figure 5.18: N_γ as function of the soil friction angle, KEM model (M2)

$$a_3 = 0.628 + 0.366 \cdot C/D \tag{5.6}$$

$$b_4 = 0.066 - 0.009 \cdot C/D \tag{5.7}$$

$$N_c \approx a_4 \cdot (\tan\varphi)^{-b_5} \qquad (\varphi \geq 15^o) \tag{5.8}$$

$$a_4 = 1.198 + 0.077 \cdot C/D \tag{5.9}$$

$$b_5 = 0.715 + 0.104 \cdot C/D \tag{5.10}$$

$$N_q \approx a_5 \cdot e^{-(b_6\ \cdot\ \tan\varphi)} \quad \text{(For C/D} \leq 1.5) \tag{5.11}$$

$$a_5 = 0.8265 - 0.4525 \cdot C/D \tag{5.12}$$

$$b_6 = 2.557 + 0.575 \cdot C/D \tag{5.13}$$

Fig. 5.21 shows the comparison between the values of N_γ, N_c and N_q obtained from the KEM simulations with those calculated from Eqs. (5.5) to (5.13), confirming the good agreement. For a practical application, the normalized support pressure $(p_u/(\gamma D))$ is plotted as a function of normalized cohesion $(c/(\gamma D))$ for different friction angles in Fig. 5.22.

5.7 Open-face tunneling

The conventional methods in tunnel construction can be categorized as closed face-tunneling and open face-tunneling (Chapman et al., 2017). In closed face-tunneling, a

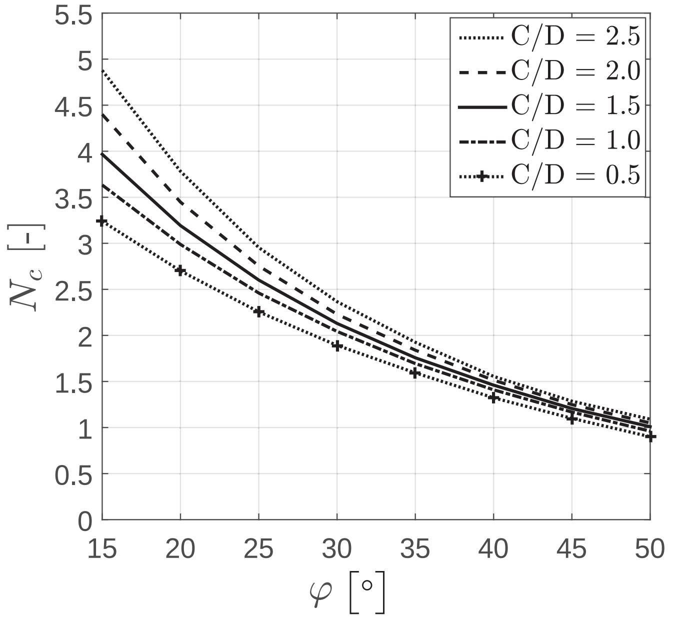

Figure 5.19: N_c as function of the soil friction angle, KEM model (M2)

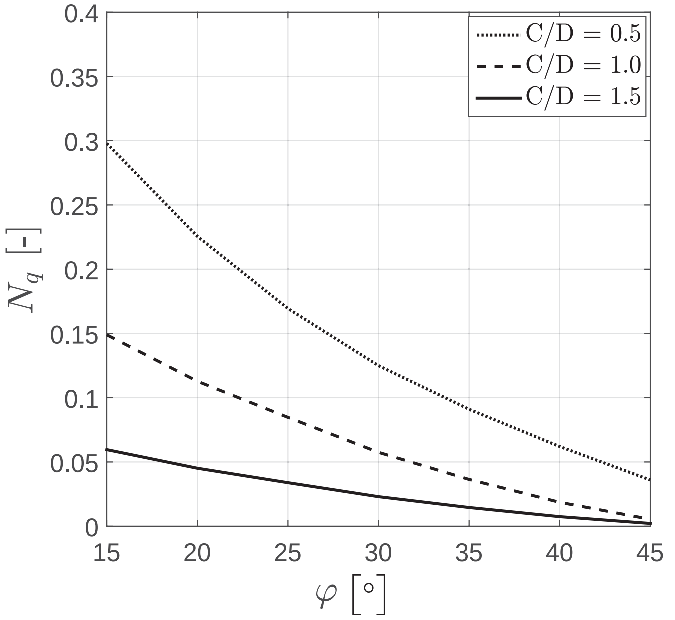

Figure 5.20: N_q as function of the soil friction angle, KEM model (M2)

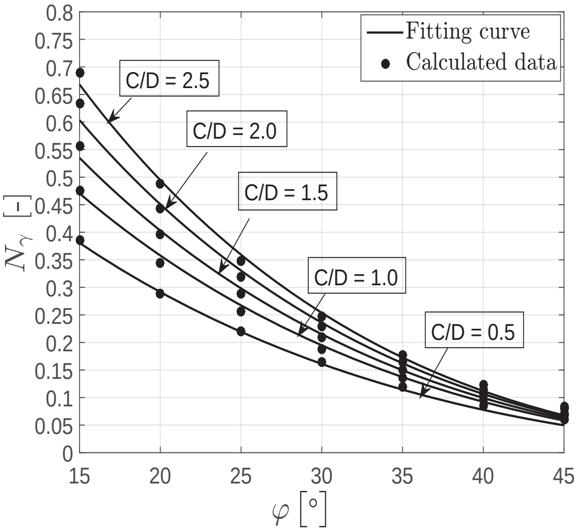

(a)

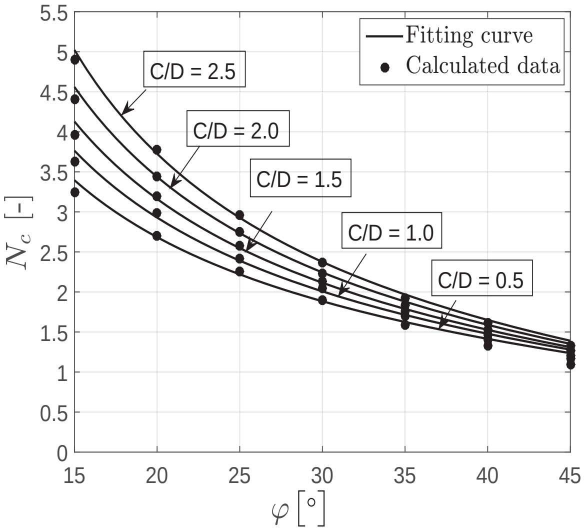

(b)

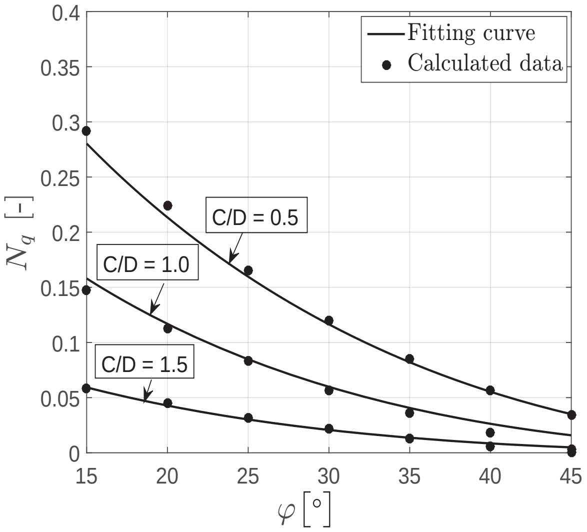

(c)

Figure 5.21: Fitting curves for the approximated equations of (a) fitting curve for N_γ, (b) fitting curve for N_c and (c) fitting curve for N_q

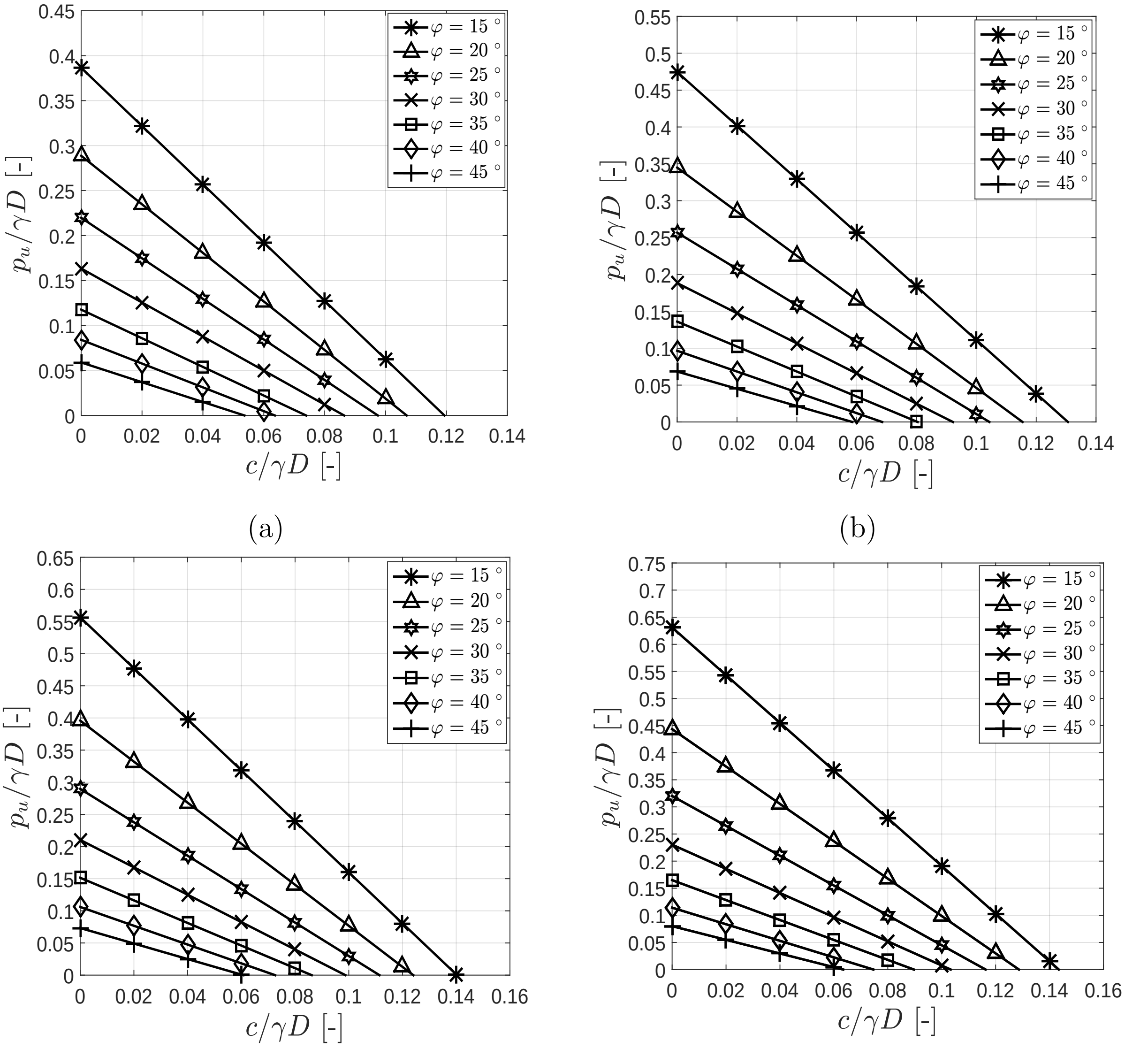

(a)

(b)

(c)

(d)

Figure 5.22: Design charts for the minimum support pressure for KEM model (M2) ($q =$ 0 kPa): (a) $C/D = 0.5$; (b) $C/D = 1$; (c) $C/D = 1.5$; (d) $C/D = 2$

Table 5.3: N_γ, N_c and N_q for various internal friction angles and C/D ratios for KEM model (M2)

	N_γ					N_c					N_q				
								C/D							
φ	0.5	1	1.5	2	2.5	0.5	1	1.5	2	2.5	0.5	1	1.5	2	2.5
15^o	0.386	0.475	0.557	0.633	0.698	3.239	3.633	3.967	4.401	4.901	0.292	0.147	0.058	0.000	0.000
20^o	0.289	0.345	0.396	0.443	0.488	2.701	2.988	3.192	3.448	3.782	0.224	0.113	0.045	0.000	0.000
25^o	0.221	0.257	0.289	0.320	0.348	2.256	2.460	2.601	2.754	2.954	0.165	0.083	0.032	0.000	0.000
30^o	0.164	0.188	0.210	0.230	0.248	1.892	2.043	2.130	2.229	3.367	0.120	0.057	0.020	0.000	0.000
35^o	0.119	0.136	0.151	0.165	0.177	1.593	1.694	1.757	1.840	1.926	0.090	0.036	0.014	0.000	0.000
40^o	0.085	0.097	0.106	0.114	0.124	1.323	1.410	1.462	1.529	1.612	0.059	0.018	0.006	0.000	0.000
45^o	0.06	0.068	0.073	0.081	0.085	1.099	1.168	1.207	1.262	1.333	0.034	0.003	0.000	0.000	0.000
50^o	0.042	0.046	0.048	0.051	0.057	0.900	0.960	1.010	106	1.130	0.000	0.000	0.000	0.000	0.000

face support pressure is needed to stabilize the tunnel face (non-stable condition). For open face-tunneling, no face support pressure is needed (stable condition) because the soil shear strength is high enough to ensure stability of the tunnel face.

5.7.1 Factor of safety for open-face tunneling

In this section, the Strength Reduction Method (SRM) (Bishop, 1955) is adopted to calculate safety factor (Fs) in open-face tunneling. The safety factor is defined as the ratio of actual shear strength (c and φ) to the reduced or increased shear strength (c_e and φ_e) at failure. The material strength parameters are simultaneously reduced or increased according to Eqs. (5.14) and (5.15).

$$c_e = c/Fs \tag{5.14}$$

$$\varphi_e = \arctan\left(\frac{\tan\varphi}{Fs}\right) \tag{5.15}$$

where, Fs is the strength reduction coefficient, which is identical to the safety factor.

The strength reduction coefficient or safety factor, respectively, can be obtained by updating c_e and φ_e until the minimum support pressure is equal to zero. The stable condition (zero support pressure) is represented by the following equation:

$$\gamma \cdot D \cdot N_\gamma - c \cdot N_c + q \cdot N_q = 0 \tag{5.16}$$

For the stable tunnel face condition, Eq. (5.16) is obtained from Eq. (5.16):

$$\lambda = \frac{N_\gamma}{N_c} = \frac{c_e}{D \cdot \gamma} \tag{5.17}$$

Generally, the non-dimensional coefficients N_γ and N_c are dependent on friction angle φ. Therefore, λ can be reformulated to be a function of $\arctan(\frac{\tan\varphi}{Fs})$.

$$\lambda = f\left(\arctan\left(\frac{\tan\varphi}{Fs}\right)\right) = \frac{c}{Fs \cdot D \cdot \gamma} \tag{5.18}$$

As an example, Krause (1987), Vermeer et al. (2002) and Anagnostou (2012) proposed the following non-dimensional coefficients N_γ and N_c:

$$N_\gamma = \frac{1}{9\ \tan\varphi} \qquad N_c = \frac{\pi}{2\ \tan\varphi} \qquad \text{(Krause, 1987)} \tag{5.19}$$

$$N_\gamma = \frac{1}{9\ \tan\varphi} - 0.05 \qquad N_c = \frac{1}{\tan\varphi} \qquad \text{(Vermeer et al., 2002)} \tag{5.20}$$

$$N_\gamma = \frac{0.05}{\tan\varphi^{1.75}} \qquad N_c = \frac{1}{\tan\varphi} \qquad \text{(Anagnostou, 2012)} \tag{5.21}$$

Using Eq. (5.15), the values of safety factor based on the models of Krause (1987), Vermeer et al. (2002) and Anagnostou (2012) as well as KEM (M) and KEM (M2) models can be obtained as follows:

$$Fs = \frac{9 \cdot c \cdot \pi}{2 \cdot D \cdot \gamma} \qquad \text{For Krause (1987) model} \tag{5.22}$$

$$Fs = \frac{9 \cdot c}{D \cdot \gamma} + 0.45 \cdot \tan\varphi \qquad \text{For Vermeer et al. (2002) model} \tag{5.23}$$

$$Fs = \left(\frac{c \cdot \tan\varphi^{0.75}}{0.05 \cdot D \cdot \gamma}\right)^{\frac{1}{1.75}} \qquad \text{For Anagnostou (2012) model} \tag{5.24}$$

$$Fs = \left(\frac{c \cdot \tan\varphi^{(b_1 - b_2)}}{a_1 \cdot D \cdot \gamma}\right)^{\frac{1}{(1+b_1-b_2)}} \qquad \text{For KEM model (M)} \tag{5.25}$$

where

$$a_1 = 0.055 + 0.007 \cdot C/D \tag{5.26}$$

$$b_1 = 1.50 \cdot (C/D - 0.37)^{0.044} \tag{5.27}$$

$$b_2 = 0.77 + 0.17 \cdot C/D \tag{5.28}$$

$$Fs = \left(\frac{a_4 \cdot c \cdot \tan\varphi^{(-b_5)}}{a_3 \cdot D \cdot \gamma \cdot b_4^{(\frac{\tan\varphi}{Fs})}}\right)^{\frac{1}{(1-b_4)}} \qquad \text{For KEM model (M2)} \tag{5.29}$$

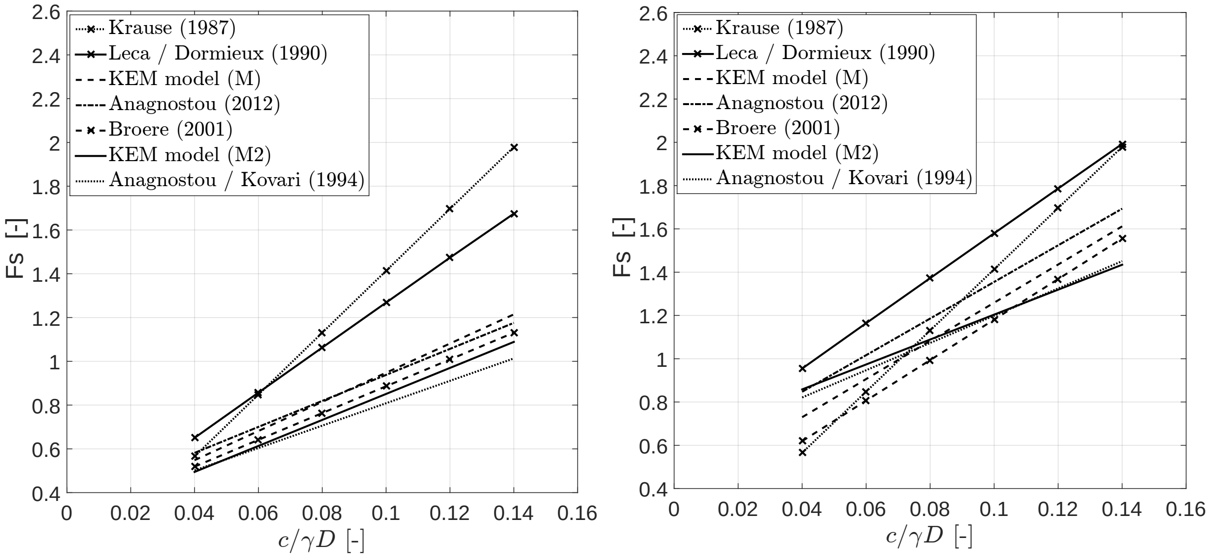

(a) (b)

Figure 5.23: Safety factor (F_s) as function of normalized cohesion ($c/(\gamma D)$) Comparison of different approaches for (a) $\varphi = 20^o$, $C/D = 1$ and (b) $\varphi = 40^o$, $C/D = 1$

where

$$a_3 = 0.628 + 0.366 \cdot C/D \tag{5.30}$$

$$b_4 = 0.066 - 0.009 \cdot C/D \tag{5.31}$$

$$a_4 = 1.198 + 0.077 \cdot C/D \tag{5.32}$$

$$b_5 = 0.715 + 0.104 \cdot C/D \tag{5.33}$$

For an unstable tunnel face $Fs < 1$, for the critical state $Fs = 1$ and for the stable tunnel face $Fs > 1$ holds.

Fig. 5.23 shows the safety factor as a function of the normalized cohesion ($c/\gamma D$) calculated by different approaches. In Fig. 5.23, for the same C/D, the safety factor increases with the increase of cohesion and friction angle with exception of the solution by Krause (1987). In the model of Krause (1987), the friction angle has no effect on the safety factor. The computed λ takes the same value for any friction angle (see Eq. (5.22)).

By examining the trend of the data in Fig. 5.23, it appears that the safety factor increases linearly with the normalized cohesion. At $\varphi = 20^o$, the model of Krause (1987) provides the highest values of safety factor for almost all values of the cohesion factor. In contrast, the model of Anagnostou & Kovari (1994) gives lower safety factor than the other models. The safety factor calculated by KEM model (M2) is in good agreement with the results

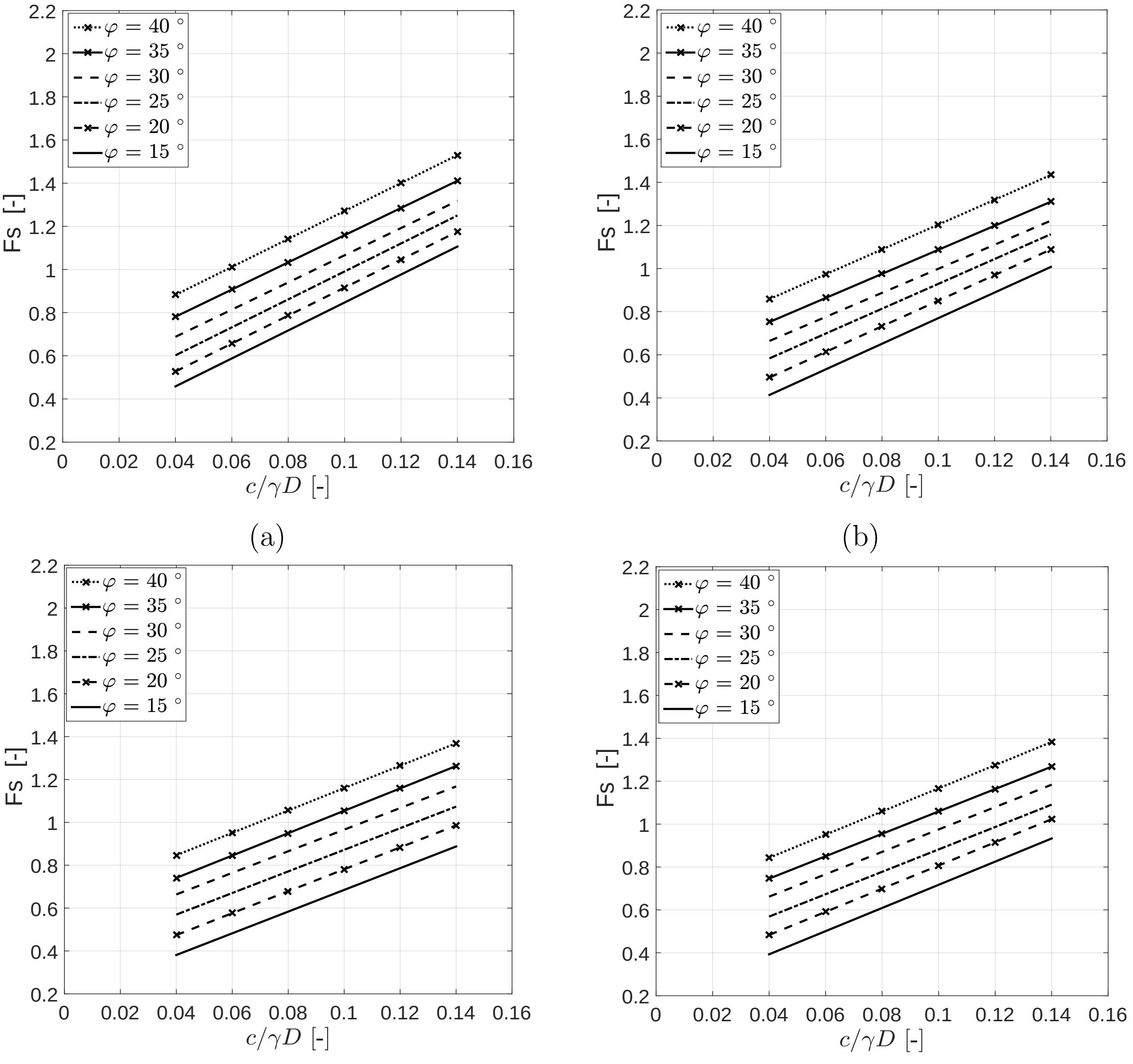

(a) (b) (c) (d)

Figure 5.24: Safety factor as function of normalized cohesion for different friction angles ($q = 0$ kPa) for KEM model (M2): (a) $C/D = 0.5$; (b) $C/D = 1$; (c) $C/D = 1.5$; (d) $C/D = 2$

of Broere (2001) and close to the Fs values obtained from the approach of Anagnostou (2012).

At $\varphi = 40^o$, the approach of Leca & Dormieux (1990) almost achieves stable tunnel face. The relationships between safety factor and cohesion factor obtained from KEM model (M2), KEM model (M) and the solution of Anagnostou & Kovari (1994) intersect at about $Fs = 1$. Beyond that point the KEM model (M) gives higher factor of safety than KEM model (M2) and the approach of Anagnostou & Kovari (1994). The safety factors according to Anagnostou (2012) are slightly larger than those from KEM model (M). For $c/(\gamma D) \geq 0.075$, Anagnostou & Kovari (1994) and KEM model (M2) attain a factor of safety of one or greater.

From the previous results, it can be concluded that as the friction angle increases, the normalized cohesion ($c/(\gamma D)$) for achieving a stable tunnel face decreases. Generally, the increase in friction angle of the soil results in an increase in the safety factor.

A comparison between KEM model (M2) and other existing approaches shows that the factor of safety derived from KEM model (M2) is close to the values obtained from wedge-silo model.

For practical purpose, design charts have been provided in Fig. 5.24, showing the safety factor (Fs) as a function of the normalized cohesion ($c/\gamma D$) for different values of friction angle φ and C/D ratio.

5.7.2 Maximum tunnel diameter for open-face tunneling

Eq. 5.16 could be reformulated to calculate the maximum tunnel diameter for open-face tunneling depending on the soil strength parameters and the surface load. The maximum tunnel diameter (D_{max}) can be obtained as follows:

1. For $q = 0$

$$D_{max} = \frac{c}{\gamma} \cdot \frac{N_c}{N_\gamma} \tag{5.34}$$

2. For $q > 0$

$$D_{max} = \frac{c \cdot N_c - q \cdot N_q}{\gamma \cdot N_\gamma} \tag{5.35}$$

Eqs. (5.34) and (5.35) demonstrate that the maximum diameter (D_{max}) in open face tunneling is linearly related to the cohesion.

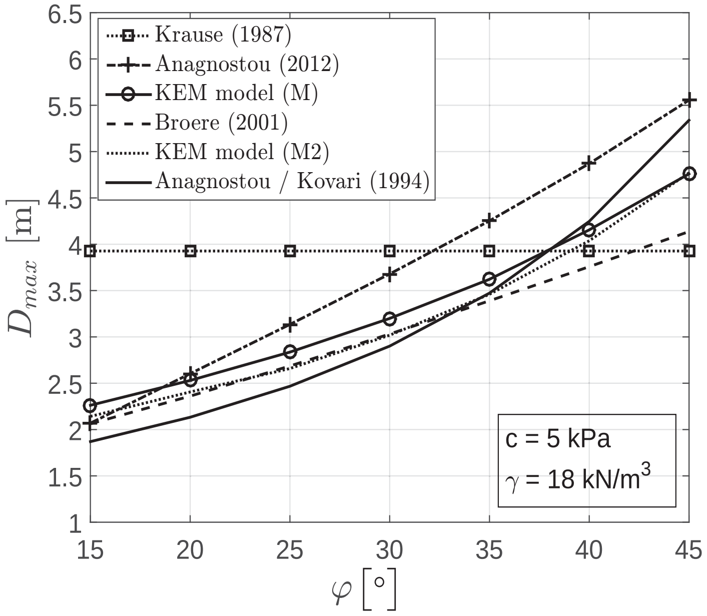

Figure 5.25: Maximum diameter (D_{max}) in open face tunneling with q = 0 kPa

Using Eq. (5.34) for $q = 0$ kPa, the maximum tunnel diameter (D_{max}) calculated by Krause (1987), Vermeer et al. (2002), Anagnostou (2012) as well as KEM (M) and KEM (M2) models are as follows:

$$D_{max} = \frac{4.5 \cdot c \cdot \pi}{\gamma} \qquad \text{For Krause (1987) model} \quad (5.36)$$

$$D_{max} = \frac{9 \cdot c}{\gamma \cdot [1 - (0.45 \cdot \tan\varphi)]} \qquad \text{For Vermeer et al. (2002) model} \quad (5.37)$$

$$D_{max} = \frac{20 \cdot c \cdot \tan\varphi^{0.75}}{\gamma} \qquad \text{For Anagnostou (2012) model} \quad (5.38)$$

$$D_{max} = \frac{c \cdot \tan\varphi^{(b_1 - b_2)}}{a_1 \cdot \gamma} \qquad \text{For KEM model (M)} \quad (5.39)$$

where

$$a_1 = 0.055 + 0.007 \cdot C/D \qquad (5.40)$$

$$b_1 = 1.50 \cdot (C/D - 0.37)^{0.044} \qquad (5.41)$$

$$b_2 = 0.77 + 0.17 \cdot C/D \qquad (5.42)$$

$$D_{max} = \frac{a_4 \cdot c \cdot \tan\varphi^{-b_5}}{a_3 \cdot \gamma \cdot {b_4}^{(\tan\varphi)}} \qquad \text{For KEM model (M2)} (5.43)$$

where

$$a_3 = 0.628 + 0.366 \cdot C/D \qquad (5.44)$$

$$b_4 = 0.066 - 0.009 \cdot C/D \qquad (5.45)$$

$$a_4 = 1.198 + 0.077 \cdot C/D \tag{5.46}$$

$$b_5 = 0.715 + 0.104 \cdot C/D \tag{5.47}$$

To examine the validity of KEM model (M) and KEM model (M2) results, Fig. 5.25 shows a comparison of the values of the maximum tunnel diameter with the results given by five different approaches for $C/D = 1$ and friction angles φ varying from 15^o to 45^o. The comparison shows that the results of KEM model (M2) are close to the results of Broere (2001). In addition, the maximum difference between KEM model (M) and KEM model (M2) does not exceed 5 % for $\varphi > 20^o$. The maximum tunnel diameter given by the solution of Anagnostou (2012) is larger than those predicted by the other approaches. Meanwhile, the model of Krause (1987) predicts a maximum tunnel diameter which is independent of the friction angles.

5.8 Practical examples

5.8.1 Closed-face tunneling

5.8.1.1 Determining the minimum support pressure

A tunnel boring machine (TBM) has a diameter $D = 8$ m and is buried at a cover depth $C = 12$ m in dry frictional-cohesive soil with $\gamma = 18$ kN/m^3, $\varphi = 25^o$ and $c = 7$ kPa. No surcharge pressure has to be considered. The safety factor is assumed to be 1. The following two steps can be used to determine the minimum support pressure for preventing the collapse of the tunnel face.

1. Calculating the dimensionless ratios $C/D = 12/8 = 1.5$ and $c/(\gamma D) = 7/(18 \cdot 8)$. C/D $=$ 1.5, $\varphi = 25^o$ and $c/(\gamma D) = 0.049$, Fig 5.22 (c) is applied. From Fig 5.22 (c), it is found that $p_u/(\gamma D) = 0.163$. Then, the minimum support pressure can be computed as $p_u = 8 \cdot 0.163 \cdot 18 = 23.5$ kPa.

5.8.1.2 Determination of maximum cover depth

A tunnel with $D = 10$ m is proposed to be excavated in dry frictional-cohesive soil with $\gamma = 18$ kN/m^3, $\varphi = 15^o$ and $c = 5$ kPa. The proposed TBM has the capacity to provide a support pressure of 75 kPa, while the surface surcharge pressure is 0 kPa. The safety factor is assumed to be 1. The following procedures can be used for calculating the maximum cover depth to maintain stability of the tunnel face.

1. Calculating dimensionless ratios $p_u/(\gamma D) = 75/(18{\cdot}10) = 0.417$ and $c/(\gamma D) = 5/(18{\cdot}10) = 0.028$.
2. From Fig 5.22 (b and c) with $p_u/(\gamma D) = 0.417$, $c/(\gamma D) = 0.028$ and $\varphi = 15^o$, it can be found that the maximum possible cover depth lies between $C = 1.5D = 1.5$ m and $C = 1.0D = 10$ m. Using Eqs. (5.5) and (5.8) with trial and error method, the maximum cover depth ratio (C/D) is approximately calculated. The obtained value $C/D = 1.23$ corresponds to, $C = 12.3$ m.

The previous example can be used in a similar manner with the same procedure to calculate the maximum tunnel diameter (D) for a given cover depth (C).

5.8.2 Open-face tunneling

5.8.2.1 Determination of the safety factor

It is proposed to to excavate a shallow tunnel in dry homogenous frictional-cohesive soil. The soil properties are $\gamma = 18$ kN/m^3, $\varphi = 30^o$, and $c = 6$ kPa. No surcharge pressure has to be taken into account. The cover above the tunnel is $C = 10$ m and the diameter of the tunnel is $D = 5$ m. The designer should determine the factor of safety for open-face tunneling (no tunnel face support pressure). Referring to Eq. (5.29), the minimum factor of safety (Fs) is obtained as 1.2.

5.8.2.2 Determination of the maximum tunnel diameter

It is proposed to excavate a shallow tunnel through dry homogenous frictional-cohesive soil. the soil properties are $\gamma = 18$ kN/m^3, $\varphi = 35^o$, $c = 8$ kPa, and $q = 0$ kPa. The cover above the tunnel (C) is 10 m thick. The designer should determine the maximum diameter for open-face tunneling.

1. From Table 5.3 and Eq. (5.34), the maximum tunnel diameter can be calculated for different C/D (0.5, 1, 1.5, 2 and 2.5) with the known data, $\gamma = 18$ kN/m^3, $\varphi = 35^o$ and $c = 8$ kPa.
2. For different C/D, it is found that the maximum tunnel diameter D_{max} is 4.95 m when $C/D = 2$.

5.9 Summary

Based on the two-blocks failure mechanism considered in KEM model (M), two different modified failure mechanisms are studied using KEM to estimate the minimum support pressure of the tunnel face. The first modified KEM model (M1) is composed of five blocks. The second modified KEM model (M2) consists of six blocks. The modified failure mechanism (M2) improves significantly the two-blocks mechanism (M) in terms of the minimum support pressure. In addition, the modified model (M1) leads to a slight improvement in the minimum support pressure for frictional and frictional-cohesive soil.

For the purpose of verification, the results proposed by KEM model (M2) are compared with the results of KEM model (M) and other solutions available from the literature in the form of dimensionless design charts. The results obtained by KEM model (M2) provide a higher minimum support pressure than KEM model (M) and are close to the minimum support pressure calculated by wedge-silo models (Anagnostou & Kovari, 1994; Broere, 2001).

KEM model (M2) has been also used to study the tunnel face stability in a ground composed of two layers. Also in that case a comparative study was conducted in which the results of KEM model (M2) were confronted with other models from literature, as well as with the upper and lower bound solutions from FELA. The values of the minimum support pressure predicted by KEM model (M2) were higher than those from FELA other the upper bound solutions.

For an open-face tunneling, the factor of safety against a collapse of the tunnel face was calculated using the strength reduction technique. A comparisons between the factor of safety obtained from KEM model (M2) and other existing approaches is presented.

Furthermore, for open-face tunneling without applying the support pressure, a formula for the maximum diameter of the tunnel is presented. The results for the maximum tunnel diameter calculated with KEM model (M2) are verified against the results from different approaches in the literature.

On the basis of the results taken from the performed parametric analysis with KEM model (M2), a number of design charts and formulas have been proposed for a practical application in tunnel face stability problems.

6 Effect of excess pore pressure on the stability of the tunnel face

6.1 Introduction

Slurry tunnel boring machine are widely used for excavating and supporting the tunnel face. In case of a slurry tunnel boring machine, the required support pressure is provided by a pressurized mixture of bentonite and water. Because the pressure of the supporting mixture is higher than the hydrostatic pore pressure, the bentonite slurry tends to infiltrate into the soil at the front of the tunnel face.

According to Maidl et al. (2012), two infiltration mechanisms are possible. Firstly, in high permeability soils or when the shear resistance of the slurry is low, the slurry significantly infiltrates into the soil and the bentonite does not form a filter cake (penetration mechanism), see Fig. 6.1. Secondly, in a low permeability soil, the bentonite forms a thin impermeable filter cake at the front of the tunnel face acting as an impermeable membrane (membrane mechanism).

The penetration of the slurry into the soil can be distinguished into two processes (Talmon et al., 2013): mud spurt and filter cake formation. When mud spurt starts, the slurry (water with bentonite) penetrates into the soil. After some time, the water is squeezed out of the slurry, leaving bentonite particles consolidated in pores of the soil and an external filter cake is formed.

During the drilling phase of the slurry shield, the filter cake is continuously removed by the cutting tools of the TBM. Within the excavation process, the pore water is displaced leading to excess pore pressure at the front of the tunnel. When the slurry shield is in stand-still phase, the cutter head rotation is stopped and the pressure in the excavation chamber is constant resulting in the formation of a filter cake. This filter cake limits the filtration and thus the pore pressure on the outer side of the filter cake decreases with time until it becomes equal to the hydrostatic pore pressure.

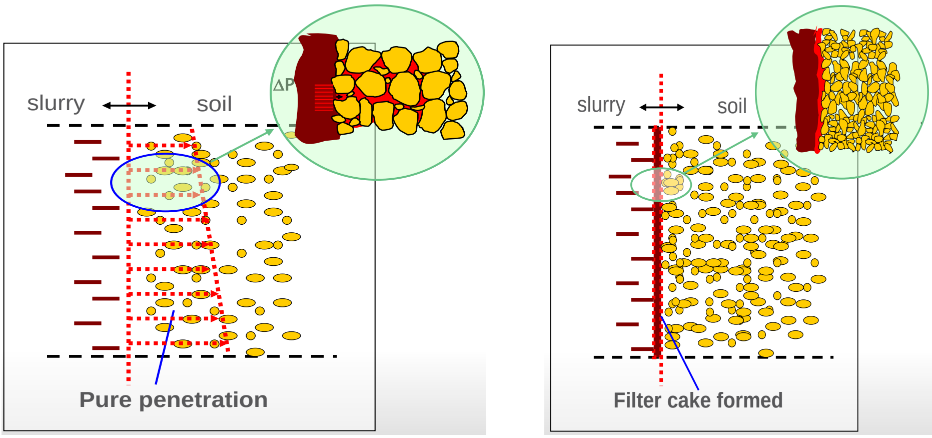
slurry
soil
ΔP
Pure penetration
slurry
soil
Filter cake formed

(a) (b)

Figure 6.1: Infiltration mechanisms, Maidl et al. (2012): (a) penetration mechanism; (b) membrane mechanism

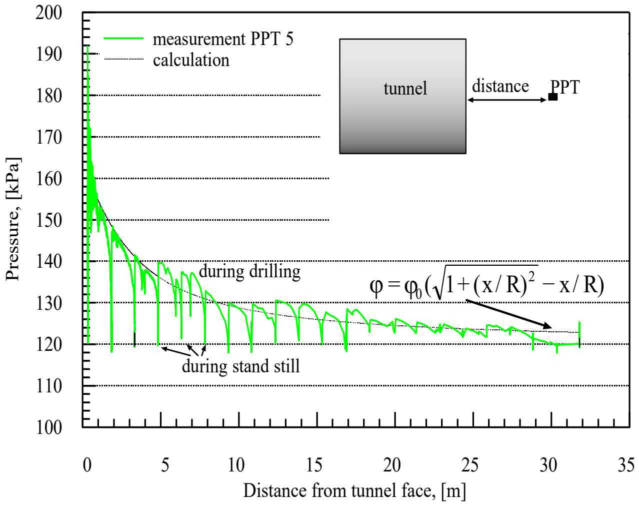

Figure 6.2: Pore pressure measured in the tunnel axis as a function of the distance to the slurry shield, data from Heinenoord tunnel, Bezuijen (2002)

The change of pore water pressure during excavation of 2nd Heinenoord-tunnel was presented by Bezuijen (2002), see Fig. 6.2. The pore pressure transducers (PPTs) were installed in the tunnel track and used until their destruction. Fig. 6.2 presents the support pressure as a function of the actual distance between the position of the transducer an the tunnel face. As it can be seen from the measurements, when the drilling phase starts, the pore water pressure increases above the hydrostatic pore pressure, whereas during the stand-still phase the pore water pressure decreases to the hydrostatic pore pressure. The closer the tunnel face is to the pressure transducer, the larger is the increase of pore pressure during the drilling phase.

To predict the development excess pore pressure at the front of the tunnel face in saturated sand, some analytical solutions have been developed (e.g., Broere, 2001; Bezuijen, 2002).

The excess pore pressure at the front of the tunnel face is associated with a hydraulic gradient between the mixing chamber and the surrounding soil of the tunnel. The hydraulic gradient leads to a fluid flow from the the tunnel face. This fluid flow changes the effective stress state resulting in lower effective stress and thus lower shear strength in the soil.

In this chapter, the influence of the increase or decrease of pore pressures on the minimum support pressure during tunnel excavation will be discussed in terms of effective and total support pressure. The calculation procedure will be elaborated by implementing the two solutions proposed by Bezuijen et al. (2016) in KEM (M2) model as well as in the models of Horn (1961), Anagnostou & Kovari (1994) and Broere (2001).

6.2 Stresses in soil under hydrostatic conditions

This section reviews briefly the key aspects related to the total stress, the pore water pressure and the effective stress in soils, see Fig. 6.3.

In homogenous saturated soil, the vertical total stress $\sigma_v(h)$ at depth z is obtained by integrating the density ϱ of the soil and water above the depth h multiplied by the gravitational acceleration:

$$\sigma_v(h) = \int_0^h \rho g \, dz \tag{6.1}$$

If ρg remains constant throughout the soil, then

$$\sigma_v(h) = \rho g h = \gamma_{sat} h \tag{6.2}$$

where γ_{sat} is the weight of the saturated soil per unit volume and h is the depth below the ground surface.

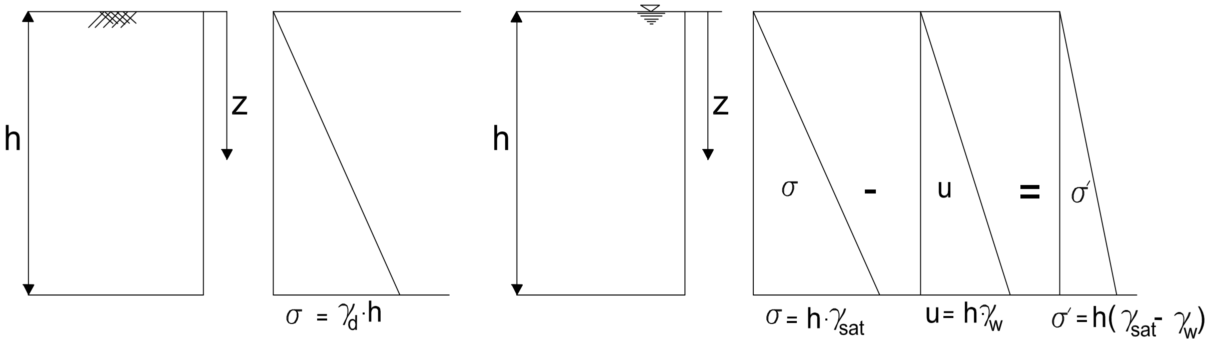

(a) (b)

Figure 6.3: Distribution of total stress, pore water pressure and effective stress with depth: (a) dry soil; (b) saturated soil

If ground water table is at the ground surface, the hydrostatic pore pressure u at depth h below the free surface can be obtained as:

$$u = \gamma_w \int_0^h dz = \gamma_w h \tag{6.3}$$

The effective vertical stress is the difference between the total vertical stress and the hydrostatic pore pressure:

$$\sigma'_v(h) = \sigma_v - u(h) = \gamma_{sat} h - \gamma_w h = \gamma' h \tag{6.4}$$

where γ' is the buoyant unit weight of the soil.

6.3 Safety factors

The soil properties such as unit weight and shear strength are determined from laboratory tests or using some empirical relationships which introduces uncertainties. The purpose of safety factors is to take into account the uncertainties in the value of the design loads and the soil properties. The safety factors for tunnels projects are regulated in German code (ZTV, 2012) "Technical contract terms and policies for civil engineering works, tunneling".

By multiplying the support forces counteracting earth and pore pressures by partial safety factors, the design value of the total force to be applied on the TBM face (P) is obtained according to Eq. (6.5):

$$P = \eta_e \cdot P_e + \eta_w \cdot P_w \tag{6.5}$$

P_e is the support force balancing the earth pressure, P_w the support force counteracting the pore pressure, η_e the safety factor for earth pressure and η_w the safety factor for water pressure. German code (ZTV, 2012) suggests η_e and η_w to be 1.5 and 1.05, respectively. In addition, German code (ZTV, 2012) recommends that for calculating the operational face pressure using the slurry shield machine, a safety margin of 10 kPa above the pressure obtained from Eq. (6.5) must be considered.

6.4 Blow out

When the support pressure is too high, the soil is heaved in front of the tunnel face. Such failure is often classified as blow out. To avoid this, the maximum allowable support pressure should be determined. The maximum support pressure (p_{max}) for the tunnel face can be estimated as (DAUB, 2016):

$$p_{max} = C \cdot \gamma_{sat} + 0.5 \cdot D \cdot \gamma_s \tag{6.6}$$

where D is the tunnel diameter, C is the cover depth, γ_{sat} is the unit weight of saturated soil and γ_s is the unit weight of support medium.

6.5 Bezuijen models

Bezuijen et al. (2002, 2016) developed two approximated solutions to describe the change of the pore pressure distribution in front of a TBM. The first solution is proposed to predict the excess pore pressure distribution in homogenous saturated sand, when drilling of tunnel occurs in an unconfined aquifer. The second solution is presented to predict the decrease in pore pressure with time during stand-still phase assuming that the pressure difference between the excess piezometric head in the mixing chamber and the piezometric head at the maximum depth of infiltration is dependent on the flow resistance and shear strength of the bentonite.

6.5.1 Bezuijen model for excess pore pressure distribution during drilling phase

In the model of Bezuijen (2002), it is assumed that the drilling speed of the slurry TBM is higher than the slurry penetration velocity and consequently no filter cake is formed. Therefore, the pressure is transferred due to the flow of slurry into the soil skeleton and the resulting shear stresses between slurry and soil without a distinct pressure drop at a

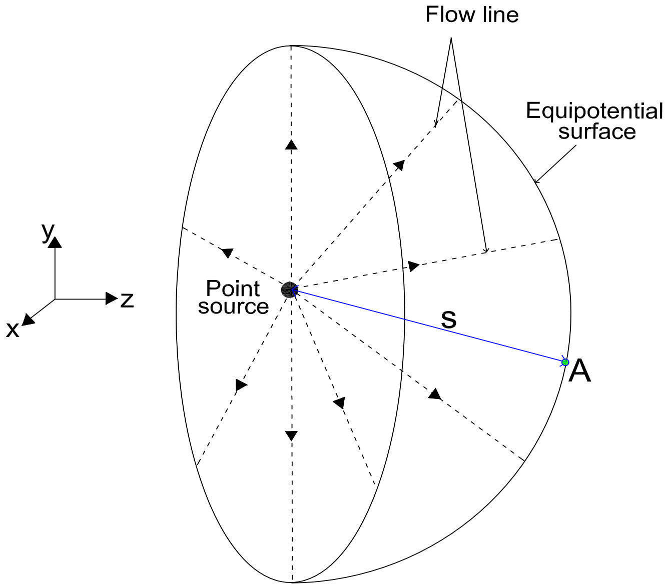

Figure 6.4: Point source and equipotential surface

filter cake. The theory was developed based on measurements of the change of pore water pressure in the front of the tunnel face at the 2nd Heinenoord as discussed before.

According to Bezuijen (2002), the increase of piezometric head at the tunnel face is caused by a constant hydraulic source over the entire tunnel face. To calculate the excess of pore pressure distribution, in the first step the increase in piezometric head caused by a point source on the surface of a half space is discussed, see Fig. 6.4. The flow rate at the point source on the surface of the half space is equal to the flow rate at a certain distance along a surface which is called an equipotential surface. A simple sketch of the flow model is shown in Fig. 6.5.

For a steady state flow, the discharge (Q) across the equipotential surface is calculated as follows:

$$Q = A \cdot k \cdot i \tag{6.7}$$

where, A is the area of the hemispherical zone, k is coefficient of permeability of the soil and i is the hydraulic gradient.

The hydraulic gradient between the point source and the equipotential surface can be obtained as:

$$i = \frac{\phi}{s} \tag{6.8}$$

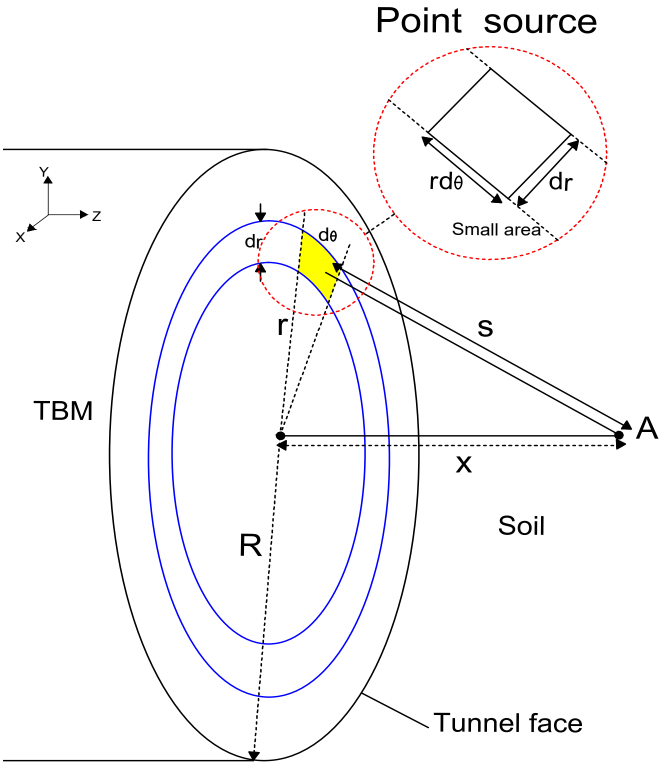

Figure 6.5: Tunnel face flow, Bezuijen (2002)

where ϕ is the piezometric head at the point source and s is the distance from point source to the equipotential surface.

$$\mathrm{A} = 2 \cdot \pi \cdot s^2 \tag{6.9}$$

Eq. (6.7) can be reformulated to obtain the piezometric head as follows:

$$\phi = \frac{Q}{2 \cdot \pi \cdot k \cdot s} \tag{6.10}$$

From Eq. (6.10), in the second step, the piezometric head at a distance s resulting from a fluid injection and over a small area $drd\vartheta$ of the tunnel face can be defined as:

$$d\phi = \frac{q \cdot rdr \cdot d\theta}{2 \cdot \pi \cdot k \cdot s} \tag{6.11}$$

To calculate piezometric head in a point A at the tunnel axis with distance x from the tunnel face for the whole area of tunnel face, Eq. (6.11) is integrated over the circumference and over the radius of the tunnel face, where $\mathrm{s} = \sqrt{x^2 + r^2}$ and R is the radius of the tunnel face.

$$\phi = \frac{q}{2 \cdot \pi \cdot k \cdot \mathrm{s}} \int_0^R \int_0^{2\pi} \frac{r\, dr\, d\theta}{\sqrt{x^2 + r^2}} \tag{6.12}$$

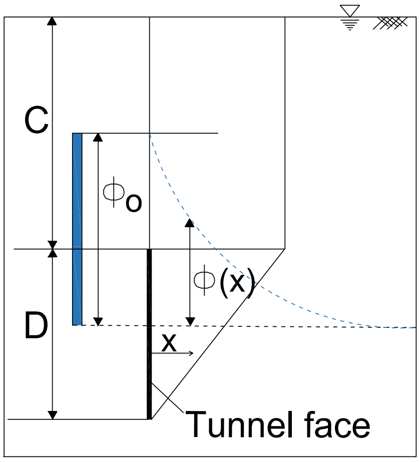

Figure 6.6: Distribution of excess piezometric head ϕ_o with distance to the tunnel face

The distribution of piezometric head (Fig. 6.6) is obtained as:

$$\phi(x) = \frac{\phi_o}{R}(\sqrt{x^2 + R^2} - x) \tag{6.13}$$

where ϕ is the excess piezometric head above hydrostatic level at distance x from the tunnel face and ϕ_o is the excess piezometric head at the tunnel face.

Taking the derivative of Eq. (6.13) at $x = 0$, the hydraulic gradient (i) at the tunnel face is obtained as:

$$i = \frac{\phi_o}{R} \tag{6.14}$$

Using Darcy's law, the penetration velocity (v_p) at front of the tunnel can be formulated as:

$$v_p = \frac{k \cdot i}{n} = \frac{k \cdot \phi_o}{n \cdot R} \tag{6.15}$$

where n is the porosity of the soil.

6.5.2 Bezuijen model for decrease of pore pressure during stand-still phase

When drilling stops, an external filter cakes forms in the soil. Bezuijen (2002) described the pressure drop over the infiltrated zone (external filter cake and mud spurt) using Darcy's law for the flow of the slurry and the water flow. Based on Bezuijen (2002) the difference between the excess piezometric head at the tunnel face ϕ_0 and the piezometric head at the far side of the mud spurt ϕ_{mx} is described with Eq. (6.16).

$$\phi_0 - \phi_{mx} = \underbrace{\frac{x \cdot \phi_0}{L}}_{\text{at the filter cake}} + \underbrace{\frac{x \cdot q}{k_g}}_{\text{at the mud spurt}} \tag{6.16}$$

where L is the maximum penetration depth after a long time, x is the penetration depth at a certain time, q is the discharge and k_g is the coefficient of permeability of the slurry.

The piezometric head at the far side of the mud spurt ϕ_{mx} can be described as

$$\phi_{mx} = \frac{q \cdot R}{k} \tag{6.17}$$

The discharge q is rewritten with Darcy's law as q = (dx/dt)n leading to the following equation

$$\phi_0 = \left(\frac{n \cdot R}{k} + \frac{n \cdot x}{k_g}\right)\frac{dx}{dt} + \frac{x \cdot \phi_0}{L} \tag{6.18}$$

Eq. (6.18) can be reformulated as follows:

$$\frac{dx}{dt} = \frac{\phi_o(1 - \frac{x}{\mathrm{L}})}{\frac{n}{R} + \frac{n}{k_g} \cdot x} \tag{6.19}$$

By solving Eq. (6.19), ϕ_o can be computed as a function of time, if the parameters R, n, L, x and k_g are known.

6.6 Implementation of excess pore pressures into different models.

In the following subsections, the procedure of taking into account the excess pore pressure in predicting the minimum tunnel face support pressure using wedge-silo (Horn, 1961; Anagnostou & Kovari, 1994; Broere, 2001) and KEM model (M2) will be presented.

In order to obtain the distribution of excess pore pressure around the tunnel face generated by tunnel excavation, the analytical model proposed by Bezuijen (2002) is integrated into the tunnel face stability models, see Fig. 6.7.

Based on the assumptions of the model of Bezuijen (2002), Eq. (6.13) can be used to predict the excess pore pressure at any distance from the center of the tunnel face. However, the flow of slurry from the TBM to the soil is a 3D flow, which would make the resulting excess pore water distribution more complex and its calculation time-consuming. To get around this 3D flow problem, Bezuijen (2002) assumed that Eq. (6.13) can be used to estimate the distribution of excess pore pressure along the distance x from the tunnel face at every point on the tunnel face.

6.6.1 Implementing the excess pore pressure in wedge-silo model

The major steps to include the effect of excess pore pressure in predicting the minimum tunnel face support pressure are as follows. Firstly, the the wedge is divided into horizontal slices and the hydraulic head difference between the assumed failure surface and the tunnel face is calculated in each slices. The effective weight of each slice including the hydrostatic forces and the seepage forces is calculated. Finally, the maximum effective support force in equilibrium condition is determined using the optimization process. The previous steps are discussed in more details in the following.

To include the excess piezometric head in the static equilibrium analysis of the wedge, the wedge is divided into several slices along the vertical direction. Each slice (i) is loaded by the effective weight from the slice above it (i-1) and below (i+1), see Figs. 6.7 and 6.8.

By integrating Eq. (6.13) from x = 0 to x_i and dividing the results by x_i, the average increment of excess pore pressure is obtained at each height from i to n:

$$\phi^{avg} = \int_0^{x_i} \frac{\phi_o}{R}(\sqrt{x^2+R^2}-x)\,dx \qquad \text{(Dias \& Bezuijen, 2016)} \qquad (6.20)$$

$$\phi_i^{avg} = \phi_o\left[0.5\left(\sqrt{{x_i}^2+R^2}-x_i\right)+\frac{R^2}{2x_i}ln\left(\sqrt{{x_i}^2+R^2}-x_i\right)-\frac{1}{2x_i}R^2ln(R)\right]$$

(Dias & Bezuijen, 2016) (6.21)

Considering the hydrostatic pore pressure, in the models of Anagnostou & Kovari (1994) and Broere (2001), the vertical effective stress at the top of the wedge is computed based on the silo theory (Janssen, 1895) as follows:

$${\sigma'}_{v_{silo}}(C) = \frac{a\cdot\gamma'-c'}{K_{silo}\cdot\tan\varphi'}(1-e^{-\frac{C}{a}\cdot K_{silo}\cdot\tan\varphi'}) \qquad (6.22)$$

In the model of Horn (1961) model, the vertical effective stress at the top of the wedge is computed as follows:

$${\sigma'}_{v_{silo}}(C) = C\cdot\gamma' \qquad (6.23)$$

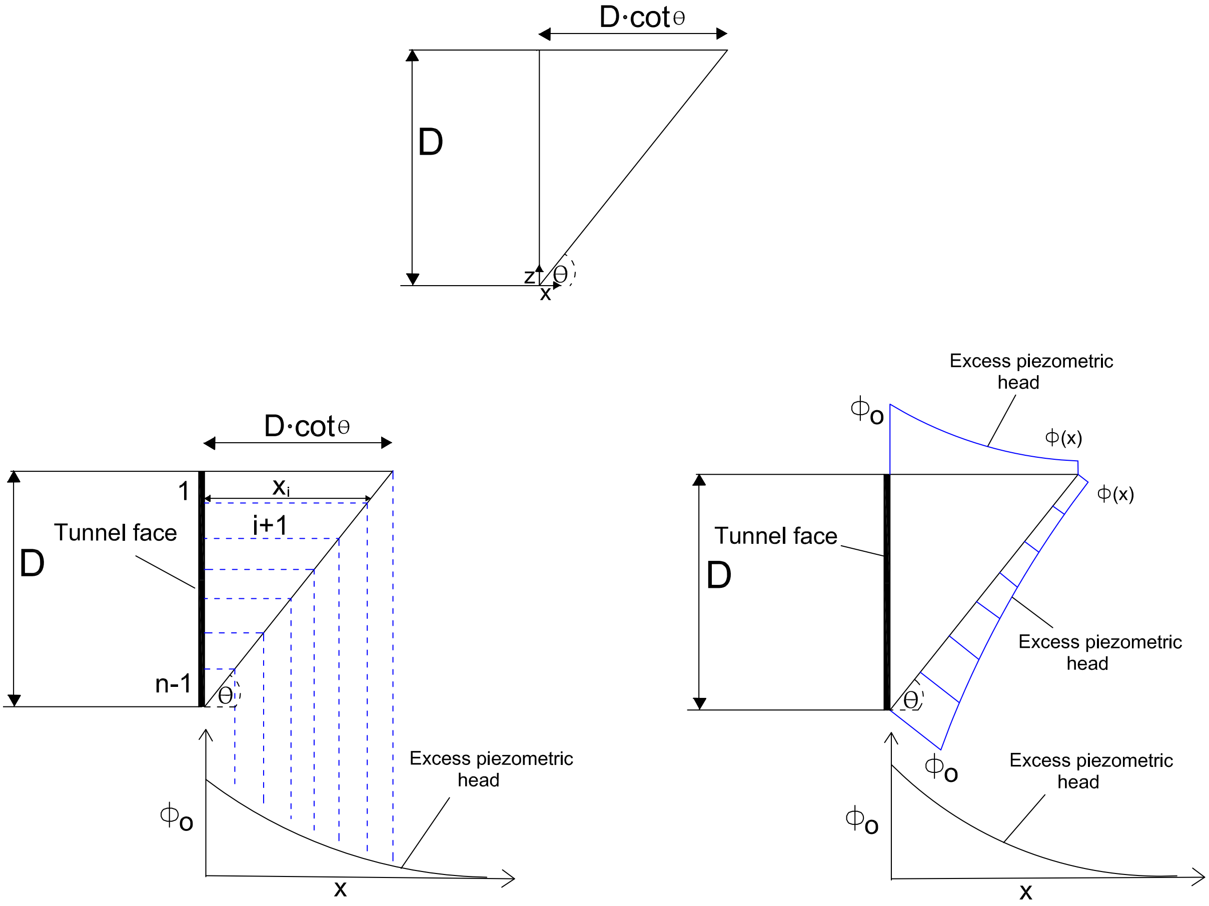
D·cotθ
D
z
x
θ
D·cotθ
1
x_i
i+1
Tunnel face
D
n-1
θ
Excess piezometric head
Φo
x
Excess piezometric head
Φo
Φ(x)
Φ(x)
Tunnel face
D
Excess piezometric head
θ
Φo
Excess piezometric head
Φo
x

Figure 6.7: Excess piezometric head distribution in the wedge

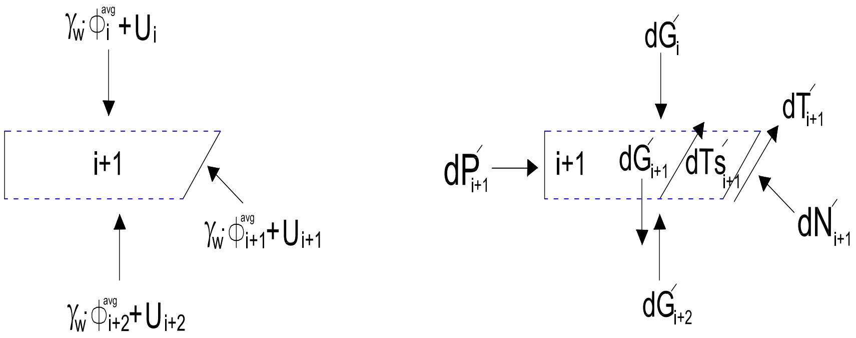
γw·Φi avg +Ui
i+1
γw·Φi+1 avg +Ui+1
γw·Φi+2 avg +Ui+2
dG'i
dT'i+1
dP'i+1
i+1
dG'i+1
dTs'i+1
dN'i+1
dG'i+2

Figure 6.8: Pressures and forces in each slice of the wedge

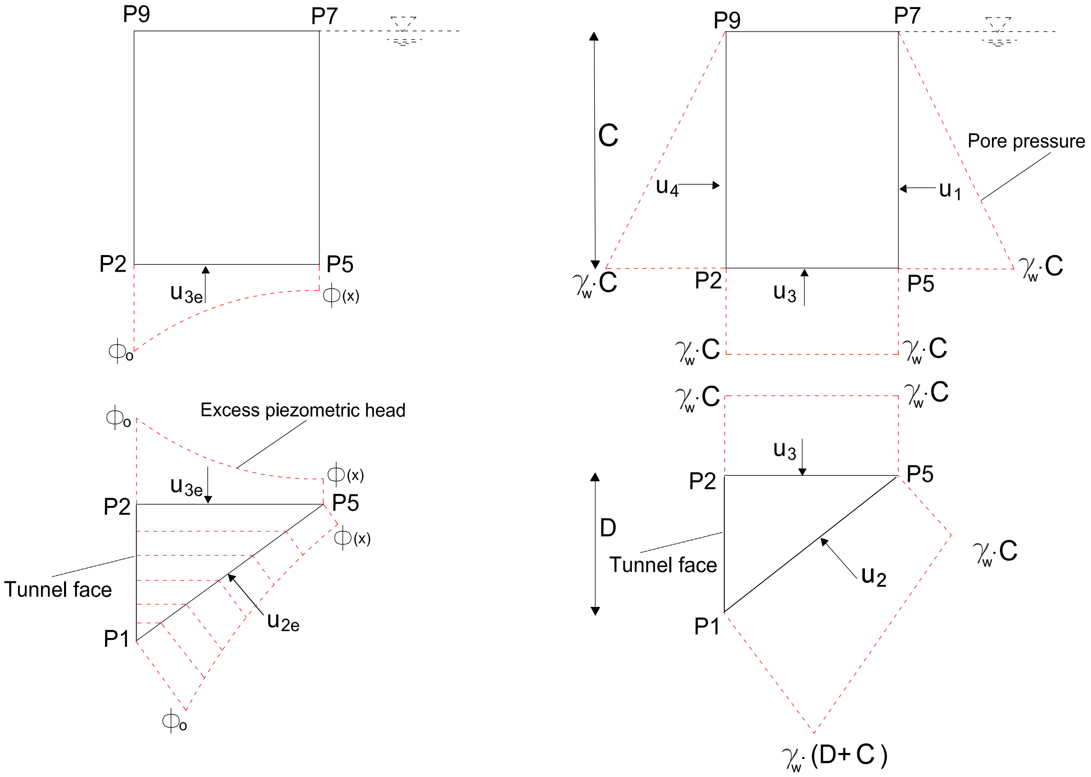
P9
P7
P2
P5
u_{3e}
$\phi(x)$
ϕ_o
ϕ_o
Excess piezometric head
u_{3e}
$\phi(x)$
P2
P5
$\phi(x)$
Tunnel face
u_{2e}
P1
ϕ_o
P9
P7
C
Pore pressure
u_4
u_1
$\gamma_w \cdot C$
$\gamma_w \cdot C$
P2
u_3
P5
$\gamma_w \cdot C$
$\gamma_w \cdot C$
$\gamma_w \cdot C$
$\gamma_w \cdot C$
u_3
P2
P5
D
Tunnel face
u_2
$\gamma_w \cdot C$
P1
$\gamma_w \cdot (D+C)$

Excess piezometric head

Hydrostatic pore pressure

Figure 6.9: Distribution of hydrostatic and excess pore pressure in KEM model (M2)

If additionally also pore water pressure is considered, the vertical effective stress at the top of the wedge is computed as follows:

$$\sigma'_{v_{\text{top}}}(C) = \sigma'_{v_{silo}}(C) - \phi^{avg}(z_i) \cdot \gamma_w \tag{6.24}$$

The total vertical stress on each slice along the sides of the wedge is calculated as:

$$\sigma_v(z_i) = (D - z_i) \cdot \gamma + \sigma_{v_{silo}}(C) \quad (0 \leq z \leq D) \tag{6.25}$$

with γ being the specific unit weight of the water-saturated soil and the vertical coordinate z running from the bottom of the tunnel face. Considering the hydrostatic and excess pore water pressures, the vertical effective stress along the sides of the wedge is calculated as:

$$\sigma'_{v_{\text{wedge}}}(z_i) = \sigma_v(z_i) - u(z_i) - \phi^{avg}(z_i) \cdot \gamma_w \tag{6.26}$$

$u(z_i)$ is the hydrostatic pore pressure and $\phi^{avg}(z_i)$ is the average excess piezometric head at distance x_i from the tunnel face.

The resisting shear force acting on both sides of the sliding wedge can be obtained as follows:

$$T'_s = 2 \cdot K_{wedge} \cdot \tan\varphi' \cdot \sum_{i=1}^{n} \left(\frac{x_i + x_{i+1}}{2} \cdot \frac{\sigma'_{v_{i_{wedge}}} + \sigma'_{v_{i+1_{wedge}}}}{2} \right) \quad \text{(Dias \& Bezuijen, 2016)} \tag{6.27}$$

The effective weight G'_w of the wedge is calculated as follows:

$$G'_w = D \cdot \sum_{i=1}^{n} \left(\frac{x_i + x_{i+1}}{2} \cdot \frac{\sigma'_{v_{i_{wedge}}} + \sigma'_{v_{i+1_{wedge}}}}{2} \right) \quad \text{(Dias \& Bezuijen, 2016)} \tag{6.28}$$

The vertical force G'_s of the silo on the top of the wedge is calculated as follows:

$$G'_s = \sigma'_{v_{silo}}(C) \cdot D^2 \cdot \cot\theta \tag{6.29}$$

The effective support force P' needed to support the tunnel face is obtained from:

$$P' = \frac{G'_s + G'_w}{\cot(\theta + \varphi')} - \frac{T'_s + c' \cdot (\frac{D^2}{\sin\theta})}{\sin \cdot\theta(\cot\theta + \tan\varphi')} \tag{6.30}$$

The effective support force will vary with the sliding angle (θ). The critical inclination θ_{crit} is determined by maximizing the effective support force P':

$$\frac{dP'}{d\theta_{crit}} = 0 \tag{6.31}$$

where $0^o < \theta_{crit} < 90^o$

The minimum effective support pressure is assumed to be uniformly distributed over the tunnel face and given by

$$p' = \frac{P'}{D^2} \tag{6.32}$$

6.6.2 Implementing the excess pore pressure in KEM model (M2)

The proposed failure mechanism of KEM model (M2) consists of 6 elements. Due to the symmetry of the failure mechanism, one half of KEM model (M2) is considered to investigate the effect of excess pore pressure on the tunnel face support pressure, as shown in Fig 5.8 (Chapter 5).

The hydrostatic forces on the contact and sliding surface are calculated as:

$$U_m = \gamma_w \cdot \int_{A_m} dA \tag{6.33}$$

where m is the number of the faces under consideration and A_m is the area of the surfaces Eq. (6.33) can be simplified to:

$$U_m = \gamma_w \cdot h_c \cdot A_m \tag{6.34}$$

with h_c being the distance from the ground surface to the centroid of the area.

The wedges are divided into slices (Fig. 6.9). The average increment of excess pore pressure in each surface is calculated using Eq. (6.23). Thereafter, the total average force caused by excess pore pressure in each face of the wedge is calculated as follows:

$$U_{ie} = \gamma_w \cdot \sum_{i=1}^{n} \phi_i^{avg} A_i \tag{6.35}$$

A_i is the area of the slice i.

By assembling the force equilibrium equations over the whole KEM model (M2) and representing them in matrix form, where the total support force and the normal forces on each surface are unknowns, the following equilibrium equation can be written:

$$[K_s]_{j\times m} \cdot [N]_{m\times 1} + [F]_{j\times 1} = 0 \tag{6.36}$$

where, $[K_s]$ is the static coefficient matrix, [N] is the normal vector of unknown forces and [F] is the vector of known forces, including inertia forces ([J]), hydrostatic forces ([U]) and the forces caused by the excess pore pressure ($[U_e]$):

$$[F]_{j\times 1} = [J]_{j\times 1} + [U]_{j\times 1} + [U_e]_{j\times 1} \tag{6.37}$$

6.7 Problem definition

Based on the analysis methods presented in the previous section, the wedge-silo (Horn, 1961; Anagnostou & Kovari, 1994 and Broere, 2001) and KEM (M2) models are used to

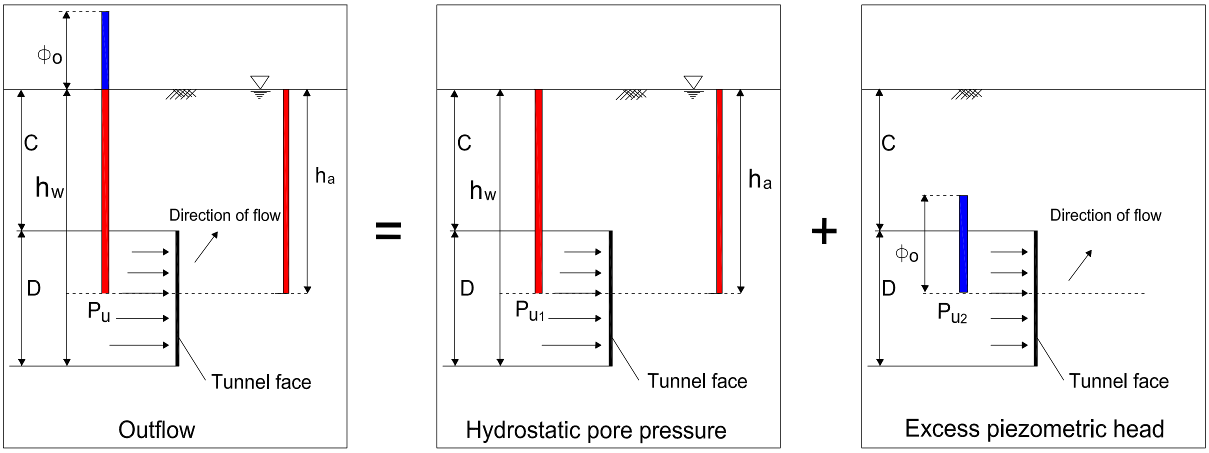

Figure 6.10: Schematic diagram for the applied pressure in TBM due to hydrostatic and excess piezometric head

investigate the stability of a circular tunnel which is excavated under the water table. The geometry of the problem and the considered pressures are shown in the schemes Fig. 6.10, where D denotes the tunnel diameter, C refers to the tunnel depth, h_w is the water table elevation measured from the bottom of the tunnel to the ground surface and ϕ_o refers to the excess piezometric head correlated to excess pore pressure in the soil at the tunnel face. The soil is assumed to be fully saturated with the ground water table at the ground surface. ϕ' and c' are the effective shear strength parameters of the soil, where ϕ' indicates the effective friction angle, c' is the effective cohesion, and γ' is the buoyant unit weight of the soil. The soil parameters and the tunnel geometry are given in Table 6.1.

The soil has been assumed to be homogeneous and under drained condition. For simplicity, the safety factors η_e and η_w are set to 1. Also, the surcharge is neglected ($q = 0$ kPa). Fig. 6.11 presents the flow chart for the procedure of incorporating the excess pore pressure in tunnel face stability models.

6.8 Results and discussion

6.8.1 Effect of hydrostatic pore pressure on the tunnel face stability

The key point in this section is to present the effect of hydrostatic pore pressure on the tunnel face stability. In the following section the effect of excess pore pressure on the tunnel face stability is addressed.

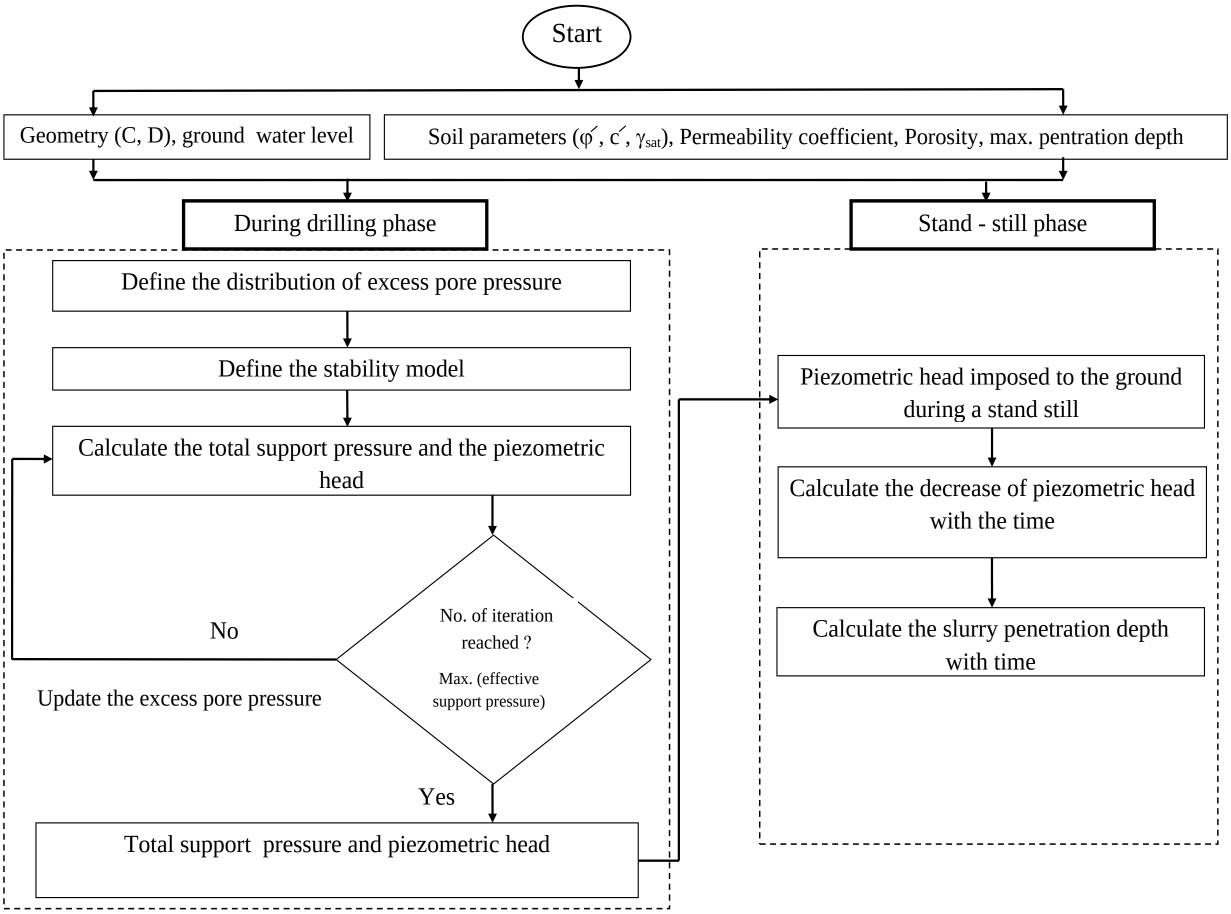
Start
Geometry (C, D), ground water level
Soil parameters (φ´, c´, γsat), Permeability coefficient, Porosity, max. pentration depth
During drilling phase
Stand - still phase
Define the distribution of excess pore pressure
Define the stability model
Calculate the total support pressure and the piezometric head
No. of iteration reached ?
Max. (effective support pressure)
No
Update the excess pore pressure
Yes
Total support pressure and piezometric head
Piezometric head imposed to the ground during a stand still
Calculate the decrease of piezometric head with the time
Calculate the slurry penetration depth with time

Figure 6.11: Flow chart for the procedure of incorporating the excess pore pressure in tunnel face stability models

Table 6.1: Soil parameters and tunnel geometry

Parameter	Value	Unit
Tunnel diameter (D)	10	[m]
Cover depth (C)	10	[m]
Maximum penetration depth (L)	0.25	[m]
Unit weight of saturated soil (γ_{sat})	20	[kN/m^3]
Unit weight of supported medium (γ_s)	12	[kN/m^3]
Permeability of the soil (k)	10^{-4}	[m/s]
Permeability of the soil for the slurry (k_g)	10^{-6}	[m/s]
Porosity of the soil (n)	0.4	[-]

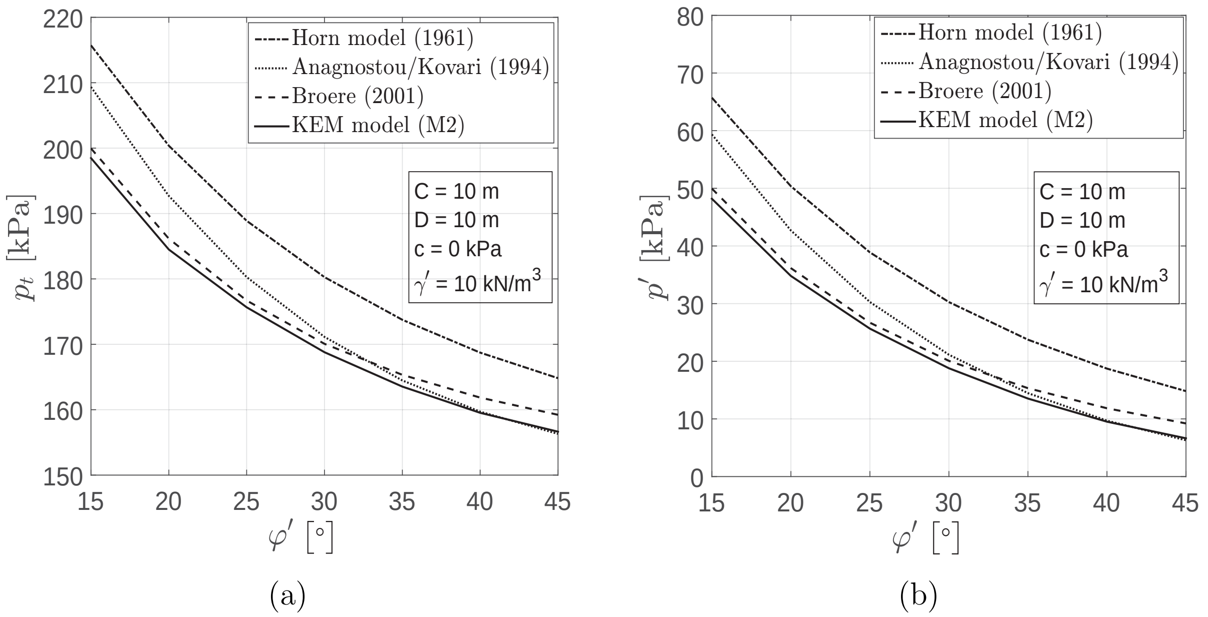

(a) (b)

Figure 6.12: Minimum support pressure considering hydrostatic pore pressure: (a) total support pressure; (b) effective support pressure

The conventional method for calculating the support pressure is simply to consider the influence of hydrostatic pore pressure distribution around the tunnel face in the stability analysis, i.e. the total support pressure at the tunnel face is obtained without considering the excess pore pressure.

When the static equilibrium of forces is set up, the maximum effective support force can be obtained using the optimization procedure. In that case, the total support pressure is equal to the sum of effective and hydrostatic pore pressure.

Fig. 6.12 presents a comparison of the total and effective support pressures obtained from KEM model (M2) and different wedge-silo models (Horn, 1961; Anagnostou & Kovari, 1994 and Broere, 2001).

As seen in Fig. 6.12, for cohesionless soil both the total and the effective support pressure decrease with the increase in friction angle. From a comparison of the two diagrams in Fig. 6.12, it can be concluded that the sum of the effective support pressure and the hydrostatic pore pressure at the center-line of the tunnel face (150 kPa) is equal to the total support pressure for the same friction angle. In addition, for $\varphi < 35^o$, the results of Broere (2001) are closer to the results of KEM model (M2) than the other models. For $\varphi > 35^o$, however, the results of KEM model (M2) agree well with the results of Anagnostou & Kovari (1994). The differences in the results between Anagnostou & Kovari

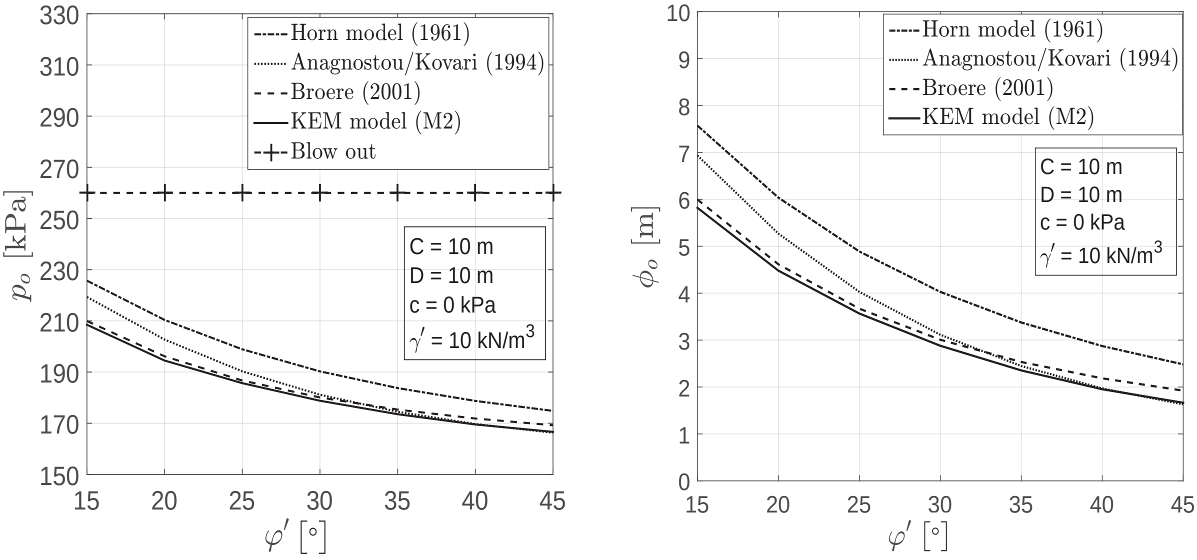

(a) (b)

Figure 6.13: Applied support pressure considering hydrostatic pore pressure: (a) operational support pressure; (b) piezometric head

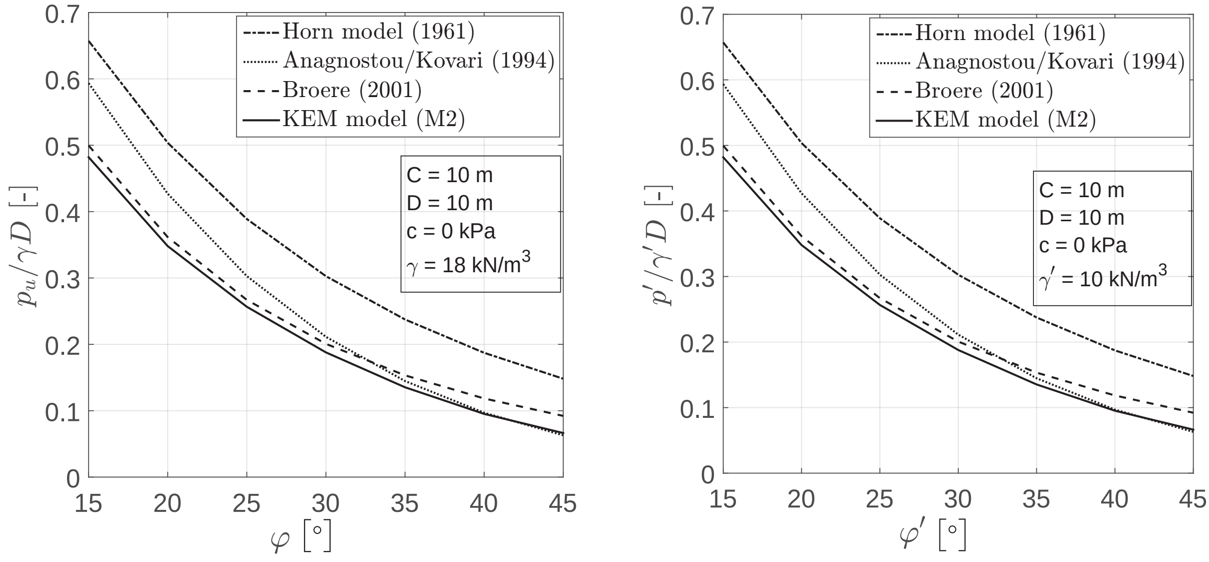

(a) (b)

Figure 6.14: Comparison of normalized minimum support pressure in dry condition and effective support pressure in saturated condition: (a) normalized support pressure in dry condition; (b) normalized effective support pressure in saturated condition

(1994) and Broere (2001) are due to the different assumptions regarding the distribution of vertical stress along the sides of the silo and the wedge.

From Fig. 6.12, it is clear that the total and the effective support pressure calculated with the model of Horn (1961) (no arching is considered) is substantially higher than the values obtained from the other models.

As mentioned before, the total support pressure is equal to the sum of the effective and the hydrostatic support pressure.

The operational pressure is considered as the total support pressure increased by a safety margin of 10 kPa (Fig. 6.13 (a)). This operational pressure must be verified against the possibility of blowout as well.

From Fig. 6.13 (a), it can be noticed that the operational support pressures calculated by different models are less than the maximum allowable support pressure. The pressure corresponding to the piezometric head ϕ_o at the tunnel face is equal to the effective pressure with a safety margin of 10 kPa ($\phi_o = \frac{p'}{\gamma_w} + 1$ m). For purely frictional soil, it can be deduced from the diagrams in Fig. 6.14 that the ratio between the minimum support pressure (p_u) in dry condition and the effective support pressure (p') in saturated condition is equal to the ratio between the dry and submerged unit weight of the soil ($\frac{\gamma}{\gamma'}$). Therefore, the following relationship can be concluded:

$$p' = p_u \cdot \frac{\gamma'}{\gamma} \tag{6.38}$$

$$p_u = N_\gamma \cdot \gamma \cdot D \tag{6.39}$$

$$p' = N_\gamma \cdot \gamma' \cdot D \tag{6.40}$$

where γ' is the buoyant unit weight of the soil, γ is the dry unit weight of the soil and N_γ is the non-dimensional coefficient representing the contribution of soil weight in dry condition to the minimum tunnel face support pressure.

In saturated soil, the total support pressure (p_{total}) at the tunnel face can be calculated as follows:

$$p_{total} = N_\gamma \cdot \gamma' \cdot D + \gamma_{water} \cdot C \qquad \text{(At the top of the tunnel face)} \tag{6.41}$$

$$p_{total} = N_\gamma \cdot \gamma' \cdot D + \gamma_{water} \cdot (C + 0.5D) \qquad \text{(At the center of the tunnel face)} \tag{6.42}$$

$$p_{total} = N_\gamma \cdot \gamma' \cdot D + \gamma_{water} \cdot (C + D) \qquad \text{(At the bottom of the tunnel face)} \tag{6.43}$$

where, γ_w is the unit weight of water.

Eqs. (6.41) to 6.43 are useful for a direct computation of the total support pressure (p_{total}) in saturated condition from the design graphs, which are given for the soil in dry conditions (e.g., Fig 5.18, Chapter 5)

6.8.2 Effect of hydrostatic and excess pore pressures on the tunnel face stability

When the tunnel is excavated under the water table, the stability analysis of the tunnel face should generally consider both the hydrostatic and the excess pore pressures. As explained above, beside the hydrostatic and the excess pore pressures leads to a further reduction of the effective stress in the soil and thus affects the tunnel face support pressure.

From the model of Bezuijen (2002), the excess pore pressure distribution at the failure surfaces can be obtained as described in Section 6.6. The forces arising from these excess pore water pressures are added as external loads in the static equilibrium of the forces.

It is clear from Fig. 6.15 that the total and effective tunnel face support pressures decrease as the effective friction angle φ' increases. Fig. 6.15 shows that the model of Horn (1961) gives a higher value of operational support pressure compared to the other analytical solutions, because soil arching is not considered. The results of KEM model (M2) lie below the results of the other models. However, the differences in operational support pressure between KEM model (M2) and the solutions of Anagnostou & Kovari (1994) and Broere (2001) does not exceed 10 %. Moreover, the operational support pressures calculated by different models are less than the maximum allowable support pressure.

Fig. 6.15 (b) shows the effective support pressure calculated by different models. Interestingly, the results calculated by the different models show a similar trend as the results of effective support pressure calculated by only considering the hydrostatic pore pressure (see Fig. 6.15 (b)).

Fig. 6.15 (c) illustrates the relationship between the excess pore pressure and the friction angle. From a comparison of all three diagrams in Fig. 6.15, it can be concluded that the sum of the excess pore pressure and the hydrostatic pore pressure at the center-line of the tunnel face (150 kPa) is equal to the total support pressure for the same friction angle.

It is expected that a consideration of the excess pore pressure in the tunnel face stability analysis will increase the total support pressure. Fig. 6.16 presents the percentage of increase in the operational support pressure by including the resulting and the excess pore water pressures in the force equilibrium. As can be seen in Fig. 6.16, the increase in

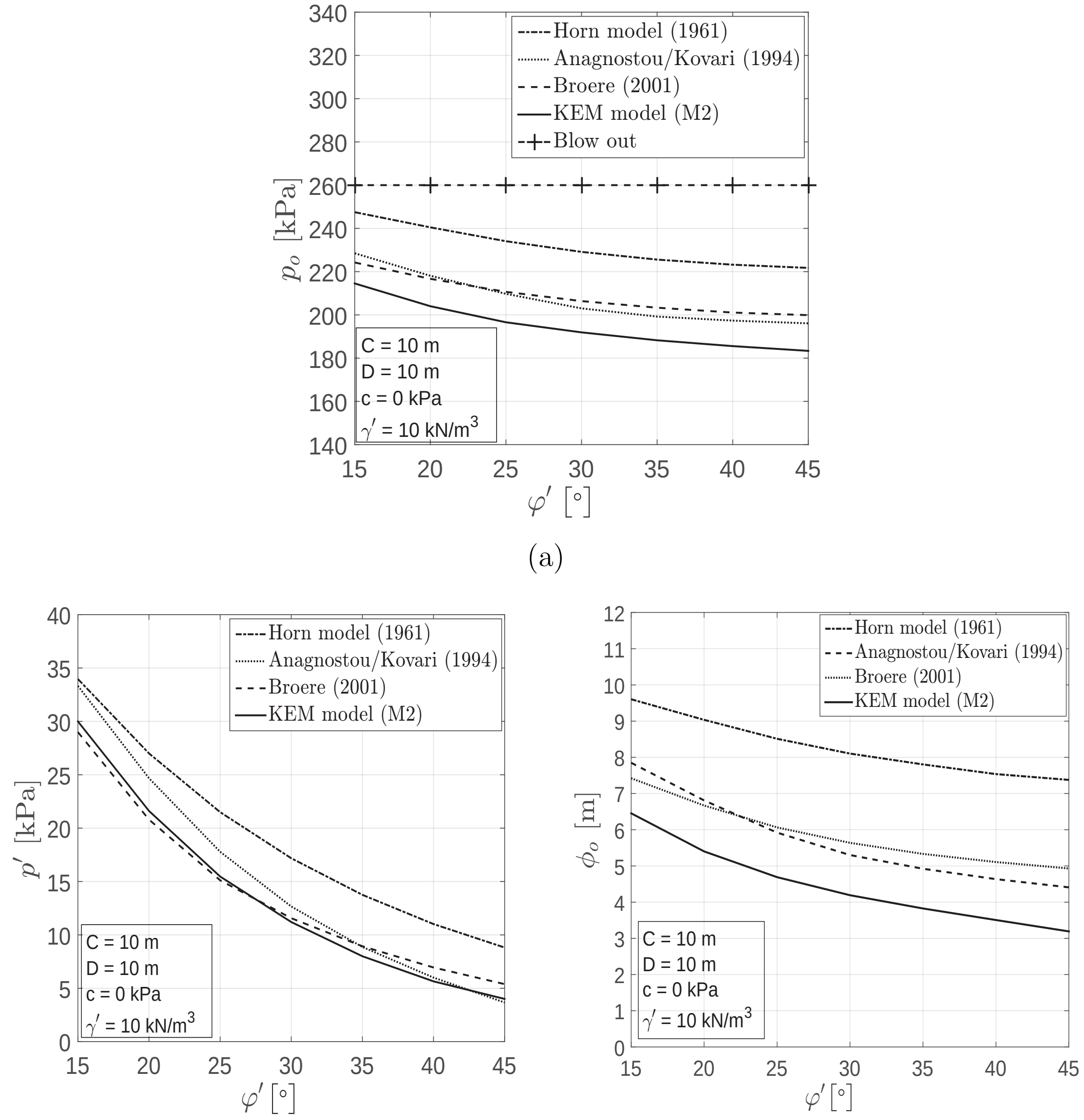

(a)

(b)

(c)

Figure 6.15: Required support pressures considering hydrostatic and excess pore pressures: (a) operational support pressure; (b) effective support pressure; (c) piezometric head

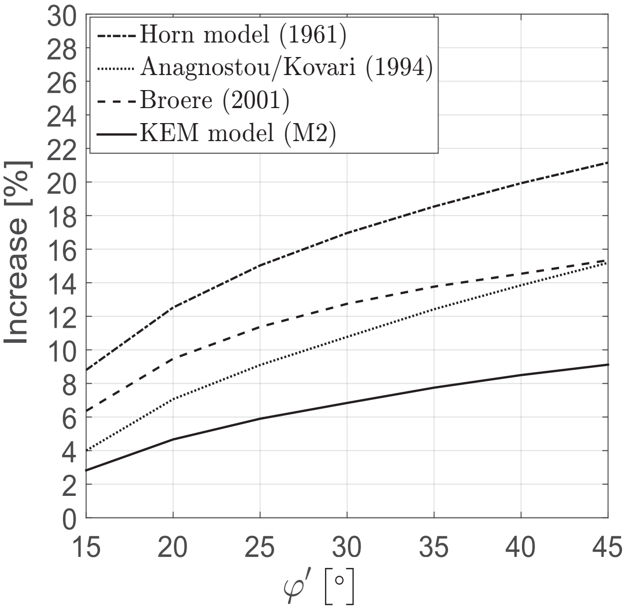

Figure 6.16: Percentage of increase in operational support pressure due to excess pore pressure

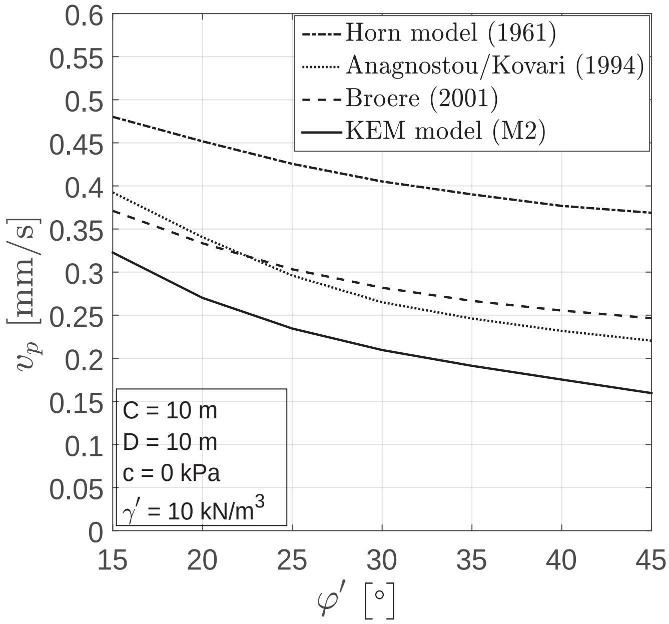

Figure 6.17: Penetration velocity versus effective friction angle

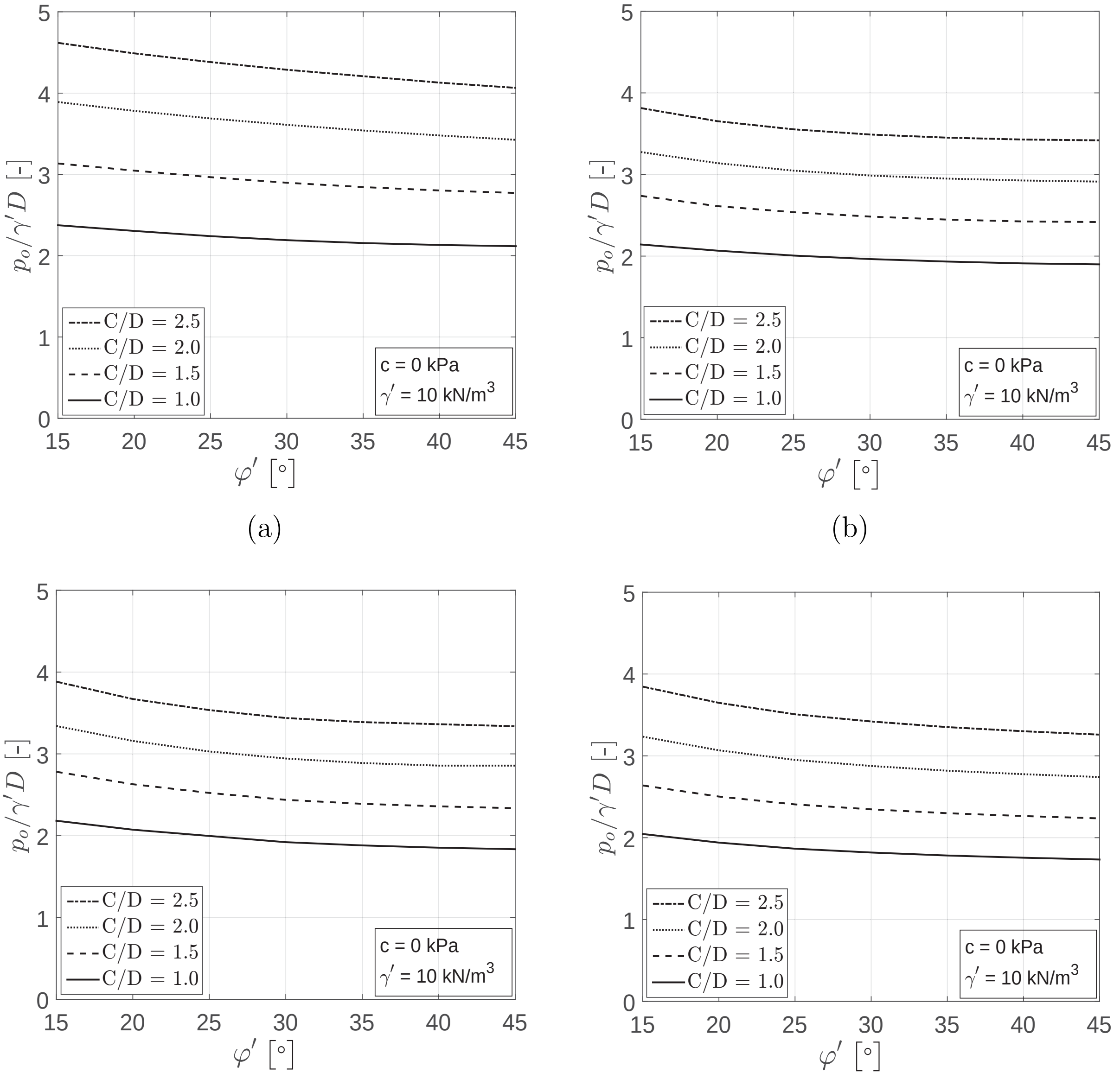

(a) (b)

(c) (d)

Figure 6.18: Design charts for normalized operational support pressure considering hydrostatic and excess pore water pressures: (a) Horn (1961) model; (b) Broere (2001) model; (c) Anagnostou & Kovari (1994) model; (d) KEM model (M2)

the minimum support pressure by considering the excess pore pressures is higher in case of the wedge-silo models compared to KEM model (M2). In addition, the differences in the percentage of increase between the different models gets smaller as the friction angle decreases.

From the previous discussion it can be concluded that the hydraulic gradient during the optimization process for computing the maximum effective support pressure is developed slightly lower in KEM model (M2) compared to the models of Anagnostou & Kovari (1994) and Broere (2001). This can be attributed to the increase in the number of elements in the failure mechanism of KEM model (M2).

Fig. 6.17 shows the penetration velocity (v_p) of the slurry calculated from Eq. (6.15) as a function of the effective friction angle. Assuming that the average TBM drilling velocity is 1 mm/s, it can be seen that the velocity of slurry penetration from the chamber to the ground is less than the TBM drilling velocity. Therefore, the cutter wheel rotation of TBM will continuously remove the bentonite, so that there is no possibility to form a filter cake.

For the condition that the soil is fully water-saturated and the ground water table is located at the ground surface, several design charts are provided in Fig. 6.18. In these design charts, the normalized operational support pressure ($p'_o/(\gamma' D)$) is plotted as a function of effective friction angle. The design charts consider the excess pore water pressures generated by the drilling process.

6.9 Drops in piezometric head with time during stand-still phase

When drilling stops, the bentonite penetrates to the soil and a filter cake will be built up causing a reduction of piezometric head in the soil behind the filter cake. Using the soil parameters summarized in Table 6.2, the decrease in piezometric head imposed to the soil is obtained from time by applying Eq. (6.19), which was solved numerically with increments of 5 second. For the different models, the drop of the piezometric head with function of time is shown in Figs. 6.19 to 6.22 for different C/D and friction angles. Furthermore, the corresponding relationships between the slurry penetration depth and time calculated from Eq. (6.19) are shown in Figs. 6.23 to 6.26.

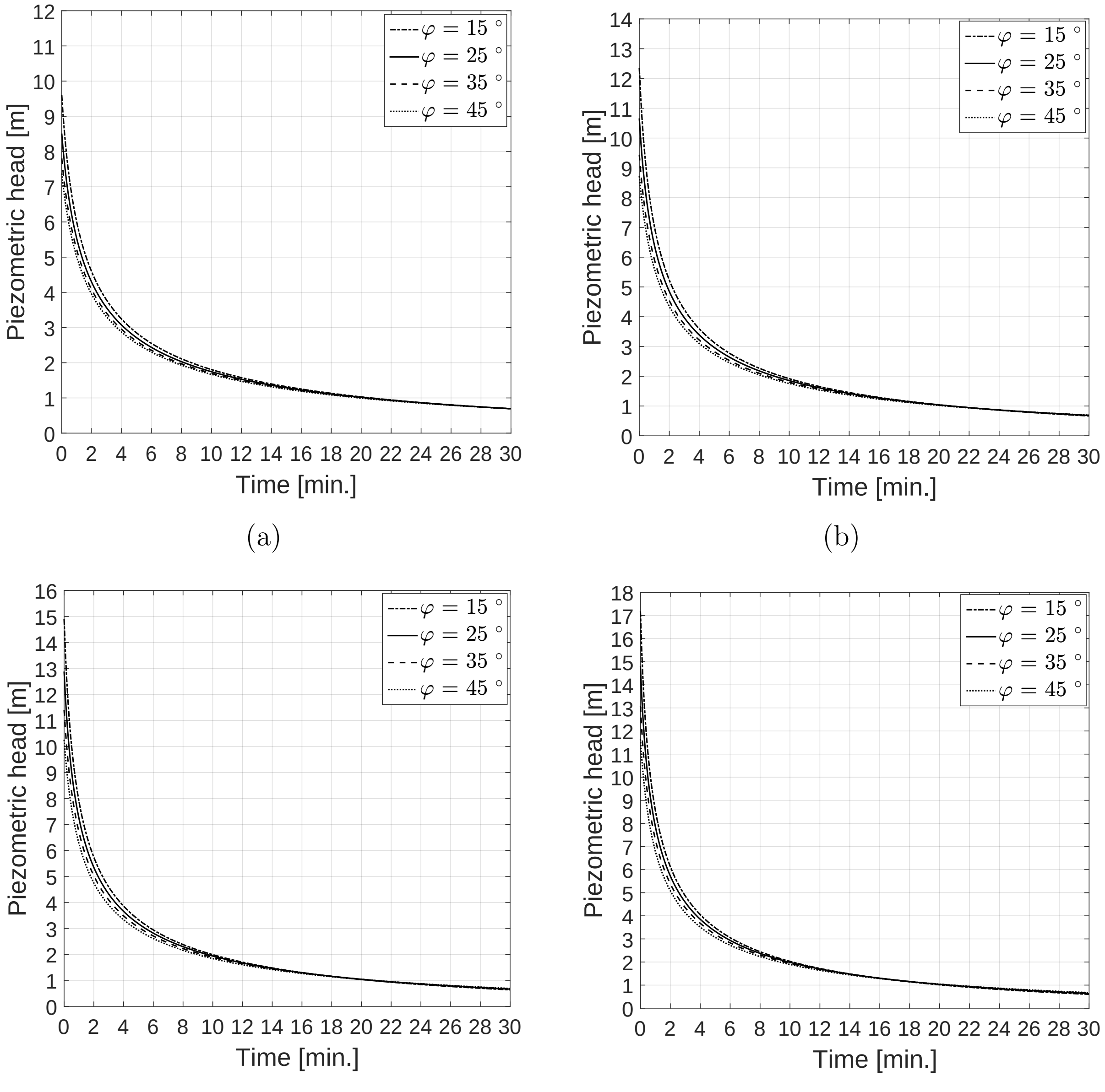

(a) (b)

(c) (d)

Figure 6.19: Development of piezometric head imposed to the soil with time for Horn (1961) model: (a) $C/D = 1$; (b) $C/D = 1.5$; (c) $C/D = 2$; (d) $C/D = 2.5$

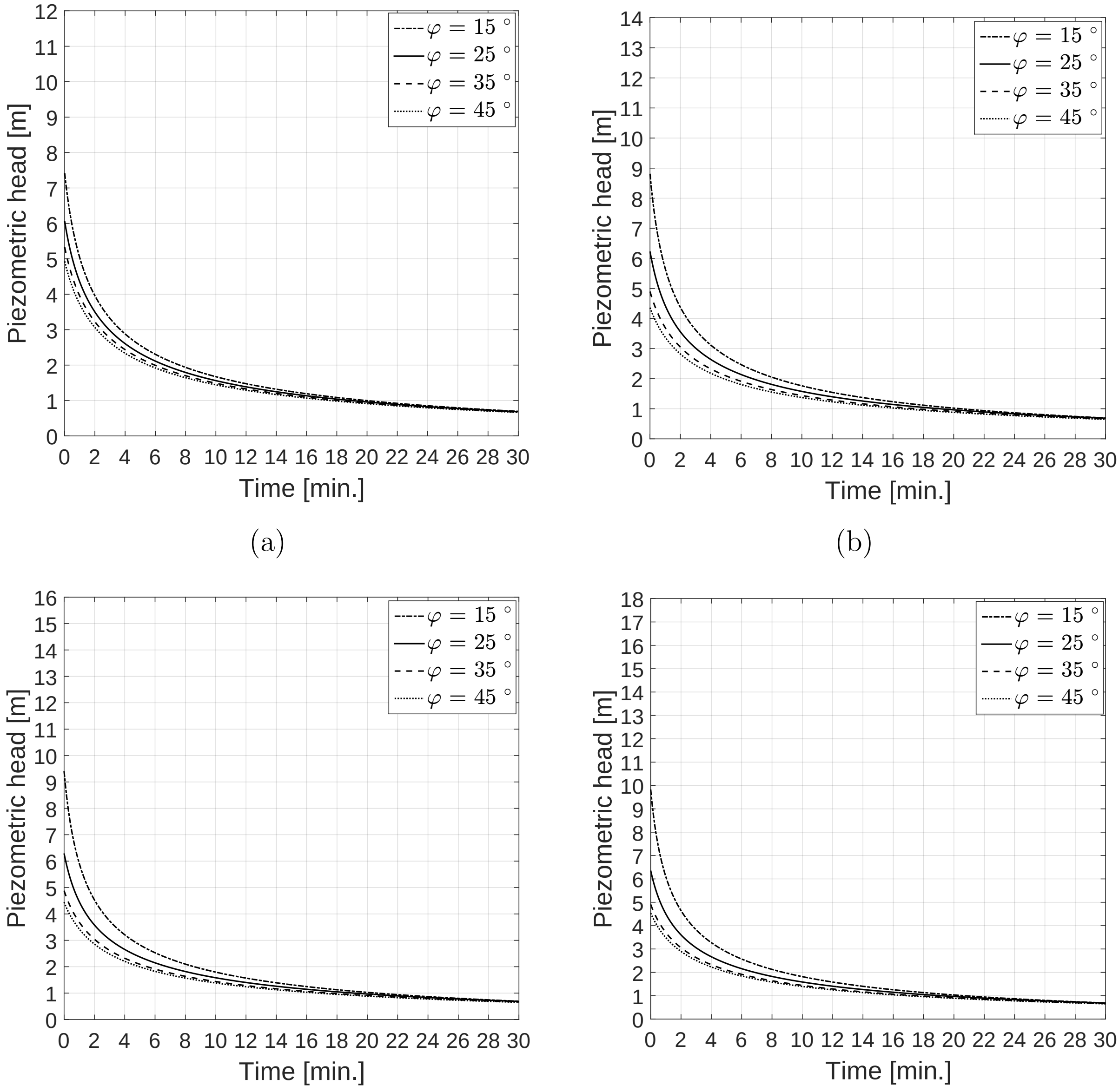

(a) (b)

(c) (d)

Figure 6.20: Development of piezometric head imposed to the soil with time for Anagnostou & Kovari (1994) model: (a) $C/D = 1$; (b) $C/D = 1.5$; (c) $C/D = 2$; (d) $C/D = 2.5$

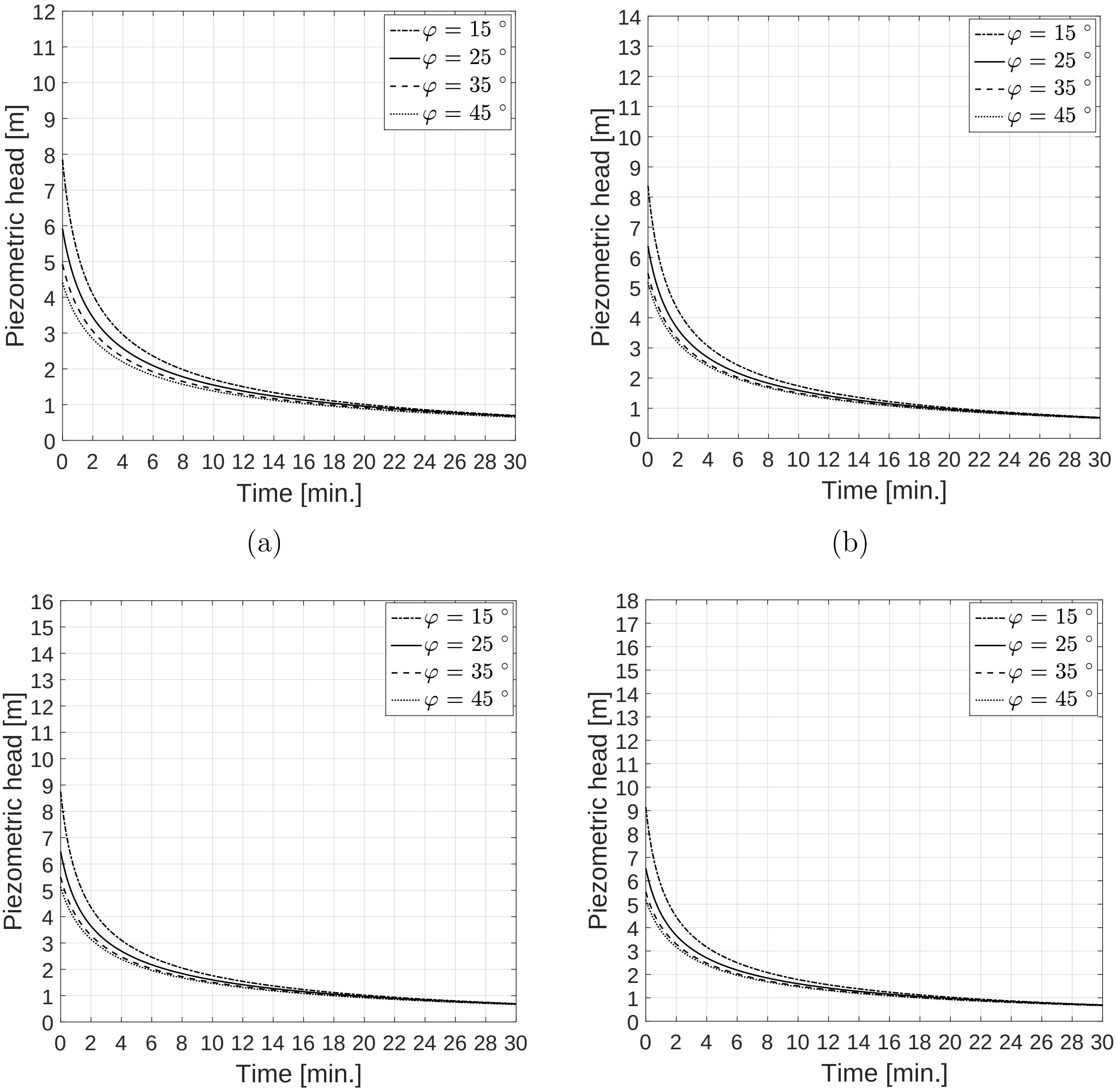

(a) (b)

(c) (d)

Figure 6.21: Development of piezometric head imposed to the soil with time for Broere (2001) model: (a) $C/D = 1$; (b) $C/D = 1.5$; (c) $C/D = 2$; (d) $C/D = 2.5$

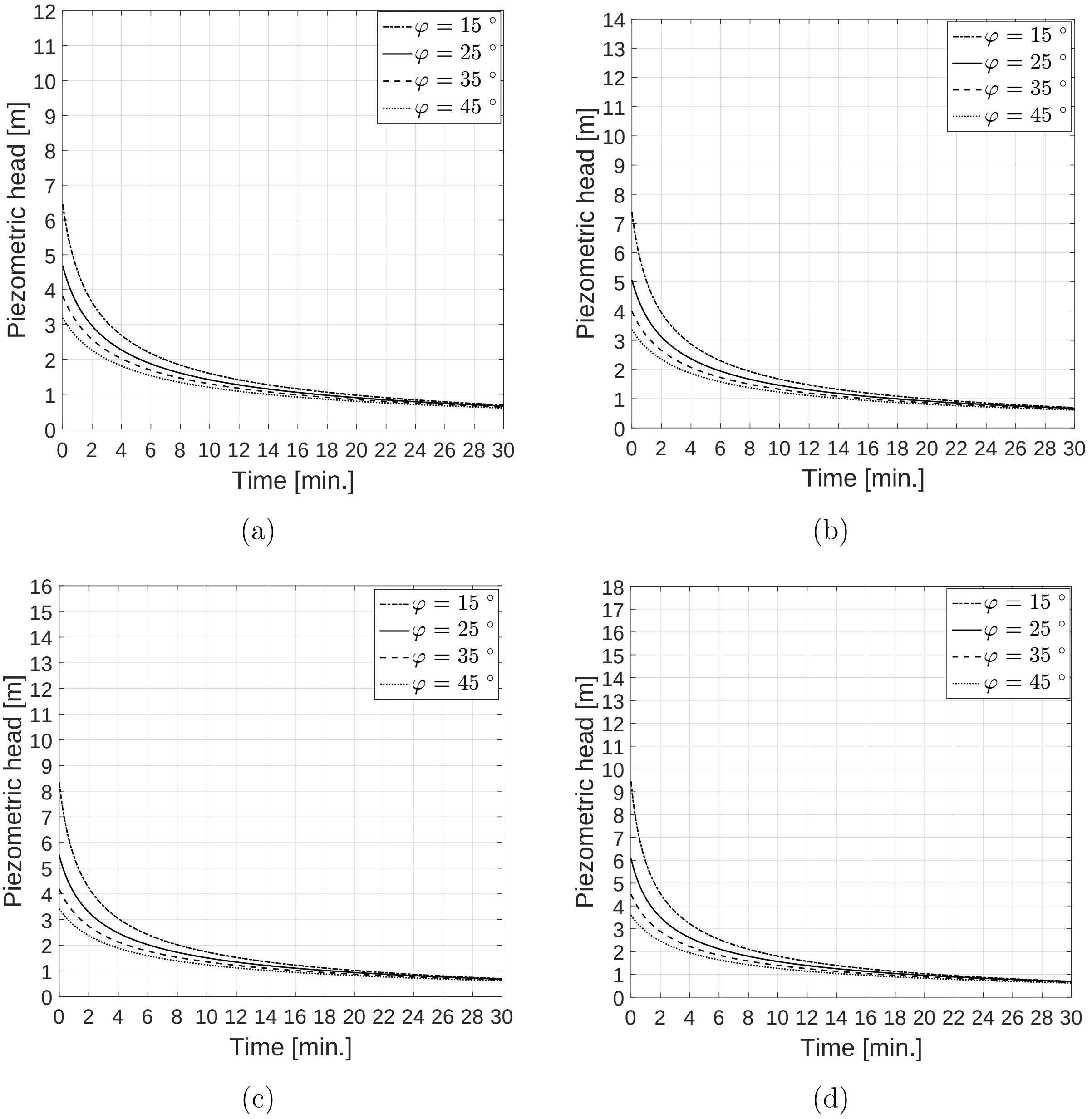

(a) (b)

(c) (d)

Figure 6.22: Development of piezometric head imposed to the soil with time for KEM model (M2): (a) $C/D = 1$; (b) $C/D = 1.5$; (c) $C/D = 2$; (d) $C/D = 2.5$

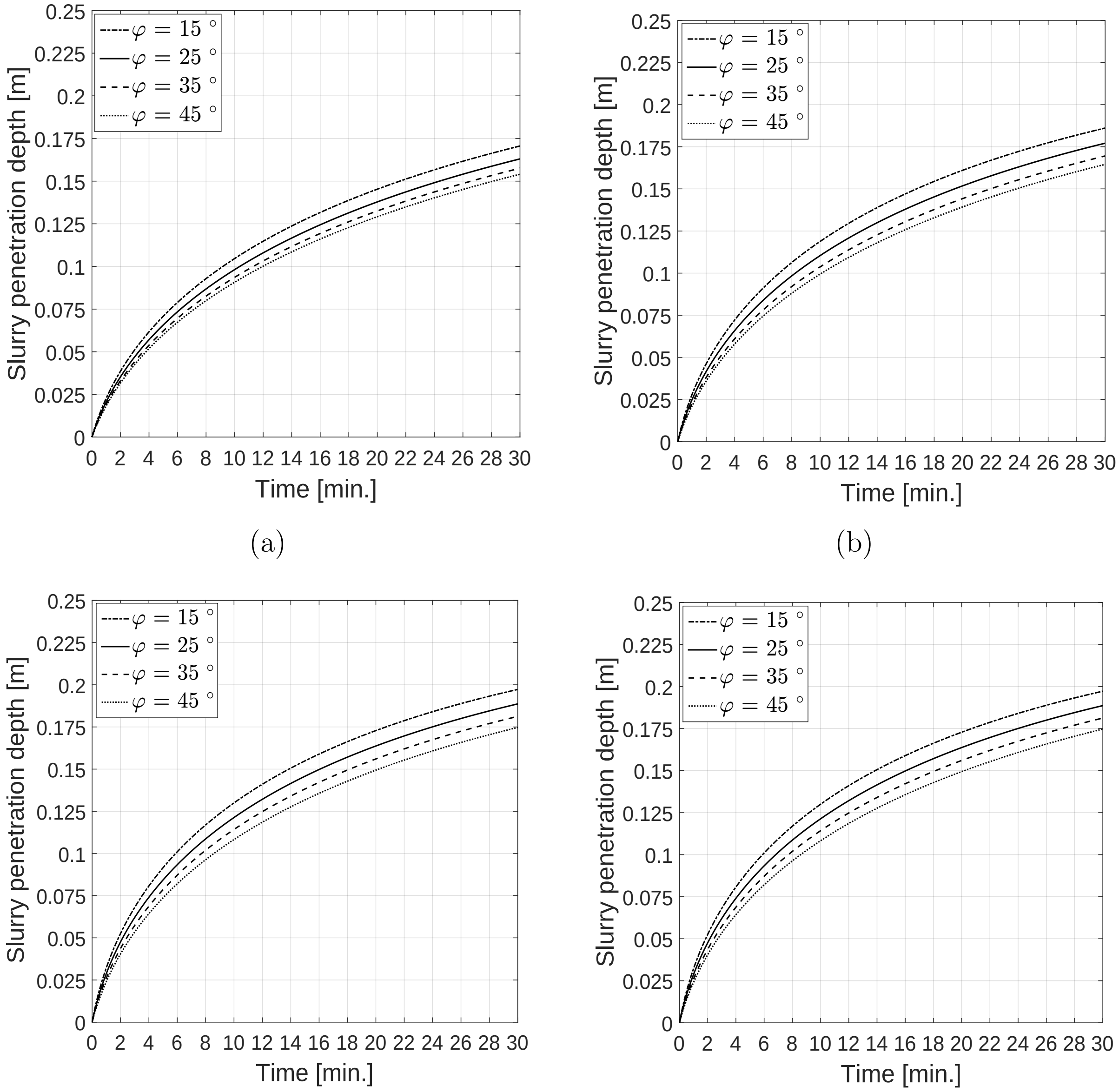

(a) (b)

(c) (d)

Figure 6.23: Slurry penetration depth with time for Horn (1961) model: (a) $C/D = 1$; (b) $C/D = 1.5$; (c) $C/D = 2$; (d) $C/D = 2.5$

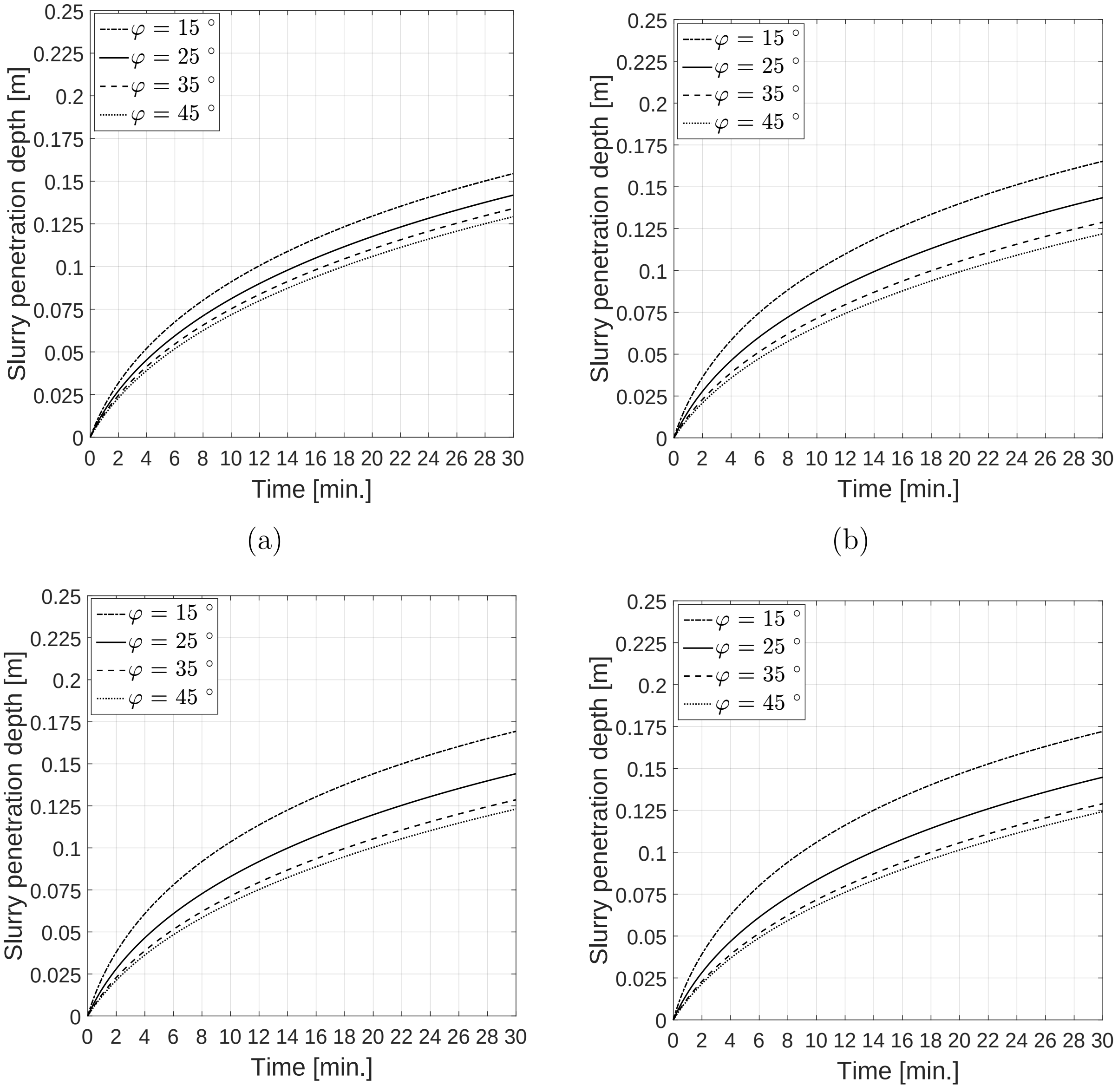

(a) (b)

(c) (d)

Figure 6.24: Slurry penetration depth with time for Anagnostou & Kovari (1994) model: (a) $C/D = 1$; (b) $C/D = 1.5$; (c) $C/D = 2$; (d) $C/D = 2.5$

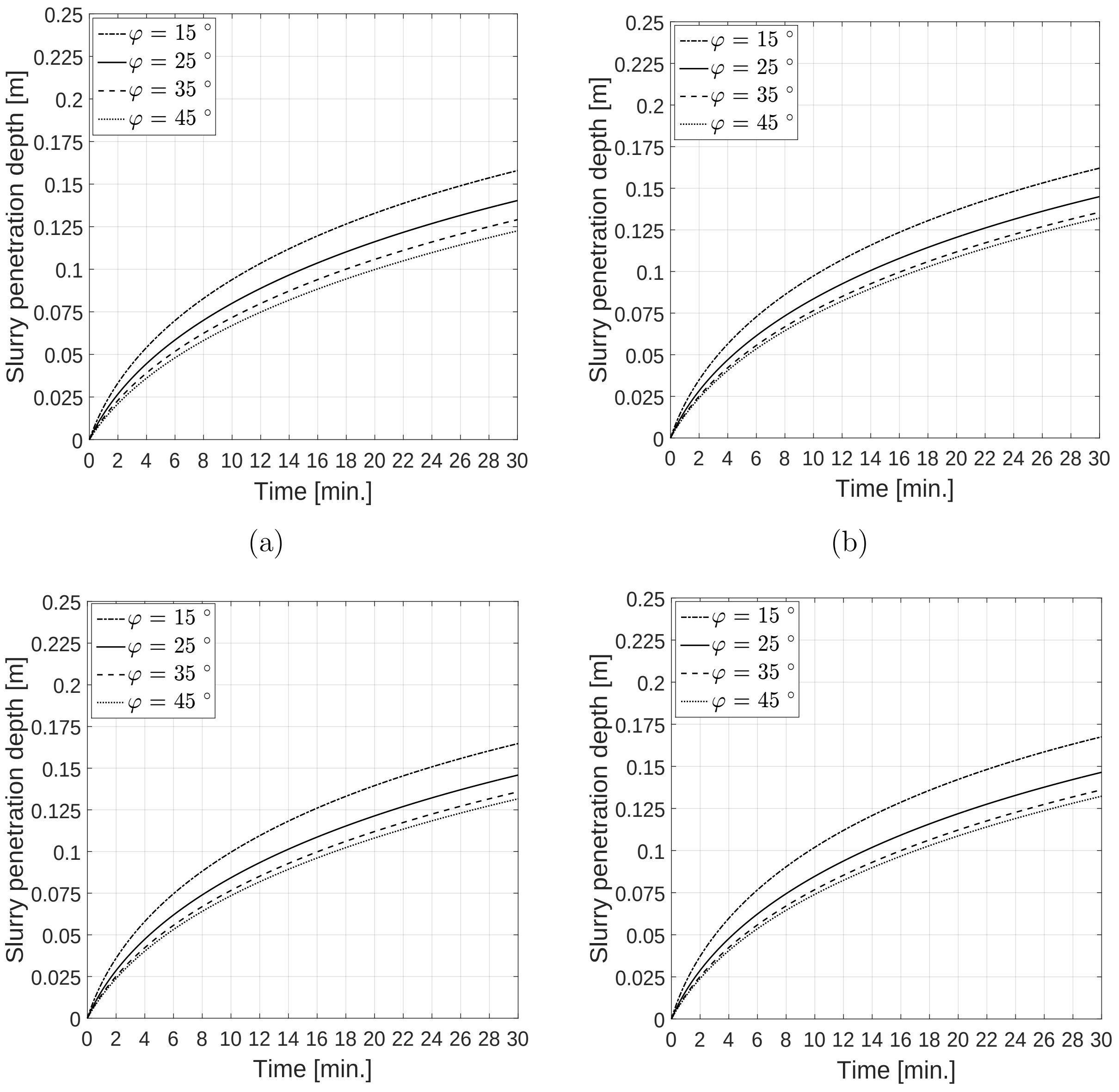

(a) (b)

(c) (d)

Figure 6.25: Slurry penetration depth with time for Broere (2001) model: (a) $C/D = 1$; (b) $C/D = 1.5$; (c) $C/D = 2$; (d) $C/D = 2.5$

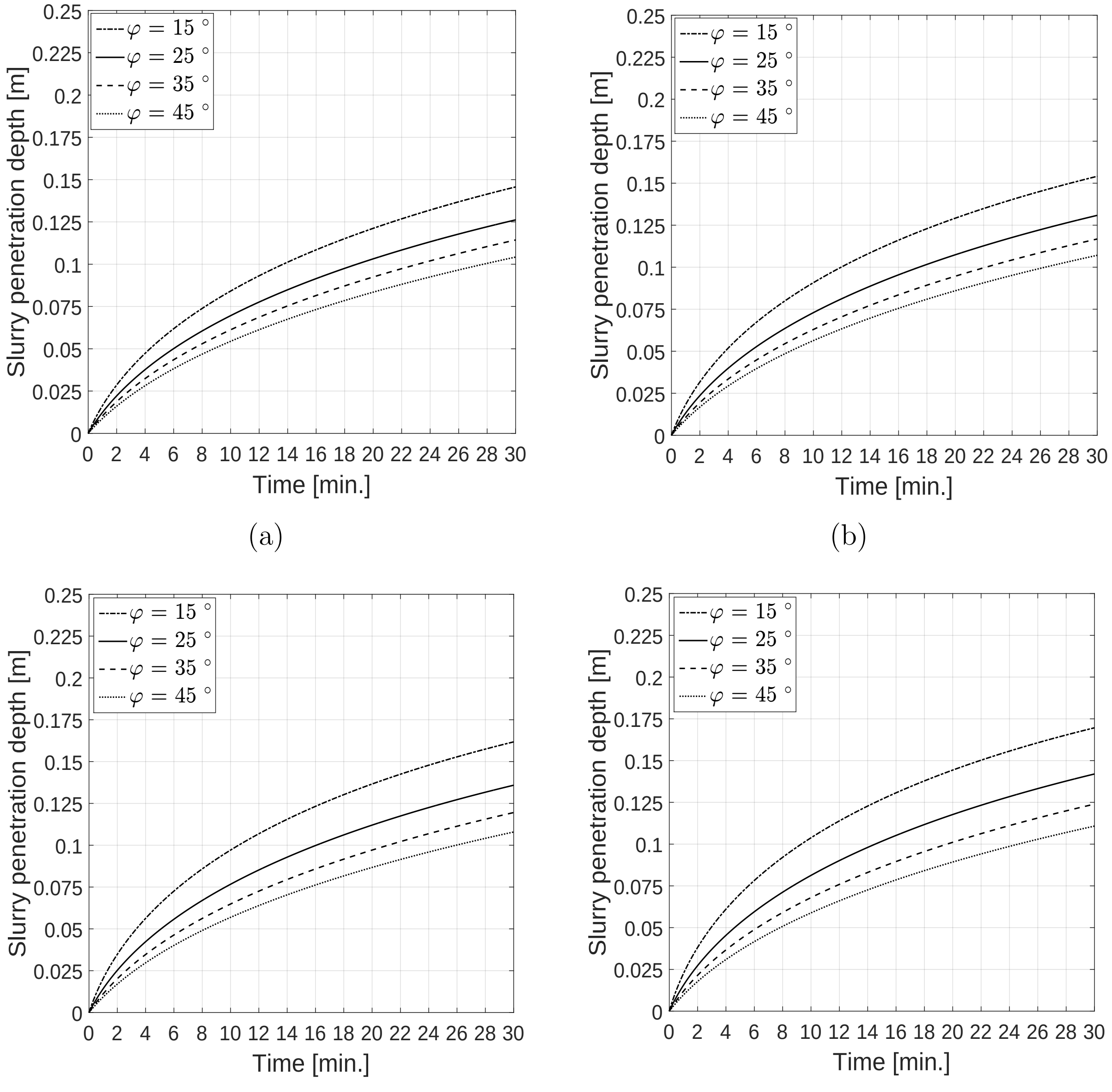

(a)

(b)

(c)

(d)

Figure 6.26: Slurry penetration depth with time for KEM model (M2): (a) $C/D = 1$; (b) $C/D = 1.5$; (c) $C/D = 2$; (d) $C/D = 2.5$

Table 6.2: Soil parameters and tunnel geometry

Parameter	Value	Unit
Tunnel diameter (D)	10	[m]
Cover depth (C)	20	[m]
Friction angle of the soil (φ')	25	[^{o}]
Cohesion of the soil (c)	0	[kPa]
Maximum penetration depth (L)	0.25	[m]
Drilling velocity of the slurry TBM (v_{TBM})	1	[mm/s]
Unit weight of saturated soil (γ_{sat})	20	[kN/m^3]
Unit weight of supported medium (γ_s)	12	[kN/m^3]
Permeability of the soil (k)	10^{-4}	[m/s]
Permeability of the soil for the slurry (k_g)	10^{-6}	[m/s]
Porosity of the soil (n)	0.4	[-]

6.10 Practical example

The following example is provided for determining the operational support pressure and the piezometric head at TBM in closed-face tunneling.

It is proposed to use a slurry the TBM to excavate a circular tunnel in homogenous purely frictional soil. The soil is assumed to be fully saturated with the ground water table at the ground surface. No surcharge surface pressure exists ($q = 0$ kPa). The soil parameters and the tunnel geometry are shown in Table 6.2. The tunnel engineer should determine the operational support pressure in the work chamber, so that the slurry TBM can be operated safely. A safety margin of 10 kPa is considered in the analysis. The analysis will be performed using four different models, KEM model (M2) and the models of Horn (1961), Anagnostou & Kovari (1994) and Broere (2001) models.

The following two methods are used to determine the operational support pressure:

1. Determining the operational support pressure considering only hydrostatic pore pressure.
2. Determining the operational support pressure considering hydrostatic and excess pore pressures.

In this example, the operational support pressure is calculated with a simple procedure using the design graphs which are given in this thesis or can be obtained from the published data in literature.

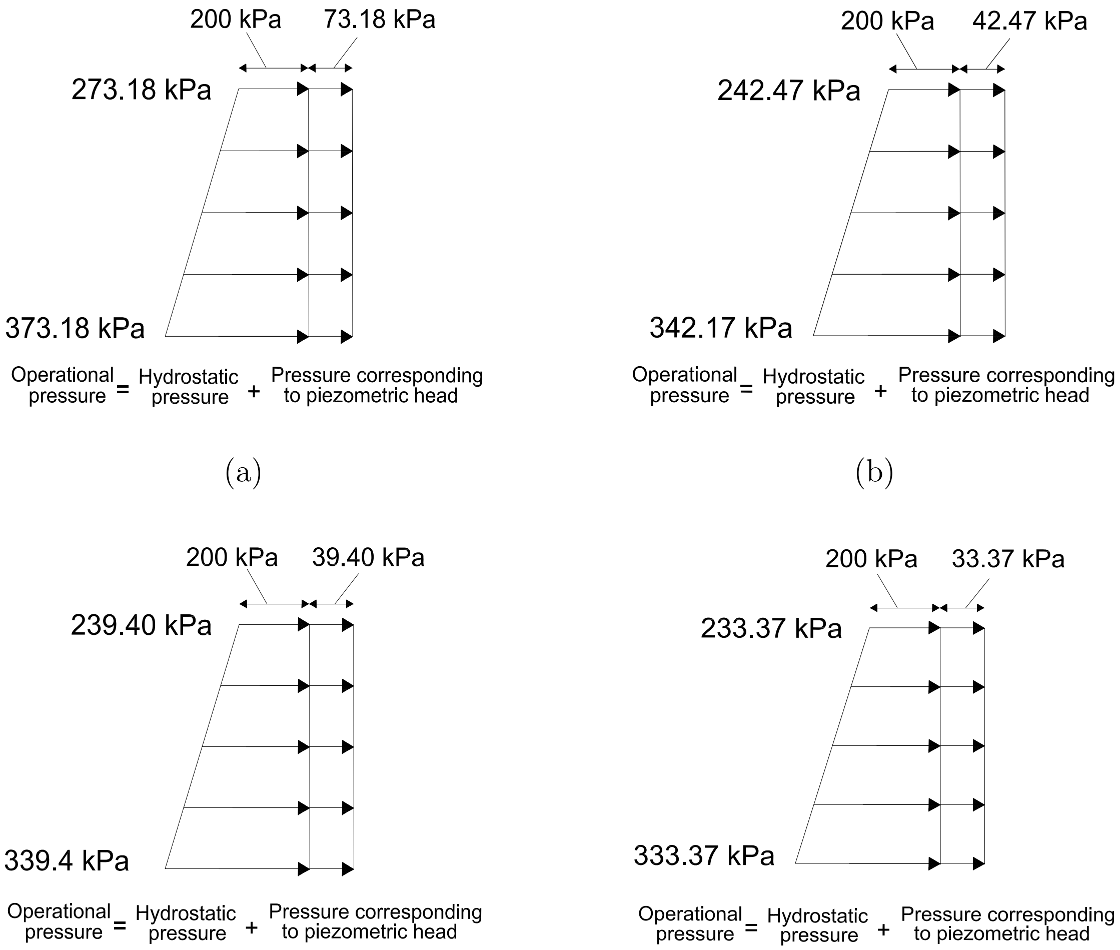
200 kPa
73.18 kPa
273.18 kPa
373.18 kPa
Operational pressure = Hydrostatic pressure + Pressure corresponding to piezometric head
200 kPa
42.47 kPa
242.47 kPa
342.17 kPa
Operational pressure = Hydrostatic pressure + Pressure corresponding to piezometric head
200 kPa
39.40 kPa
239.40 kPa
339.4 kPa
Operational pressure = Hydrostatic pressure + Pressure corresponding to piezometric head
200 kPa
33.37 kPa
233.37 kPa
333.37 kPa
Operational pressure = Hydrostatic pressure + Pressure corresponding to piezometric head

(a) (b)

(c) (d)

Figure 6.27: Operational support pressure considering hydrostatic pore pressure: (a) Horn (1961) model; (b) Anagnostou & Kovari (1994) model; (c) Broere (2001) model; (d) KEM model (M2)

Table 6.3: Operational support pressure for different models considering only hydrostatic pore pressure

Operational support pressure (kPa)	Horn (1961)	Anagnostou & Kovari (1994)	Broere (2001)	KEM model (M2)
Crown	273.18	242.47	239.40	233.37
Center	323.18	292.47	289.40	283.37
Bottom	373.18	342.47	339.40	333.37

Table 6.4: Piezometric head for different models considering only hydrostatic pore pressures

Piezometric head (m)	Horn (1961)	Anagnostou & Kovari (1994)	Broere (2001)	KEM model (M2)
Crown	7.32	4.25	3.94	3.34
Center	7.32	4.25	3.94	3.34
Bottom	7.32	4.25	3.94	3.34

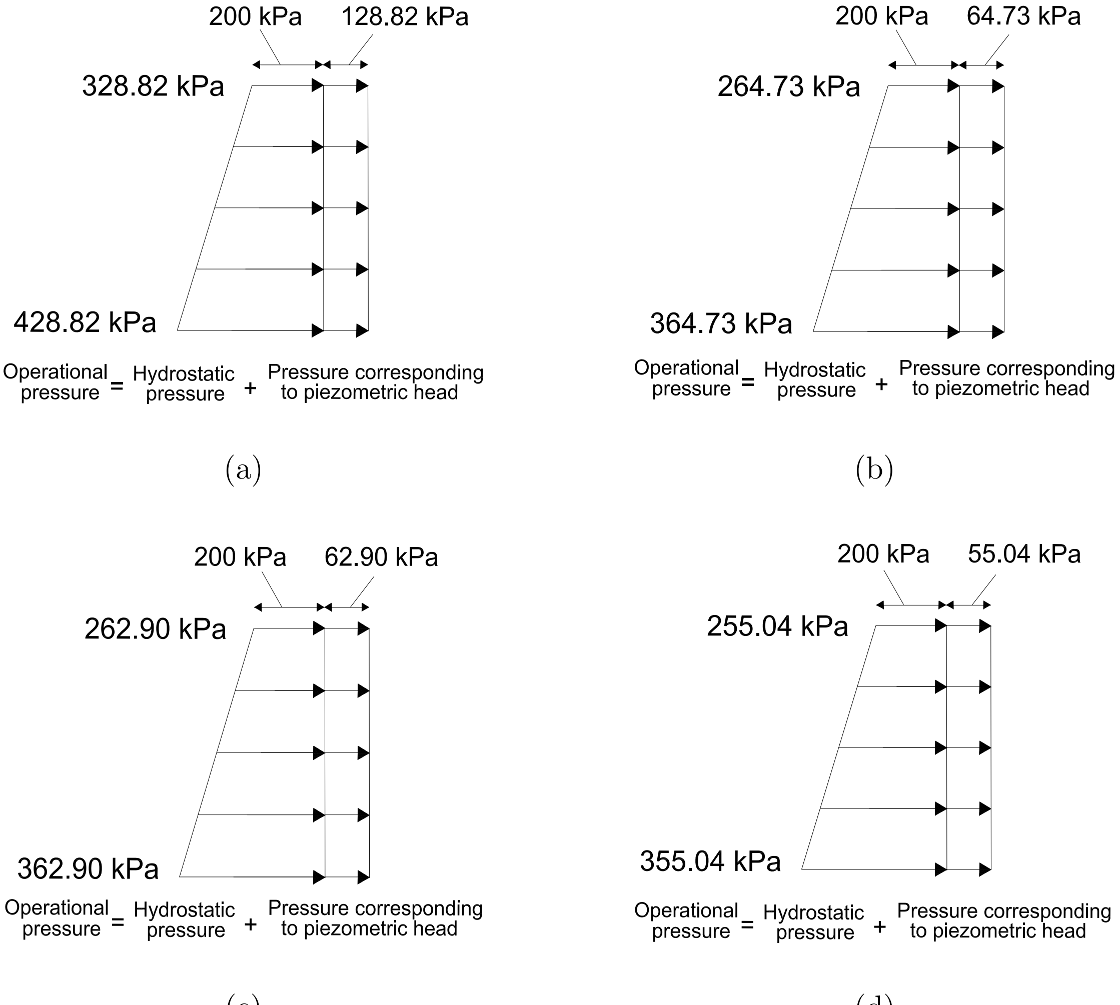
200 kPa
128.82 kPa
328.82 kPa
428.82 kPa
Operational pressure = Hydrostatic pressure + Pressure corresponding to piezometric head
200 kPa
64.73 kPa
264.73 kPa
364.73 kPa
Operational pressure = Hydrostatic pressure + Pressure corresponding to piezometric head
200 kPa
62.90 kPa
262.90 kPa
362.90 kPa
Operational pressure = Hydrostatic pressure + Pressure corresponding to piezometric head
200 kPa
55.04 kPa
255.04 kPa
355.04 kPa
Operational pressure = Hydrostatic pressure + Pressure corresponding to piezometric head

(a) (b)

(c) (d)

Figure 6.28: Operational support pressure considering hydrostatic and excess pore pressures: (a) Horn (1961) model; (b) Anagnostou & Kovari (1994) model; (c) Broere (2001) model; (d) KEM model (M2)

Table 6.5: Operational support pressure for different models considering hydrostatic and excess pore pressures

Operational support pressure (kPa)	Horn (1961)	Anagnostou & Kovari (1994)	Broere (2001)	KEM model (M2)
Crown	328.82	264.73	262.9	255.04
Center	378.82	314.73	312.90	305.04
Bottom	428.82	364.73	362.90	355.04

Table 6.6: Piezometric head for different models considering hydrostatic and excess pore pressures

Piezometric head (m)	Horn (1961)	Anagnostou & Kovari (1994)	Broere (2001)	KEM model (M2)
Crown	12.89	6.49	6.27	5.50
Center	12.89	6.49	6.27	5.50
Bottom	12.89	6.49	6.27	5.50

Table 6.7: Penetration velocity (v_p) for different models

	Horn (1961)	Anagnostou & Kovari (1994)	Broere (2001)	KEM (M2)
Pore velocity (mm/s)	0.64	0.32	0.31	0.27

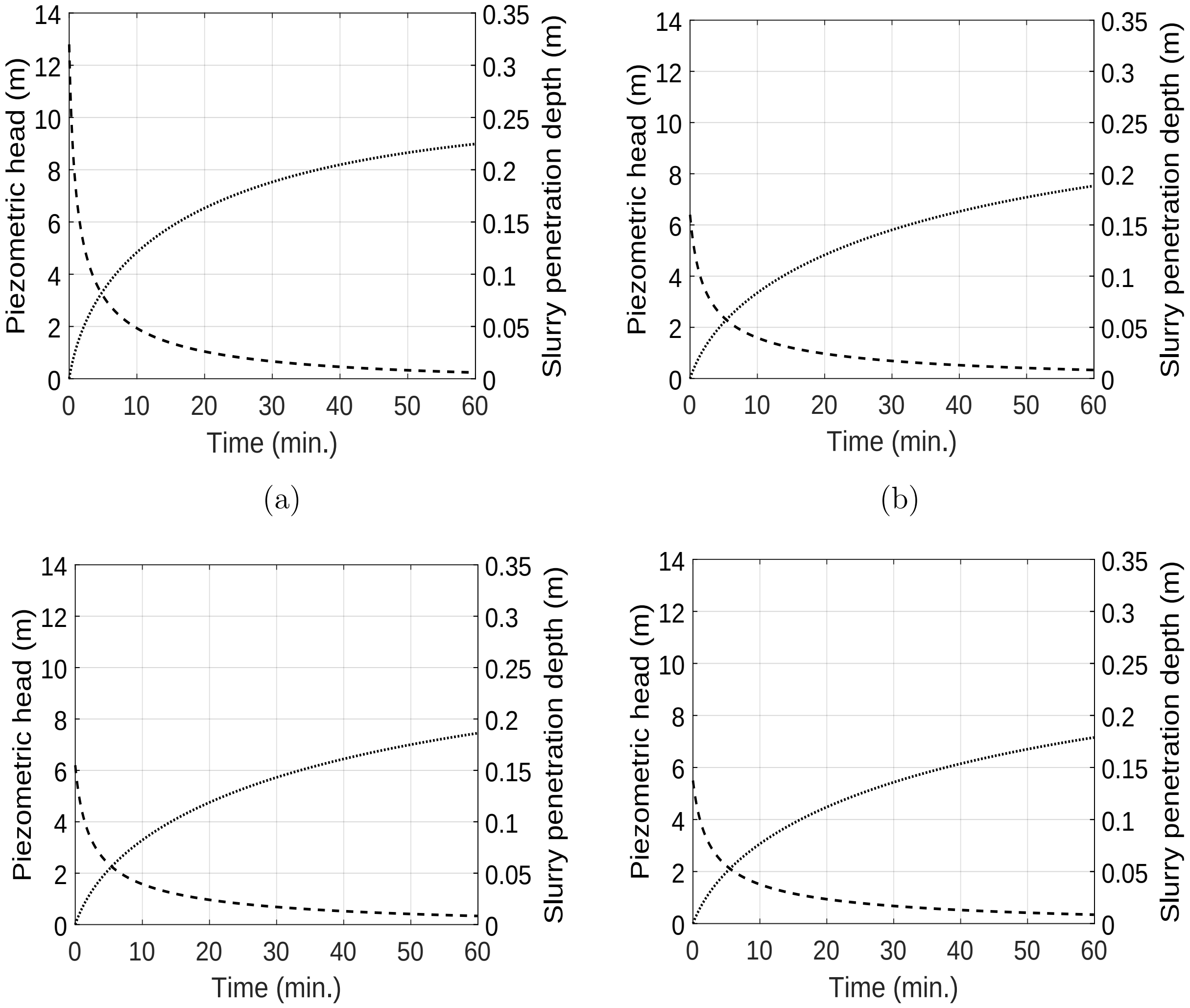

Figure 6.29: Slurry penetration depth with time for different model: (a) Horn (1961) model; (b) Anagnostou & Kovari (1994) model; (c) Broere (2001) model; (d) KEM model (M2)

6.10.1 Determination of operational support pressure considering only hydrostatic pore pressure

Within this method, only the effect of hydrostatic pore pressure on the operational support pressure is considered. The calculation results are presented in Tables 6.3 and 6.4. The presented values for the operational support pressure are the sum of effective and the pore pressure at the crown, axis or the bottom of the tunnel face.

The following four steps are used to determine the operational support pressure.

1. Calculating N_γ for dry soil which can be obtained from given graph in this thesis (e.g., Fig 5.18, Chapter 5) or from publications on the applied wedge-silo models. Then, use Eqs. (6.41), (6.42) and (6.43) for calculating the effective and the total support pressure.
2. Adding the safety margin of 10 kPa for the effective support pressure resulting in the pressure corresponding to the piezometric head.
3. The operational support pressure p_o is equal to the sum of the pressure corresponding to the piezometric head and the hydrostatic pore pressure.
4. The maximum support pressure (p_{max}) is calculated using Eq. (6.6) resulting in $p_{max} = 460$ kPa, for the given example, which is higher than the operational support pressure for all stability models, see Table 6.3.

The calculated operational support pressures are graphically shown in Fig. 6.27.

6.10.2 Determination of operational support pressure considering hydrostatic and excess pore pressures

In this method, both the effect of hydrostatic and excess pore pressures on the operational support pressure p_o is considered. The values of the operational support pressures are presented in Table 6.5 at the crown, axis or the bottom of the tunnel face.

The following five steps are used to determine the operational support pressure.

1. Obtaining the value of $p_o/\gamma' D$ from Fig. 6.18 ($C/D = 2$, $\varphi' = 25^o$) for different stability models. Thereafter, the operational support pressure p_o is calculated. The calculated operational support pressures are graphically shown in Fig. 6.28.

2. The maximum support pressure (p_{max}) is 460 kPa, which is higher than the operational support pressure for all stability models, see Table 6.5
3. The pressure corresponding to piezometric head u_{ϕ_o} is calculated by subtracting the hydrostatic pore pressure from the operational support pressure ($u_{\phi_o} = p_o - u$). Thereafter, the piezometric head ϕ_o is calculcaltd by dividing u_{ϕ_o} with γ_w ($\phi_o = \frac{u_{\phi o}}{\gamma_w}$), see Table 6.6
4. The penetration velocity (v_p) is calculated for each stability model using Eq. (6.15). Then, the penetration velocity is compared with drilling velocity of TBM (v_{TBM}). As can be seen from Tables 6.2 and 6.7, the penetration velocity (v_p) for every stability model is less than the drilling velocity of TBM (v_{TBM} = 1 mm/s) . This means that the supporting fluid will not be able to penetrate further than the depth that is scraped away during each cutterhead rotation.
5. Calculating the drop in piezometric head with time for each stability model during the stand-still phase using Eq. (6.18) or using Figs. 6.19 to 6.22. The results for each model are presented in Fig. 6.29.

6.11 Summary

Tunnels are often constructed below the water table. Therefore, the destabilizing effect induced by the hydrostatic and excess pore pressure should be taken into account in calculating the minimum support pressure. The traditional wedge-silo models and KEM model (M2) have been extended to consider with the excess pore pressure.

The excess pore pressure distribution resulting from the model of Bezuijen (2002) has been integrated into these stability models. After adding the external forces caused by the excess pore pressure into the equations of static equilibrium, the total support pressure for stabilizing the tunnel face is obtained. The results show a significant influence of excess pore pressure on the calculated operational support pressure.

Numerous calculations were carried out and dimensionless graphs for the operational support pressure were developed. These graphs allow a quick assessment of the tunnel face stability in case of fully saturated soil. A practical example is provided, demonstrating the potential use of the proposed design charts.

7 Conclusions and future work

7.1 Conclusions

The stability and safety of the excavation face has always been of great concern in tunnel construction. The support pressure needed at the face of the tunnel can be determined using various analytical and numerical methods. The main goal of this research is to apply the principle of Kinematical Element Method (KEM) to investigate the stability of the tunnel face in dry or saturated homogenous or layered soil. In order to achieve this objective, three-dimensional (3D) stability KEM models (M, M1 and M2) have been developed. Firstly, 3D KEM model (M) consists of two rigid blocks, a tetrahedron wedge block and a triangular prism block. Thereafter, two different modified KEM models with a failure mechanisms consisting of either five (model M1) or six (model M2) blocks are proposed. The KEM models (M and M2) have been used to investigate the effect of cover to diameter ratio (C/D), internal friction (φ) and cohesion on minimum the support pressure in dry soil. Furthermore, KEM model (M2) has been applied to study the influence of hydrostatic and excess pore pressure on the stability of the tunnel face.

The conclusions derived from the simulations with the three different KEM models have been grouped in three main subsections as follows: conclusions from the basic KEM model (M), conclusions from modified KEM models (M1 and M2) and finally the conclusions drawn regarding the effect of excess pore pressure on the stability of the tunnel face.

KEM model (M)

1. A computer program w with graphical user interface (KEM-3D-T) was developed. Thereafter numerous calculations were carried out with this program. The results were presented in terms of stability charts. These stability charts represent a tool for a convenient estimation of the minimum support pressure on a circular face of a tunnel in dry soil.

2. Based on earth pressure measured above the tunnel crown in physical model tests (Chen et al., 2013), a 3D active earth pressure acting on the one of the surfaces of the vertical prism (silo block) is assumed. The consideration of the 3D active earth pressure on one of the vertical surfaces of the silo block arching in KEM model (M) supersedes any further assumptions.

3. The results of KEM model (M) for minimum support pressure are compared with the results of analytical models, numerical simulations (FEM and DEM) and physical model tests from the literature as well as with the results of own simulations using the Finite Element Limit analysis (FELA). The results show a reasonable agreement with the outcome of these methods for $\varphi \geq 20^o$. Furthermore, the KEM simulations have the advantage of reduced computation time when compared to FEM and FELA models.

4. A formula for calculating the minimum support pressure is proposed in terms of the sum of unit weight of the soil (γ), cohesion (c) and surcharge load (q) multiplied by non-dimensional bearing capacity coefficients N_γ, N_c and N_q respectively. The parametric studies showed that N_γ, N_c and N_q are decreasing with an increase in the friction angle of the soil. The value of N_q becomes equal to zero for C/D ratios greater than or equal to 1.5 at $\varphi \geq 15^o$.

5. The results of KEM model (M) revealed that the cover to diameter ratio C/D has a significant influence on the minimum support pressure. This effect is also deduced from the solutions of other limit equilibrium methods (e.g., Jancsecz & Steiner, 1994; Anagnostou & Kovari, 1994; Broere, 2001) and has been also observed in physical model tests (Chambon & Corte, 1994; Chen et al., 2011).

6. The results of the KEM simulations indicate that for all surfaces of the silo part above the tunnel face, the values of the 3D lateral earth pressure coefficients (K_{3D}) are very close. A new equation for the determination of the 3D lateral earth pressure coefficient (K_{3D}) between the silo and the adjoining soil is proposed.

7. As a result of searching for the minimum support pressure in the optimizing process of the failure mechanism, the sliding surface between the silo block (upper part) and the wedge block (lower part) is found to be inclined instead of horizontal as assumed by some of the analytical methods. The inclination of this internal failure plane depends on the soil strength parameters, as well as the geometry of the tunnel.

Modified KEM models (M1 and M2)

1. The increase in the number of blocks within the wedge in case of the modified failure mechanism (M1) slightly improves the value of the minimum support pressure, meaning that this value slightly increases. The modified failure mechanism (M1) with its curved failure zone in the soil in front of the tunnel face is more consistent with the failure zones that were observed in physical model tests.
2. The minimum support pressure obtained from KEM model (M2) is higher than that predicted by KEM model (M), which indicates that the solution of the modified failure mechanism (M2) is conservative compared to the failure mechanism assumed in model (M).
3. The results of KEM model (M2) are much closer to the results of Broere (2001) than to those of Anagnostou & Kovari (1994) for $\varphi < 30^o$. In contrast for $\varphi > 30^o$, the solution of KEM model (M2) agrees well with the results of Anagnostou & Kovari (1994).
4. In case of a ground composed of two soil layers, the results of KEM model (M2) predicted a higher minimum support pressure than KEM model (M), FELA and other upper bound solutions. However, the simulations with KEM model (M2) gave a lower minimum support pressure than wedge-silo models.
5. For open face tunneling, as expected the result of the KEM calculations indicate that by increasing the friction angle and the cohesion of the soil, the safety factor increases. The results also demonstrate that the ratio of cover to diameter (C/D) has a significant effect on the safety factor.
6. On the basis of the results from simulations with KEM model (M2), a number of design charts and fitting formulas have been established. These charts and formulas enable an assessment of the support pressure that needs to be applied on the tunnel face to ensure the stability of the tunnel face. These charts can be used by geotechnical engineers for preliminary design of closed face and open face tunneling.

Effect of excess pore pressure on the stability of the tunnel face

1. A tunnel excavation below the ground water table elevation exerts a significantly unfavourable impact on stability of the tunnel face. In particular, the face pressure required is increasing due to the hydrostatic pore pressure. A large amount of the operational support pressure is needed to equilibrate the hydrostatic pore pressure.

2. The excess pore pressure is incorporated into KEM model (M2) as external forces acting on each face of the wedge. The model of Bezuijen (2002) is used to predict the excess pore water pressures acting on of each face of the failure mechanism.
3. As expected the results of the KEM simulations show that under the influence of hydrostatic and excess pore pressure, an increase of the friction angle of the soil leads to a decrease of the operational support pressure as well as the piezometric head in the TBM chamber.
4. A comparison between the results of different models considering the excess pore pressure revealed that the KEM model (M2) gives lower operational support pressures than the methods of Anagnostou & Kovari (1994) and Broere (2001). However, the differences do not exceed 10%.
5. The excess pore pressure acting on the tunnel face should be considered for proper design and consequently safe construction of a tunnel. Therefore, as a result of a parametric study, a number of design graphs is proposed, in which the normalized operational support pressure is plotted as a function of friction angle for different C/D ratios and for different models.
6. In order to demonstrate the influence of excess pore pressure on the operational support pressure, a practical example is presented.

7.2 Future work

While, the objectives of this research have been achieved, there are some valuable extensions that deserve further studies in future. The potential developments can be stated as follows:

1. Although, KEM model (M2) is composed of six blocks in the failure mechanism gives a good results in comparison to other approaches, a further modification can be implemented to the failure mechanism of KEM model (M2) by increasing the number of blocks in the wedge.
2. A further study can be carried out to investigate the stability of a circular tunnel in purely cohesive soils where the undrained shear strength is either constant or increases linearly with depth.
3. The present study does not take into account the heterogeneity of natural soil. The stability of the tunnel face in multilayered soil with different geometrical soil profiles

(plane, or sloping ground surface, and horizontal or inclined layers) could be further investigated using KEM model (M2).

4. The coupling of KEM model (M2) with other numerical methods (e.g., FEM) can be potentially implemented in suitable computer codes to investigate the effect of excess pore pressure on the operational support pressure.

Bibliography

AFTES (2000), Choosing mechanized tunnelling techniques, recommendations, Technical report.

Anagnostou, G. (2012), 'The contribution of horizontal arching to tunnel face stability', *Geotechnik* **35**, 34–44.

Anagnostou, G. & Kovari, K. (1994), 'The face stability of slurry-shield-driven tunnels', *Tunnelling and Underground Space Technology* **9**, 165–174.

Anagnostou, G. & Kovari, K. (1996), 'Face stability conditions with earth-pressure-balanced shields', *Tunnelling and Underground Space Technology* **11**, 165–173.

Beaver, P. (1972), *A History of Tunnels*, the Citadel Press.

Bezuijen, A. (2002), The influence of permeability on the properties of a foam mixture in a tbm. 4th int, *in* 'Symp. On Geotechnical Aspects of Underground Construction in Soft Ground-IS Toulouse'.

Bezuijen, A., Steeneken, S. & Ruigrok, J. (2016), Monitoring and analysing pressures around a tbm, *in* '13th International conference underground construction', Vol. 1, pp. 1–9.

Bishop, W. (1955), 'The use of the slip circle in the stability analysis of slopes', *Geotechnique* **5**, 7–17.

Broere, W. (2001), Tunnel face stability and new CPT applications, PhD thesis, University of Delft.

Broere, W. & van Tol (2000), 'Influence of infiltration and groundwater flow on tunnel face stability', *Geotechnical Aspects of Underground Construction in Soft Ground, Tokyo, Japan,* pp. 339–344.

Broms, B. & Bennermark, H. (1967), 'Stability of clay in vertical openings', *J. Soil Mech. Found. Div.* **93**, 71–94.

Cairncross, A. M. (1973), Deformations around model tunnels in stiff clay, PhD thesis, University of Cambridge.

Chambon, P. & Corte, J. (1994), 'Shallow tunnels in cohesionless soil: Stability of tunnel face', *Journal of Geotechnical Engineering* **120**, 1148–1165.

Chapman, D. N., Metje, N. & Stark, A. (2017), *Introduction to tunnel construction*, Crc Press.

Chen, R. P., Li, J., Kong, L. G. & Tang, L. J. (2013), 'Experimental study on face instability of shield tunnel in sand', *Tunnelling and Underground Space Technology* **33**, 12–21.

Chen, R. P., Tang, L. J., Ling, D. S. & Chen, Y. (2011), 'Face stability analysis of shallow shield tunnels in dry sandy ground using the discrete element method', *Computers and Geotechnics* **38**, 187–195.

Chen, R. P., Tang, L. J., Yin, X. S., Chen, Y. M. & Bian, X. C. (2015), 'An improved 3D wedge prism model for the face stability analysis of the shield tunnel in cohesionless soils', *Acta Geotechnica* **10**, 683–692.

Date, K., Mair, R. J. & Soga, K. (2008), Reinforcing effects of forepoling and facebolts in tunnelling, *in* '6th International Symposium, Shanghai', CRC Press, pp. 635–641.

DAUB (2016), Deutscher Ausschuss für unterirdisches Bauen e. V. (DAUB). Recommendations for Face Support Pressure Calculations for Shield Tunneling in Soft Ground, Technical report.

Davis, E., Gunn, M., Mair, R. & Seneviratne, H. (1980), 'The stability of shallow tunnels and underground openings in cohesive material', *Geotechnique* **30**(4), 397–416.

Dias, D. (2011), 'Convergence-confinement approach for designing tunnel face reinforcement by horizontal bolting', *Tunnelling and Underground Space Technology* **26**, 517–523.

Dias, T. & Bezuijen, A. (2016), A different view on TBM face equilibrium in permeable ground, *in* 'ITA World Tunnel Congress, San Francisco, USA'.

Drucker, D., Greenberg, W. & Prager, W. (1951), 'The safety factor of an elastic plastic body in plane strain', *Trans. ASME J. Appl. Mech.* **73**, 371–378.

Funatsu, T., Hoshino, T., Sawae, H. & Shimizu, N. (2008), 'Numerical analysis to better understand the mechanism of the effects of ground supports and reinforcements on the stability of tunnels using the distinct element method', *Tunnelling and Underground Space Technology* **23**, 561–573.

Gussmann, P. (1982), Kinematical elements for soils and rocks, *in* 'Proceedings of 4th international conference on numerical methods in geomechanics, Edmonton', pp. 47–52.

Gussmann, P. (1986), Kinematical Element Method for 3D Problems in Geomechanics, *in* 'ECONMIG, Stuttgart', Vol. 2.

Gussmann, P., König, D. & Schanz, T. (2016), 'Die methode der kinematischen elemente in der geotechnik–aktuelle entwicklungen und anwendungen', *geotechnik* **39**(1), 40–53.

Han, K., Zhang, C. & Zhang, D. (2016), 'Upper-bound solutions for the face stability of a shield tunnel in multilayered cohesive-frictional soils', *Computers and Geotechnics* **79**, 1–9.

Hemphill, B. (2012), *Practical Tunnel Construction*, John Wiley and Sons, New York.

Hisatake, M. & Ohno, S. (2008), 'Effects of pipe roof supports and the excavation method on the displacements above a tunnel face', *Tunnelling and Underground Space Technology* **23**, 120–127.

Horn, N. (1961), 'Horizontaler Erddruck auf senkrechte Abschlussflächen von Tunnelröhren', *National Conference of the Hungarian Civil Engineering Industry, Budapest* pp. 7–16.

Huder, J. (1972), Stability of bentonite slurry trenches with some experiences in swiss practice, *in* '5th European conference on soil mechanics and foundation engineering. Madrid', pp. 517–522.

Ibrahim, E., Soubra, A. H., Mollon, G., Raphael, W., Dias, D. & Reda, A. (2015), 'Three-dimensional face stability analysis of pressurized tunnels driven in a multilayered purely frictional medium', *Tunnelling and Underground Space Technology* **49**, 18–34.

Idinger, G., Aklik, P., Wu, W. & Borja, R. (2011), 'Centrifuge model test on the face stability of shallow tunnel', *Acta Geotechnica* **6**, 105–117.

ITA (2009), General report on conventional tunneling method, Technical report.

Jaky, J. (1944), 'The coefficient of earth pressure at rest', *Journal for Society of Hungarian Architects and Engineers* **78**, 355–358.

Jancsecz, S. & Steiner, W. (1994), Face support for a large mix-shield in heterogeneous ground conditions, *in* '7th International Symposium Tunnelling , London', pp. 189–195.

Janssen, H. (1895), 'Versuche über Getreidedruck in Silozellen', *Zeitschrift des Vereines deutscher Ingenieure* **39**, 1045–1049.

Juneja, A., Hedge, A., Lee, F. & Yeo, C. (2010), 'Centrifuge modelling of tunnel face reinforcement using forepoling', *Tunnelling and Underground Space Technology* **25**, 526–542.

Kennedy, J. & Eberhart, R. (1995), Particle swarm optimization (pso), *in* 'Proc. IEEE International Conference on Neural Networks, Perth, Australia', pp. 1942–1948.

Khezri, N., Mohamad, H., Hassani, M. & Fatahi, B. (2015), 'The stability of shallow circular tunnels in soil considering variations in cohesion with depth', *Tunnelling and Underground Space Technology* **49**, 230–204.

Kim, S. H. & Tonon, F. (2010), 'Face stability and required support pressure for TBM driven tunnels with ideal face membrane drained case', *Tunnelling and Underground Space Technology* **25**, 526–542.

Kimura, T. & Mair, R. (1981), Centrifugal testing of model tunnels in soft soil, *in* '10th Int. Conf. Soil Mech. Found. Engng., Stockholm', Vol. 1, pp. 319–322.

Kirsch, A. (2009), *On the face stability of shallow tunnels in sand*, Advances in geotechnical engineering and tunnelling No.16, Logos, Berlin.

Kirsch, A. (2010*a*), 'Experimental investigation of the face stability of shallow tunnels in sand', *Acta Geotechnica* **5**, 43–62.

Kirsch, A. (2010*b*), Numerical investigation of the face stability of shallow tunnels in sand, *in* 'Numerical Methods in Geotechnical Engineering', CRC Press, pp. 795–800.

Kirsch, A. & Kolymbas, D. (2005), 'Theoretische Untersuchung zur Ortsbruststabilität', *Bautechnik* **82**(7), 449–456.

Klar, A., Osman, A. & Bolton, M. (2007), '2d and 3d upper bound solutions for tunnel excavation using elastic flow fields', *Int. J. Numer. Anal. Meth. Geomech.* **31**(12), 1367–1374.

Krabbenhoft, K., Lyamin, A. & Krabbenhoft, J. (2015), 'Optum computational engineering (optumg2)', *Computer software. URL: https://www. optumce. com* .

Krause, T. (1987), Schildvortrieb mit flüssigkeits und erdgestützter Ortsbrust, PhD thesis, Technischen Universität Carolo-Wilhelmina, Braunschweig.

Leca, E. & Dormieux, L. (1990), 'Upper and lower bound solutions for the face stability of shallow circular tunnels in frictional material', *Geotechnik* **40**, 581–606.

Lee, M. & Nam, W. (2004), 'Effect of tunnel advance rate on seepage forces acting on the underwater tunnel face', *Tunnelling and Underground Space Technology* **19**, 273–281.

Li, Y., Emeriault, F., Kastner, R. & Zhang, Z. (2009), 'Stability analysis of large slurry shield-driven tunnel in soft clay', *Tunnelling and Underground Space Technology* **24**, 472–481.

Lin, X., Liu, Y., Kang, X., Chen, J. & Chen, R. (2018), Numerical simulation on the development of soil arching induced by epbs tunnelling, *in* 'Proceedings of the 2nd International Symposium on Asia Urban GeoEngineering', Springer, pp. 575–582.

Liu, W., Zhao, Y., Shi, P., Li, J. & Gan, P. (2018), 'Face stability analysis of shield-driven tunnels shallowly buried in dry sand using 1-g large scale model tests', *Acta Geotechnica* **13**, 693–705.

Liu, X., Wang, F., Fang, H. & Yuan, D. (2019), 'Dual-failure-mechanism model for face stability analysis of shield tunneling in sands', *Tunnelling and Underground Space Technology* **85**, 196–208.

Lyamin, A. & Sloan, S. (2000), Stability of a plane strain circular tunnel in a cohesive frictional soil, *in* ‘J.R. Booker Memorial symposium, Sydney’, pp. 139–153.

Maidl, B., Herrenknecht, M., Maidl, U. & Wehrmeyer, G. (2012), *Mechanised Shield Tunnelling*, Ernst and Sohn.

Mair, R. (1979), Centrifugal modeling of tunnel construction in soft clay, PhD thesis, University of Cambridge.

Mayer, P., Hartwig, U. & Schwab, C. (2003), ‘Standsicherheitsuntersuchungen der Ortsbrust mittles Bruchkörpermodell und FEM’, *Bautechnik* **80**, 452–467.

Maynar, M. & Rodriguez, L. (2005), ‘Discrete numerical model for analysis of earth pressure balance tunnel excavation’, *Journal of Geotechnical and Geoenvironmental Engineering* **131**, 1234–1242.

Messerli, J., Pimentel, E. & Anagnostou, G. (2010), ‘Experimental study into tunnel face collapse in sand’, *Springman, Laue, Seward (Eds.), Physical Modelling in Geotechnics* **1**, 575–580.

Michalowski, R. L. (1997), ‘An estimate of the influence of soil weight on bearing capacity using limit analysis’, *Soils Found.* **4**(37), 57–64.

Michalowski, R. L. (2001), ‘Upper bound load estimates on square and rectangular footings’, *Geotechnique* **9**(51), 787–798.

Moller, S. (2006), Tunnel induced settlements and structural forces in linings, PhD thesis, Stuttgard University, Germany.

Mollon, G., Dias, D. & Soubra, A. (2012), ‘Continuous velocity fields for collapse and blowout of a pressurized tunnel face in purely cohesive soil’, *International Journal for Numerical and Analytical Methods in Geomechanics* **37**(13), 2061–2083.

Mollon, G., Dias, D. & Soubra, A. H. (2010), ‘Face stability analysis of circular tunnels driven by a pressurized shield’, *Journal of Geotechnical and Geoenvironmental Engineering* **136**, 215–229.

Ng, W. & Lee, G. (2002), ‘A three dimensional parametric study of the use of soil nails for stabilising tunnel faces’, *Computers and Geotechnics* **29**, 673–697.

Ohta, T. & Kiya, H. (2001), ‘Experimental study and numerical analysis on stability of tunnel face in sandy ground’, *Quarterly Report of RTRI* **42**(3), 156–160.

Osman, A., Mair, R. & Bolton, M. (2006), 'On the kinematics of 2D tunnel collapse in undrained clay', *Geotechnique* **56**(9), 585–595.

Peila, D. (1994), 'A theoretical study of reinforcement influence on the stability of a tunnel face', *Geotechnical and Geological Engineering* **12**, 145–168.

Rankine, M. (1857), 'On the stability of loose earth', *Philos. Trans. R. Soc. London* **1**, 9–27.

Schofield, A. N. (1980), 'Cambridge geotechnical centrifuge operations', *Geotechnique* **30**, 227–268.

Senent, S. & Jimenez, R. (2015), 'A tunnel face failure mechanism for layered ground, considering the possibility of partial collapse', *Tunnelling and Underground Space Technology* **47**, 182–192.

Sloan, S. & Assadi, A. (1993), Stability of shallow tunnels in soft ground, *in* 'Holsby GT; Schofield AN, editors. Predictive Soil Mechanics, Proceedings of the Wroth Memorial Symposium. London: Thomas Telford', pp. 644–653.

Sloan, S. W. (1988), 'Lower bound limit analysis using finite elements and linear programming', *International Journal for Numerical and Analytical Methods in Geomechanics* **12**, 61–77.

Sloan, S. W. (1989), 'Upper bound limit analysis using finite elements and linear programming', *International Journal for Numerical and Analytical Methods in Geomechanics* **13**, 263–282.

Sloan, Sand Assadi, A. (1994), 'Undrained stability of a plane strain heading', *Can. Geotech. J.* **31**, 443–450.

Soubra, A. H. & Regenass, P. (2000), 'Three-dimensional passive earth pressures by kinematical approach', *Geotech. Geoenviron. Eng.* **11**(126), 969–978.

Sterpi, D. & Cividini, A. (2004), 'A physical and numerical investigation on the stability of shallow tunnels in strain softening media', *Rock Mechanics and Rock Engineering* **37**, 277–298.

Takano, D., Otani, J., Nagatani, H. & Mukunoki, T. (2006), Application of X-ray CT boundary value problems in geotechnical engineering-research on tunnel face failure, *in* 'Geocongress, ASCE, Reston, VA,', pp. 1–6.

Talmon, A. M., Mastbergen, D. R. & Huisman, M. (2013), 'Invasion of pressurized clay suspensions into granular soil', *Journal of Porous Media* **16**, 351–365.

Tang, W., Liu, W., Albers, B. & Savidis, S. (2014), 'Upper bound analysis of tunnel face stability in layered soils', *Acta Geotechnica* **9**, 661–671.

Terzaghi, K. (1943), *Theoretical soil Geomechanics*, Wiley and Sons, New York.

tom Wörden, F. & Achmus, M. (2013), 'Numerical modeling of three-dimensional active earth pressure acting on rigid walls', *Computers and Geotechnics* **51**, 83–90.

tunnelingonline (2019), 'Tunnel business magazine', *URL: https://www. optumce. com* .

Vermeer, P. A., Ruse, N. M. & Marcher, T. (2002), 'Tunnel heading stability in drained ground', *Felsbau* **20**, 8–18.

Walz, B. & Prager, J. (1978), 'Der Nachweis der äußeren Standsicherheit suspensionsgestützter Erdwände nach der Elementscheibentheorie', *Veröffentlichungen des Grundbauinstituts der Technischen Universität Berlin, Heft 4* .

Washbourne, J. (1984), 'The three-dimensional stability analysis of diaphragm wall excavations', *Ground Eng.* **17**, 24–29.

Yamamoto, K., Lyamin, A. V., Wilson, D. W., Sloan, S. W. & Abbo, A. J. (2011), 'Stability of a single tunnel in cohesive frictional soil subjected to surcharge loading', *Canadian Geotechnical Journal* **48**, 1841–1854.

Yamamoto, K., Lyamin, A. V., Wilson, D. W., Sloan, S. W. & Abbo, A. J. (2013), 'Stability of dual circular tunnels in cohesive-frictional soil subjected to surcharge loading', *Computers and Geotechnics* **50**, 41–54.

Zhang, C., Han, K. & Zhang, D. (2015), 'Face stability analysis of shallow circular tunnels in cohesive frictional soils', *Tunnelling and Underground Space Technology* **50**, 345–357.

Zhang, Z., Hu, X. & Scott, K. D. (2011), 'A discrete numerical approach for modeling face stability in slurry shield tunnelling in soft soils', *Computers and Geotechnics* **38**(1), 94–104.

ZTV (2012), Zusätzliche Technische Vertragsbedingungen und Richtlinien für Ingenieurbauten. Teil 5: Tunnelbau. Abschnitt 3: Maschinelle Vortriebsverfahren. Bundesanstalt für Straßenwesen, in German, Technical report.

Schriftenreihe des Lehrstuhls für Grundbau, Boden- und Felsmechanik der Ruhr-Universität Bochum

Herausgeber: H.L. Jessberger

1 (1979) **Hans Ludwig Jessberger**
Grundbau und Bodenmechanik an der Ruhr-Universität Bochum

2 (1978) **Joachim Klein**
Nichtlineares Kriechen von künstlich gefrorenem Emschermergel

3 (1979) **Heinz-Joachim Gödecke**
Die Dynamische Intensivverdichtung wenig wasserdurchlässiger Böden

4 (1979) **Poul V. Lade**
Three Dimensional Stress-Strain Behaviour and Modeling of Soils

5 (1979) **Roland Pusch**
Creep of soils

6 (1979) **Norbert Diekmann**
Zeitabhängiges, nichtlineares Spannungs-Verformungsverhalten von gefrorenem Schluff
unter triaxialer Belastung

7 (1979) **Rudolf Dörr**
Zeitabhängiges Setzungsverhalten von Gründungen in Schnee, Firn und Eis
der Antarktis am Beispiel der deutschen Georg-von-Neumayer- und Filchner-Station

8 (1984) **Ulrich Güttler**
Beurteilung des Steifigkeits- und Nachverdichtungsverhaltens von
ungebundenen Mineralstoffen

9 (1986) **Peter Jordan**
Einfluss der Belastungsfrequenz und der partiellen Entwässerungsmöglichkeiten auf die Verflüssigung von Feinsand

10 (1986) **Eugen Makowski**
Modellierung der künstlichen Bodenvereisung im grundwasserdurchströmten
Untergrund mit der Methode der finiten Elemente

11 (1986) **Reinhard A. Beine**
Verdichtungswirkung der Fallmasse auf Lastausbreitung in nichtbindigem
Boden bei der Dynamischen Intensivverdichtung

12 (1986) **Wolfgang Ebel**
Einfluss des Spannungspfades auf das Spannungs-Verformungsverhalten
von gefrorenem Schluff im Hinblick auf die Berechnung von Gefrierschächten

13 (1987) **Uwe Stoffers**
Berechnungen und Zentrifugen-Modellversuche zur Verformungsabhängigkeit
der Ausbaubeanspruchung von Tunnelausbauten in Lockergestein

14 (1988) **Gerhard Thiel**
Steifigkeit und Dämpfung von wassergesättigtem Feinsand unter Erdbebenbelastung

15 (1991) **Mahmud Thaher**
Tragverhalten von Pfahl-Platten-Gründungen im bindigen Baugrund,
Berechnungsmodelle und Zentrifugen-Modellversuche

16 (1992) **Rainer Scherbeck**
Geotechnisches Verhalten mineralischer Deponieabdichtungsschichten
bei ungleichförmiger Verformungswirkung

17 (1992) **Martin M. Bizialiele**
Torsional Cyclic Loading Response of a Single Pile in Sand

18 (1993) **Michael Kotthaus**
Zum Tragverhalten von horizontal belasteten Pfahlreihen aus langen Pfählen in Sand

19 (1993) **Ulrich Mann**
Stofftransport durch mineralische Deponieabdichtungen:
Versuchsmethodik und Berechnungsverfahren

20 (1992) **Festschrift anlässlich des 60. Geburtstages von**
Prof. Dr.-Ing. H. L. Jessberger
20 Jahre Grundbau und Bodenmechanik an der Ruhr-Universität Bochum

21 (1993) **Stephan Demmert**
Analyse des Emissionsverhaltens einer Kombinationsabdichtung im Rahmen der
Risikobetrachtung von Abfalldeponien

22 (1994) **Diethard König**
Beanspruchung von Tunnel- und Schachtausbauten in kohäsionslosem Lockergestein
unter Berücksichtigung der Verformung im Boden

23 (1995) **Thomas Neteler**
Bewertungsmodell für die nutzungsbezogene Auswahl von Verfahren zur Altlastensanierung

24 (1995) **Ralph Kockel**
Scherfestigkeit von Mischabfall im Hinblick auf die Standsicherheit von Deponien

25 (1996) **Jan Laue**
Zur Setzung von Flachfundamenten auf Sand unter wiederholten Lastereignissen

26 (1996) **Gunnar Heibrock**
Zur Rissbildung durch Austrocknung in mineralischen Abdichtungsschichten
an der Basis von Deponien

27 (1996) **Thomas Siemer**
Zentrifugen-Modellversuche zur dynamischen Wechselwirkung zwischen Bauwerken
und Baugrund infolge stoßartiger Belastung

28 (1996) **Viswanadham V. S. Bhamidipati**
Geosynthetic Reinforced Mineral Sealing Layers of Landfills

29 (1997) **Frank Trappmann**
Abschätzung von technischem Risiko und Energiebedarf bei Sanierungsmaßnahmen
für Altlasten

30 (1997) **André Schürmann**
Zum Erddruck auf unverankerte flexible Verbauwände

31 (1997) **Jessberger, H. L. (Herausgeber)**
Environment Geotechnics, Report of ISSMGE Technical Committee TC 5
on Environmental Geotechnics

Herausgeber: Th. Triantafyllidis

32 (2000) **Triantafyllidis, Th. (Herausgeber)**
Boden unter fast zyklischer Belastung: Erfahrung und Forschungsergebnisse (Workshop)

33 (2002) **Christof Gehle**
Bruch- und Scherverhalten von Gesteinstrennflächen mit dazwischenliegenden Materialbrücken

34 (2003) **Andrzej Niemunis**
Extended hypoplastic models for soils

35 (2004) **Christiane Hof**
Über das Verpressankertragverhalten unter kalklösendem Kohlensäureangriff

36 (2004) **René Schäfer**
Einfluss der Herstellungsmethode auf das Verformungsverhalten von Schlitzwänden
in weichen bindigen Böden

37 (2005) **Henning Wolf**
Zur Scherfugenbänderung granularer Materialien unter Extensionsbeanspruchung

38 (2005) **Torsten Wichtmann**
Explicit accumulation model for non-cohesive soils under cyclic loading

39 (2008) **Christoph M. Loreck**
Die Entwicklung des Frischbetondruckes bei der Herstellung von Schlitzwänden

40 (2008) **Igor Arsic**
Über die Bettung von Rohrleitungen in Flüssigböden

41 (2009) **Anna Arwanitaki**
Über das Kontaktverhalten zwischen einer Zweiphasenschlitzwand und nichtbindigen Böden

Herausgeber: T. Schanz

42 (2009) **Yvonne Lins**
Hydro-Mechanical Properties of Partially Saturated Sand

43 (2010) **Tom Schanz (Herausgeber)**
Geotechnische Herausforderungen beim Umbau des Emscher-Systems
Beiträge zum RuhrGeo Tag 2010

44 (2010) **Jamal Alabdullah**
Testing Unsaturated Soil for Plane Strain Conditions: A New Double-Wall Biaxial Device

45 (2011) **Lars Röchter**
Systeme paralleler Scherbänder unter Extension im ebenen Verformungszustand

46 (2011) **Yasir Al-Badran**
Volumetric Yielding Behavior of Unsaturated Fine-Grained Soils

47 (2011) **Usque ad finem**
Selected research papers

48 (2012) **Muhammad Ibrar Khan**
Hydraulic Conductivity of Moderate and Highly Dense Expansive Clays

49 (2014) **Long Nguyen-Tuan**
Coupled Thermo-Hydro-Mechanical Analysis: Experimental and Back Analysis

50 (2014) **Tom Schanz (Herausgeber)**
Ende des Steinkohlenbergbaus im Ruhrrevier: Realitäa und Perspektiven für die Geotechnik Beiträge zum RuhrGeo Tag 2014

51 (2014) **Usque ad finem**
Selected research papers

52 (2014) **Houman Soleimani Fard**
Study on the Hydro-Mechanical Behaviour of Fiber Reinforced Fine Grained Soils with Application to the Preservation of Historical Monuments

53 (2014) **Wiebke Baille**
Hydro-Mechanical Behavior of Clays - Significance of Mineralogy

54 (2014) **Qasim Abdulkarem Jassim Al-Obaidi**
Hydro-Mechanical Behavior of Collapsible Soils

55 (2015) **Veselin Zarev**
Model Identification for the Adaption of Numerical Simulation Models - Application to Mechanized Shield Tunneling

56 (2015) **Meisam Goudarzy**
Micro and Macro Mechanical Assessment of Small and Intermediate Strain Properties of Granular Material

57 (2016) **Oliver Detert**
Analyse einer selbstregulierenden interaktiven Membrangründung für Schüttkörper auf geringtragfähigen Böden

58 (2016) **Yang Yang**
Analyses of Heat Transfer and Temperature-induced Behaviour in Geotechnics

59 (2016) **Alborz Pourzargar**
Application of suction stress concept to partially saturated compacted soils

60 (2017) **Hanna Haase**
Multiscale analysis of clay-polymer composites for Geoenvironmental applications

61 (2017) **Kavan Khaledi**
Constitutive modeling of rock salt with application to energy storage caverns

62 (2017) **Nina Silvia Müthing**
On the consolidation behavior of fine-grained soils under cyclic loading

63 (2017) **Elham Mahmoudi**
Probabilistic analysis of a rock salt cavern with application to energy storage systems

64 (2017) **Negar Rahemi**
Evaluation of liquefaction behavior of sandy soils using critical state soil mechanics and instability concept

65 (2018) **Chenyang Zhao**
A contribution to modeling of mechanized tunnel excavation

66 (2018) **Tom Schanz (Herausgeber)**
Innovationen im Spezialtiefbau und in der Umweltgeotechnik Geotechnik
Beitrage zum RuhrGeo Tag 2018

67 (2019) **Linzhi Lang**
Hydro-Mechanical Behaviour of Bentonite-Based Materials Used for
Disposal of Radioactive Wastes

68 (2019) **Usama Al-Anbaki**
Hydraulic Interaction of Soil and Nonwoven Geotextiles under Unsaturated Conditions

69 (2019) **Abhishek Rawat**
Coupled Hydro-mechanical Behavior of a Compacted Bentonite-Sand Mixture: Experimental and Numerical Investigations

Herausgeber: T. Wichtmann

70 (2019) **Mahmoud Qarmout**
Tunnel face stability using Kinematical Element Method (KEM)

curriculum vitae

Personal information

Surname	Mahmoud
Name	Qarmout
E-mail	Mahmoud.Qarmout@rub.de
Nationality	Palestinian
Date of birth	04.11.1977

Education and training

Ph.D.	
Duration	2014 to 2019
Name of Institute	Ruhr Universität Bochum, Germany
Principal subject	Geotechnical Engineering
Title of qualification awarded	Doktor der Ingenieurwissenschaften
Post-Graduation	
Duration	2007 to 2009
Name of Institute	Islamic university of Gaza
Principal subject	Civil Engineering with specialization in Geotechnical Engineering
Title of qualification awarded	Master of science
Graduation	
Date	1996 to 2001
Name of Institute	Islamic university of Gaza
Principal subject	Civil Engineering
Title of qualification awarded	Bachelor of civil Engineering

Publications and articles submitted (In Journal)

Author(s) and title	Arafa M., Shihada S. and Qarmout M. (2010) “Mechanical properties of ultra high performance concrete produced in the Gaza Strip”.
Journal	Asian Journal of Materials Science
Vol. and Pg. No.	2, 1-12
Status	Published
Author(s) and title	Qarmout, M, König, D., Gussmann, P, Thewes, M., Schanz, T. (2019):,“ Tunnel face stability analysis using Kinematical Element Method”.
Journal	Tunneling and Underground Space Technology
Vol. and Pg. No.	85, 354-367.

Status	Published

Publications and articles submitted (In Conference)

Author(s) and title	Qarmout, M., Mohammed, S., Ali, F., 2008,“ Case Study on Slope Stability using 2D finite element method”.
Publication place	*The 2h International Conference on geotechnical engineering, Islamic university of Gaza (IUG).*
Author(s) and title	Blumenthal, A. v., Hölter, R, Qarmout, M., Gussmann, P., Lavasan, A. A., König, D., Schanz, T. (2015):, “Untersuchung der Grundbruch Problematik bei besonderen Randbedingungen mit der KEM”.
Publication place	*Darmstädter Geotechnik-Kolloquium*
Author(s) and title	Qarmout, M,, Schmüdderich, C., König, D., Gussmann, P, Thewes, M. (2019):,‘ “Face stability of a circular tunnel excavated in dry frictional- cohesive soil”.
Publication place	*Tunneling and Underground Construction Conference, Egypt.*

,

Journal reviews

Journal	Tunneling and Underground Space Technology
Number of reviews	5
Journal	**Scientia Iranica (SCI)**
Number of reviews	1
Journal	Applied Sciences
Number of reviews	1